



FACULTY OF ELECTRICAL ENGINEERING
UNIVERSITY OF BANJA LUKA

ELECTRONICS

FACULTY OF ELECTRICAL ENGINEERING UNIVERSITY OF BANJA LUKA

Address: Patre 5, 78000 Banja Luka, Bosnia and Herzegovina

Phone: +387 51 211824

Fax: +387 51 211408

ELECTRONICS

Web: www.electronics.etfbl.net

E-mail: electronics@etfbl.net

Editor-in-Chief:

Branko L. Dokić, Ph. D.
Faculty of Electrical Engineering
University of Banja Luka, Bosnia and Herzegovina
E-mail: bdokic@etfbl.net

International Editorial Board:

- Goce Arsov, St. Cyril and Methodius University, Skopje, Republic of Macedonia
- Petar Biljanović, University of Zagreb, Croatia
- Milorad Božić, University of Banja Luka, Bosnia and Herzegovina
- **Demal Kolonić**, University of Banja Luka, Bosnia and Herzegovina
- Vladimir Katić, University of Novi Sad, Serbia
- Vančo Litovski, University of Niš, Serbia
- Danilo Mandić, Imperial College, London, United Kingdom
- Vojin Oklobdžija, University of Texas at Austin, USA
- Zorica Pantić, Wentworth Institute of Technology, Boston, USA
- Aleksandra Smiljanić, University of Belgrade, Serbia
- Slobodan Vukosavić, University of Belgrade, Serbia
- Volker Zerbe, Technical University of Ilmenau, Germany
- Mark Zwoliński, University of Southampton, United Kingdom
- Deška Markova, Technical University of Gabrovo
- Chakresh Kumar, Galgotias College of Engineering and Technology, Greater Noida, India

Secretary:

Mladen Knežić, M.Sc.
E-mail: mladen_knezic@etfbl.net

Željko Ivanović, M.Sc.
E-mail: zeljko@etfbl.net

Publisher:

Faculty of Electrical Engineering
University of Banja Luka, Bosnia and Herzegovina
Address: Patre 5, 78000 Banja Luka, Bosnia and Herzegovina
Phone: + 387 51 211824
Fax: + 387 51 211408
Web: www.etfbl.net

Number of printed copies: 100

Guest Editorial

WE would like to thank the Editor-in-Chief of *Electronics*, Prof. Branko L. Dokić, for giving us the opportunity to edit this special issue. At the same time, we would like to welcome the readers. This issue represents a selection of the extended versions of the best papers from the 55th Conference for Electronics, Telecommunications, Computers, Automatic Control and Nuclear Engineering (ETRAN), held in Banja Vrućica, Republika Srpska on June 6-9, 2011. Throughout the decades, ETRAN has become a traditional conference in the field of electrical and electronics engineering. Nowadays it is maybe the oldest and most prestigious conference in this field in the whole of the Western Balkans.

Each of the present manuscripts underwent a triple selection. The best ETRAN presentations were first nominated by the session chairs. The supervision and subsequent proposals were done by the chairs of the ETRAN Programme Committee Sections. The final choice of the papers was entrusted to us. All authors were requested to revise and expand their manuscripts, which were further reviewed in a single-blind process.

Although ETRAN consists of 16 independent sections dedicated to different fields of the electrical and electronic engineering, it is readily visible that some themes are of common interest and appear repeatedly in different sections. Among these, telecommunications and multimedia attracted by far the largest attention of the authors. Information security was analyzed through digital signature encryption algorithms by Bojan Pajčin and Predrag N. Ivaniš (Telecommunication Section, chairs Dušan Drajić, Faculty of Electrical Engineering, Belgrade and Zorica Nikolić, Faculty of Electronics, Niš). Sensors for human-machine interfaces for multimedia were handled by Miloš Petković *et al* (Electronics Section, chair Predrag Petković, Faculty of Electronics Niš). Communications and computing for distance learning were considered by Milica B. Naumović *et al* (Computers Section, chair Jovan Đorđević, Faculty of Electrical Engineering, Belgrade). Another paper dedicated to multimedia, this time through an analysis of problems related with digital TV, was authored by Dušan Milosavljević (also Computers Section). Image processing for databases in traffic control, ID documents, etc were handled by Ivan Božić *et al* (Electric Circuits and systems and signal processing Section, chair Miroslav Lutovac, Faculty of Electrical Engineering, Belgrade), while linearization of Doherty amplifiers was considered by Aleksandar Atanasković and Nataša Maleš Ilić (Microwave and Submillimeter Technique Section, chair Vera Marković, Faculty of Electronics Niš).

Another group were papers dedicated to power engineering. These included analysis of phase locked loops in power systems – Evgenije Adžić *et al* (Power Engineering Section, chair Andrija T. Sarić, Technical Faculty, Čačak), wind turbines – Đorđe Klisić *et al* (Metrology Section, Vladimir Vujičić, Faculty of Technical Sciences, Novi Sad), control of thermal power plants using robust adaptive identification – Goran S. Kvaščev *et al* (Automatic Control Section, chair Željko Đurović, Faculty of Electrical Engineering, Belgrade). Nanotechnologies were investigated by Katarina Radulović and Sylvia Jenei in their paper on optical tweezers (nanoETRAN workshop within the Microelectronics and Optoelectronics Section, chair Zoran Jakšić, Institute for Chemistry, Technology and Metallurgy, Belgrade). Microstrip circuits were analyzed by Biljana P. Stošić and Jugoslav Joković (again Microwave Section). Humanoid robot walk was considered by Branislav Borovac (Robotics and Flexible Automation Section, chair Aleksandar Rodić, Institute Mihajlo Pupin, Beograd) and clustering techniques for control of industrial processes and error detection were analyzed by Milan R. Rapaić *et al* (Automatic Control Section). The ecological influences of bombing by depleted uranium were investigated by Zora S. Žunić *et al* (Nuclear Engineering Section, chair Miodrag Milošević, Institute Vinča, Belgrade) and defectoscopy by quadrasonic ultrasonic transmission method was analyzed by Zoran Ebersold *et al* (New Materials Section, chair Nebojša Mitrović, Technical Faculty, Čačak).

A significant overlapping between themes and topics can be seen among different sections. Some themes reappear throughout different papers, like those of measurement and control, computers and telecommunications. It is readily visible that the topics covered are fully congruent with those appearing in the contemporary world literature. Also, it was sometimes heard that the scope of the ETRAN conferences is too wide and related with too many different topics. When observing the mentioned overlaps, the rationale for the existence of such a conference become self-evident. In this multidisciplinary world such a wide coverage is exactly what makes the ETRAN conference a modern one.

The editors of this special issue hope that reading of this collection of papers will be as interesting to the readers as its collecting was to the editors.

Bratislav Milovanović
Zoran Jakšić

Guest Editors

Bratislav Milovanovic Biography



Bratislav Milovanovic, Full Professor at the Faculty of Electronic Engineering, University of Niš, was born in 1948 in the village Rosica near Ribarska Banja, Serbia. He received his Dipl.-Ing., Mag. Sci. and Ph.D. degrees in electrical engineering (Telecommunications) in 1972, 1975, and 1979, respectively. Since September 1972, he is with same

Faculty, where he has been promoted to the academic positions Reaching Assistant, Assistant Professor, Associate Professor, and Full Professor in 1972, 1980, 1985, and 1990, respectively.

He founded one laboratory for students' practical exercises and two research laboratories. Professor Milovanović is the author of 5 student's textbooks. He supervised 11 Ph.D. theses, 16 M.Sc. theses, and more than 150 diploma works. From 1981 to 1984 he was head of the Chair for Theoretical Electrical Engineering and from 1994 to 2000 and again from 2004 he was head of the Chair for Telecommunication. He was the Vice-dean of the Faculty of Electronic Engineering in Nis in the period from 1987 to 1991 and Dean from 1994 to 1998. From 1996 to 2001 he was the President of the Administrative Committee of Ei HOLDING Co., Nis.

Professor Milovanović has achieved outstanding results in the field of research and scientific work in numerical electromagnetics, microwave technique and telecommunications. He is the author of more than 500 scientific papers in telecommunications - three published in international monographs, over 50 published in world-known scientific journals, over 170 were presented at international conferences, over 30 published in domestic journals, etc.. Professor Milovanović has been the editor of 13 international conference proceedings. He has also been a reviewer of several world-leading scientific journals and conferences and a

member of several editorial boards of the international scientific journals. He was also a guest-editor eleven times of special issues of international and national scientific journals (IJRIS, Electronics, Facta Universitatis: Series: Electronics&Energetics, Microwave Review and etc.). Professor Milovanović is a founder and chairman of the high-level international IEEE conference on telecommunications - TELSIS. As the chairman or a member of organizing or technical program committees he also has given a significant contribution to the organization of a number of other scientific and professional conferences (ICEST, NIKOLA TESLA, ETRAN, YU INFO, NEUREL, TELFOR and InfoTeh-Jahorina).

Professor Milovanović is a member of the international professional associations (IEEE, EuMA, WISAS and ARFTG), president of the National MTTS Society (since 2000), president of the National IEEE MTT Chapter (since 2004), vice-president and president of the ETRAN Society Chairmanship (since 2000). He is the founder and he was the first president of the ETRAN Committee for Microwave, and Submillimeter Technique. He was the member of Commission on accreditation and quality evaluation of the Republic of Serbia. Since 2006 he has been vice-president of the Advisory Council of the Republic Telecommunication Agency. He has been a member of the Serbian Scientific Society since 1999, a corresponding member of the Yugoslav Engineering Academy since 2000 and full member of Academy of Engineering Sciences of Serbia since 2004.



Prof. Dr. Bratislav Milovanović
University of Niš, Serbia

Zoran Jakšić Biography



Zoran Jakšić, Full Research Professor – Principal Research Fellow of the Center of Microelectronic Technologies and Single Crystals, a department of the Institute of Chemistry, Technology and Metallurgy, University of Belgrade, Serbia, was born in 1960 in Pancevo, Serbia. He received his Dipl.-Ing., Mag. Sci. and Ph.D. degrees in electrical engineering (engineering physics), all

from the School of Electrical Engineering, University of Belgrade, Serbia.

His fields of interest are mesoscopic and subwavelength electromagnetic optics/nanooptics and nanophotonics including photonic band gap materials; plasmonics and nanoplasmonics, including negative refractive index metamaterials, subwavelength plasmonic crystals, etc.; advanced solid-state sensors, photonic sensors, MEMS and NEMS devices; long-wavelength infrared semiconductor photodetectors, including Auger-suppressed nonequilibrium devices; narrow-bandgap semiconductors.

Between 1984 and 1987 Zoran Jakšić worked with the R&D Department of Utva Aircraft Factory, Pančevo, Serbia (avionics division). Since 1987 he has been with the Belgrade-based Institute of Chemistry, Technology and Metallurgy (ICTM). Since 1989 he was also engaged at the School of Electrical Engineering, University of Belgrade, where he introduced three new courses (*Microelectromechanical Systems; Elements of Nanooptics and Nanophotonics; and Photonic Crystals and Optical Metamaterials*).

Currently Zoran Jakšić is the Deputy Director for Scientific Affairs with the ICTM's Center of Microelectronic Technologies and Single Crystals.

He authored more than 220 peer-reviewed publications, including 48 international journal papers and five international

book chapters. He edited proceedings of the International Workshop on Nanoscience and Nanotechnology IWON and 3rd Mediterranean Conference on Nanophotonics MediNano-3. He also edited 9 proceedings from national conferences. He is the chair of Technical Programme Committee of the ETRAN Society. He is a founder and chairman of the series of annual workshops on nanosciences and nanotechnologies nanoETAN (since 2005). He has been a member of organizing or technical program committees of several international conferences, including MediNano, IEEE MIEL and Nikola Tesla. He has also been a reviewer of 15 world-leading scientific journals with high impact factors, including *Optics Express*, *Optics Letters*, *Journal of Optics*, *New Journal of Physics*, *Journal of Physics C*, *Infrared Physics and technology*, *Semiconductor Science and Technology*, *Optics Communications*, *IEEE Sensors*, *Physica Scripta*, etc.

Zoran Jakšić is a Senior Member of the IEEE (The Institute of Electrical and Electronics Engineers) – Photonics and MTT Societies, a member of the OSA (Optical Society of America), the OSS (Optical Society of Serbia), National Society for Microwave Technique and Technologies of Serbia and the ETRAN (Electronics, Telecommunications, Computers, Automatic Control and Nuclear Engineering) Society.



Zoran Jakšić
*Institute of Chemistry, Technology and Metallurgy
University of Belgrade, Serbia*

Improved PLL for Power Generation Systems Operating under Real Grid Conditions

Evgenije M. Adžić, Milan S. Adžić, and Vladimir A. Katić

Abstract—Distributed power generation systems (DPGS) based on renewable energy sources need accurate grid phase angle information in order to achieve different control algorithms usual for this application. Phase-locked loop (PLL) is the most modern and most common method for determination of the phase angle and frequency of the grid voltage. However, there are still serious limitations of reported PLL algorithms in real grid voltage conditions, as in unbalanced and distorted distribution grid. This paper proposes improved PLL which gives excellent and almost perfect grid voltage phase angle and frequency in highly unbalanced and distorted grid. This is achieved by a cascade of finite impulse response filters which eliminates characteristic harmonic components and extracts only fundamental harmonic signal. In that way, proposed PLL allows setting of higher bandwidth frequency of the PLL filter and much faster response which is especially important during grid voltage sags and frequency variations. Performance has been evaluated in details through simulation in Matlab/Simulink.

Index Terms—Distributed power generation systems, synchronization method, phase-locked loop, distorted grid.

I. INTRODUCTION

THE worldwide electrical energy consumption is rising. Therefore, increase of the demands on the power capacities, efficient generation, distribution and utilization of energy are noticeable [1]. In power systems sector there is a key movement from a relatively small number of large, centrally controlled conventional power stations connected to the transmission system towards a greater number renewable energy generating plants such as wind turbines, photovoltaic generators and fuel cells, now connected to the distribution grid. Power electronics, being the technology for efficiently converting electrical power, represents essential part that enabled such a development. Power electronics devices serve as an interface between DPGS and a grid, with the task to

adapt the produced power to the numerous grid requirements.

In general, DPGS contains a power converter connected to the grid, whose main task is to control the transfer of active and reactive power between the DPGS and the grid. Different control structures for the grid connected converter have been proposed in the relevant literature [2], where grid voltage oriented vector control is usually employed [3]. Vector control principle depends on accurate and precise determination of the grid voltage phase angle, which is required in order to achieve independent control of active and reactive power. This task is performed by grid synchronization unit.

The quality of the grid synchronization, in addition to current regulators in the control structure, is a key factor which determines the quality of the entire control structure [2], [4]. Error in the phase angle estimation can lead to significant error in the imposed converter output voltage and its distortion, thus resulting in the error between the reference and injected power into the grid and in inappropriate operation during various grid disturbances.

In the literature related to the grid synchronization field, different methods can be found which are applied in practice for DPGS [2], [4]. The zero crossing detection is the simplest method, but achieve slow dynamic and a fast tracking of the phase angle is impossible. This method is subject to a great influence of grid voltage harmonics and voltage dips. There are methods based on filtering of grid voltage in α - β stationary and rotating d-q reference frame, although filtering enters delay in the output phase angle signal which makes this method vulnerable to a relatively frequent voltage sags in the distribution grid. The most common method used today for grid synchronization is a phase-locked loop (PLL) implemented in the d-q synchronous rotating reference frame, which block diagram is shown in Fig.1. It contains a filter, usually proportional-integral (PI) controller type, that determines its dynamics. Especially, it is influenced by presence of unbalance and distortion in the grid voltage. Therefore, filter bandwidth is a compromise between filtering undesirable harmonics that occur in the PLL system due to the voltage unbalance and harmonics, and fast response time necessary for tracking voltage during a voltage sags and frequency variations in the grid. Therefore, it is often necessary to significantly reduce the filter bandwidth at the expense of poor and slow response during the grid disturbances.

This paper was financially supported by Ministry of the Republic of Serbia within the project III42004. Some results of this paper were presented at 55th ETRAN Conference, Banja Vrućica, June 6-9, 2011.

E. M. Adžić is with the Faculty of Technical Sciences, University of Novi Sad, Trg Dositėja Obradovica 6, Novi Sad, Serbia (phone: +381214852504; fax: +381214750572; e-mail: evgenije@uns.ac.rs).

M. S. Adžić is with the Subotica Tech – College of Applied Sciences, University of Novi Sad, Marka Oreskovica 16, Subotica, Serbia (e-mail: adzicm@vts.su.ac.rs).

V. A. Katić is with the Faculty of Technical Sciences, University of Novi Sad, Serbia (e-mail: katav@uns.ac.rs).

In this paper, an improved pre-filter based PLL for three-phase grid interface converters is proposed. Proposed PLL obtains accurate and almost perfect grid voltage phase angle and frequency even in highly unbalanced and distorted voltage conditions. This is achieved by employing a cascade of finite impulse response filters (FIR) which eliminates characteristic harmonic components in the PLL system caused by grid voltage distortions and extracts only fundamental harmonic signal represented in d-q reference frame. With proposed PLL it is possible to have fast dynamic and consequently it has much better response with grid frequency variations and voltage sags. Extensive simulation results are provided for validation of the proposed algorithm.

II. PLL PRINCIPLE OF OPERATION AND MODEL

A block diagram of the conventional PLL implemented in d-q synchronous rotating reference frame is depicted in Fig. 1. Its principle of operation can be explained through the following steps:

- Three-phase grid voltages v_a , v_b , and v_c are measured. At first, a balanced three-phase set of voltages could be assumed, where θ represent actual phase angle of grid voltage in the first phase (a):

$$\begin{aligned} v_a &= V_g \cdot \cos \theta \\ v_b &= V_g \cdot \cos(\theta - 2\pi/3) \\ v_c &= V_g \cdot \cos(\theta + 2\pi/3) \end{aligned} \quad (1)$$

- Measured phase voltages are transformed to a α - β stationary reference frame using Clarke transformation, resulting in voltage components v_α and v_β :

$$\begin{aligned} v_\alpha &= 2/3 \cdot [v_a - (v_b - v_c)/2] \\ v_\beta &= 1/\sqrt{3} \cdot (v_b - v_c) \end{aligned} \quad (2)$$

- α - β voltage components are transformed to d-q synchronous rotating reference frame using Park transformation with estimated phase angle $\hat{\theta}$ from the PLL output. Grid voltage components v_d and v_q are obtained:

$$\begin{aligned} v_d &= v_\alpha \cdot \cos \hat{\theta} + v_\beta \cdot \sin \hat{\theta} \\ v_q &= -v_\alpha \cdot \sin \hat{\theta} + v_\beta \cdot \cos \hat{\theta} \end{aligned} \quad (3)$$

After applying Park transformation d-q components are equal to:

$$\begin{aligned} v_q &= V_g \cdot \sin(\theta - \hat{\theta}) \\ v_d &= V_g \cdot \cos(\theta - \hat{\theta}) \end{aligned} \quad (4)$$

- Error signal e is formed by subtracting the reference signal v_q^* and obtained grid voltage component v_q , which is set to the input of PLL filter. Setting the reference v_q^* to 0 is responsible for tracking the phase angle of grid phase voltage (v_a). As PLL filter, proportional-integral (PI) controller is selected, in order to reduce the error signal e to zero:

$$e = 0 - v_q = -V_g \cdot \sin(\theta - \hat{\theta}) \wedge e = 0 \Rightarrow \hat{\theta} = \theta \quad (5)$$

which would lead to steady-state equalization of estimated and actual grid voltage phase angle. PI controller is selected as the

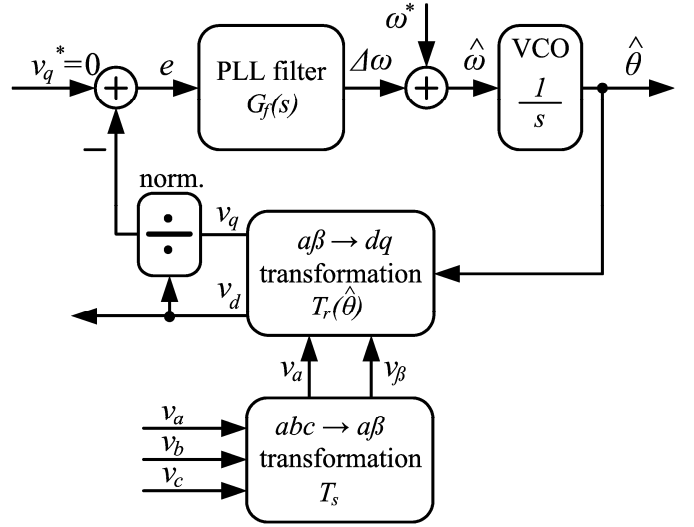


Fig. 1. Block diagram of the conventional dq-PLL system.

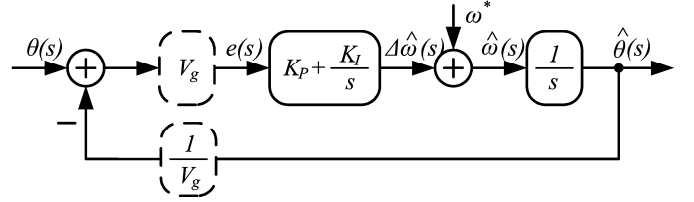


Fig. 2. Linearized model of conventional dq-PLL system.

filter type, because in the steady-state the error signal would be zero for abrupt changes in the voltage phase angle, but also for the abrupt changes of the voltage frequency (ramp input), which is expected in DPGS applications due to a weak distribution grid where failures are common. Near the steady-state, where small difference between the real and estimated phase angle exist, error signal can be linearized in order to obtain a suitable model and simplify PLL analysis:

$$e \approx V_g \cdot (\theta - \hat{\theta}) \quad (6)$$

- Base on error signal e , PI controller calculates the grid voltage angular frequency change $\Delta\omega$, which in the continuous Laplace s-domain can be represented with:

$$\Delta\omega(s) = G_f(s) \cdot e(s) = \left(K_p + \frac{K_I}{s} \right) \cdot e(s) \quad (7)$$

- $\Delta\omega$ at the PI controller output is added to the reference angular frequency ω^* , which is set to the value of actual grid angular frequency (e.g. $2\pi \cdot 50$ rad/s). This would result with a estimated grid angular frequency $\hat{\omega}$ value .

- Integrating the estimated angular frequency $\hat{\omega}$ in time, estimated grid voltage phase angle is obtained:

$$\hat{\theta}(s) = \frac{1}{s} \cdot \hat{\omega}(s) \quad (8)$$

- Estimated phase angle $\hat{\theta}$ is used to calculate new voltage d-q components, until v_q becomes zero and v_d becomes constant equal to the grid voltage amplitude, and finally when the difference between actual phase angle of the grid voltage and estimated phase angle becomes zero.

- Estimated grid voltage amplitude (v_d) is used to

normalize voltage q-component at the PI controller feedback input, in order to eliminate grid voltage amplitude variations influence on the PLL response [9] determined and designed with filter (PI) parameters (see Fig. 2).

From previous, linearized PLL model in continuous Laplace domain could be extracted, which is shown in Fig. 2. The transfer function of the closed loop conventional d-q PLL is of second order with one zero and could be rewritten in general form as:

$$G_c(s) = \frac{s \cdot K_P + K_I}{s^2 + s \cdot K_P + K_I} = \frac{s \cdot 2\xi\omega_n + \omega_n^2}{s^2 + s \cdot 2\xi\omega_n + \omega_n^2} \quad (9)$$

where are: ξ – relative damping factor, and ω_n – system natural frequency. It is the size of ξ and ω_n which characterize system performance in the transient-state in time domain. From the transfer function form, one could conclude that the desired character of the PLL response is achieved by tuning parameters of the PI controller [8]:

$$\omega_n = \sqrt{K_I} \quad \xi = \frac{K_P}{2} \sqrt{\frac{1}{K_I}} \quad K_I = \frac{K_P}{T_I} \quad (10)$$

III. PLL IN UNBALANCED AND DISTORTED GRID CONDITIONS

In practice, distribution grid voltage has not a pure sinusoidal waveform but it is disturbed by various factors such as load unbalance and nonlinearities [5]. Resulted three-phase voltage waveforms are unbalanced and with harmonics. The possible grid voltage signal offset is often introduced by the measurement and conversion electronic circuits, but its influence is not considered in this paper.

A. Grid Voltage Unbalance

The unbalanced set of three-phase voltages can be expressed as:

$$\begin{aligned} v_a &= V_g \cdot \cos \theta \\ v_b &= V_g \cdot (1+a) \cdot \cos(\theta - 2\pi/3) \\ v_c &= V_g \cdot (1+b) \cdot \cos(\theta + 2\pi/3) \end{aligned} \quad (11)$$

where constants a and b indicates unbalance level. After transformation in α - β stationary reference frame they can be expressed as:

$$\begin{aligned} v_\alpha &= V_g \cdot \cos \theta + V_g \cdot \frac{a+b}{6} \cdot \cos \theta + V_g \cdot \frac{b-a}{2\sqrt{3}} \cdot \sin \theta \\ v_\beta &= V_g \cdot \sin \theta + V_g \cdot \frac{a+b}{2} \cdot \sin \theta + V_g \cdot \frac{b-a}{2\sqrt{3}} \cdot \cos \theta \end{aligned} \quad (12)$$

The second and third terms in (12) are produced by the phase unbalance. Assuming that error $e = \theta - \hat{\theta}$ is small (near zero in steady-state) and $\theta + \hat{\theta} = 2\theta$, the voltage d-q components can be derived after Park transform as:

$$\begin{aligned} v_d &= V_g + V_g \cdot \frac{a+b}{3} + V_g \cdot \left(\frac{b-a}{2\sqrt{3}} \cdot \sin 2\theta - \frac{a+b}{6} \cdot \cos 2\theta \right) \\ v_q &= V_g \cdot \sin e + V_g \cdot \frac{a+b}{3} \cdot \sin e \\ &+ V_g \cdot \left(\frac{a+b}{6} \cdot \sin 2\theta + \frac{b-a}{2\sqrt{3}} \cdot \cos 2\theta \right) \end{aligned} \quad (13)$$

Since the voltage q-component is controlled to zero by the PLL system, error caused by unbalanced grid would be:

$$e \approx -V_g \cdot \left(\frac{a+b}{6} \cdot \sin 2\theta + \frac{b-a}{2\sqrt{3}} \cdot \cos 2\theta \right) \quad (14)$$

One can note that second harmonic component would propagate through the PLL system if three-phase grid voltage is unbalanced.

B. Grid Voltage Harmonics

Another significant effect which influences PLL operation is voltage harmonics. A consequence of numerous nonlinear loads in the distribution grid is distorted grid voltage waveform, which is usually flattened (or sharpened at the converter-side of the distribution transformer) in the region of its maximal values, and contains dominant 5th and 7th harmonic components. Therefore, distribution grid voltage with the dominant harmonics can be represented as follows:

$$\begin{aligned} v_a &= V_g \cdot \cos \theta + V_{g5} \cdot \cos 5\theta + V_{g7} \cdot \cos 7\theta \\ v_b &= V_g \cdot \cos(\theta - 2\pi/3) + V_{g5} \cdot \cos[5 \cdot (\theta - 2\pi/3)] + \\ &+ V_{g7} \cdot \cos[7 \cdot (\theta - 2\pi/3)] \\ v_c &= V_g \cdot \cos(\theta + 2\pi/3) + V_{g5} \cdot \cos[5 \cdot (\theta + 2\pi/3)] + \\ &+ V_{g7} \cdot \cos[7 \cdot (\theta + 2\pi/3)] \end{aligned} \quad (15)$$

where V_{g5} and V_{g7} represents amplitudes of 5th and 7th harmonics, respectively. α - β stationary reference frame components of the grid voltage given with (15) can be expressed as:

$$\begin{aligned} v_\alpha &= V_g \cdot \cos \theta + V_{g5} \cdot \cos 5\theta + V_{g7} \cdot \cos 7\theta \\ v_\beta &= V_g \cdot \sin \theta - V_{g5} \cdot \sin 5\theta + V_{g7} \cdot \sin 7\theta \end{aligned} \quad (16)$$

The second and third terms in (16) are produced by the voltage harmonics. Assuming that error $e = \theta - \hat{\theta}$ is small (near zero in steady-state) and $5\theta + \hat{\theta} = 6\theta$ and $7\theta - \hat{\theta} = 6\theta$, the voltage d-q components can be derived after Park transformation as:

$$\begin{aligned} v_d &= V_g + (V_{g5} + V_{g7}) \cdot \cos 6\theta \\ v_q &= V_g \cdot \sin e - (V_{g5} - V_{g7}) \cdot \sin 6\theta \end{aligned} \quad (17)$$

Therefore, the PLL error which would occur in estimated phase angle and frequency due to the 5th and 7th harmonic can be represented with following expression:

$$e \approx (V_{g5} - V_{g7}) \cdot \sin 6\theta \quad (18)$$

Besides the sixth harmonic component in the PLL system, frequency components of 120, 180, ... would appear if higher harmonic components, characteristic for the distribution grid, are included. They are not considered in this paper, because

they are negligibly small in real grid compared to 5th and 7th harmonics.

IV. CRITERIA AND SELECTION OF PLL FILTER PARAMETERS

PLL operation is subject to the influence of various disturbances in the grid, as shown in previous section. Grid voltages unbalance and distortion introduce second and (dominantly) sixth harmonic components (errors) in d-q PLL system.

In addition, in section II it is shown that the PLL system dynamic depends on the parameters of the filter. It can be concluded that the slow dynamic of the filter would give very filtered and stable phase angle, but with longer synchronization time. On the other hand, filter with high dynamic would give a phase angle that follows rapid variations in a grid voltage (necessary during grid faults), but the grid disturbances (harmonics, unbalance, offset) would propagate through the filter, resulting in erroneous phase angle. Therefore, when designing a PLL filter, one usually must make a compromise, or select slow or fast filter dynamic due to the purpose of the system.

Most commonly in relevant literature, one can found that cut-off frequency of 50 Hz or response settling time of 20 ms are selected for PLL filter (if grid frequency is 50 Hz), explaining it with the fact that grid frequency needs to be fast followed [2]. It is the right selection if synchronization algorithm is employed to detect or response to grid faults and frequency variations. However, undesirable consequence is that a large bandwidth (due to the high filter gains) amplifies and propagates even small harmonics due to the grid voltage distortion. It represents large disadvantage for synchronizing the control variables to the grid voltage vector in order to have an accurate synchronization and good quality control. Considering that grid regulations in some countries require normal operation of distributed generators in the case of grid frequencies between 47 and 53 Hz, another selection of cut-off frequency could be around 3 Hz. Such PLL synchronization system would have opposite behavior compare to previous one (where cut-off frequency is 50 Hz).

It is known that in the general case of a second order system step response, there are two parameters defined: settling time T_{set} , and overshoot P , that determines system performance in the transient-state in time-domain. Their correlation with relative damping factor ζ , and system natural frequency ω_n , could be expressed with following:

$$\zeta = \frac{\sqrt{(\ln P/\pi)^2}}{1 + (\ln P/\pi)^2} \quad \omega_n = \frac{4,6}{\zeta \cdot T_{set}} \quad (19)$$

where T_{set} represents required time for response signal to enter in $\pm 1\%$ zone around steady-state reference step value. Correlations (10) and (19) provide, based on pre-specified settling time T_{set} and overshoot P , determination of the required gains in PLL filter. Another approach for filter design is to use desired system frequency bandwidth ω_{bw} instead of settling time, as an input design parameter. In a rough

approximation for second-order system one can use equal bandwidth and system natural frequency, or could use following exact correlation:

$$\omega_{bw} = \omega_n \cdot \sqrt{|2\zeta^2 - 1| + \sqrt{\zeta^4 - 4\zeta^2 + 2}} \quad (20)$$

It is desirable that the PLL response has no excessive overshoot and no oscillations in order to avoid possible active and reactive power oscillations between a grid-side converter of distributed generators and a grid [4]. It is considered that the response with overshoot less than 5% is well-damped, so the damping coefficient ζ should be larger than 0.7. For desired aperiodical response $\zeta = 1$, and based on given equations, parameters of the PLL filter are supposed to be as follows:

$$K_P = \sqrt{2} \cdot \omega_{bw} \quad \wedge \quad K_I = \frac{\omega_{bw}^2}{2} \left(K_I^z = K_I T_s \right) \quad (21)$$

For example, for bandwidth frequency $f_{bw} = 3$ Hz parameters $K_P = 26.6$ and $K_I = 177.6$ are obtained. The digital filter implementation (discrete z-domain) integral gain should be multiplied by the PLL loop sampling period T_s . Figs 3 and 4 gives step time-response and frequency response for design bandwidths of 3 Hz and 50 Hz, respectively. From Fig. 3 it can be observed that in both cases response overshoot is larger then designed and equal to 13.5 %. Fig. 4 shows slightly deviation of achieved bandwidths 5.2 Hz and 87.5 Hz compare to 3 Hz and 50 Hz set by design. These variations are consequences of existence of zero in the PLL transfer function that has been ignored during design. In order to eliminate this effect, some authors suggest introducing a lead-lag compensator in the PLL loop [2].

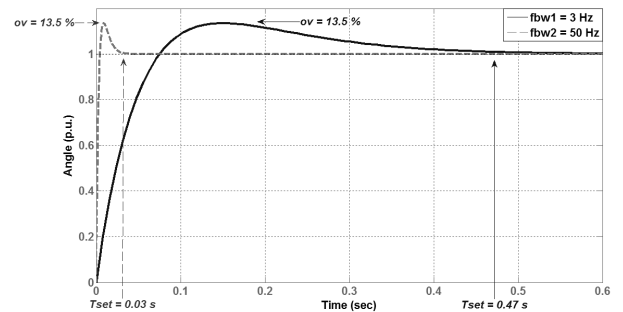


Fig. 3. Conventional d-q PLL step response for two different filter desired frequency bandwidth – 3 Hz (solid line) and 50 Hz (dashed line).

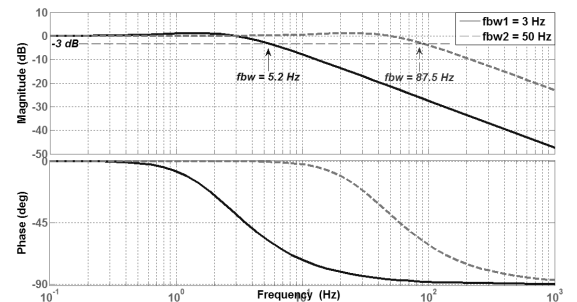


Fig. 4. Conventional d-q PLL frequency response for two different filter desired frequency bandwidth – 3 Hz (solid line) and 50 Hz (dashed line).

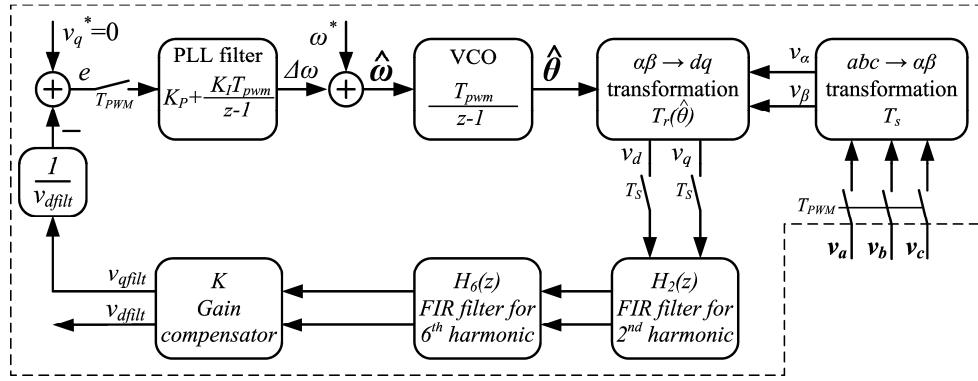


Fig. 5. Block diagram of the proposed pre-filter based d-q PLL system. Pre-filtering done on d-q voltage components eliminates characteristic harmonics influence.

V. PROPOSED PLL WITH PRE-FILTERING

In this section, an improved pre-filter based PLL is described and analyzed in details, which is simultaneously capable for rejecting characteristic errors due to grid unbalance and distortion and for achieving fast and appropriate response during grid frequency variations and voltage sags.

Proposed method basically consists of a synthesis of the second order FIR subsections that eliminates characteristic harmonic components which could occur in the PLL estimated phase angle and frequency. The complete FIR filter is implemented as a cascade of these modules. Block diagram of the proposed PLL is depicted in Fig. 5. It can be observed that pre-filters are used for rejecting harmonics in voltage d-q components and then used as inputs for conventional PLL. All further analysis and simulations are done in discrete z-domain.

Second order FIR filter which eliminates harmonic component f_i and have unity gain for selected fundamental frequency f_1 can be expressed as:

$$H_i(z) = \frac{1 - 2\cos(2\pi f_i / f_s)z^{-1} + z^{-2}}{2[\cos(2\pi f_1 / f_s) - \cos(i \cdot 2\pi f_1 / f_s)]} \quad (22)$$

where i represent harmonic order for which transfer function have zero gain. In discrete domain term z^{-1} represent sample in previous sampling period, where f_s is the sampling frequency. In Fig. 5, $H_2(z)$ denotes transfer function of FIR filter employed to remove second harmonic component in PLL due to unbalanced grid, and $H_6(z)$ denotes FIR transfer function dedicated for removing sixth harmonic component due to distorted grid with 5th and 7th harmonics.

Amplitude- and phase-frequency characteristic of the FIR filters cascade is denoted in Fig. 6. One can observe that the filter completely attenuates characteristic harmonics and it has unity-gain for grid frequency (50 Hz). Good feature of the proposed filter is that it does not introduce delay for constant signal such are d-q components. That means there is neither need for phase compensator, as in [6], which would correct introduced phase shift by filters (at fundamental frequency) if it was implemented in original phase abc-domain. However, gain correction is needed and from given Bode diagram in Fig. 6 one can found that correction gain is equal to

$$K = 1/1.4142 (=1/\sqrt{2}).$$

Special consideration must be taken into account when choosing sampling frequency for FIR filters [11]. On the one hand, it is desirable to have as highest possible sampling frequency (e.g. at pulse-width modulation level in power converters) in order to have fast updating of estimated phase angle and small error due to discretization. This is especially important in the case when FIR filtering is done in original phase abc-domain, but not the case when it is done in synchronous rotating reference frame where d-q components are constant values in steady-state. On the second hand, FIR filter (and also phase compensator) has amplitude characteristic with an increasing gain for higher frequencies then zero-gain frequency f_i , which is denoted in Fig. 7. Between designed zero-gain frequency $f_i = 300\text{Hz}$ and half of sampling frequency $f_s/2 = 4000/2$ Hz, such filter would significantly amplify eventual higher harmonics occurring in

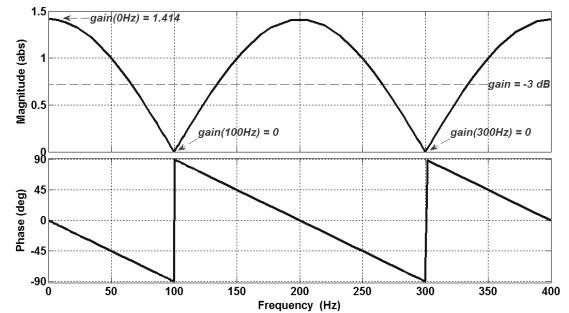


Fig. 6. Frequency characteristic of FIR filters cascade.

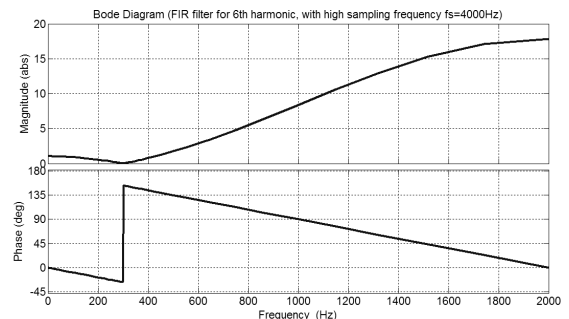


Fig. 7. Example of FIR filter frequency characteristic with high sampling frequency ($f_s = 4$ kHz). High gains for higher frequencies are not acceptable.

the system. Considering the existence of other higher harmonics in the grid (11th, 13th...) as well as the presence of a significant noise typical for this application, previous fact put limitations for selecting sampling frequency f_s . That is the reason why in this paper sampling frequency is chosen to be equal to 800 Hz. In that way proposed FIR filter does not propagate next possible 12th harmonic through the PLL system, due to 11th and 13th harmonic components in the grid voltage.

Fig. 8 shows frequency response of entire proposed PLL structure with FIR pre-filtering. Bandwidth frequency used in (conventional) PLL filter design is 25 Hz. Fig. 8 validates that proposed PLL has high frequency bandwidth (62.3 Hz) and as a consequence fast response required for tracking grid voltage angle during grid faults, but simultaneously cancels characteristic harmonic components at 100 Hz and 300 Hz. Gain for constant signals equals to 3 dB ($\sqrt{2}$ abs.) indicating that gain compensator ($1/\sqrt{2}$) must be used (look Fig. 5).

VI. SIMULATION RESULTS

In this section, simulation results which verify effectiveness and usefulness of the proposed PLL algorithm are presented. Simulation is carried out in MATLAB/Simulink. During course of this work at the input of the simulated PLL system there was a highly distorted and unbalanced grid voltage with nominal grid frequency of 50 Hz.

Fig. 9 shows grid voltage waveforms used in the simulation. Fundamental harmonic with amplitude 1.0 p.u. is distorted with 5th and 7th harmonics, each with amplitude 0.05 p.u. In that way, total harmonic distortion (THD) of the simulated

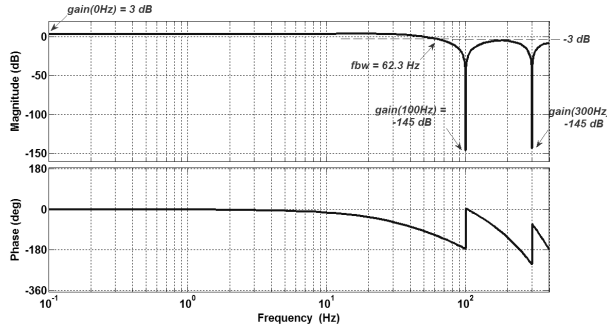


Fig. 8. Frequency characteristic of proposed PLL structure (without gain compensator).

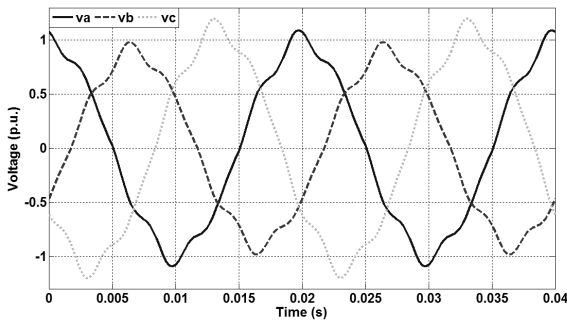


Fig. 9. Grid phase voltage waveforms used in simulation. Simulated unbalance is 10% and total harmonic distortion 7.07% (with 5th and 7th harmonics).

grid voltage is 7.07% which is higher than allowed by standards (5%) for the distribution grid. Phase shift of the harmonics is set in order to have typical waveform of the grid voltage at which power converter is connected. Unbalance of 10% is additionally introduced in the voltage waveforms, with constants indicating unbalance level $a = -0.1$ and $b = 0.1$.

At first, the proposed synchronization algorithm is tested against phase angle jumps and response was compared to conventional PLL. Change in reference q-voltage component at the PLL input is analogue to the grid voltage phase jump, but response details are easier to observe and analyze. Obtained response details are important because they would determine system response during faults where grid voltage could experience phase jump [10]. Voltage amplitude change during faults would result in second harmonic content in PLL system, so it is in some extent included by introduced unbalance (10%). Figs 10 and 11 illustrates behavior of conventional and proposed PLL in the situation of highly disturbed grid voltages (from Fig. 9) when q-voltage reference is set to 0 at 0.04 s (equivalent phase jump 90°) and to 0.5 p.u. at instant 0.6 s (equivalent phase jump of 60°). As it can be observed, the proposed PLL is able to track the new phase angle in about 2 fundamental periods (0.04 s), with a 20 % overshoot during transient. This is due to the higher bandwidth 25 Hz set in proposed system, compare to 3 Hz in conventional PLL which is set in order to limit d-q voltage components oscillations due to the unbalanced and distorted grid. Even though, oscillations in conventional system are much larger, and it could be observed in Fig. 12. It gives q-voltage component during 2 fundamental voltage periods, in

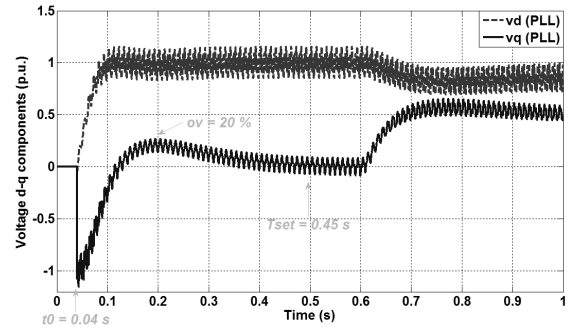


Fig. 10. d-q grid voltage components at the input of the conventional PLL system. Response to abrupt grid voltage phase shift of 60 degrees (at 0.6 s).

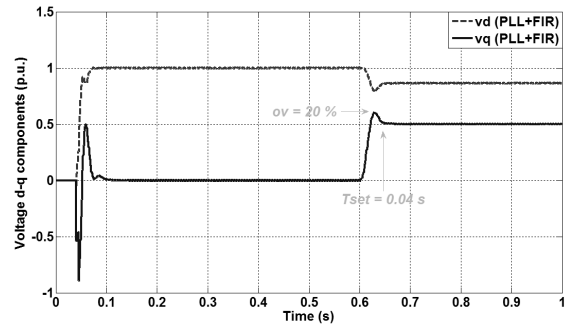


Fig. 11. d-q grid voltage components at the input of the proposed PLL with pre-filtering. Response to abrupt grid voltage phase shift of 60 degrees (at 0.6 s).

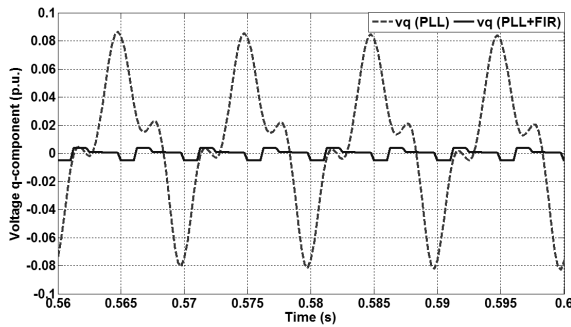


Fig. 12. Grid voltage q-component in conventional (dashed) and proposed (solid) PLL. 2nd and 6th harmonics are not propagated through proposed PLL.

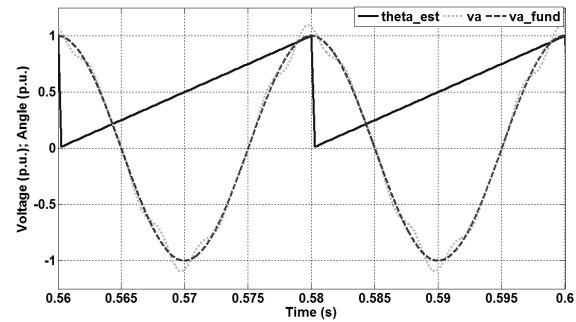


Fig. 14. Estimated grid voltage phase angle is clear and precisely aligned with fundamental harmonic of the grid voltage.

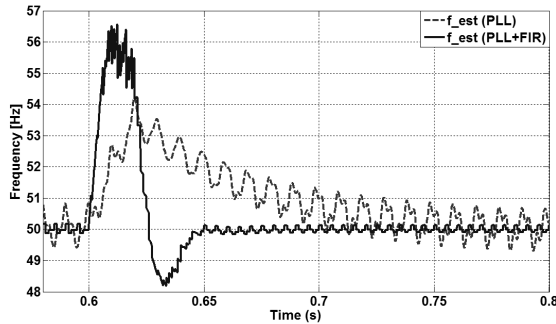


Fig. 13. Estimated grid voltage frequency in conventional (dashed) and proposed (solid) PLL. Proposed PLL gives faster response without harmonics.

steady-state when reference is set to 0. It verifies that the new system perform better compare to conventional where one can observe presence of 100 Hz and 300 Hz harmonic components. Such oscillations would propagate through the PLL filter which would result in the same oscillatory estimated frequency, as shown in Fig. 13. New system is more aggressive with higher overshoot in estimated frequency during transient (at 0.6 s in Fig. 13), but it settles much faster in about 2 fundamental periods and result in much cleaner frequency information without oscillations. Finally, Fig. 14 shows the estimation of the grid voltage phase angle using the proposed pre-filtered PLL. It proves that proposed PLL rejects the unbalance and harmonics effects, generating a clean synchronization signal (θ_{est}), aligned to the amplitude of fundamental harmonic (v_{a_fund}) of distorted voltage in phase a (v_a).

Additionally, the proposed PLL system and its contribution to the control quality are tested considering entire voltage oriented vector control structure. In order to verify voltage oriented control principle and test its operation under unbalanced and distorted grid voltage conditions, detailed average model of space vector modulated (SVPWM) grid-connected voltage-source converter has been developed, according to Fig. 15. Parameters of the system are given in appendix.

Firstly, grid-side converter response to d-q current references was tested using conventional PLL (with set bandwidth 3 Hz). Figs 16 and 17 show obtained results with dashed lines. Till 0.04 s, d-q current references were set to

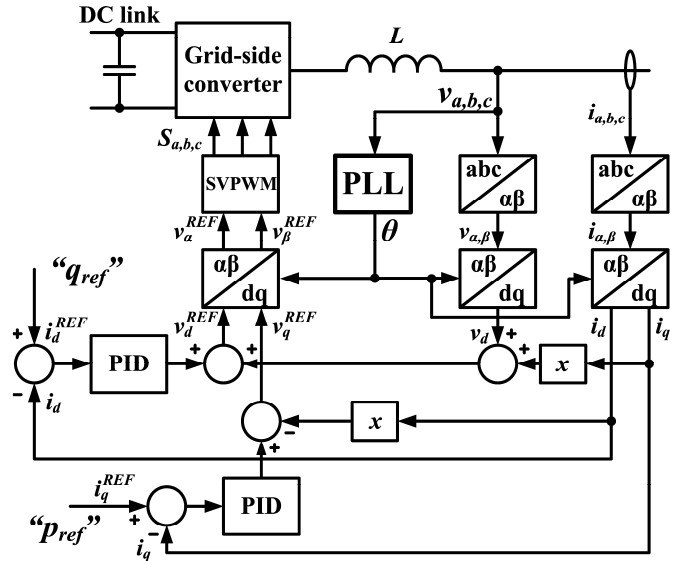


Fig. 15. Grid voltage oriented vector control structure for grid-side power converter. Independent control of active and reactive power is achieved.

zero, when q-current references determined active power to the grid is set to 0.5 p.u., and after that at 0.1 s d-current component determined reactive power is set to 0.3 p.u. Simulation showed that obtained current components contain characteristic harmonics at 100 Hz and 300 Hz with amplitude of 15 % (of fundamental signal). That results in distorted phase current waveforms, particularly in the region of its maximum values, which could be observed in Fig. 17. Here, it must be noted that besides PLL introduced errors additional influence on control quality also has d-q current controllers. Used current controllers are PI type controllers without any additional part charged for rejecting grid disturbances. Main goal was to observe how proposed PLL contribute to the quality control in terms of generated grid current distortion. Results using proposed PLL instead conventional are given in the same figures with solid lines. Obtained current oscillations are about twice reduced, using the same current controller gains. It results in more sinusoidal grid current waveform compare to the situation when conventional method was used (Fig. 17). Improvement comes exclusively from cleaner synchronization angle (without harmonic content) used for current transformation in d-q reference frame.

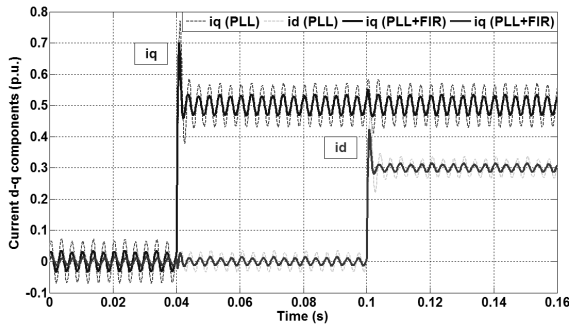


Fig. 16. Converter d-q grid current components and their response to current references when conventional (dashed) and proposed (solid) PLL is used.

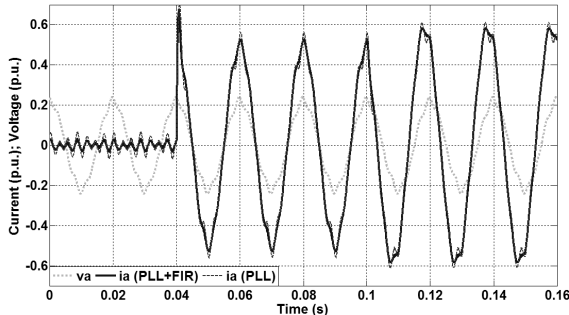


Fig. 17. Grid-side converter line current when conventional (dashed) and proposed (solid) PLL is used in control structure.

VII. CONCLUSION

This paper presented an improved pre-filter based PLL for phase angle and frequency estimation necessary for achieving proper vector control method in grid-connected converter applications. Proposed PLL method is especially suitable for application in highly unbalanced and distorted grid voltage conditions, because it is not subject to their influence. Therefore, authors consider it is appropriate for application in growing sector of distributed power generation systems based on renewable energy sources. Besides, proposed PLL method allows setting of much higher bandwidth than usual which is favorable in the case of grid voltage sags and frequency variations. Grid frequency variations and grid voltage offset are not considered in the paper. As fundamental grid frequency is not constant, certain coefficients in the FIR filter subsections must be recalculated on-line. Also due to the offset in voltage signals introduced by measuring devices, oscillation error at

fundamental frequency would appear in the estimated phase angle and frequency. Their influence will be considered in some future work.

APPENDIX

Parameters of the system used in simulation: coupling inductance 7.5 mH, coupling resistance 0.26 Ω , grid voltage 212 V, DC-link voltage 580 V, current and PLL sampling frequency 4000 Hz, base voltage 960 V, base current 8 A, current controller gains $K_P = 0.41$ and $K_{I_z} = 0.2$, PLL filter gains $K_P = 26.6$ and $K_{I_z} = 0.04$ for $f_{bw} = 3$ Hz and $K_P = 222.4$ and $K_{I_z} = 3.08$ for $f_{bw} = 25$ Hz, PLL pre-filter sampling frequency 800 Hz.

REFERENCES

- [1] F. Blaabjerg, Z. Chen, and S.B. Kjaer, "Power Electronics as Efficient Interface in Dispersed Power Generation Systems", *IEEE Trans. Power Electronics*, vol. 19, no. 5, pp. 1184-1194, Sept. 2004.
- [2] F. Blaabjerg, R. Teodorescu, M. Liserre, and V. Timbus, "Overview of Control and Grid Synchronization for Distributed Power Generation Systems," *IEEE Trans. Ind. Electronics*, vol. 53, no. 5, pp. 1398-1409, October 2006.
- [3] E. Adzic, D. Marcetic, V. Katic, and M. Adzic, "Grid-connected Voltage Source Converter under Distorted Grid Voltage", in *Proc. IEEE EPE-PEMC 2010*, Sept. 2010.
- [4] A. Timbus, R. Teodorescu, F. Blaabjerg, and M. Liserre, "Synchronization Methods for Three Phase Distributed Power Generation Systems. An Overview and Evaluation", in *Proc. IEEE PESC 2005*, June 2005, pp. 2474-2481.
- [5] S-K. Chung, "A Phase Tracking System for Three Phase Utility Interface Inverters", *IEEE Trans. Power Electronics*, vol. 15, no. 3, pp. 431-438, May 2000.
- [6] R.K. Sinha, P. Sensarma, "A pre-filter based PLL for three-phase grid connected applications", *Electric Power Systems Research*, vol. 81, pp. 129-137, July 2010.
- [7] H. Awad, J. Svensson, and M. J. Bollen, "Tuning Software Phase-Locked Loop for Series-Connected Converters", *IEEE Trans. Power Delivery*, vol. 20, no. 1, pp. 300-308, January 2005.
- [8] E. Adzic, M. Adzic, V. Katic, "Tuning of Grid Synchronization Unit for Distributed Power Generation Systems", in *Proc. ETRAN 2011*, June 2011.
- [9] V. Kaura, V. Blasko, "Operation of a phase locked loop system under distorted utility conditions", *IEEE Trans. on Ind. Appl.*, vol. 33, no. 1, pp. 58-63, Jan./Feb. 1997.
- [10] A. Timbus, T. Teodorescu, F. Blaabjerg, M. Liserre, P. Rodriguez, "PLL Algorithm for Power Generation Systems Robust to Grid Voltage Faults," in *Proc. IEEE 37th PESC 2006*, pp.1-7, June 2006.
- [11] E. Adzic, M. Adzic, J. Tomic, V. Katic, "Improved Phase-Locked Loop for Distributed Power Generation Systems", in *Proc. SISY 2011*, Sept. 2011.

Linearization of Two-way Doherty Amplifier by Using Second and Fourth Order Nonlinear Signals

Aleksandar Atanasković and Nataša Maleš-Ilić

Abstract—In this paper, a two-way Doherty amplifier with the additional circuit for linearization has been realized in order to experimentally verify the linearization influence of the fundamental signals' second harmonics and fourth-order nonlinear signals to the third- and fifth-order intermodulation products. The signals for linearization—second harmonics and fourth-order nonlinear signals are extracted at the output of the peaking cell, adjusted in amplitude and phase and injected at the input of the carrier cell in Doherty amplifier. Additionally, the linearization effects of three variants of the linearization approach have been analyzed by Advance Design System simulator: one that was tested experimentally, the case when the signals for linearization are injected only at the carrier amplifier output and when they are put simultaneously at the input and output of the amplifier.

Index Terms—Doherty amplifier, linearization, second harmonics and fourth-order nonlinear signals, intermodulation products.

I. INTRODUCTION

WITH the advent of spectrally efficient wireless communication systems, linearization techniques for nonlinear microwave power amplifiers have gained significant interest. Demanding requirements of new systems (CDMA2000, W-CDMA, OFDMT etc.), in order to meet both linearity and high power efficiency present a serious task for transmitter designers. The Doherty amplifier is capable of achieving a high efficiency of power amplifiers in base station. Different linearization methods exist with the aim to reduce nonlinear distortions while keeping power amplifier in a nonlinear and efficient mode. The various linearization methods of Doherty amplifier have been reported: post-distortion-compensation [1], the feedforward linearization technique [2], the predistortion linearization technique [3] and

combination of those two linearization techniques [4].

The linearization effects of the fundamental signals' second harmonics (IM2) and fourth-order nonlinear signals (IM4) at frequencies that are close to the second harmonics to the standard (two-way, three-way and three-stage) Doherty amplifiers were investigated in [5] for LDMOSFETs in carrier and peaking amplifiers with the same periphery and in [6] for periphery relations 1:2.5:2.5. We applied the approach where IM2 and IM4 signals are injected together with the fundamental signals into the carrier amplifier input and put at its output [7]. In addition, three-stage Doherty amplifier was loaded with harmonic control circuit (HCC), which represents an optimal impedance for the second harmonics and either an open or short circuit for the third harmonics at the output of cells. Various configurations of loading were considered for the case of the same transistors in amplifying cells [8], [9] and with the transistor size ratio 1:2.5:2.5 [10]. Analysis of the linearization of Doherty amplifiers was carried out for sinusoidal signals and digitally modulated signals through the simulation process by ADS software.

In this paper, two-way Doherty amplifier with the additional circuit for linearization is realized. The effects of linearization are verified by measurements. The linearization technique applied utilizes the second harmonics and fourth-order nonlinear signals at frequencies close to the second harmonics, which are generated at the output of the peaking cell. They are adjusted in amplitude and phase through the linearization branch and run at the carrier amplifier input over frequency diplexer. Also, the results of simulation that refer to the linearization approach tested in experiment, the linearization when the signals for linearization are led only at the carrier amplifier output and the linearization with the signals that are fed at the input and output of the amplifier are given in parallel.

II. THEORETICAL ANALYSIS OF LINEARIZATION TECHNIQUE APPLIED IN EXPERIMENT

Theoretical analysis of the proposed linearization approach is based on the nonlinearity of the drain-source current of LDMOSFET in amplifier circuit which is expressed by a polynomial model [11], [12] under the assumption of neglecting a memory effect, as represented by (1).

The authors would like to thank the Ministry of Education and Science of Republic Serbia for supporting the research reported in this paper within the projects TR-32052 and III44006. Some results shown in this paper were presented at 55th ETRAN Conference, Banja Vrućica, June 6-9, 2011.

A. Atanasković, and N. Maleš-Ilić, are with the Faculty of Electronic Engineering, University of Niš, Aleksandra Medvedeva 14, 18000 Niš, Serbia, E-mails: [natasa.males.ilic; aleksandar.atanaskovic] @elfak.ni.ac.rs.

$$\begin{aligned}
i_{ds}(v_{gs}, v_{ds}) = & \\
& K_{10}v_{gs}(t) + K_{20}v_{gs}^2(t) + K_{30}v_{gs}^3(t) + K_{40}v_{gs}^4(t) + K_{50}v_{gs}^5(t) + \\
& + K_{11}v_{gs}(t)v_{ds}(t) + K_{21}v_{gs}^2(t)v_{ds}(t) + K_{12}v_{gs}(t)v_{ds}^2(t) + \dots
\end{aligned} \quad (1)$$

The spectrum of a digitally modulated fundamental signal is given by the expression: $V_B(j\omega) \otimes \frac{1}{2}\delta(\omega \pm \omega_0)$, where $V_B(j\omega)$ represents a baseband spectrum.

Equation (1) connects the nonlinearity of the drain-source current i_{ds} , in reference to the voltage v_{gs} between gate and source, which is represented by the coefficients K_{10} to K_{50} . Higher order nonlinear terms K_{40} and K_{50} are included into the equation according to the analysis performed in [12] that favours the terms of output current as function of v_{gs} up to the fifth-order. The nonlinearity of drain-source current in terms of the voltage between drain and source, v_{ds} , which is expressed by the coefficients K_{01} to K_{03} , is assumed to have a negligible contribution to the intermodulation products according to [11] and [12], so that they are omitted from the equation. However, the equation encompasses “mixing” terms K_{11} , K_{12} and K_{21} .

The drain-source current at IM3 and IM5 frequencies can be written by (2) and (3), where $(\rho_2^{(i)}, \varphi_2^{(i)}, \rho_4^{(i)}, \varphi_4^{(i)})$ stand for the amplitudes and phases of the IM2 and IM4 signals put at the amplifier input, whereas $(\rho_2^{(o)}, \varphi_2^{(o)}, \rho_4^{(o)}, \varphi_4^{(o)})$ are amplitudes and phases of IM2 and IM4 signals that exist at the amplifier output due to both an inherent nonlinearity of transistor and transferred signals from the input.

The signal distorted by the cubic term of the amplifier, K_{30} , is included into analysis by (2) as the first term. The cubic term is considered as a dominant one according to [11] and [12] in causing IM3 products and spectral regrowth. The term K_{20} (second term) is created by the gate-source voltage of fundamental signal and voltage of second harmonic fed at the amplifier input. The mixing product of the fundamental signal and second harmonic appearing at the amplifier output is expressed as the third term. Additionally, the fundamental signal at the output of amplifier mingles with the second harmonic injected at the amplifier input generating the fourth term. The amplitude of output voltage at the fundamental signal frequency that is 180° out of phase in reference to the input signal is denoted as ρ_1 . The third and fourth terms can be neglected for lower signal power. In case of higher power, they may reduce each other. The mixing terms between drain and gate, K_{12} and K_{21} , produce drain-source current at IM3 frequencies with the opposite phases, so that they reduce each other [11].

$$\begin{aligned}
I_{ds}(j\omega)|_{IM3} \approx & \left\{ \left[\frac{3}{4}K_{30} + \frac{1}{4}K_{20}\rho_2^{(i)} e^{-j\varphi_2^{(i)}} + \right. \right. \\
& \left. \left. + \frac{1}{4}K_{11}\rho_2^{(o)} e^{-j\varphi_2^{(o)}} - \frac{1}{4}K_{11}\rho_1\rho_2^{(i)} e^{-j\varphi_2^{(i)}} \right] \right. \\
& \left. (V_B(j\omega) \otimes V_B(j\omega) \otimes V_B(j\omega)) \right\} \otimes \frac{1}{2}\delta(\omega \pm \omega_0)
\end{aligned} \quad (2)$$

According to the previous analysis, it is possible to reduce spectral regrowth caused by the third-order distortion of fundamental signal by choosing appropriate amplitude and phase of the second harmonics ($\rho_2^{(i)}$ and $\varphi_2^{(i)}$).

The first term in (3) expressing the drain-source current of the fifth-order intermodulation products (IM5) is formed from the fundamental signals due to an amplifier nonlinearity of the fifth-order, K_{50} . The second term is the mixing product between the fundamental signal at amplifier input and IM4 signal inserted to its input, too. Therefore, the original IM5 product (the first term) can be reduced by adjusting the amplitude and phase of IM4 signals that are injected at the amplifier input. The IM5 products are also expressed in terms of K_{30} coefficient-the third term in (3) made by reaction between two IM2 signals and fundamental one at the amplifier input. Also, the fundamental signal at the amplifier output reacts with the IM4 signal at the amplifier input over K_{11} term producing IM5 product (fourth term). The fifth term is made between the input fundamental signal and IM4 signals at the amplifier output. All mixing terms which stand by K_{12} and K_{21} in (3) are generated due to reaction between two second harmonics and fundamental signal. The signals taken in consideration are observed at the input and output of the amplifier. The K_{12} and K_{21} terms produce current at the frequencies of IM5 products with the opposite phases, so that they reduce each other. Consequently, their influence to the power of IM3 and IM5 products can be cancelled.

$$\begin{aligned}
I_{ds}(j\omega)|_{IM5} \approx & \\
& \left\{ \left[\frac{5}{8}K_{50} + \frac{1}{4}K_{20}\rho_4^{(i)} e^{-j\varphi_4^{(i)}} + \frac{1}{8}K_{30}\rho_2^{(i)2} e^{-j2\varphi_2^{(i)}} \right. \right. \\
& \left. \left. - \frac{1}{4}\rho_1 K_{11}\rho_4^{(i)} e^{-j\varphi_4^{(i)}} + \frac{1}{4}K_{11}\rho_4^{(o)} e^{-j\varphi_4^{(o)}} \right. \right. \\
& \left. \left. + \frac{1}{8}K_{12}\rho_2^{(o)2} e^{-j2\varphi_2^{(o)}} - \frac{1}{8}K_{12}\rho_1\rho_2\rho_2^{(o)} e^{-j(\varphi_2^{(i)} + \varphi_2^{(o)})} \right. \right. \\
& \left. \left. + \frac{1}{8}K_{21}\rho_2^{(i)}\rho_2^{(o)} e^{-j(\varphi_2^{(i)} + \varphi_2^{(o)})} - \frac{1}{8}K_{21}\rho_1\rho_2^{(i)2} e^{-j2\varphi_2^{(i)}} \right] \right. \\
& \left. (V_B(j\omega) \otimes V_B(j\omega) \otimes V_B(j\omega) \otimes V_B(j\omega) \otimes V_B(j\omega)) \right\} \\
& \otimes \frac{1}{2}\delta(\omega \pm \omega_0)
\end{aligned} \quad (3)$$

As in the case of IM3 products, third to fifth terms have negligible impact for lower power of the fundamental signals, while in case of higher power, it can be assumed that fourth and fifth terms cancel each other. However, for higher power, the mixing K_{30} term (the third term in (3)) may increase IM5 products if IM4 signals injected at the amplifier input do not have enough power against the K_{30} term to control it.

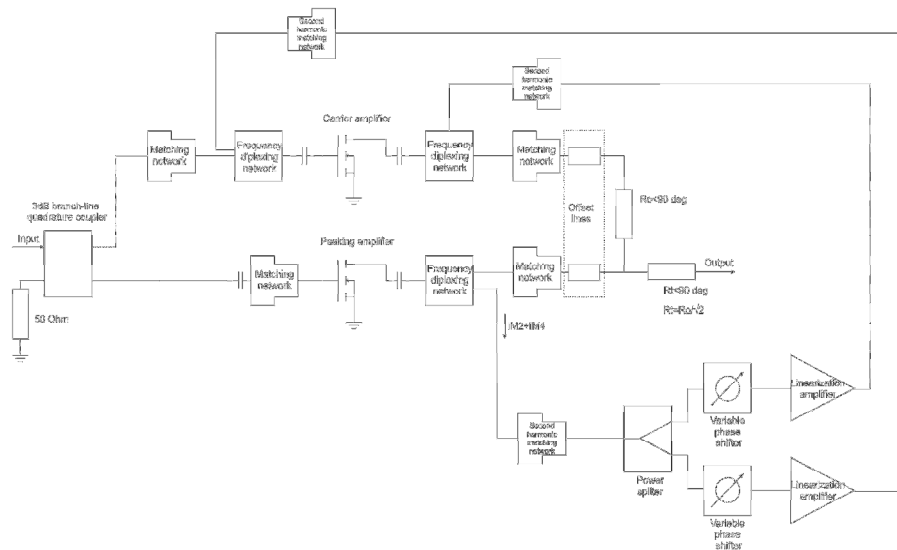


Fig. 1. Schematic diagram of two-way Doherty amplifier with additional circuit for linearization.

III. DESIGN OF AMPLIFIER AND LINEARIZATION CIRCUITS

Agilent Advanced Design System-ADS software has been used for the design of conventional two-way Doherty amplifier, which schematic diagram is shown in Fig. 1.

Two-way Doherty amplifier was designed in standard configuration [1], [2], [4], [5]. The carrier and peaking amplifiers have input and output matching circuits, which transform the input impedance of the device to 50Ω and the optimum load impedance Z_{opt} to 50Ω . In low-power region, the peaking amplifier should be an open circuit and load impedance of the carrier amplifier should be doubled to $2Z_{opt}$ by a quarter-wave impedance transformer with the characteristic impedance $R_0=50\Omega$. Also, the quarter-wave transmission line with the characteristic impedance $R_l = R_0\sqrt{2}$ transforms 50Ω to 25Ω that is a load impedance of the output combining circuit when the peaking amplifier is turned on in higher power region. Phase difference of 90° is required at the inputs of the carrier and peaking amplifier to compensate for the same phase difference between those two amplifiers caused by the quarter-wave impedance transformer at the output.

The output impedance of the LDMOSFET is strongly reactive with low resistance so in low-power region considerably power leaks from the carrier amplifier to the peaking amplifier. The output impedance seen at the output of the peaking transistor is transformed to the open by the output matching circuit and the proper offset line.

The carrier and peaking cells were designed using Freescale's MRF281S LDMOSFET which non-linear MET model is incorporated in ADS library.

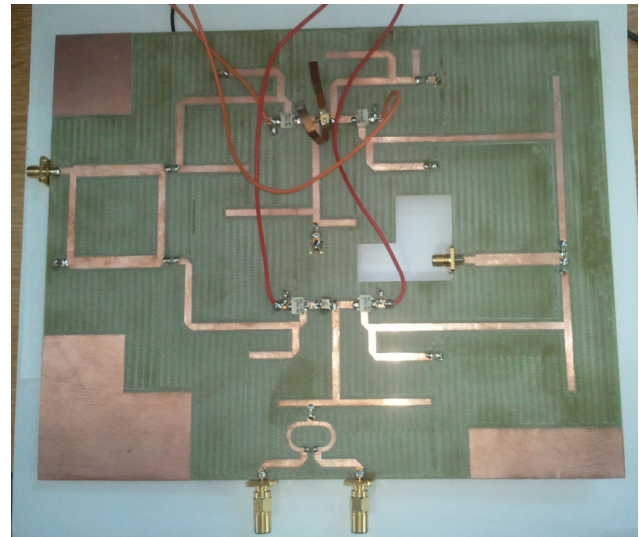


Fig. 2. Realized two-way Doherty amplifier.

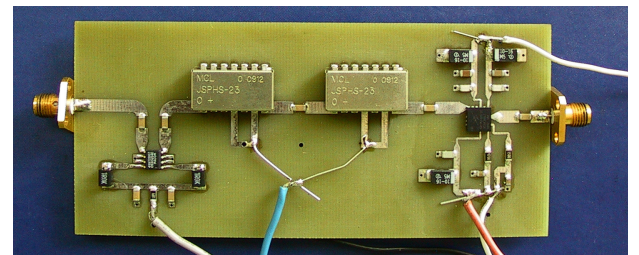


Fig. 3. Realized linearization circuit.

The transistor shows a 4-W peak envelope power. The matching impedances for source and load at 1GHz are $Z_S=5.5+j15\Omega$ and $Z_L=12.5+j27.5\Omega$, respectively. These impedances were obtained by using load-pull and source-pull analysis in ADS. The matching impedances for the second harmonics at 2GHz for source and load are $Z_S=3.1-j2.4\Omega$ and $Z_L=12.5+j9.2\Omega$, respectively. These impedances are taken from the authorized Freescale catalogue.

The carrier amplifier is biased in class-AB ($V_D=26V$, $V_G=5.1V$ (13.5%IDSS)), whereas the peaking amplifier operates in class-C ($V_D=26V$, $V_G=3.6V$).

In simulation of two-way Doherty amplifier, ideal elements from ADS library was utilized for the linearization circuit components. The linearization circuit fabricated for the experiment comprises from M/A-COM PIN diode variable attenuator MA4VAT2007-1061T, two Mini-Circuits 180° voltage variable phase shifters JSPHS-23+ to provide phase shift of 360° and Skyworks high linear 2W power amplifier-SKY65120. The second harmonics, IM2, and fourth-order nonlinear signals at frequencies close to the second harmonics, IM4, which are generated at the output of the peaking amplifier, are extracted through the diplexer circuit [5] that was designed to separate the fundamental signals and signals for linearization matched to the impedance for their adequate power level. The linearization circuit adjusts IM2 and IM4 signals in amplitude and phase before they are inserted at the carrier amplifier input over the frequency diplexer designed with the independent matching circuits for the fundamental and signals for linearization. Linearization branch can vary power of the signals for linearization from -10dB to 7dB in reference to the generation point at the peaking amplifier output.

Both, two-way Doherty amplifier (Fig. 2) and linearization circuit (Fig. 3) are realized on FR4 substrate with 1.55 mm thickness and $17.5\mu m$ metallization layer. The printed circuit boards for the circuits were manufactured on LPKF ProtoMat S100 in laboratory.

IV. SIMULATED AND MEASURED RESULTS

S-parameters of Doherty amplifier obtained by ADS simulator as well as the measured parameters are shown in Fig. 4. The figure compares the characteristics achieved in the case of the ideal lossless amplifier circuit (dashed line) and in the case when losses and discontinuity effects of tee-sections and banded microstrip lines are included into the analysis. One can notice that the amplifier operational frequency is shifted from the design frequency of 1GHz to 1.006GHz in the fabricated amplifier.

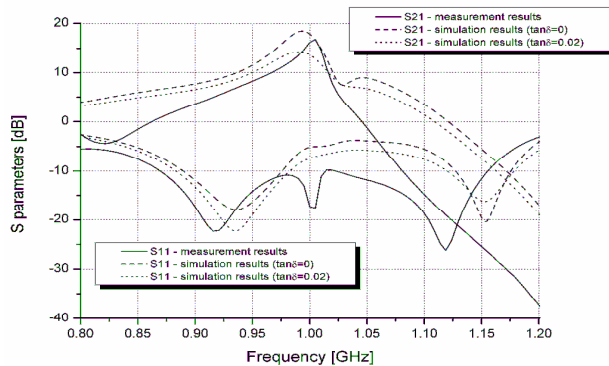


Fig. 4. S-parameters of two-way Doherty amplifier.

The results before and after linearization for two-tone test of two-way Doherty amplifier at frequencies 988MHz and 990GHz are given in Fig. 5 for the range of fundamental signal

output power (8dBm-30dBm). These figures compare the linearization effects for three cases of linearization depending on whether the signals for linearization are injected at: 1. the amplifier input, 2. the amplifier output and 3. the amplifier input and output. Denotation in the figures is as follows: IM3- at 986MHz, IM3+ at 992MHz, IM5- at 984MHz and IM5+ at 994MHz. In the lower power range (8dBm-24dBm), the presented results relate to the case when the amplitudes and phases of IM2 and IM4 signals are adjusted on the optimal values at 22dBm output power where IM3 products are suppressed for 14dB and 7dB in the first case, 10dB and 12dB in the second and 12dB and 14dB in the third case. The IM5 products are more asymmetrical before linearization, so that at 22dBm IM5- product is kept almost the same to the level before linearization in all cases considered, whereas IM5+ is lessened by 6dB in the first and 8dB in the third case and deteriorates by 3dB in the second case. In case of higher power (24dBm-30dBm) the amplitude and phases of the signals for linearization were adjusted on the optimal values for each single power level. As far as the whole power range is observed the best reduction of IM3 products was achieved by the injection of the signals for linearization at the input and output, whereas the injection only at the carrier amplifier input brings slightly better suppression of IM5 products.

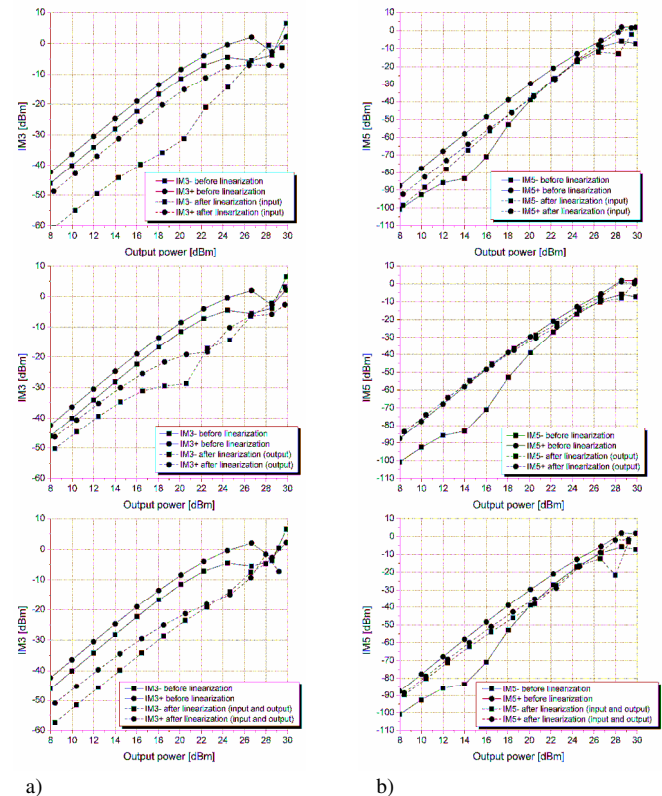


Fig. 5. Simulated intermodulation products before and after linearization of two-way Doherty amplifier for a power range: a) third-order; b) fifth-order products.

The measured output spectra of Doherty amplifier before and after applying the linearization for two sinusoidal signals at 8dBm input power at frequencies 1.0065GHz and

1.0075GHz are compared in Fig. 6. The fundamental signal output power is about 19.96dBm before and 19.35dBm after the linearization. The third-order intermodulation products at frequencies 1.0055MHz and 1.0085GHz are lowered by linearization from -8dBm to -16dBm and -13dBm, respectively. The fifth-order intermodulation products are reduced by around 6dB at frequencies 1.0045MHz and 1.0095GHz.

The results from Fig. 7 show the effects of two-way Doherty amplifier linearization accomplished for the output power ranging from 10dBm to 26dBm (upper signal power is constrained by the laboratory equipment capability to the power that is 10dB below the maximal catalogue power level of the transistor applied). These results are compared to the case when linearization is not carried out. Fig. 7a) relates to the power reduction of IM3 at 1.0055GHz (IM3-) and 1.0085GHz (IM3+), whereas Fig. 7b) shows results connected to the IM5 products at 1.0045GHz (IM5-) and 1.0095GHz (IM5+).

It is evident from these figures that the linearization with the proposed approach gives satisfactory results in improvement of IM3 products for the power range up to approximately 18dBm and becomes asymmetrical at higher power. However, IM5 products decrease slightly at lower power levels, whereas they get worse at higher power range considered, still retained below the levels of the linearized IM3 products. According to (2) and (3), IM2 and IM4 signals can reduce both IM3 and IM5 products that depends on the relations between amplitudes as well as phases of the IM2 and IM4 signals generated at the peaking amplifier output. However, when the required relations are not fulfilled, only one kind of the intermodulation products can be reduced sufficiently.

Doherty amplifier drain efficiency (DE) obtained in simulation for ideal circuit case without losses, the simulated characteristic gained for the loss microstrip circuit with included discontinuities and the measured values are compared in Fig. 8. The good agreement can be observed between the curves relating to the real simulated Doherty amplifier and experimental results up to 34dBm power that is maximal level that can be reached by the available laboratory equipment. At this power level, there is a maximal discrepancy between the simulated and measured result of 5%. The maximal efficiency achieved by the realized circuit is 32.7%.

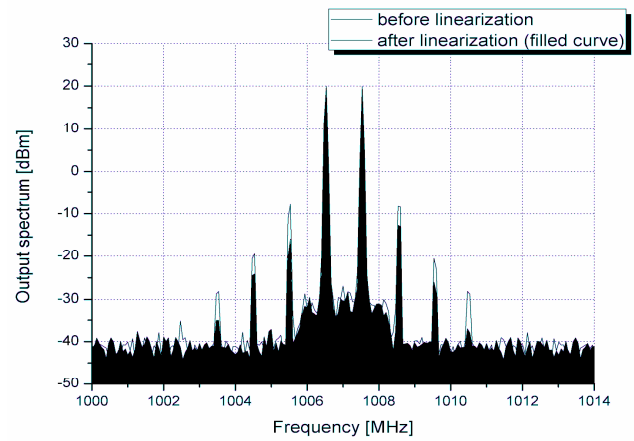
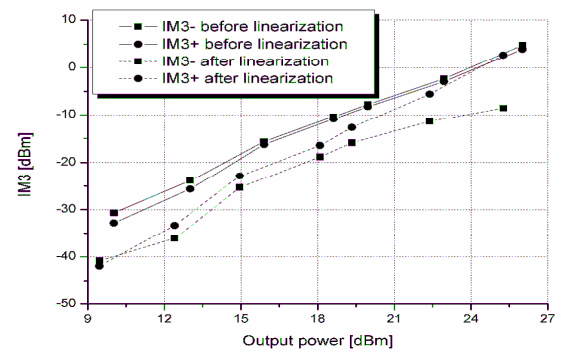
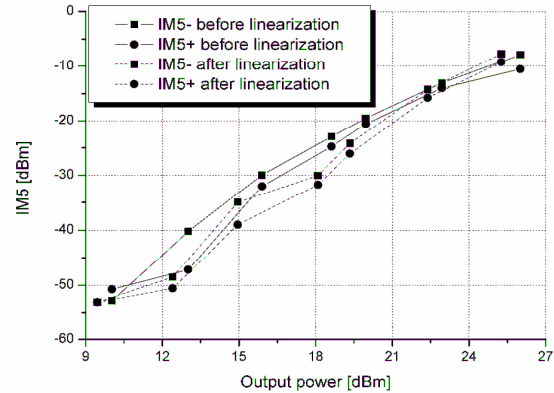


Fig. 6. Measured output spectra for 8dBm input power of fundamental signals; before and after linearization (filled curve).



a)



b)

Fig. 7. Measured intermodulation products before and after linearization of two-way Doherty amplifier for a power range: a) third-order; b) fifth-order products.

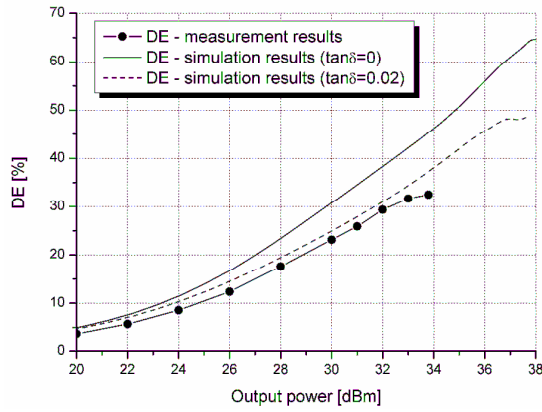


Fig. 8. Drain efficiency of two-way Doherty amplifier.

V. CONCLUSION

This paper presents for the first time the experimental verification of two-way Doherty amplifier linearization by simultaneous injection of the second harmonics and fourth-order nonlinear signals at the input of carrier amplifier. The linearization approach achieves very good results in a reduction of the third-order intermodulation products, even for a wider power range. When the fifth-order intermodulation products are concerned, the mild suppression is observed at low-power levels, however these products deteriorate at high-power range. Measurements are constrained by the laboratory equipment to the lower power that is 10dB below the maximal available power of transistors utilized. Additionally, the results of simulation obtained by Advance Design System program are introduced in the paper for three variances of the linearization approach concerning the injection point of the signals for linearization: 1. input, 2. output, and 3. input and output of the carrier amplifier. It can be observed the similar behaviour of the designed and realized two-way Doherty amplifier in linearization process.

We would like to point out that the crucial matter in the linearization approach used for Doherty amplifier linearization is the possibility to exploit the peaking amplifier as a source of signals for linearization and therefore avoid the necessity for additional nonlinear sources that will increase the circuit complexity and total energy consumption.

REFERENCES

- [1] K. J. Chao, W. J. Kim, J. H. Kim and S. P. Stapleton, "Linearity optimization of a high power Doherty amplifier based on post-distortion compensation", *IEEE Microwave and Wireless Components Letters*, vol.15, no.11, pp.748-750, 2005.
- [2] K. J. Cho, J. H. Kim and S. P. Stapleton, "A highly efficient Doherty feedforward linear power amplifier for W-CDMA base-station applications", *IEEE Trans., Microwave Theory Tech.*, vol. 53, no. 1, pp.292-300, 2005.
- [3] B. Shin, J. Cha, J. Kim, Y. Y. Woo, J. Yi, B. Kim, "Linear power amplifier based on 3-way Doherty amplifier with predistorter", *IEEE MTT-S Int. Microw. Symp. Digest*, pp.2027-2030, 2004.
- [4] T. Ogawa, T. Iwasaki, H. Maruyama, K. Horiguchi, M. Nakayama, Y. Ikeda and H. Kurebayashi, "High efficiency feed-forward amplifier using RF predistortion linearizer and the modified Doherty amplifier", *IEEE MTT-S Int. Microw. Symp. Digest*, pp.537-540, 2004.
- [5] Aleksandar Atanasković, Nataša Maleš-Ilić, Bratislav Milovanović, "The linearization of Doherty amplifier", *Microwave review*, No.1, Vol. 14, pp.25-34, September 2008.
- [6] Aleksandar Atanasković, Nataša Maleš-Ilić, Bratislav Milovanović: "The linearization of high-efficiency three-way Doherty amplifier", *TELFOR2008, Conference Proceedings on CD*, 3.17, Beograd, Srbija, 25-27. November, 2008.
- [7] A. Atanasković, N. Maleš-Ilić, B. Milovanović, "The suppression of intermodulation products in multichannel amplifiers close to saturation", *Proceedings of 11th WSEAS International Conference on Circuits*, pp. 198-201, Greece, July 2007.
- [8] Nataša Maleš-Ilić, Aleksandar Atanasković, Bratislav Milovanović: "High-efficient three-way Doherty amplifier with improved linearity", *Recent Advances in Circuits - Proceedings of the 13th WSEAS International Conference on CIRCUITS (part of the 13th WSEAS CSCC Multiconference)*, Rodos, Greece, July 22-24, WSEAS Press, pp.137-140, 2009.
- [9] Nataša Maleš-Ilić, Aleksandar Atanasković, Bratislav Milovanović: "Harmonic-Controlled Three-Way Doherty Amplifier with Improved Linearity", *WSEAS Transaction on Circuits and Systems*, WSEAS Press, Vol.8, Issue 9, pp.769-778, September 2009, ISSN:1109-2734
- [10] Aleksandar Atanasković, Nataša Maleš-Ilić, Bratislav Milovanović: "Harmonic controlled three-way Doherty amplifier with improved efficiency and linearity", *Proceedings of the 9th International Conference on Telecommunications in Modern Cable, Satellite and Broadcasting Services - TELSIKS 2009*, Niš, Serbia, October 7-9, Vol.1, pp.36-39, 2009.
- [11] M.J. P. Aikio, T. Rahkonen, "Detailed distortion analysis technique based on simulated large-signal voltage and current spectra", *IEEE Trans. Microwave Theory and Techniques*, Vol. 53, pp. 3057-3065, 2005.
- [12] A. Heiskanen, J. Aikio, T. Rahkonen, "A 5-th Order Volterra study of a 30W LDMOS power amplifier", *Proc. IEEE Int. Symp. on Circuits and Systems (ISCAS)*, pp. 616-619, Bangkok, Thailand, 2003.

Realization of Primitives by Using SVM for Humanoid Robot Walk Generation

Branislav Borovac, Mirko Raković, and Milutin Nikolić

Abstract—To ensure motion of bipedal humanoid robots in unstructured environment, in general, it is not possible to use preprogrammed trajectories. This paper describes the approach to motion generation from primitives that ensures on-line modification of locomotor activity. Primitives represent simple movements that are either reflex or learned. Each primitive has its parameters and constraints that are determined on the basis of the movements capable of performing by a human. The set of all primitives represents the base from which primitives are selected and combined for the purpose of performing the corresponding complex movement. SVM regression is used to learn primitives which are verified in the task of walk generation

Index Terms—Humanoid robot, locomotion, primitives, SVM.

I. INTRODUCTION

THE important features of biped humanoid robots are human-like shape and movements. It is expected from a robot to be able to perform motion the way people do. For successful operation in human environment the robot should be able to walk and move like a human: to climb up stairs, to use doors, to detect and avoid obstacles, walk on uneven terrain, run, etc. In the realization of their movements, most humanoid robots perform motions that are synthesized in advance. In [1-4], the main goal in their realization being to prevent fall, i.e. to preserve dynamic balance, and then, realize the intended movement in a most faithful way. However, for use of humanoids in unstructured environment realization of appropriate motion is main problem.

Humanoid robot motion in unstructured environment is considered in [5, 6]. In [5] is described 3D linear inverted pendulum mode to generate walking pattern. Authors in [6] use predefined zero moment point trajectory and the foot landing position is calculated using short cycle pattern

This work was funded by the Ministry of Science and Technological Development of the Republic of Serbia in part under contract TR35003 and in part under contract III44008 and by Provincial Secretariat for Science and Technological Development under contract 114-451-2116/2011. Some results of this paper were presented at 55th ETRAN Conference, Banja Vrućica, June 6-9, 2011.

B. Borovac is with the Faculty of Technical Sciences, University of Novi Sad, Serbia (e-mail: borovac@uns.ac.rs).

M. Raković is with the Faculty of Technical Sciences, University of Novi Sad, Serbia (e-mail: rakovicm@uns.ac.rs).

M. Nikolić is with the Faculty of Technical Sciences, University of Novi Sad, Serbia (e-mail: milutinn@uns.ac.rs).

generator.

Motivation for motion generation using primitives is found in [7]. Authors in [7] showed that electrical micro stimulation of same spinal interneuronal region of spinal cord evoked synergistic contractions that generate forces that direct hand limb toward an equilibrium point in space. The collection of the measured forces corresponded to a well-structured spatial pattern (vector field) that was convergent and characterized by single equilibrium point. Second, there are important findings about modular organization of spinal motor systems in the frog spinal cord. These experiments found that only a few distinct types of motor outputs could be evoked by such stimulation. However, when stimulation was applied simultaneously, to two different sites in the spinal cord, each of which when stimulated individually produced a different type of motor output, the resulting motor output was a simple combination of separate motor outputs [7]. Based on these observations it was proposed that complex movements might be produced by the flexible combination of a small number of spinally generated motor patterns.

There are differences among researchers in the use of term primitive movement. For example, in [8-11], the authors used the entire movement as a primitive (overall gait, transition from standing to walking, etc.). In [8] authors used a library of motion primitives where each primitive is a single step. Library of motion primitives actually represents set of different steps. Depending on the requirements and robot state, each time a new primitive is selected from library. In [9] authors describe approach to generate walking primitive databases where each primitive is cyclic walking pattern with different parameters. They also generate a different primitive for transition from one walking pattern to another. In [10] was presented a general framework for learning motor skills which is based on a thorough, analytically understanding of a robot task representation and execution. In [11] was presented an approach for on-line segmentation of whole body human motion observation and learning.

An essential difference between approach in [8-11] and the one proposed in this work is that the on-line motion is formed by a combination of set of basic movements which are such composed to constitute walking pattern and not of the complex movements recorded in advance. Complex movements were decomposed into simple movements, called primitives (e.g. leg stretching, leg bending, hip turning, etc.). The basic idea is to

enable system to learn to execute on-line each primitive with different parameters (let say, leg bending to different knee and hip angles) from different initial positions. Movement may be continued (if needed) with another primitive (also, on-line selected) to perform complex movement. For example, movement of leg in swing phase during walk consists of leg bending immediately followed by leg stretching. In this work we will be focused to introduce idea of composing complex movements from simple building blocks, and basic explanations of the notion and forms of primitives. Our approach will be illustrated on the example of walk realization.

II. HUMANOID ROBOT MODEL

Model of humanoid robot consists of the main link to which are connected several open kinematic chains [12-13]. The links are interconnected by simple rotational joints with only one degree of freedom (DOF). Fig. 1 shows the mechanism structure with 46 links. The joints with more DOFs (ankle and hip) are modeled as a series of one-DOF joints, connected by massless links of infinitesimal length (fictitious links). For example, the spherical joint at the left hip is modeled by three simple joints (the orts of rotation axes \bar{e}_{10} , \bar{e}_{11} and \bar{e}_{12} are mutually orthogonal), connected by the links having zero length, mass and moment of inertia (fictitious links 10 and 11).

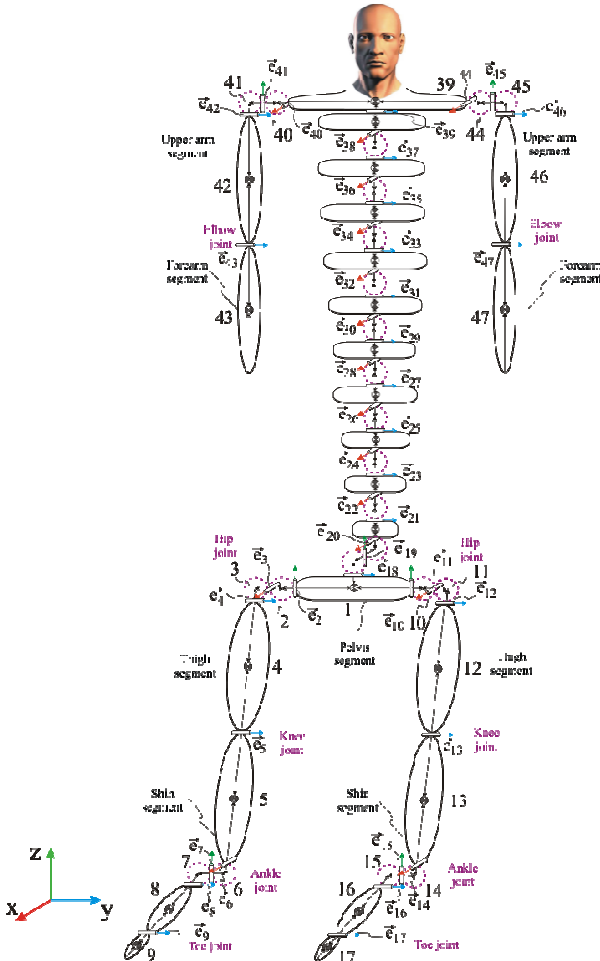


Fig. 1. Mechanical structure of the robot.

The pelvis link was chosen as the base one, and its position and orientation in the space are presented by $\mathbf{X} = [x, y, z, \theta, \varphi, \psi]^T$ three translatory and three angular coordinates. To the pelvis are connected the other kinematic chains, of which the first chain (links 1-9) represents the right leg; the second (links 1, 10-17) stands for the left leg; the third (links 1, 18-43) represents the 10-link trunk and the right arm, whereas the fourth kinematic chain represents the 10-link trunk (the links are interconnected by 2-DOF joints) and the left arm (links 1, 18-39, 44-47). The feet are two-link ones. Between the foot body and toes there exists one DOF.

The motion of each joint is described by one coordinate (q_1, q_2, \dots, q_{45}). Taking into account 6 coordinates needed for the positioning of the base link in the space we obtain that the overall number of DOFs of the described mechanism is 51, whereas the system's position is described by the following expression:

$$\mathbf{Q} = [\mathbf{X}^T, \mathbf{q}^T]^T = [x, y, z, \theta, \varphi, \psi, q_1, \dots, q_{46}]^T$$

Each joint has its own actuator that generates the driving torque τ_j , whereas the first six DOFs of the vector \mathbf{Q} , i.e. x, y, z, θ, φ and ψ are unpowered. The vector of torques at the actuated joints is $\boldsymbol{\tau} = [\tau_1, \tau_2, \dots, \tau_{46}]^T$, and the expanded vector of generalized forces is

$$\mathbf{T} = [0, 0, 0, 0, 0, 0, \tau_1, \tau_2, \dots, \tau_{46}]^T.$$

During locomotion the system passes from the single-support to the double-support phase. In the beginning, the leg that performs stepping is not in contact with the ground, the contact is being realized when the stepping is ended. Also, in the course of the contact realization, slipping may occur between the foot and the ground, and during the settling phase the rear leg can separate from the support. Because of that, it is of great importance to model appropriately the foot-ground contact, i.e. describe in the most reliable way all the effects that may arise between the two bodies in contact.

A. Modeling of the contact

The two-link foot is rectangular, with a flat contact area, so that for an exact identification of the contact type it suffices to observe only six characteristic points shown in Fig. 2. Four contact points (1-4 in Fig. 2) are the foot body corners, whereas the points 5 and 6 are at the top of the toes. By observing only these six points we can describe all the possible configurations of the foot-ground contact. If three or more points (which are not collinear) are in contact with the support,

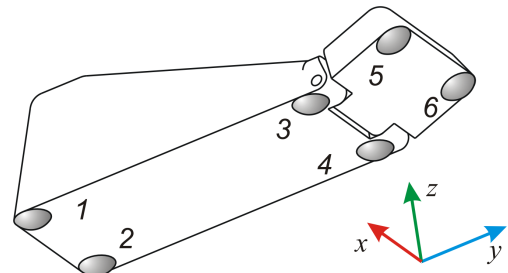


Fig. 2. Two-link foot with marked contact points.

the contact is planar; if two points are involved, it is a linear and, finally, there may exist one-point contact.

Since there are two feet, the total number of contact points that are to be observed is 12. However, not all the points are always in contact with the ground. To model the contact of a particular point with the ground use was made of the model of rigid body with a visco-elastic layer. [14-16].

B. Overall system model

By uniting the model of the robot's mechanical structure and of the elastic foot-ground contacts, the overall system can be described by the following set of differential equations:

$$\mathbf{H}\ddot{\mathbf{Q}} + \mathbf{h}_0 = \mathbf{T} + \sum_{i \in S} \mathbf{J}^{iT} \begin{bmatrix} \mathbf{F}^i \\ \delta^i \times \mathbf{F}^i \end{bmatrix} \quad (1)$$

where $\ddot{\mathbf{Q}}$ represents the vector of generalized accelerations of the mechanical system; \mathbf{H} is the system inertia matrix; \mathbf{h}_0 is the column vector of which includes moments induced by Coriolis, centrifugal and gravitational forces. \mathbf{T} is the column vector of driving torques; S is the set of points in contact with the ground; δ^i and \mathbf{F}^i are the deformation and contact force at the i -th contact point, respectively; \mathbf{J}^i is the Jacobi matrix calculated for the i -th contact point. The contact force and deformation derivative for each contact point are calculated by according to the contact model. [15-16]

III. MOTION DECOMPOSITION AND SYNTHESIS

Motion can be considered as composed from set of basic movements which can be learned and easily combined. In this chapter we will show how walk on flat surface can be combined from basic primitives.

A. Primitives- basic

The term primitive stands for a simple reflex or learned movement that a human or robot is capable to realize [17]. A primitive itself should be simple in order it could be easily performed by simultaneous and synchronized action of one or more joints and easily combined with the other primitives. Selection of movement to be adopted as a primitive is not unique but is based on our expertise. This implies that certain primitive can be included in different complex movements.

Each primitive is parameterized and has the following parameters: intensity of the movement in the span of 0-1 (which determines the extent to which, for example, a leg is to be bent or stretched), time instant from which the primitive execution should be started, and duration of the primitive execution. Each of the primitives is realized by activating one or more DOFs. Thus, for example, the primitive for bending the leg in swing phase involves activation of the joints at the hip, knee and ankle of the swing leg. It is worth noting that the primitives can be changed very easily in the sense of varying the range of the changing angle (by multiplying with a factor smaller than 1), as well as by changing the duration of its realization (faster or slower movement execution). Also, it is possible to change parameters of particular primitive during its

execution.

Considering kinematics, each primitive consists of of simple "s" shape motion at each activated joint. However, motion is realized by applying appropriate driving torques at joints, and for same shape of movement (with different starting points) driving torques at joints varies. Exact driving torque depends of "gravity contribution" to joint load which vary with different position of leg in space etc. This means that shape of motor control variable do not correspond to movement shape.

B. Walk composed from primitives

In this section is presented horizontal flat surface walking motion entirely synthesized using primitives. At the initial moment robot is standing still with both feet in contact with ground (double support phase). When motion starts, robot first transfer complete weight to right leg and started first half-step by lifting up left leg (single support phase) and moving it to front position. When left leg touched ground double-support phase was established again. Walking process continued and left leg become support leg, right leg was deployed from ground (right leg become leg in swing phase) and it was transferred from back to front position.

In Fig. 3 are shown stick diagrams of synthesized motion.

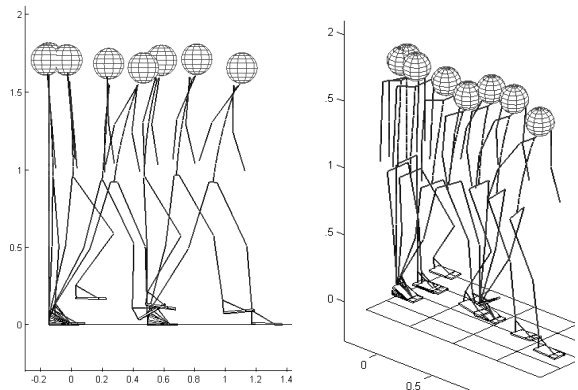


Fig. 3. Side view (left) and perspective view (right) at the stick diagram representing starting walking.

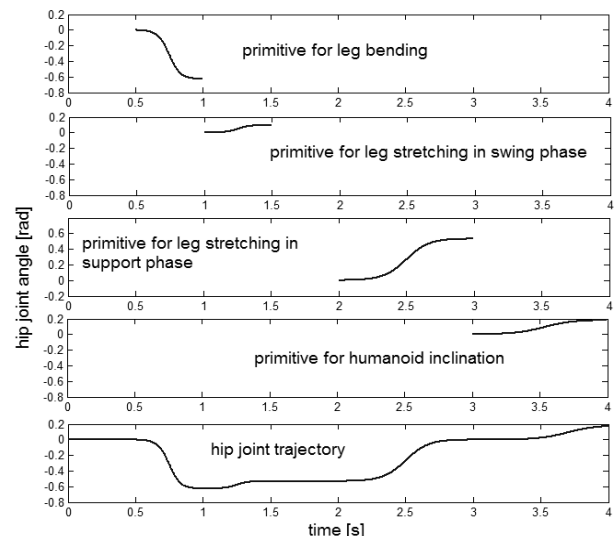


Fig. 4. Diagrams of composing the motion at the at the hip joint of left leg by superimposing primitives.

Primitives were applied at each joint. To obtain highly anthropomorphic walk it is very important to define appropriate starting and ending points for each primitive and motion intensity.

In Fig. 4. Is illustrate resulting trajectory at the hip joint of left leg for rotation about axis orthogonal on the motion direction. The following primitives were applied. Leg bending was applied with intensity 0.6, followed by leg in swing phase stretching with intensity 0.15. Then, for next 0.5s no additional primitives were applied and joint keep its current position. Then, leg at swing phase come to contact with ground and it become support leg and primitive for support leg stretching with intensity 1 was applied. Last primitive applied is inclination of overall system with intensity 0.35. Complete movement duration is 4s.

This example is given just to explain and illustrate basic idea of composing movements. However, primitives are not composed by selecting motion for each joint separately, but by selecting motion „as a whole“. For example, motion of leg in swing phase is composed by realization of two primitives: leg bending followed by leg stretching. Each primitive ensures synchronized motion of all joints involved.

IV. MOTION LEARNING

Simple motion of human limbs (for example, 3D human hand motion along straight line) requires very complex, simultaneous and well synchronized change of joints angles. Task is becoming even more complex when it is clear that it has to be synthesized and performed on-line on the basis of current state of the robot-environment interaction and can't be prepared in advance.

Having in mind findings reported in [7] we believe that human learn some basic motions and when needed it just have to be recalled and replayed. Another important point of [7] is that same stimuli drive limb to same point irrespective of its initial position (whole vector field is formed). And finally, those vector fields are additive. We believe approach with similar characteristics is needed for robots, too.

It have to be underlined difference between kinematic and dynamic composition of primitives. In case of kinematic composition just shape of movement have to be achieved while dynamics composition suppose learning of driving torques to achieve desired movement. Let us explain approach we advocate on the example of bending leg in swing phase. The first characteristic of this movement is that spatial trajectory of ankle is approximately straight line during normal walking without obstacles. Bending intensity and bending speed is choice of human, and it is possible to realize movement with different motion parameters and from different initial positions.

In Fig. 5 are illustrated two different examples of leg bending. In both cases small circles denote initial and terminal position of swing leg ankle (terminal position is defined by bending intensity). If bending intensity is larger ankle terminal position is higher.

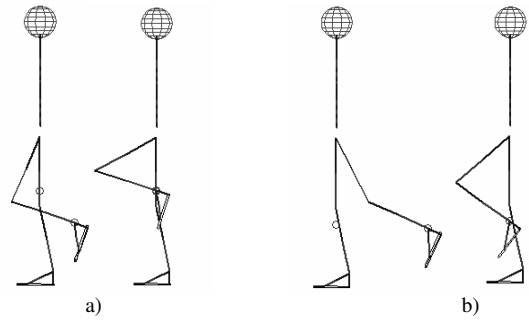


Fig. 5. Examples of leg bending with different starting positions and different intensities; a) leg bending intensity is 91%, b) leg bending intensity is 50%

For leg bending realization it is necessary to define set of inputs and outputs. As inputs were adopted: bending intensity, movement velocity (specified by movement duration), current velocity of ankle, current values of angles and current angular velocities at knee and hip (3 DoFs - at hip rotation is about x-axis (joint unit vector is parallel to walking direction) and y-axis (joint unit vector is orthogonal to walking direction), and at knee rotation is about y axis). Outputs are driving torques at hip and knee. At starting position leg is not moving and driving torques has to be such defined to ensure that (just to compensate gravity). Then, torques should be such to ensure linear ankle trajectory whose terminal point is defined by bending intensity. When ankle terminal point is reached torques should be such to keep leg at this position.

If movement velocity increase time needed for motion realization (t_{prim}) is shorter, but intensity of maximal ankle velocity is increased. On the basis of:

$$\dot{\mathbf{q}}_L = \mathbf{J}_L^{-1} \cdot \mathbf{v}_{skz} \quad (2)$$

angular velocities $\dot{\mathbf{q}}_L$ at knee and hip joint can be determined. \mathbf{v}_{skz} denotes desired ankle velocity, while values of Jacobian matrix represent relationship between leg's joints angular velocities and ankle linear velocity. From (1) we see that driving torques can be calculated as:

$$\mathbf{T} = \mathbf{H}\ddot{\mathbf{Q}} + \mathbf{h}_0 - \sum_{i \in S} \mathbf{J}^i T \begin{bmatrix} \mathbf{F}^i \\ \delta^i \times \mathbf{F}^i \end{bmatrix} \quad (3)$$

To use SVM regression for obtaining necessary driving torques we need to ensure proper training set. Let us remind once more that inputs for primitives (and also for SVM) are bending intensity, movement velocity (specified by movement duration), current ankle velocity, current leg posture, i.e. current values of angles and current angular velocities of performing leg, while outputs are driving torques (Fig. 6).

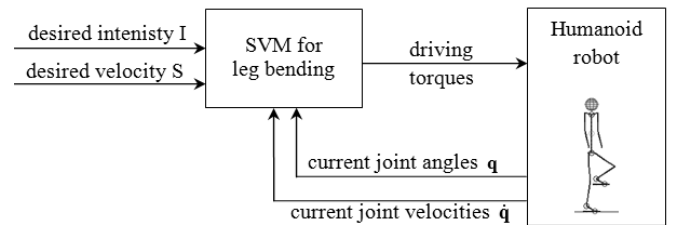


Fig. 6. Illustration of control scheme for leg bending primitive realization.

Because bending can be performed from any possible initial position training set should span, as much as possible, over initial postures which may appear. Training set should also span whole range of all possible bending intensities and velocities. First, leg initial posture, bending intensity and movement velocity are randomly determined.

The procedure of determining the input and output quantities for training data set is as follows:

1. Starting posture of the robot's leg is determined by random selection of hip and knee joint angles from predefined range.
2. Intensity (I) of leg bending and movement duration (S) are also selected randomly.
3. Desired velocity profile of ankle is calculated.
4. Then, procedure for driving torques computation at each time instant is following:
 - a. Desired ankle velocity profile is known. In each iteration corresponding angular velocities at leg's joints are calculated from (2).
 - b. After that, at each joint are calculated angle and angular acceleration.
 - c. Since whole system state is known (angles, angular velocities and accelerations at all joints) driving torques are calculated from (3).

In this way all input and output data for SVM training set for this time instant are specified. Then, procedure continue for next time instant

5. Procedure is repeated till ankle is sufficiently close to its terminal position, and when ankle velocity is sufficiently low. Then, procedure for this movement is stopped, new ankle starting position is randomly selected (target point is defined by intensity of leg bending) and steps 1-4 are repeated.
6. After sufficient number of performed movements, the procedure is stopped.

In this way the leg bending is simulated from the arbitrary starting point to the target point defined by intensity of leg bending. For each time instant, the values of all input and output quantities needed for SVM training are obtained. The input vector $[I \ S \ \mathbf{v}_{skz} \ \mathbf{q}_L \ \dot{\mathbf{q}}_L]^T$ for the training set is of dimension 11 whereas the dimension of the output vector $\boldsymbol{\tau}$ is 3.

A. SVM Regression

Since, we are using SVMs to calculate driving torques for primitives it is necessary to briefly describe what SVM represents and how it works.

There are a number of algorithms for approximating the function for establishing the unknown interdependence between the input (\mathbf{x}) and output (y) data, but an ever-arising question is how good is the approximation of the function $f_a(\mathbf{x})$. In determining the approximation function, it is necessary to minimize some of the error functions. The majority of the algorithms for the function approximation minimize the empirical error.

With the function approximation algorithms that minimize only the empirical error, there arises the problem of a large generalization error. The problem appears when the training set is small compared to the number of different data that can appear at the input. Structural Risk Minimization (SRM) [19] is a new technique of the statistical learning theory, which apart from minimizing the empirical errors, also minimizes the generalization errors (elements of the weight matrix \mathbf{w}). Hence, it follows that the structural error will be minimized by minimizing function of the form:

$$R = \frac{1}{2} \|\mathbf{w}\|^2 + C \sum_{i=1}^l |y_i - f_a(\mathbf{x}_i, \mathbf{w})|_\varepsilon \quad (4)$$

In (4), the error function with the ε - insensitivity zone was used as the norm. The parameter C is the penalty parameter which determines the extent to which the empirical error is penalized relatively to the penalization of the large values in the weighting matrix. Network input is denoted by \mathbf{x} , and desired output is denoted by y . Approximating function is denoted by $f_a(\mathbf{x}, \mathbf{w})$ and it has to be chosen in advance. Since case considered is highly nonlinear, for approximating function we have chosen radial basis function network (RBF network) with Gaussian kernel, for which output is calculated by:

$$f_a(\mathbf{x}, \mathbf{w}) = \sum_{i=1}^N w_i \exp(-\gamma \|\mathbf{x} - \mathbf{c}_i\|^2) + \rho$$

The nonlinear SVM regressions (minimization of (4)) determines the elements of the weight matrix \mathbf{w} and bias ρ . During the SVM training, support vectors (\mathbf{c}_i) are chosen from set of input training data. Design parameter ρ defines the shape of RBFs, and it is experimentally chosen to minimize VC-dimension, which provides good generalization.

B. Leg bending

According to described procedure for collecting training data set simulation was performed which lasted 100s. In this period 178 different initial postures were generated and same number of leg bending were performed. Training set has been formed on the basis of data from every sampling period (in this case it was 1 ms) and it was collected 100 000 input-output pairs. As a training set for SVM was selected just 10% of all collected data¹. Penalty parameter C and ε zone of insensitivity has been selected as 100 and 0.1. Those parameters are specific for each particular task and values were obtained by trial-and-error till satisfactory response was obtained.

After SVM training has been completed performance testing was performed by simulation. On the basis of specified leg bending intensity, movement duration, current ankle velocity and current leg posture and joints angular velocities (at knee and hip) driving torques are obtained from SVM and applied on robot. Torques drive system to new state, new torques are obtained, and procedure repeats till movement is completed. In

¹ There are three reasons to select just 10% of available data. First one is that for training set quadratic programming problem have to be solved. This requires large memory resources and training is time consuming. The second reason is that by selecting such size of training set problem of over fitting is avoided. Third reason is that such training set size was proven to be enough large for successful training for such kind of problems [17,18].

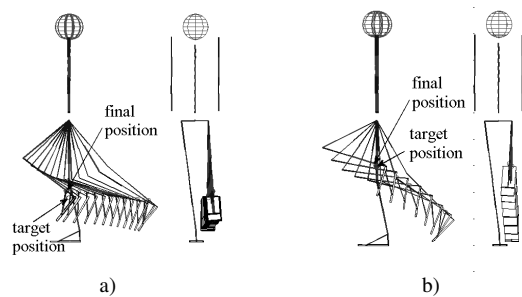


Fig. 7. Humanoid robot performing leg bending: a) bending intensity 41%, parameter S is 45% b) bending intensity 92%, parameter S is 70%

Fig. 7 are shown two examples of leg bending performed using trained SVM. Starting posture (angles at hip and knee) are selected to correspond approximately to posture of swing leg after deployment from ground during walking. Bending intensity and movement duration are defined randomly.

In example sketched in Fig 7.a) initial angles intensities (hip rotation about x and y axis, and knee joint rotation about y axis) were 0° , 40° and 10° , respectively. Bending intensity was 41%, and motion duration (parameter S) was 45%. As a consequence, movement was performed for $t_{\text{prim}}=0.69\text{s}$. Distance between target ankle position (defined by bending intensity) and achieved position was 6.3 cm.

In second example (sketched in Fig. 7.b)) initial angles intensities were 0° , 30° i 15° , respectively. Bending intensity was 92%, and motion duration (parameter S) was 70%. Motion was performed for $t_{\text{prim}}=0.46\text{s}$. Distance between target ankle position (defined by bending intensity) and achieved position was 2.7cm.

C. Walk generation

To perform complete walk movement of the leg in swing phase leg bending have to be continued by leg stretching. Also appropriate primitives have to be realized in supporting leg. In Fig. 8 is shown the stick diagram of walk composed using learned primitives by applying driving torques obtained from SVM.

At the beginning, robot stands still with both feet in contact with the ground. When walk starts, first a right leg bending is performed followed by leg stretching. Trunk is moved forward and robot is inclined forward. When right leg touches ground, the double support phase starts. After that the left leg bending is performed followed by leg stretching. Two half step simulation lasted for 2.3 s.

V. CONCLUSION

In this paper a novel approach of on-line synthesise of complex motions from basic movements (called primitives) is

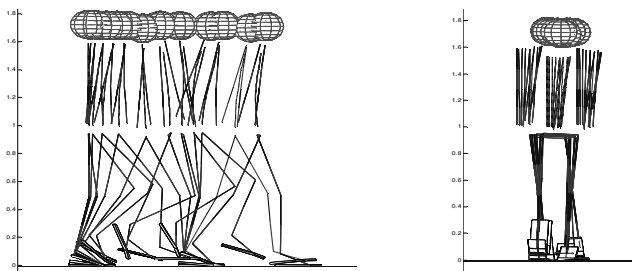


Fig. 8. Humanoid robot walk composed from primitives.

presented. Basic characteristic of proposed method is that, once trained, system is able to perform primitive from different starting points with different motion parameters. Also, new primitive can be added when previous is finished (or even before movement is over) without time consuming calculations. This enable human-like motion and on-line motion synthesis of humanoids in unstructured environment.

REFERENCES

- [1] M. Vukobratović, "How to control the artificial anthropomorphic systems", *IEEE Trans. on System, Man and Cybernetics*, SMC-3, pp. 497-507, 1973
- [2] M. Vukobratović, *Legged locomotion systems and anthropomorphic mechanisms*, Mihajlo Pupin Institute, Belgrade 1975, also published in Japanese, Nikkan Shimbun Ltd. Tokyo, in Russian, "MIR", Moscow, 1976, in Chinese, Beijing 1983
- [3] M. Vukobratović, B. Borovac, D. Surla, D. Stokić, *Biped locomotion – Dynamics, stability, control and application*, Springer-Verlag, Berlin, 1990
- [4] M. Vukobratović, B. Borovac, "Zero-Moment Point- Thirty five years of its life", *Int. Jour. of Humanoid Robotics*, Vol. 1, No. 1, pp. 157-173, 2004
- [5] A Realtime Pattern Generator for Biped Walking Shuuji Kajita, Fumio Kanehiro, Kenji Kaneko, Kiyoshi Fujiwara, Kazuhito Yokoi and Hirohisa Hirukawa
- [6] Online Walking Control System for Humanoids with Short Cycle Pattern Generation K. Nishiwaki S. Kagami
- [7] F.A. Mussa-Ivaldi, S.F. Giszler, E. Bizzi, "Linear combinations of primitives in vertebrate motor control", *Proc. Natl. Acad. Sci.* 91, pp. 7534-7538, 1994
- [8] K. Hauser, T. Bretl, J.C. Latombe, "Using motion primitives in probabilistic sample-based planning for humanoid robots" *Algorithmic foundation of robotics VII*, Vol. 47 Springer Berlin / Heidelberg , pp. 507-522, 2008
- [9] J. Peters, S. Schaal, "Policy learning for motor skills", *Neural Information Processing*, Springer Berlin / Heidelberg , Vol. 4895, pp. 233-242, 2008
- [10] J. Denk, G. Schmidt, "Synthesis of walking primitive databases for biped robots in 3D-environments", *Proc of the IEEE Int. Conf. on Robotics and Automation*, Vol. 1, pp. 1343-1349, Taipei, Taiwan, 2003
- [11] D. Kulić, Y. Nakamura, "Incremental learning and memory consolidation of whole body motion patterns", *Int. Conf. on Epigenetic Robotics*, pp. 61-68, 2008
- [12] M. Vukobratović, V. Potkonjak, B. Borovac, K. Babković, "Simulation model of general human and humanoid motion" *Multibody System Dynamics*, Vol. 17, No 1, pp 71-96, 2007
- [13] M. Vukobratović, B. Borovac, M. Raković, V. Potkonjak, M. Milinović, "On Some Aspects of Humanoid Robots Gait Synthesis and Control at Small Disturbances", *Int. Jour. of Humanoid Robotics*, Vol. 5, No 1, pp 119-156, 2008
- [14] P. Song, P. Kraus, V. Kumar, P. Dupont, "Analysis of Rigid-Body Dynamic Models for Simulation of Systems With Frictional Contacts", *Journal of Applied Mechanics*, Vol. 68, No 1, pp 118-128, 2001
- [15] S. Goyal S, E. M. Pinson, F. W. Sinden, "Simulation of dynamics of interacting rigid bodies including friction I: General problem and contact model", *Engineering with Computers*, Vol. 10, No 3, pp 162-174, 1994
- [16] B. Borovac, M. Nikolić, M. Raković M. "How to compensate for the disturbances that jeopardize dynamic balance of a humanoid robot" *International Journal of Humanoid Robotics*, In Print 2011.
- [17] B. Borovac, M. Raković, M. Nikolić, "One Approach for On-line Generation of Motion of Humanoid Robots Using Primitives", *55th ETRAN*, Teslić, Republika Srpska, 2011
- [18] M. Raković, M. Nikolić, B. Borovac, "Humanoid Robot Reaching Task Using Support Vector Machine", *Procc of Int. Conf. Eurobot 2011*, Prague, Czech Republic, 2011
- [19] Keeman V. "Learning and Soft Computing: Support Vector Machines, Neural Networks, and Fuzzy Logic Models", The MIT Press, Cambridge Massachusetts, 2001

Real Time Method for Image Recognition and Categorization

Ivan Božić and Ivan Lazić

Abstract—In this paper we propose a method for digital image recognition and classification in real-time applications. The paper describes this method in both ways, giving a theoretical background and our implementation. The method can be useful in different scientific fields, and can be utilized for research, education and professional purposes. In this article we present results obtained by our method in the fields of security services and traffic control. All results were obtained using a stand-alone application developed in MATLAB software package and using C++ program language.

Index Terms—Categorization, digital image processing, recognition, real-time application, standalone software.

I. INTRODUCTION

IN this stage of industrial development, the biggest question is how to automatize processes in manufacturing, transport, delivery and pricing of products and transport and identification of people. Therefore, the main contemporary research in digital signal processing is concentrated to the development of quality software algorithms and methods for recognition and categorization of different signal types. In the following text we describe a possible solution for image processing.

Through the increase of the processing power of computers, digital image processing has been rapidly developing and now is a part of almost every industrial branch. Different operations on image are used today in various fields, from space research, to different industries and security services to medicine and entertainment industry. The main goal in all of these different fields is to recognize two identical images or to recognize some parts of two different images and categorize them. There are many existing solutions, but we still have open questions in this field. This paper presents one possible solution regarding the open topics of real-time image processing which can be used in different (research, educational and professional) purposes. The main goals of this method are to recognize the same images and categorize them in some type of databases [1].

Software was developed in MATLAB software package and

C++ program language. We chose this specific combination in developing to assure the best characteristics from both tools. MATLAB offers a large number of methods to process images, and C++ is a very efficient language. Also, both tools are object-oriented. As we mentioned above, our method and software can be used as a research or educational tool, or for professional purposes as a stand-alone application. As an educational tool this method has many possibilities for learning about operations which are useful in different stage of digital image processing (for example: acquisition, segmentation, edge detection, etc.). Software allows students to experiment with many parameters in every stage of processing. In that way they can learn and understand important factors and their effects on final results. Researchers can benefit from this software in different ways. However, the most important software property is the possibility to change different methods for specific purpose, or more radically, every researcher can write his/her own method which can be incorporated in our software. In that way researchers can modify our software for their specific applications. For professional purposes the software offers a special function for generating C code, which can be used along with microcontrollers, microprocessors, PLA, etc. Using all abilities which the software provides, one can modify the method and adjust it for specific operations and after that generate a standalone application or C code. This method and the developed software merge three main stages in digital image processing: acquisition of image and/or video, which can be used for creating database or test image (video), preprocessing, and recognition and categorization (Fig. 1). Therefore, this software can be used as a part in an integrated system. During the developing phase we wanted to derive an efficient method and software for image detection and classification for security services (checking of IDs, passports, driver licenses, etc.) and traffic control (detection of car plates, traffic signs, etc.). The presented results were obtained during developing, testing and verifying this method on different images.

II. THEORETICAL BACKGROUNDS

This section described methods which are used in different software functions: acquisition, preprocessing, recognition and categorization. We will describe only the main characteristics of standard and well defined function in literature and every

A part of this paper was presented at the 55th ETRAN conference, Banja Vrucica, 6-9. June 2011.

I. Božić (corresponding author to provide phone: +381-64-2174568; e-mail: msc.ivan.bozic@gmail.com).

I. Lazić, was with Faculty of Traffic and Transport Engineering, University of Belgrade, Belgrade, Serbia (e-mail: ivanlazicsf@yahoo.com).

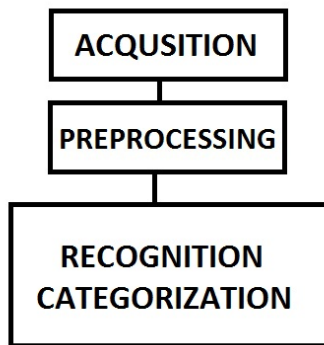


Fig. 1. Operation provided in presented method and software.

part of the algorithms proposed by the authors.

A. Acquisition

Acquisition provides operations for camera set-up, camera calibration, and radial distortion removal. Camera calibration is one of important operations while recording image and/or video of the same scene from different angles. There are many parameters that can be defined in the calibration section as: selecting the plugged-in camera, image or video format, brightness, contrast, color scheme, type of output file, etc. Also, the user must take control on type of acquisition, for database or testing. Radial distortion is the main problem during recording with a real lens, because that it is important to remove this distortion from images and videos. Quality of recordings is important during recognition and categorization stage. Every camera introduces radial distortion and we can remove it only using appropriate software solutions, and it cannot be removed by hardware solutions, because hardware mainly creates this distortion.

B. Preprocessing

All preprocessing operations can be divided in three main groups: determination of feature vectors, calculating stable points and segmentation (Fig. 3). Also, in preprocessing we include fixture processing's which is done by other software methods. Algorithms we use in preprocessing are common and the most used for particular operation. For the determination of features vectors our software uses SIFT (Scale Invariant Feature Transform) and SURF (Speed Up Robust Features) detectors; for calculating stable points we used the RANSAC (RANdom Sample Consensus) method, and for segmentation we choose the iterative Graph Cut method. In the further text all these methods will be briefly described, also, we will include detailed information about parameters and the function which were proposed by us.

At the first step, SIFT [2] determines the key-points on the sequence of images and stores them in a database, after which this method select some number of key-points useful for recognition phase. In the next step this method compares the key-points from the test image with the key-points from all images in the database and the best candidate is chosen by different metrics conditions. This method is the most

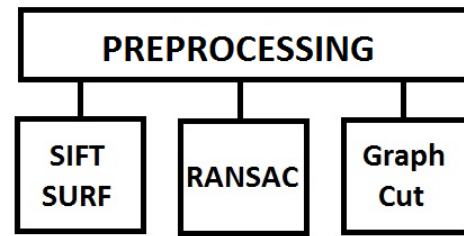


Fig. 2. Preprocessing.

commonly used, because it is robust toward different kinds of noise and gives a large number of key-points for comparison [4,5]. SURF [3] is another detector used in our software. It is a newer method than SIFT, and it is based on it. The main difference between these two methods is time efficiency, which is better in SURF than in SIFT [5].

RANSAC method determines stable points from set of key-points which are obtained by using one of feature vectors detectors. This method can be used in many different applications which need fitting some points, regardless of the fact if these points can or cannot be described by some models. The implementation and the results for this method hugely depend on specific parameters. Except the standard parameters we proposed using one additional parameter to determine the distance between two frames in which the RANSAC method is implemented. Every user should be extremely careful with this parameter, because if properly selected the RANSAC process will be much more effective, but on the other hand it could cause the divergence of the whole process.

The Graph Cut method [7,8,9] is an iterative method for segmentation. The main advantage of this method is that the user has an opportunity to affect the result of segmentation by parameters. These methods use two types of input parameters, vector of points in the foreground and the background. These two vectors are used as the initial conditions. The method stops the iterative process when all points on the image belong to the first or to the second vector of initial conditions. In our solution we proposed two methods that automatically define the initial conditions. One of them used stable points, and the other uses the intensity levels and threshold. Also, we obtained a function which gives the opportunity to the user to manually define vectors of initial conditions or to incorporate some automatic solution that they made.

C. Recognition and Categorization

For recognition and categorization this software use several different methods, but the most useful are: NNS (Nearest Neighbor Search), histogram and covariance region descriptor. During categorization we use three different measures for distance: Euclidean, Manhattan, and Mahalanobis.

NNS [15] is used for determine the same object in big databases. This is an optimization problem in which we look for the nearest neighbor points in different metrics. In the program we use several different algorithms for this method such as: linear NNS, space partitioning and locality sensitive hashing. For the software purposes we combine these three

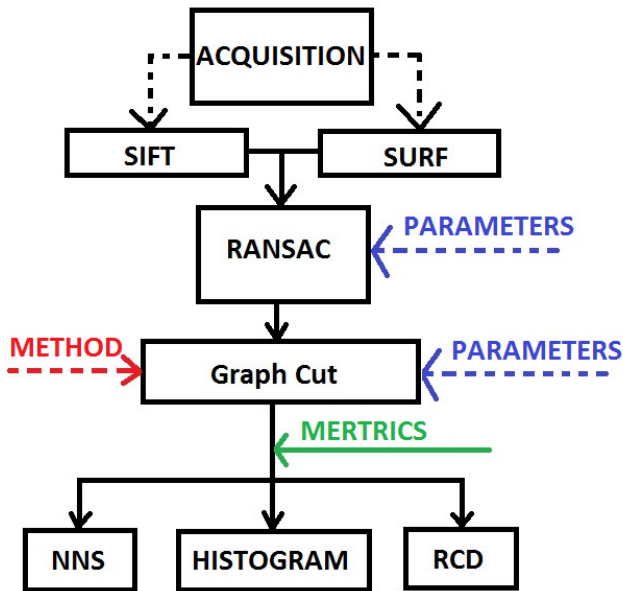


Fig. 3. Software block diagram.

algorithm with different metrics (Euclidean, Manhattan, and Mahalanobis). Also, the software supports the k-NNS algorithm in which we are looking for k nearest neighbor.

The histogram comparison is also a powerful technique for recognition and categorization. Here all three metrics are used as in the previous method. This method compares pixel levels, it is of utmost importance to always use normalized histograms. If we do not normalize them we introduce an error and process of categorization becomes unsuccessful.

Region covariance descriptor is based on covariance matrix and integral images. Integral images are used for faster computation of region sum and it's define for (x',y') pair as sum of all pixels values in image region $I(0:x',0:y')$. For image I of dimension $W \times H$ is defined F as a $W \times H \times d$ dimensional features image provided from I with any mapping operation (intensity, color, gradients...). After that we choose region R such that is subset of F and for some $z_k, k=1, \dots, n$, d -dimensional features point inside R . We represent a region R as $d \times d$ covariance matrix of features points as:

$$C_R = \frac{1}{n-1} \sum_{k=1}^n (z_k - \mu)(z_k - \mu)^T \quad (1)$$

Because the covariance matrix does not lie in the Euclidean space, is necessary for using this algorithm to find the way for computing distance between the points for NNS algorithm. There used distance measured based on dissimilarity of two covariance matrices as:

$$\rho(C_1, C_2) = \sqrt{\sum_{i=1}^n \ln^2 \lambda_i(C_1, C_2)} \quad (1)$$

III. SOFTWARE IMPLEMENTATION

As we mentioned above, our software is implemented as a standalone application using MATLAB and C++. Graphical user interface has one main window from which the user can



Fig. 4. Four type of testing documents, from top to bottom: biometric passport, biometric ID, driver license and registration certificate.

access some of the functions offered by the software. Every particular operation has its own window. Thus we have five additional windows, and they implement the following functions: acquisition, detection of feature vectors, and determination of stable points, segmentation, recognition and

categorization (categorization is used only if database is loaded) and generating executable C code. A block diagram of this software realization is shown on Fig. 3.

Software may – or may not – start with acquisition. Acquisition is an optional operation and the rest of the software procedure doesn't depend on it. Therefore, acquisition can be used as a separate part for creating database or individual snapshots. Also, if the user skips the acquisition step, in the next step he/she has an option to load a database or a test image (images whose existence is checked in database), and of course there is a possibility to load sequences of test images. After completing the first step (acquisition or loading) the user must select the appropriate descriptor. Both realized detectors have their advantages and disadvantages, and the success of algorithm for recognition and categorization depends on their appropriate selection. Independently on the chosen detector, the next step in the method is the RANSAC algorithm. In this phase the user can again modify the original software. In this moment he/she can add an additional parameter which can adjust difference in the number of frames which are compared. As we mentioned above, this parameter can be extremely useful for the experienced users and it is not recommended for new users to experiment with it. The next operation is segmentation. Segmentation is the most important operation, and because of that it has the largest number of options. Besides manually placing parameters, there are three more available developed algorithms for automatic placement of boundary conditions which are based on stable points [1,2,3,6], pixels levels and edge detection [13,19,20]. Choosing some of these options gives the user an opportunity to change their parameters. There is no a general better solution, because of that they should be used for basic needs. Therefore, in this place the user can add his/her own solution. This option is primarily designed for the experienced users. After completed segmentation, the image is shifted to ideal position with regard to the reference database. This is the only phase that the user cannot influence, and it is fully automated. After segmentation there is a final step and the main goal of the whole algorithm. In this moment the user can select one of three possible methods for recognition and categorization. In the future versions of the software we plan to expand the available methods. The selection of methods, their realization and metrics should depend on practical problems and the desire is that all methods give equally good results in every particular case.

The closing step available to the user is the generation of C code with all parameters and methods which were used during the software operation. This code can be used with other C assemblers and while creating integrated systems.

IV. RESULTS

In this section we present and analyze results. We start with the description of databases used during software validation. Then we describe the methods and parameters of software used to obtain the presented results, and at the end we

introduce a method for evaluating the quality of software (using two types of errors).

As a result we present the results obtained on five databases. One database is used in verifying stage. This database consists from different types of business cards; the distribution of business cards is presented in Table I.

TABLE I
BUSINESS CARD DATABASE

Image description	Number
Total number	100
Horizontal images	78
Vertical images	22
With white background	40
With colored background	30
Multi colored business cards	20
Illustrated business cards	10

TABLE II
TEST RESULTS ON BUSINESS CARDS

Business card	NNS	Histogram	RCD
White	98.2	99.1	99.8
Colored	99	97.6	99.4
Colorful	96.5	99.2	98.9
Illustrated	97.3	98.1	99.2

The distribution in database is thus created to give the best possible description of real problems (the biggest number of business cards in database, 70 %, has one-color background), illustrated and multicolor business cards are also included. Business cards are an ideal object for software testing, because they share the same characteristics with the target documents. All documents that we wanted to process using this software had a number of similar characteristics: every document had known fixed dimensions, all documents has rectangular shape, except the traffic signs which can be rectangular, rhomb-shaped or circular and every group of documents had the same backgrounds. Other four databases were used for testing software and consisted of a database with biometric IDs of Republic of Serbia, a database with biometric passports of Republic of Serbia, a database of driver license of Republic of Serbia, and registration certificates for cars of Republic of Serbia. The databases of documents on which the software was tested were smaller and included forty images biometric passports, sixty five images of biometric IDs, fifty four images of registration certificates, and forty images of driver license, as shown in Table III.

The first results obtained with business cards represent comparison of different algorithms that can be generated with software. Table II shows a part of results related to a success in recognition of business cards (in percent) on which the SIFT method was applied, depending on the chosen classifier. For all classifiers we used Euclidian metrics (except for RCD).

TABLE III
DOCUMENTS DATABASES

Type of documents	Number
Biometrics ID	65
Biometrics passport	40
Driver license	30
Registration certificate	54

TABLE IV
RESULTS ON DOCUMENTS

Document	FAR	FRR
Biometric IDs	1.0	1.8
Biometric passports	1.08	2.5
Driver license	1.20	2.4
Registration certificate	1.9	4.2

As we can conclude from Table II, the results with SIFT detector are satisfactory, and the comparison with the remaining data has shown that is the best combination of parameters is, if we choose the next algorithm. For the determination of feature vectors we should use the SIFT method; in the RANSAC procedure good results are obtained if we, together with standard parameters, use a new realized parameter. This parameter determines the difference between two compared frames, and it should be set to five. For the segmentation we used the method implemented by stable points and additional processing. This method is very effective and accurate. For recognition and categorization we use the covariance matrix, because it gives the best results.

For the verification of the accuracy we introduce two types of errors. The FAR (False Accept Error) error describes the percent of images recognized as members of database, although they are not in the database. The FRR (False Reject Error) error describes the percent of images that are members of database, but were not recognized as such. Although there are no good errors, it is important in security services that the number of the FAR errors is lower than that of the FRR.

The obtained results for all four testing databases are presented in Table IV.

The obtained results show that this kind of solution can be equally useful in research, educational and professional purposes. Further research should consider the usefulness of our solution in traffic, especially if we further minimize errors.

V. DISCUSSION AND CONCLUSION

All results have small FAR errors, but the FRR is significantly different between different databases. Also, there are very similar differences between the FRR and the FAR errors for all databases. As expected, databases with documents which include pictures give better results than the documents without pictures. That can be discussed from different angles. Better recognition and categorization is very likely a result of stable key-points on the personal image on documents. On the other hand, a document like an ID or passport includes even more, two pictures, personal signs and

fingerprints. In contrast to these documents registration certificates include only textual data, which produce weaker and lower number of stable points. FAR results are better primarily because the backgrounds are clearly different in every type of documents, and the software easily recognized if a picture belonged to that database. FRR errors are greater primarily because there are not enough to determine if this image belongs to this database. Software must recognize if this image has a match with any other image in the database.

For future research we put before ourselves a task to recognize different features, which is important for automatic traffic control. This problem is very interesting, because quality recognition and categorization of traffic signs is the main problem in automatic traffic control. We will analyze the efficiency of the software in the recognition and categorization of car plates and traffic signs. This will present a similar problem, but a different approach will be needed. When we analyze documents we have a static situation, recorded images or videos are stationary. On the other hand, recording of car plates and traffic signs would be dynamic situation. Furthermore, recording car plates and traffic signs are different problems, because when we record plates, we have fixed position of camera and plates are dynamic, on the other hand traffic signs are fixed and camera is moving. For these two problems it is important to determine the best position of the camera, regardless of the fact if the camera is fixed or moving. Additional problems in traffic control applications are time is available for recording and successful categorization, or the existence of more than one traffic sign on the same pillar [23]. There are some solutions for this type of problems, but no solution is perfect and this situation may be considered as an open problem.

The presented results and the obtained errors show that this solution can be very useful for different purposes and applications. In further work we will try to decrease the number of errors and implement better solutions, or time-efficient solutions. Also, we plan to create an integrated system and test it in real traffic situations.

REFERENCES

- [1] A. Forsyth and J. Ponce, *Computer Vision: A Modern Approach*, Prentice Hall, 2003.
- [2] DG. Lowe, "Distinctive image features from scale invariant keypoints," *International Journal of Computer Vision*, vol. 60, pp. 91-110, Januar 2004.
- [3] H. Bay, T. Tuytelaars and L. Van Gool, "SURF: Speed Up Robust Features," *ECCV 06*, November 2006.
- [4] K. Mikolajczyk and C. Schmid, "A performance evaluation of local descriptors," *IEEE Trans. Pattern Recognition and Machine Intelligence*, vol. 27, pp. 1615-1630, October 2005.
- [5] L. Juan and O. Gwun, "A comparison of SIFT, PCA-SIFT and SURF," *International Journal of Image Processing*, vol. 3, pp. 143-152, August 2009.
- [6] MA. Fischler and RC. Bolles, "Random sample consensus: A paradigm for model fitting with application to image analysis and automated cartography," *Graphics and Image Processing*, vol. 24, pp. 381-395, June 1981.
- [7] AP. Eriksson O. Barr and K. Astrom, "Image Segmentaions using minimal graph cuts," *Proceedings SSBA06*, pp. 45-48, March 2006.

- [8] J. Malcom, Y. Arthi and AR. Tannenbaum, "A graph cut approach to image segmentation in tensor space," IEEE Conferencion on Computer Vision and Pattern Recognition CVRP07, pp. 1-8, June 2007.
- [9] E. Vincent and R. Laganiere, "Detecting planar homographies in an image pair," Proceedings of the 2nd International Symposium on Image and Signal Processing and Analysis, pp. 182-187, June 2001.
- [10] A. Pinz, "Object Categorization," Computer Graphics and Vision, vol 1, pp. 255-353, 2006.
- [11] S. Dickinson, A. Leonardis, B. Schiele and MJ. Tarr, Object Categorization: Computer and Human Vision Perspective, Cambridge University Press, 2009.
- [12] E. Fazl and JS. Zelek, "Region detection and description for object categorz recognition," CRV07, pp. 3321-3328, May 2007.
- [13] J. Canny, "A computational approach to edge detection," IEEE Trans. Pattern Recognition and Machine Inteilgence, vol. 8, pp. 679-698, November 1986.
- [14] P. Felzenszwalb, R. Girshick, D. McAllester and D. Ramanan, "Object detection with discriminatively trained part-based models," IEEE Trans. Pattern Recognition and Machine Inteilgence, vol. 32, pp. 1627-1645, September 2010.
- [15] L. Andrews, "A template for nearest neighbore problem," C/C++ Users Journal, vol. 19, pp. 40-49, November 2001.
- [16] D. Stanković, "Prepoznavanje i detekcija lica sa digitalne slike korišćenjem algoritma za filtriranje Gausovog šuma zasnovanog na LPA-ICI tehnicu," Zbornik radova 53, konferencije ETRAN RT6.2, pp. 1-4, Jun 2009.
- [17] S. Milovanov, R. Benčik and B. Mišić, "Primena Support Vector Machine klasifikatora u prepoznavanju karaktera sa registarskih tablica," Zbornik radova 53, konferencije ETRAN AU1.9, pp. 1-3, Jun 2009.
- [18] A. Mijatović and D. Dujković, "Primena hromatske segmentacije i geometrijskih karakteristika za detektovanje saobraćajnih znakova na slici," Zbornik radova 52, konferencije ETRAN EK3.5, pp. 1-4, Jun 2008.
- [19] Đ. Klisić, I. Božić and M. Petrović, "3D IMPRO DYNAMIC – program za digitalnu obradu medicinskih slika," Zbornik radova 52, konferencije ETRAN EK3.7, pp. 1-4, Jun 2008.
- [20] Đ. Klisić and I. Božić, "MedPicPro – program za digitalnu obradu medicinskih slika," 16. Telekomunikacioni forum TELFOR, pp. 621-624, Novembar 2008.
- [21] O. Tuzel, F. Porikli and P- Meer, "Region Covariance: A fast detector for Detection and Classification," ECCV06, pp. 589-600, May 2006.
- [22] I. Božić, A. Savić, K. Savić and M. Gavrilović, „Softver za obradz elektrofizioloških signala“, Zbornik radova 54. konferencije ETRAN ME1.3, pp. 1-4, Jun 2010.
- [23] I. Lazić, N. Bjelobaba, I. Božić, and M. Beljin, „Detekcija i klasifikacija slika u saobraćaju“ Zbornik radova 55. Konferencije ETRAN EK1.6. pp. 1-3, Jun 2011

Matlab/Simulink Implementation of Wave-based Models for Microstrip Structures utilizing Short-circuited and Opened Stubs

Biljana P. Stošić, Darko I. Krstić, and Jugoslav J. Joković

Abstract—This paper describes modeling and analyzing procedures for microstrip filters based on use of one-dimensional wave digital approach. Different filter structures are observed. One filter is based on quarter-wave length short-circuited stubs and connecting transmission lines. The other one is based on cross-junction opened stubs. Frequency responses are obtained by direct analysis of the block-based networks formed in Simulink toolbox of MATLAB environment. This wave-based method allows an accurate and efficient analysis of different microwave structures.

Index Terms—Microstrip filters, microwave circuits, wave digital approach, block-based models.

I. INTRODUCTION

THE concepts of wave digital networks (WDNs) have their origins in the field of filter design, where they are designated more specifically as wave digital filters [1] – [4]. Generally speaking, WDNs can be viewed as a powerful modeling and analysis tool, as shown in [5] - [9].

In microwave structures, different junctions with several arms (i.e. of several transmission lines) are often employed. This paper outlines the concept of WDN and its use for the modeling and analysis of microstrip circuits which contain junctions with three and four arms. The special contribution is that it develops a global algorithmic view to WDN with respect to modeling and simulation purposes. Moreover, special emphasis has been put on a plain but concise presentation of the underlying ideas in order to address both readers with and without background in one-dimensional (1D) wave digital approach.

This paper is supported by Ministry of Education and Science under grant number TR32052. A part of the results shown in this paper is presented on 55th ETRAN Conference, Banja Vrućica, June 6-9, 2011.

B. P. Stošić is with University of Niš, Faculty of Electronic Engineering, Aleksandra Medvedeva 14, Niš, Serbia (phone:+381 18 529 303; fax: +381 18 588 399; e-mail: biljana.stosic@elfak.ni.ac.rs).

D. I. Krstić is with Serbian Armed Forces, VP 2822, Prokuplje, Serbia (e-mail: darko.krstic.1983@gmail.com).

J. J. Joković is with University of Niš, Faculty of Electronic Engineering, Aleksandra Medvedeva 14, Niš, Serbia (phone:+381 18 529 302; e-mail: jugoslav.jokovic@elfak.ni.ac.rs).

The paper is organized as follows. A brief review of 1D wave digital approach and a way of determining a minimal number of sections in WDN is described in Section 2. This modeling approach is critically dependent on precise determination of section numbers.

The wave digital models of a short-circuited transmission line and an opened line, which are presented in Section 3, represent the background to the modeling strategy that follow.

The WDN of the observed structures are given in Sections 4 and 5. They can be formed directly in the Simulink toolbox of MATLAB environment. In Section 6, block-based wave digital models of the structures are described. Response in WDNs can be found by use of formed block-diagram networks and some basic MATLAB functions.

Finally, a simulation validation of the proposed modeling and analysis approaches provided by means of a microstrip ultra-wideband filter utilizing short-circuited stubs and a low-pass filter of wide stop-band is presented and discussed in Section 7.

II. A BRIEF REVIEW OF WAVE DIGITAL APPROACH

Some general properties and the basic aspects of the 1D wave digital approach that are of considerable importance, related to this work, will be discussed here briefly. Generally speaking, the block-based 1D wave digital approach to analysis entails modeling structure as a network of interconnected blocks. WDNs containing adaptors are suitable for the modeling of a wide range of physical structures.

A lossless uniform transmission line is modeled by a two-port digital element with a delay occurring in the forward path. This wave digital two-port network is called the unit element (UE) [2]. The port resistances of the UE are equal and correspond to the characteristic impedance of uniform segment. The connection of two UE with different port resistances is achieved by two-port series/parallel adaptors [3].

A complex structure has to be divided into a cascade connection of uniform transmission lines (so-called uniform segments) where each segment is modeled by unit wave digital elements. In the complex microstrip structures, the delays of transmission lines vary from one another, and because of this each uniform segment has to be represented as a cascade connection of a certain number of UEs. The initial step in the

proposed modeling methodology is to determine a minimal section numbers (i.e. number of cascaded UEs in uniform segments). This determination is based on the given relative error as shown below. An appropriate choice of a minimal section number in that model is very important because of the direct influence on the sampling frequency of that digital model, and on accuracy of the desired response.

A. Minimal Section Numbers [7]

A real delay T_Σ of a complex microstrip structure differs from the delay T_t of the WDN. In complex microstrip structures, delays of transmission lines are not multiple integers of the minimum delay. The number of sections n_k used for modeling an individual transmission line is found as the nearest integer of the ratio $q \cdot T_k / T_{\min}$, i.e.

$$n_k = \text{round}[q \cdot T_k / T_{\min}], \quad (1)$$

where $q \geq 1$ is a multiple factor, T_k is a delay on the k^{th} transmission line, $T_{\min} = \min\{T_1, T_2, \dots, T_M\}$ is a minimum delay, $k = 1, 2, \dots, M$ and M is the number of uniform segments in the complex microstrip structure.

According to these data, the total delay for the digital model of the structure is

$$T_t = n_t \cdot T_{\min} / q, \quad (2)$$

where the total number of UE in the WDN is

$$n_t = \sum_{i=1}^M n_k. \quad (3)$$

The relative error of a total delay in percentages is found as

$$er[\%] = \frac{T_\Sigma - T_t}{T_\Sigma} \cdot 100, \quad (4)$$

where

$$T_\Sigma = \sum_{k=1}^M T_k \quad (5)$$

is the sum of all transmission line delays, i.e. the total real delay of the structure, and T_t is given by (2).

The minimal number of sections needed for the modeling of the observed structure is found by using the relative error $n_er[\%]$, which is already known. The procedure for determining the minimal number of sections with the error less than the given one can be done in a few steps. At the beginning, errors $er[\%]$ are found for different values of the multiple factor $q = 1, 2, \dots, q_{\max}$, where q_{\max} is an arbitrary chosen value. Then, the first relative error with an absolute value less than the previously given error $|er[\%]| \leq n_er[\%]$ is chosen. The number of sections for the k^{th} transmission line n_k , $k = 1, 2, \dots, M$, the total number of sections n_t , and the total delay of a digital model of the structure T_t , corresponding to that error are then used for modeling.

B. Sampling Frequency

The sampling frequency of the digital model of the planar structure is found for the chosen minimal number of sections, and is

$$F_s = 1/T_s, \quad (6)$$

where

$$T_s = T_t / n_t \quad (7)$$

is the sampling period of the planar structure modeled by n_t sections. In order to match the response of the digital model with a real response, a new frequency is defined

$$F_{sm} = F_s / 2. \quad (8)$$

III. WAVE DIGITAL MODELS

A. Model of a Short-Circuited Transmission Line

Consider a short-circuited transmission line depicted in Fig.1.

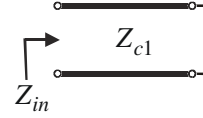


Fig. 1. A short-circuited transmission line.

An input impedance of a lossless transmission line terminated by impedance Z_l has complex value

$$Z_{in} = Z_c \cdot \frac{Z_l + S \cdot Z_c}{Z_c + S \cdot Z_l}. \quad (9)$$

According to this equation and the fact that $Z_l = 0$ for a short-circuited, an input impedance of the line shown in Fig.1 is

$$Z_{in} = S \cdot Z_{c1}. \quad (10)$$

Billinear frequency transformation is

$$S = (1 - z^{-1}) / (1 + z^{-1}), \quad (11)$$

where $z = e^{ST}$ is a complex variable and $S = j\Omega$ is a normalized complex frequency.

By replacing the normalized complex frequency in the relation (10), the reflection coefficient is

$$\frac{B}{A} = \frac{Z_{in} - Z_{c1}}{Z_{in} + Z_{c1}} = -z^{-1}. \quad (12)$$

That means, the relation between the wave variables in frequency domain is

$$B = -z^{-1} \cdot A. \quad (13)$$

So, a short-circuited transmission line (Fig. 1) can be transform into wave digital network shown in Fig. 2 by using billinear transformation (11).

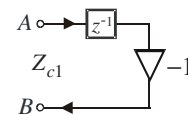


Fig. 2. Wave digital network of a short-circuited line.

B. Model of an Opened Transmission Line

Consider an opened line depicted in Fig. 3.

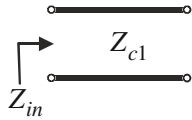


Fig. 3. An opened transmission line.

According to equation (9) and the fact that $Z_c = Z_{c1}$ and load impedance $Z_L \rightarrow \infty$ for an opened circuit, an input impedance of the line shown in Figure 3 is

$$Z_{in} = Z_{c1} / S. \quad (14)$$

By replacing the normalized complex frequency in the relation (14), the reflection coefficient is

$$\frac{B}{A} = \frac{Z_{in} - Z_{c1}}{Z_{in} + Z_{c1}} = z^{-1}. \quad (15)$$

That means, the relation between the wave variables in frequency domain is

$$B = z^{-1} \cdot A. \quad (16)$$

So, an opened transmission line (Fig. 3) can be transform into wave digital network shown in Fig. 4 by using billinear transformation.

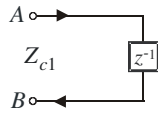


Fig. 4. Wave digital network of an opened line.

IV. WAVE DIGITAL NETWORK AS MODELING TOOL FOR STRUCTURE UTILIZING SHORT-CIRCUIED STUBS

Given is a microstrip structure, Fig. 5 [10]; it is assumed that this structure consists only of uniform segments where one segment is short-circuited stub. From such a structure an algorithmic model in the form of a wave digital network can be created, which is a rather complex reformulation where several constraints are to be met.

A wave digital network which corresponds to the observed segment connection is depicted in Fig. 6. The uniform segments have different characteristic impedances Z_{ck} , $k=1,2,3$. All uniform segments are modeled by several cascaded UEs, short: $n_k \times T$ blocks.

These blocks, i.e. models of uniform segments UTL1, UTL2 and UTL3, are connected by use of one three-port parallel adaptor with port 2 being dependent. Adaptors are memoryless devices whose task is to perform transformations between pairs of wave variables that are referred to different levels of port resistance.

A parallel adaptor serves to interconnect, in parallel, n -ports with arbitrary port resistances R_1, R_2, \dots, R_n . A network of three-port parallel adaptor with port 2 being dependent is depicted in Fig. 7, [1-4]. The adaptor coefficients α_1 and α_2 are shown explicitly next to the ports 1 and 3, respectively. The coefficients are

$$\alpha_j = 2 \cdot G_j / (G_1 + G_2 + G_3), \quad j=1,2, \quad (17)$$

where the port conductances are $G_k = 1 / Z_{ck}$, $k=1,2,3$.

A series adaptor serves to interconnect, in series, n -ports with arbitrary port resistances R_1, R_2, \dots, R_n . In the symbolic representation of a two-port series adaptor [1-4] given in Fig. 8, it is shown explicitly the parameter α next to the port 1.

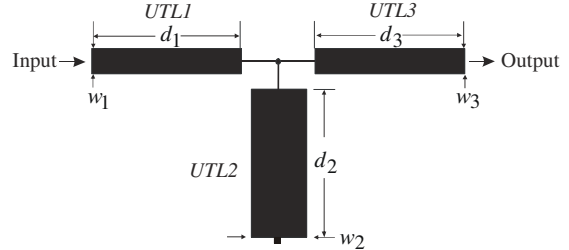


Fig. 5. Segment connection in microstrip structure.

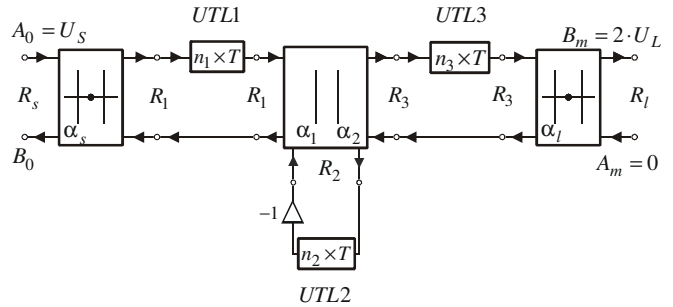


Fig. 6. WDN of the structure given in Fig. 5.

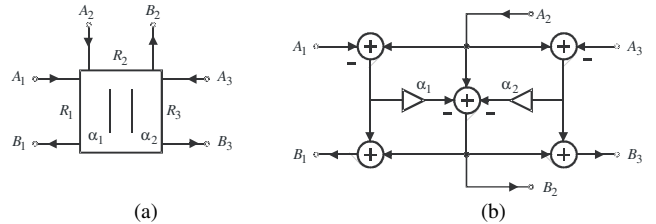


Fig. 7. Three-port parallel adaptor with port 2 being dependent: (a) symbol, and (b) WDE.

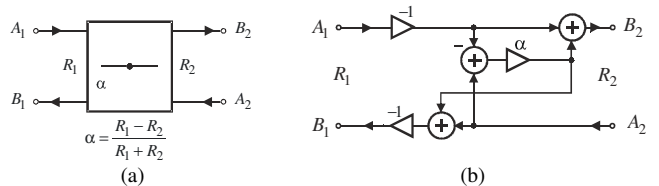


Fig. 8. Two-port series adaptor: (a) symbol, and (b) WDE.

V. WAVE DIGITAL NETWORK AS MODELING TOOL FOR STRUCTURE WITH CROSS-JUNCTION OPENED STUBS

Another case of considerable interest is a circuit containing junction of four transmission lines. Given is a connection of segments in one microstrip structure with cross-junction opened stubs, Fig. 9; it is assumed that this structure consists only of uniform segments assigned from UTL1 to UTL4.

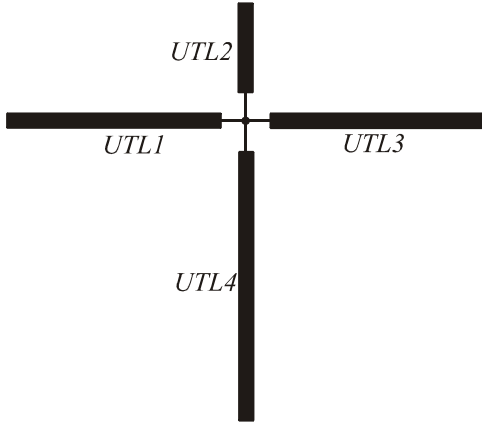


Fig. 9. Microstrip circuit: uniform segment connection.

It is easy to form an equivalent WDN of such structure, Figure 10, by proceeding according to the general method outlined in Section II. This figure illustrates a resultant network, i.e. structure model that consists of $n_t = \sum_{k=1}^4 n_k$ UEs, one four-port parallel adaptor and two two-port series adaptors.

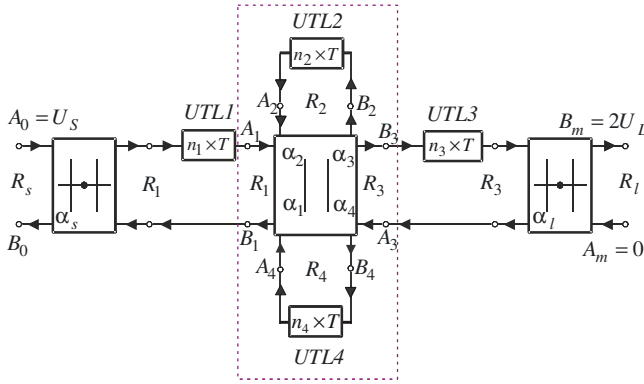


Fig. 10. Wave digital network of a planar microstrip structure with cross-junction opened stubs.

The equation set for four-port parallel adaptor, symbolically given in Fig. 10, is:

$$B_k = (\alpha_1 A_1 + \alpha_2 A_2 + \alpha_3 A_3 + \alpha_4 A_4) - A_k, \quad (18)$$

where the adaptor coefficients

$$\alpha_k = \frac{2G_k}{\sum_{j=1}^n G_j}, \quad k=1,2,3,4, \quad (19)$$

depend on port conductances $G_k = 1/R_k$, with R_k being port resistances, and

$$\sum_{k=1}^4 \alpha_k = 2. \quad (20)$$

According to the last equation, it is possible to eliminate one coefficient in order to reduce number of adders in resultant wave digital network of this adaptor. In this case, the new equations are:

$$B_4 = A_4 - \sum_{k=1}^3 \alpha_k (A_4 - A_k), \quad (21)$$

$$B_k = B_4 + (A_4 - A_k), \quad k=1,2,3. \quad (22)$$

VI. MATLAB/SIMULINK IMPLEMENTATION OF WDNS

In order to generate a method for construction of algorithm that efficiently implements microstrip structures utilizing short-circuited stubs or cross-junction opened stubs, their layouts have to be observed. A correct equivalent wave-based model depends on structure geometry.

MATLAB is an excellent tool for simulating structure, and for creating the valuable “proof of concept”. Block diagram is a representation of physical structure using blocks. Individual blocks can be put together to represent the structure in block diagram form. Individual blocks can be the basic blocks or they can be subsystems. They are considered in the text given below.

The formed Simulink model of WDN in Fig. 6 is depicted in Fig. 11. The blocks **TLine_1**, **Stub_2** and **TLine_3** represent models of uniform segments. For these blocks, the Integer Delay blocks from Simulink/Discrete Library are used. The Integer Delay block delays its input by N sample periods. The block accepts one input and generates one output.

The blocks **ADP-S** and **ADP-L** represent two-port series adaptors, and block **ADP-T1S2T3** three-port adaptor. The two-port adaptors at the ends are used for matching source and load resistances to the rest of the WDN. The adaptor coefficients for the blocks **ADP-S** and **ADP-L** in the WDN are

$$\alpha_s = (R_s - Z_{c1}) / (R_s + Z_{c1}), \quad (23)$$

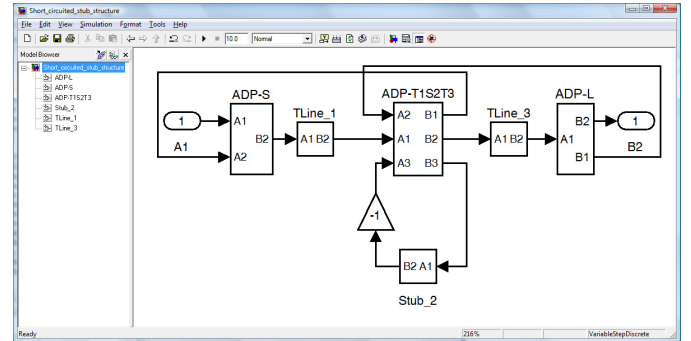
$$\alpha_l = (Z_{c3} - R_l) / (Z_{c3} + R_l).$$


Fig. 11. Simulink model of WDN given in Fig. 6.

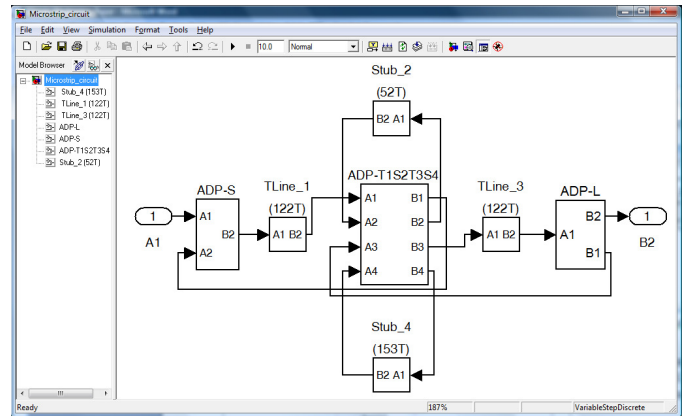


Fig. 12. Simulink model of WDN from Fig. 10.

The formed Simulink model of WDN in Fig. 10 is depicted in Fig. 12. The blocks **TLine_1**, **Stub_2**, **TLine_3** and **Stub_4** represent models of uniform segments. Block **ADP_T1S2T3S4** represent four-port parallel adaptor.

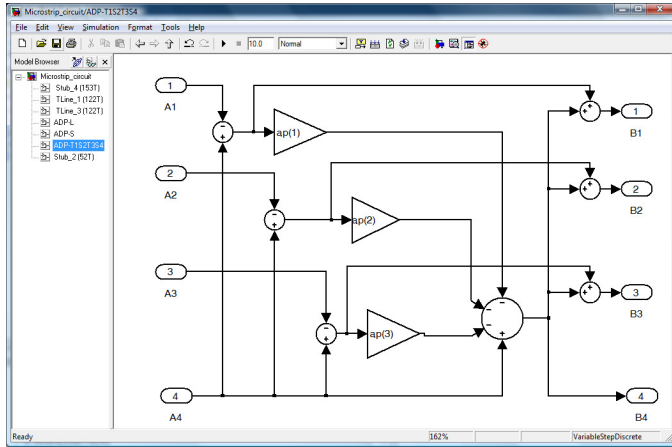


Fig. 13. Simulink model of four-port parallel adaptor with port 4 being dependent.

According to relations (21) –(22), Simulink model of four-port parallel adaptor with port 4 being dependent, is depicted in Fig. 13.

A very simple method of analysis of the WDN is a block-diagram method. Each Simulink model represents a series of MATLAB and Simulink commands and functions which are used for its creation. Response is obtained directly in the time domain, and Fourier transformation is used for frequency response calculation. A major part here is formed Simulink model (mdl-file), whereby the mdl-file is run by m-file that is provided for initialization, response calculation and plotting, Fig. 14.

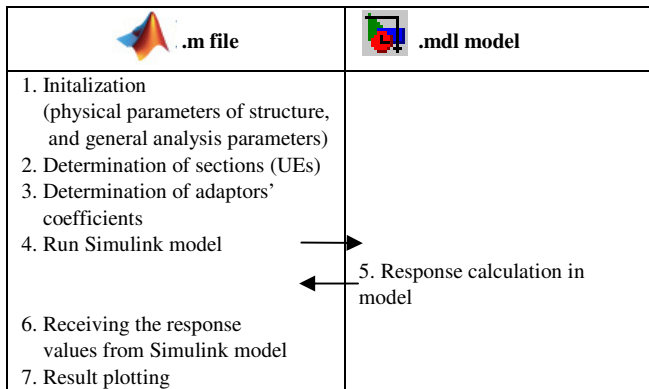


Fig. 14. Algorithm for the implementation of WDN.

MATLAB built-in functions *dlinmod.m*, *dimpulse.m* and *fft.m* are employed to find a response of observed WDN. *Dlinmod.m* function obtains linear model from discrete system described by block-diagram. *Dimpulse.m* function gives impulse response of discrete-time linear systems. Function *fft.m* is the discrete Fourier transform, i.e. it gives response in the frequency domain.

VII. APPROACH VERIFICATION

A. A filter with short-circuited stubs

To demonstrate the main idea and approach, a microstrip ultra-wideband filter with a central frequency of 2.1 GHz [10], [11] is depicted. The filter is based on quarter-wave length short-circuited stubs and connecting transmission lines. The layout is shown in Fig. 15. It is analyzed on FR-4 substrate with dielectric constant $\epsilon_r = 4.6$, and the board thickness $h = 0.6 \text{ mm}$. Metallization is copper and the metal thickness is $t = 17.5 \mu\text{m}$. Simulink model of WDN for filter is depicted in Fig. 16.

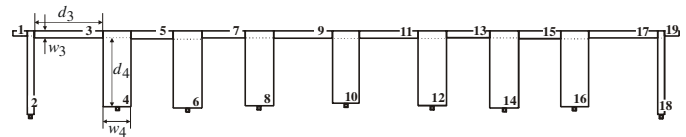


Fig. 15. Layout of ultra wide-band filter with short-circuited stubs.

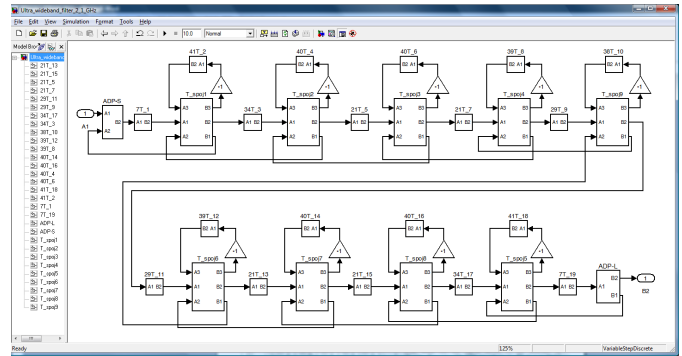


Fig. 16. Simulink model of the filter.

TABLE I
SEGMENT PARAMETERS

n	d [mm]	w [mm]	Zc [Ohm]	T [ps]
1,19	3.1000	1.1000	49.5082	19.2338
2,18	18.0000	1.5000	40.9808	113.1258
3,17	14.8000	1.5000	40.9808	93.0145
4,16	16.3000	6.0000	14.3797	108.8778
5,15	9.0000	1.7000	37.7671	56.8691
6,14	16.6000	6.2000	13.9839	111.0299
7,13	9.3000	1.5000	40.9808	58.4483
8,12	16.1000	6.1000	14.1790	107.6145
9,11	12.6000	1.6000	39.3056	79.4078
10	15.6000	5.7000	15.0181	103.9822

The filter is approximated by connection of 19 uniform segments with parameters given in the Table I. For given error of $n_{er} = 0.01\%$, a total minimal number of sections in WDN is $n_t = 582$. The numbers of sections in individual segments n_k are 7, 41, 34, 40, 21, 40, 21, 39, 29, 38, 29, 39, 21, 40, 21, 40, 34, 41, and 7, respectively. A total delay for the digital model of the structure is $T_t = 1599.1561 \text{ ps}$, a multiple factor

is $q=7$ and a minimum delay is $T_{\min}=19.2338\text{ ps}$. A total real delay of the structure is $T_{\Sigma}=1599.2257\text{ ps}$. A sampling frequency of the digital model of the planar structure for the chosen minimal number of sections is $F_s=363.9420\text{ GHz}$. In this case, a relative error of delay is $er=0.004352\%$. According to relation (17), the three-port adaptor coefficients are: $\alpha_1=\alpha_{18}=0.5855$, $\alpha_2=\alpha_{17}=0.7073$, $\alpha_3=\alpha_{16}=0.4053$, $\alpha_4=\alpha_{15}=0.4398$, $\alpha_5=\alpha_{14}=0.4327$, $\alpha_6=\alpha_{13}=0.3988$, $\alpha_7=\alpha_{12}=0.4054$, $\alpha_8=\alpha_{11}=0.4227$, $\alpha_9=\alpha_{10}=0.4332$. The two-port adaptor coefficients, relation (23), are $\alpha_S=-\alpha_L=0.004942$.

The results obtained by direct analysis of WDN, and by simulations (linear and momentum) in ADS (Advanced Design System) [12], are depicted in Fig. 17. It can be concluded that WDN and ADS curves show a good agreement in whole frequency range.

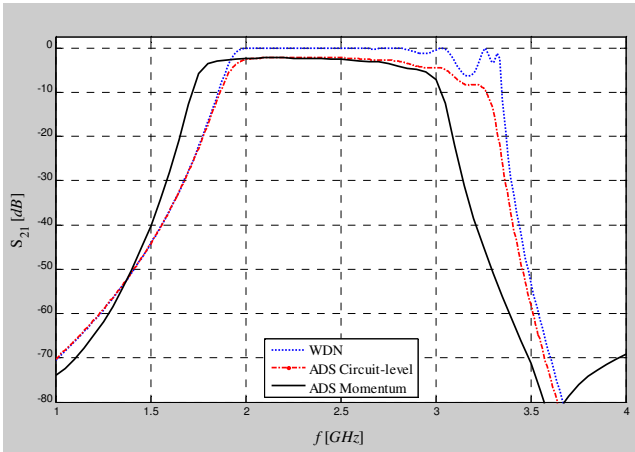


Fig. 17. Frequency response comparison.

B. Structure with cross-junction opened stubs – A simple microstrip circuit

The layout of a structure with cross-junction opened stubs is shown in Fig. 18. It is analyzed on substrate with dielectric constant $\epsilon_r=2.2$, and the board thickness $h=3.175\text{ mm}$. The filter is symmetrical and approximated by connection of 4 uniform segments with parameters given in the Tables II and III. Simulink model of WDN for this structure is depicted in Fig. 12.

For given error of $n_er=0.01\%$, a total minimal number of sections in WDN is $n_t=449$. The numbers of sections in individual segments n_k are 122, 52, 122, and 153, respectively. A total delay for the digital model of the structure is $T_t=2521.9705\text{ ps}$ where a multiple factor is $q=52$ and a minimum delay is $T_{\min}=292.0507\text{ ps}$. A total real delay of the structure is $T_{\Sigma}=2521.7453\text{ ps}$. A sampling frequency of the digital model of the planar structure for the chosen minimal number of sections is $F_s=178.0513\text{ GHz}$. In this case, a

relative error of delay is $er=0.0089\%$. According to the relation (22), the four-port adaptor coefficients are $\alpha_1=\alpha_2=\alpha_3=0.5$. The two-port adaptor coefficients are $\alpha_S=-\alpha_L=-0.002894$.

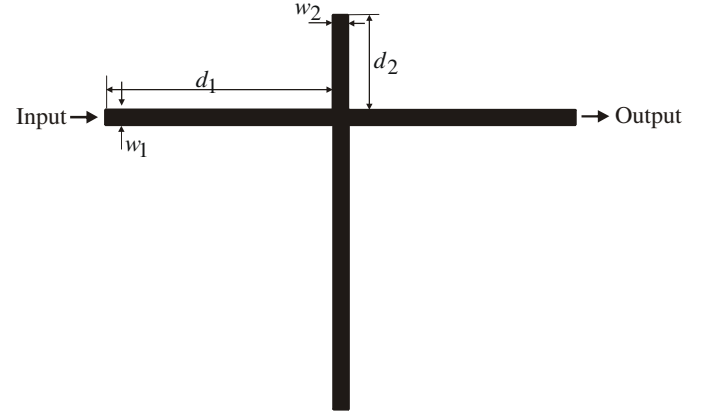


Fig. 18. Layout of a microstrip circuit with cross-junction opened stubs.

TABLE II
PARAMETERS OF UNIFORM SEGMENTS
WITHOUT ANY DISCONTINUITY EFFECTS

nLine	d [mm]	w [mm]	Zc [Ohm]	T [ps]
1	150.0000	9.7800	50.2902	683.9538
2	62.5000	9.7800	50.2902	284.9808
3	150.0000	9.7800	50.2902	683.9538
4	187.5000	9.7800	50.2902	854.9423

TABLE III
PARAMETERS OF UNIFORM SEGMENTS
WITH EFFECTS OF OPENED STUBS

nLine	d [mm]	w [mm]	Zc [Ohm]	T [ps]
1	150.0000	9.7800	50.2902	683.9538
2	64.0505	9.7800	50.2902	292.0507
3	150.0000	9.7800	50.2902	683.9538
4	189.0505	9.7800	50.2902	862.0122

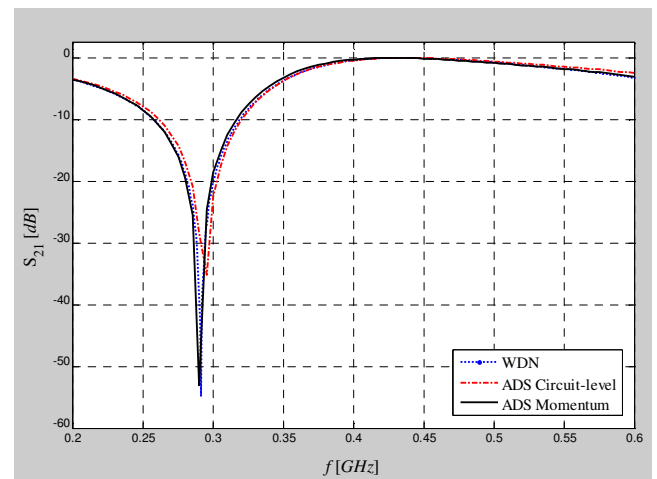


Fig. 19. Microstrip resonator utilizing opened stubs: amplitude-frequency response of S_{21} parameter.

Fig. 19 shows amplitude-frequency responses of S_{21} parameter both simulated in MATLAB by a new proposed approach and obtained in ADS simulator (Advanced Design Software).

C. Structure with cross-junction opened stubs – Low-pass filter of wide stop-band

A novel microstrip structure for low-pass filter of wide stop-band with cross-junction opened stubs, which layout is shown in Fig. 20, is proposed by Liu *et al.* in [13]. The dielectric constant of material is $\epsilon_r = 2.22$ with a thickness $h = 0.254 \text{ mm}$. As a wave digital approach to analysis entails modeling a microstrip structure as a network of interconnected blocks, this filter is approximated by connection of 10 uniform segments. ADS model of the filter is depicted in Fig. 22. Simulink model of WDN for this low-pass filter of wide stop-band is depicted in Fig. 23. Tables IV and V show the lengths and widths of uniform segments in the layout, before and after inclusion of open-end discontinuity effects.

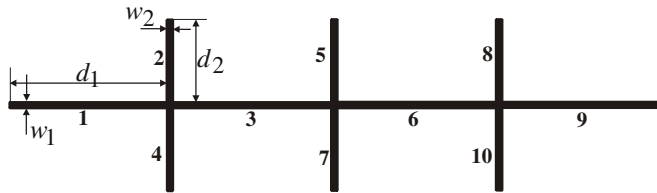


Fig. 20. Layout of filter with cross-junction opened stubs.

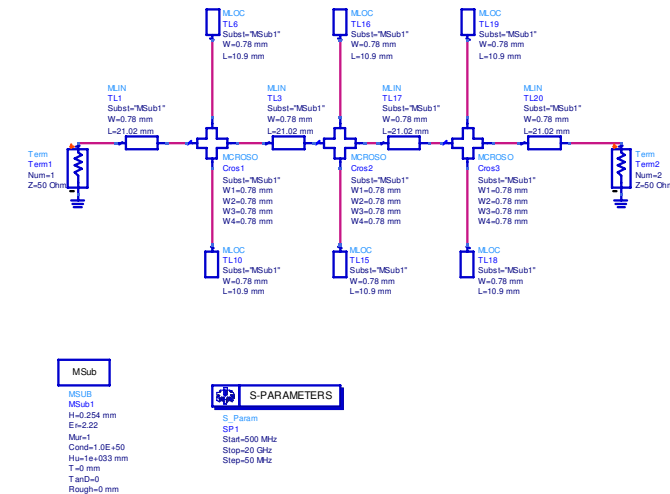


Fig. 21. ADS circuit-based model of the filter with cross-junction opened stubs.

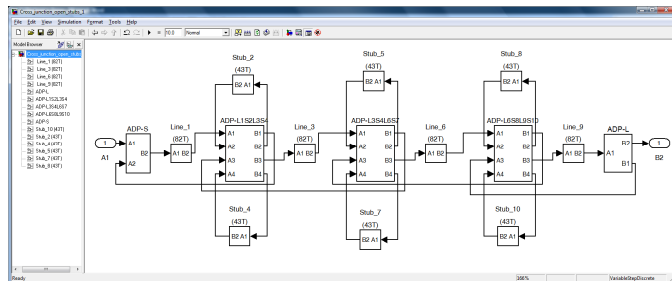


Fig. 22. Simulink model of low-pass filter.

TABLE IV
PARAMETERS OF UNIFORM SEGMENTS
WITHOUT ANY DISCONTINUITY EFFECTS INCLUDED

nLine	d [mm]	w [mm]	Zc [Ohm]	T [ps]
1,3,6,9	21.0200	0.7800	50.2000	96.2073
2,4,5,7,8,10	10.9000	0.7800	50.2000	49.8886

TABLE V
PARAMETERS OF UNIFORM SEGMENTS
WITH INCLUDED EFFECTS OF OPENED STUBS

nLine	d [mm]	w [mm]	Zc [Ohm]	T [ps]
1,3,6,9	21.0200	0.7800	50.2000	96.2073
2,4,5,7,8,10	11.0237	0.7800	50.2000	50.4549

For given error of $n_{er} = 0.01\%$, a total minimal number of sections in WDN is $n_t = 586$. The numbers of sections in individual segments n_k are 82, 43, 82, 43, 43, 82, 43, 43, 82, and 43, respectively. A total delay for the digital model of the structure is $T_t = 687.5584 \text{ ps}$ where a multiple factor is $q = 43$ and a minimum delay is $T_{\min} = 50.4549 \text{ ps}$. A total real delay of the structure is $T_{\Sigma} = 687.5944 \text{ ps}$. A sampling frequency of the digital model of the planar structure for the chosen minimal number of sections is $F_s = 852.2466 \text{ GHz}$. In this case, a relative error of delay is $er = -0.0052\%$. According to the relation (22), the four-port adaptor coefficients are $\alpha_k = 0.5$, $k = 1, 2, \dots, 9$. The two-port adaptor coefficients are $\alpha_S = -\alpha_L = -0.001996$.

Amplitude-frequency responses of S_{21} parameter, both simulated in MATLAB by a new proposed approach and obtained in ADS simulator (Advanced Design Software), are shown in Figs. 23 and 24.

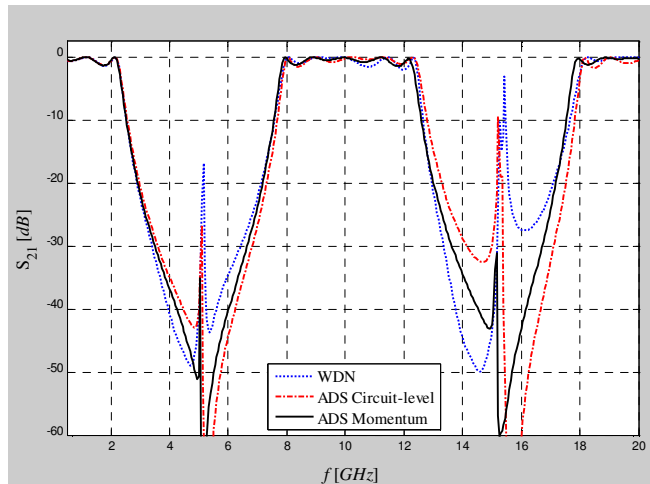


Fig. 23. Microstrip filter with cross-junction opened stubs: amplitude-frequency response of S_{21} parameter.

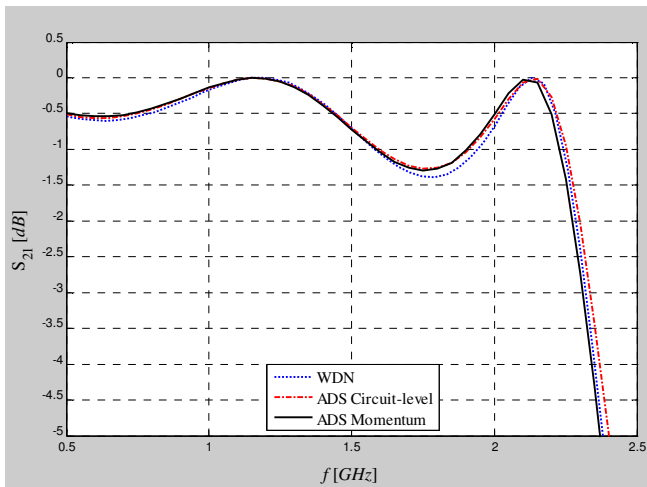


Fig. 24. Microstrip filter with cross-junction opened stubs: amplitude-frequency response of S_{21} parameter in passband.

D. Result Discussion

The S_{21} parameter responses, shown in Figs. 17, 19, 23 and 24, are counted by analyzing WDNs in MATLAB as well as by using known software package ADS (Advanced Design System). The obtained results are similar in general. In all figures, the WDN results show a small differences in comparison with the results of Momentum (electromagnetic 2.5D MoM) simulation done in ADS. These differences can be from not exact modeling of discontinuities, as well as not including conductor and dielectric losses.

According to these findings, a simple wave-based models and their implementation in MATLAB/Simulink, can produce results that are similar to the much more sophisticated methods.

VIII. CONCLUSION

Recently, much work has concentrated on the development of wave digital approach for modeling and analysis of different physical systems. A detailed review of application of WDF structures for electromagnetic field simulation is given in [14] and [15]. After an extensive search in the literature it was found an application of ADS [12] to simulations of different microstrip structures based on their wave digital network representations [16]. In [17], a framework for the automated generation of the wave digital structures is presented, and the reference circuit is assumed to comprise arbitrary connection types.

In this paper, a framework for the generation of equivalent wave digital networks for planar microstrip structures has been presented. The concept of a generalized method which was established earlier for stepped-impedance structures and structures with opened stubs, is extended to another interesting problems with junction of several transmission lines.

This wave-based digital approach into MATLAB/Simulink enables an efficient and easy simulation of microstrip structures of different geometries. Also, allows the user to get

the responses in both the frequency and time domains in short time intervals.

The broadband accuracy of the suggested procedures has been demonstrated in analyses of filters realized in the microstrip line technique.

REFERENCES

- [1] A. Fettweis, "Digital Circuits and Systems", *IEEE Transactions on Circuits and Systems*, vol. CAS-31, no. 1, January, 1984, pp. 31-48.
- [2] A. Fettweis, "Wave Digital Filters: Theory and Practice", *Proc. IEEE*, vol. 74, 1986, pp. 270-327.
- [3] W. K. Chen, *The Circuits and Filters Handbook*, CRC Press, 1995 (Wave Digital Filters, pp. 2634-2661).
- [4] M. V. Gmitrović, *Microwave and Wave Digital Filters*, Faculty of Electronic Engineering, Niš, 2007.
- [5] B. P. Stošić, *Analysis of Planar Microwave Structures Modeled by Wave Digital Elements*, Doctoral thesis, Faculty of Electronic Engineering, University of Niš, September 2008.
- [6] B. P. Stošić and M. V. Gmitrović, "Implementation of Wave Digital Model in Analysis of Arbitrary Nonuniform Transmission Lines", *Microwave and Optical Technology Letters*, vol. 49, no. 9, September 2007, pp. 2150-2153.
- [7] B. P. Stošić and M. V. Gmitrović, "Wave Digital Approach - Different Procedures for Modeling of Microstrip Step Discontinuities", *International Journal of Circuits, Systems and Signal Processing*, vol. 2, no. 3, 2008, pp. 209-218.
- [8] B. P. Stošić and M. V. Gmitrović, "Block-based Analysis of Microstrip Structures with Stubs by use of 1D Wave Digital Approach", *XLIV Intern. Scientific Conf. on Information, Communication and Energy Systems and Technologies - Icest 2009*, Bulgaria, Veliko Tarnovo, June 25-27, 2009, pp. 23-26.
- [9] B. P. Stošić, "Block-based Wave Digital Network of an Elliptic Filter in MATLAB/Simulink", *XLV Intern. Scientific Conf. on Information, Communication and Energy Systems and Technologies - Icest 2010*, Macedonia, Ohrid, June 23-26, 2010, vol. 1, pp.127-130.
- [10] B. P. Stošić, and J. J. Joković, "Generation of Wave-based Model of Microstrip Ultra-wideband Filter utilizing Short-circuited Stubs and its MATLAB/Simulink Implementation", *Proc. 55th ETRAN Conference*, Republic of Srpska, Banja Vrućica (Teslić), June 6-9, 2011, MT1.1-1-4.
- [11] N. Timko, M. Kovač and M. Potrebić, "Miniaturization of Microwave Ultra-wideband Filter utilizing Short-circuited Stubs", *Proc. 54th ETRAN Conference*, Serbia, Donji Milanovac, June 7-11, 2010, pp. MT1.5-1-4.
- [12] Advanced Design Software 2002, Agilent Technologies 1983-2002, 395 Page Mill Road, Palo Alto, CA 94304, USA.
- [13] H. Liu, Z. Li, X. Sun and J. Mao, "A Novel Photonic Band-gap Microstrip Structures for Low-pass Filters of Wide Stop-band", *Microwave and Optical Technology Letters*, vol. 37, no. 6, June 20, 2003, pp. 470-472.
- [14] J. A. Russer, Y. Kuznetsov, and P. Russer, "Discrete-time Network and State Equation Methods Applied to Computational Electromagnetics", *Microwave Review*, July 2010, vol. 16, no. 1, pp. 2-14.
- [15] S. Bilbao, *Wave and Scattering Methods for Numerical Simulation*, Hoboken, New Jersey: Wiley, 2004.
- [16] F. Maggioni, "Time Domain Electrical Simulation using Equivalent Digital Wave Networks in ADS", *ADS User Group Meeting*, Rome, May 13, 2009.
- [17] D. Franken, J. Ochs and K. Ochs, "Generation of Wave Digital Structures for Networks Containing Multiport Elements", *IEEE Transaction on Circuits and Systems I: Regular Papers*, March 2005, vol. 52, no. 3, pp. 586-596.

Population Exposure to Depleted Uranium in the Han Pijesak Region

Zora S. Žunić, Rodoljub Simović, Zoran Ćurguz, Olivera Ćuknić, Jerzy Mietelski, Predrag Ujić, Igor Ćeliković, Predrag Kolarž, and Branko Predojević

Abstract—In September 1995 the Han Pijesak area of Republic of Srpska was heavily attacked by Depleted Uranium (DU) ammunition. In this area, from 2003 to 2004, during one year, the components of natural ionizing radiation sources like radon, thoron, and gamma radiation were measured. In addition, during the same period, the samples of soil, moss, and lichen were collected in order to identify the content of technologically enhanced natural radionuclides in them and particularly their isotopic ratios, which determine radioactive contamination by depleted uranium. The paper presents techniques, methods, and results of the research carried out in Han Pijesak area on identification and quantification of depleted uranium being found in the environmental samples over the Han Pijesak region.

Index Terms—Ammunition, contamination, depleted uranium, Han Pijesak, radionuclides, radon, thoron.

I. INTRODUCTION

ENDOGENOUS and environmental pollutants (ionizing radiation, stable chemical elements, oxides of nitrogen, ozone, organic solvents, pesticides etc.) cause oxidative stress. The oxidative stress is the cause of many diseases and aging. The pollutants initiate the formation of free radicals, which even in small quantities endanger the health because of their high reactivity and possible damage of DNA, RNA, enzymes, and membrane lipid components. Ionizing radiation of various

origin and properties is a fundamental characteristic of the environment. Man-made radioactivity occurs as a result of operation of nuclear power plants, or use of nuclear energy for military purposes, and lately from the use of ammunition and missiles with DU and transuranic elements. The wars in Iraq 1991 and 2003, in Kuwait, Bosnia and Herzegovina (bombing of Hažici, Lukavica, and Han Pijesak) 1995, Serbia (Kosovo and Metohija and south Serbia) 1999, and Afghanistan 2002, represent a series of dramatic events which have started the extensive investigation of the influence DU on environment and human health [1, 2].

Han Pijesak is a region of Republic of Srpska with population of about 5.500 inhabitants where in 1995 twelve military and civilian buildings were bombed with DU projectiles [3]. In total, more than 10.800 bullets were fired at different locations throughout Republic of Srpska (mainly in the area of Sarajevo), which corresponds to about 3.3 tonnes of scattered DU. Of these, Han Pijesak received 2.400 bullets which corresponds to about 730 kg of DU. The soil in this area is mainly limestone. In 2003, a one year research was carried out to study the ionizing radiation background level in the area, measuring radon, thoron activity concentration, and gamma radiation. The research was conducted by members of Electrochemical laboratory for developing nuclear track detectors (ECE Lab), Institute for nuclear sciences „Vinča“ [4]. Research included soil, moss, and lichen sampling. The analysis of the samples from Han Pijesak was conducted by two methods, gamma and alpha spectrometry, which had been developed in the ECE Lab in collaboration with the Institute of Nuclear Physics, PAN, Krakow, Poland [5,6]. The goal was to determine the content of natural and man-made radionuclides in the environment and to determine the level of DU contamination on the basis of their isotopic relations.

II. METHOD AND EXPERIMENTAL WORK

In order to identify the presence of DU in the samples in concentrations below 1 pg/g of material, or in a small sample a few grams, we used a very accurate radiochemical sample preparation and very sensitive analytical techniques. The research presented in this paper employed two methods the alpha and the gamma spectrometry. The samples analyzed are different types of moss, lichen and soil collected in April and November of 2000, eight years after the bombing of Han

This work has been partially supported by the Ministry of Education and Science, Republic of Serbia, under project 41028. Some results of this paper were presented at 55th ETRAN Conference, Banja Vrućica, June 6-9, 2011.

Z. S. Žunić is with ECE Lab, Institute of Nuclear Sciences „Vinča“, University of Belgrade, Serbia (e-mail: zzunic@verat.net).

R. Simović is with JP Nuclear Objects of Serbia (e-mail: simovicr@vinca.rs).

Z. Ćurguz is with the Faculty of Transport Dobož, University in East Sarajevo, Republic of Srpska (e-mail: zoranc@teol.net).

O. Ćuknić is with the JP Nuclear Objects of Serbia (e-mail: olivera.cuknic@nuklearnobjekti.rs).

J. Mietelski is with the Institute of Nuclear Physics, Krakow, Poland (e-mail: jerzy.mietelski@ifj.edu.pl).

P. Ujić is with the Institute of Nuclear Sciences „Vinča“, University of Belgrade, Serbia (e-mail: ujjic@vinca.rs).

I. Ćeliković is with the Institute of Nuclear Sciences „Vinča“, University of Belgrade, Serbia (e-mail: icelikovic@vinca.rs).

P. Kolarž is with the Institute of Physics, University of Belgrade (e-mail: kolarz@ipb.ac.rs).

B. Predojević is with the Faculty of Science, University of Banja Luka, Republic of Srpska (e-mail: bpredojevic@teol.net).

Pijesak with DU ammunition. From total number of collected samples following 25 were analyzed (Table I): 8 samples of soil, 6 samples of the lichen and moss, a sample of tree resin, and 4 mixed samples (bark with lichen, moss and soil and two samples of moss and lichen). Gamma and alpha spectrometry measurements were done at the Institute PAN in Krakow. For gamma spectrometric measurements all the samples of moss, lichen and soil were dried over night or longer at 105 °C, homogenized, and inserted into the Marinelli vessels, on top of HPGe detectors protected with layers made of 10 cm Pb, 2 mm Cd and 18 mm Cu, associated with Silen gamma spectrometer (4096 channel). Spectrometer was calibrated at 662 keV (^{137}Cs), 911 keV (^{228}Ac) and 1461 keV (^{40}K) [7]. Efficiency calibration at 1001 keV ($^{234\text{m}}\text{Pa}$, which we assume to be in equilibrium with ^{238}U) was achieved by interpolation of the efficiency for the above enumerate radionuclides. The systematic error was well below of 10%.

Despite the complicated and long radiochemical sample preparation, alpha spectrometry technique is necessary for reliable measurements of DU activity concentration because this method reaches significantly lower limit of detection and directly determines the isotopic activity ratio $^{234}\text{U}/^{238}\text{U}$.

Radiochemical preparation of samples for alpha spectrometry measurements [5] requires burning to ash at 600 °C to remove the organic compounds. One gram of ash was placed in PTFE vessels in which acid mixture (9 ml of concentrated HNO_3 , 3 ml of concentrated HCl , 3 ml concentrated HF) was added, independently into each vessel. Samples were then mineralized by heating to 200 °C in microwave digester. After mineralization, each vessel was rinsed with 12 ml of 7M HNO_3 . In the next step all the solutions used for individual samples were joined in 250 ml PTFE vessels and vaporized. Evaporation was repeated after adding of 30 ml concentrate HNO_3 . This was followed by adding of 50 ml of concentrate HCl and heating, as well as 2 g H_3BO_3 in order to remove traces of fluoride [6].

As mentioned previously, for reliable identification of the presence of DU contamination we used alpha spectrometric analysis which was particularly useful for samples of low mass and very low intensity gamma lines (0.38%).

In these cases only the upper limit of uranium activities was established. For alpha spectrometry, it is necessary to make appropriate radiochemical separation and to measure ^{238}U , ^{235}U and ^{234}U activities as well as activity ratios $^{235}\text{U}/^{238}\text{U}$, and

TABLE I
RESULTS OF GAMMA SPECTROMETRY MEASUREMENTS OF ENVIRONMENTAL SAMPLES COLLECTED IN HAN PIJESAK

Number and sample code	Sample weight [g]	Sample type and description of sampling	Activity concentration ^{137}Cs [Bq/kg]	Activity concentration ^{228}Ac [Bq/kg]	Activity concentration ^{40}K [Bq/kg]	Activity concentration ^{238}U [Bq/kg]
1/HP 1	193.5	Soil, house 1	47.9 ± 1.3	43.4 ± 1.8	328 ± 14	< 26
2/ HP 3	1.8	Lichen, house 2	68 ± 10	< 24	61 ± 100	< 1216
3/ HP 4	3.4	Lichen, house 2	88 ± 10	< 24	255 ± 94	< 1917
4/ HP 5	34.3	Bark with lichen, house 2	5.4 ± 1.2	2.6 ± 3.5	37 ± 20	< 99
5/ HP 5a	23	Tree resin, house 2	8.9 ± 0.8	2.4 ± 1.9	< 7.2	158 ± 87
6/ HP 6	9.7	Moss, house 2	76 ± 6	27 ± 13	200 ± 70	1190 ± 570
7/ HP 7	5.9	Moss, barracks	< 5	< 14	560 ± 160	< 926
8/ HP 8	14.4	Lichen, barracks	30.9 ± 2.7	29 ± 7	370 ± 390	< 476
9/ HP 8a	109.9	Moss and land, barracks	143 ± 4	29 ± 34	332 ± 20	< 116
10/HP 9	67.2	Moss, barrack, barracks	41 ± 1.6	16 ± 3	174 ± 17	1150 ± 130
11/ HP 10	110.7	Moss, barrack, barracks	38.8 ± 1.2	12.3 ± 1.3	151 ± 9	< 47
12/ HP 11	141.2	Soil, concrete, bullet hole, barrack	17.3 ± 1	9.9 ± 1.9	165 ± 13	5540 ± 170
13/ HP 16	45.6	Moss with lichen, barrack	209 ± 3	13 ± 3	87 ± 15	210 ± 80
14 / HP 17	70.2	Soil, barrack, barracks inside	38.7 ± 1.5	2.0 ± 1.7	46 ± 9	< 154
15/ HP 18	32.9	Soil, barrack, barracks inside	675 ± 8	11.2 ± 3.5	140 ± 20	2550 ± 210
16/ HP 20	3.3	Lichen with moss, house 3	27 ± 5	12 ± 15	236 ± 61	< 1301
17/ HP 21	14.6	Lichen, house 3	26 ± 3	< 6	81 ± 26	< 777
18/HP 22	14.4	Moss, house 3	128 ± 5	18 ± 10	347 ± 49	< 204
19/HP 23	106.5	Arable soil, garden house 3	98 ± 2	46 ± 3	446 ± 19	< 88
20/HP 24	81.1	Arable soil, garden house 4	113 ± 2	30 ± 3	495 ± 20	< 51
21/HP 26	18	Lichen, barrack, forest	152 ± 4		137 ± 20	< 215
22/HP 27	81.5	Moss, house 5	499 ± 14	33 ± 3	294 ± 19	< 137
23/HP 29	215.7	Soil, house 5	6.0 ± 0.6	45 ± 3	548 ± 27	133 ± 51
24/HP 30	13	Lichen, garden house 4	19 ± 3	11 ± 6	245 ± 38	< 660
25/HP 31	109.2	Arable soil, house 6	75 ± 2	61 ± 3	102 ± 9	< 65

$^{234}\text{U}/^{238}\text{U}$. If the ratio of isotope activities $^{234}\text{U}/^{238}\text{U}$ is below of 0.3, it clearly indicates the presence of DU in the sample.

III. RESULTS

From a total of 25 samples analyzed, in five samples coming from the military barracks in Han Pijesak, (HP 9 – moss, HP 10 – moss, HP 11 – land, HP 16 – moss and lichens and HP 18 – land) the presence of DU was found. In papers [8-10] the lower value of isotope activity ratios was approximately 0.20, while in this paper, the lowest value was 0.117 ± 0.001 , determined in soil from the hole from the bullet that pierced a concrete barrack. To determine the homogeneity of the uranium distribution in the samples, we performed additional radiochemical separation and alpha spectrometry measurements of samples with high weight (HP 8, HP 10, HP 11 and HP 18), which resulted in 19 additional sub-samples, which were further analyzed.

It was found that only the sample HP 8 contained natural

uranium while all others showed the presence of DU (Table I). Since the ratio between the highest and lowest measured ^{238}U activity was less than 2 (HP 11 and HP 18) and significantly lower for the HP 10, as was also observed in HP 8, which contained natural uranium, it was concluded that the distribution of uranium in the samples was uniform. The highest mean ^{238}U activity measured in the samples from Han Pijesak was 5630 ± 890 Bq/kg (sample 12/HP 11, Table II). Sansone et al. [11] reported the results of approximately 230.000 Bq/kg, which is two orders of magnitude greater value. Similar results on the presence of DU in samples of lichen and moss have been published in other publications [11-14]. This finding supports the knowledge of lichens and mosses as excellent indicators of DU contamination of the air.

IV. CONCLUSION

From the total of 25 analyzed samples (moss, lichen, soil, agricultural soil, and mixed samples) the presence of DU was

TABLE II
THE ^{238}U , ^{235}U AND ^{234}U ACTIVITY CONCENTRATION AND ACTIVITY RATIO $^{235}\text{U}/^{238}\text{U}$ GAINED BY ALPHA SPECTROMETRIC MEASUREMENTS

Number and sample code	Activity ^{238}U (Bq·kg ⁻¹)	Activity ^{235}U (Bq·kg ⁻¹)	Activity ^{234}U (Bq·kg ⁻¹)	Activity ratio ($^{235}\text{U}/^{238}\text{U}$)	Activity ratio ($^{234}\text{U}/^{238}\text{U}$)
1/HP 1	23.8 ± 3.1	< 0.33	26.8 ± 3.6	< 0.014	1.12 ± 0.11
2/HP 3	4.4 ± 0.5	0.86 ± 0.16	5.1 ± 0.6	0.20 ± 0.03	1.17 ± 0.10
3/HP 4	1.6 ± 0.3	0.29 ± 0.22	1.5 ± 0.3	0.19 ± 0.14	0.93 ± 0.22
4/HP 5	-	-	-	-	-
5/HP 5a	-	-	-	-	-
6/HP 6	2.4 ± 0.3	< 0.31	2.8 ± 0.3	< 0.13	1.14 ± 0.12
7/HP 7	5.8 ± 0.8	0.61 ± 0.40	5.4 ± 0.8	0.11 ± 0.07	0.92 ± 0.12
8/HP 8	27.0 ± 5.1	1.16 ± 0.84	26.9 ± 3.1	0.05 ± 0.04	1.01 ± 0.13
9/HP 8a	43.9 ± 6.6	2.2 ± 2.1	41.9 ± 6.4	0.05 ± 0.05	0.95 ± 0.09
10/HP 9	590 ± 72	7.9 ± 1.7	83 ± 10	0.013 ± 0.002	0.140 ± 0.004
11/HP 10	234 ± 33	3.7 ± 1.5	50.9 ± 9.0	0.013 ± 0.005	0.22 ± 0.03
12/HP 11	5600 ± 900	66 ± 22	660 ± 110	0.013 ± 0.002	0.117 ± 0.001
13/HP 16	99 ± 11	1.47 ± 0.91	25.6 ± 3.0	0.015 ± 0.009	0.26 ± 0.01
14/HP 17	1.6 ± 0.2	0.07 ± 0.04	1.4 ± 0.2	0.05 ± 0.03	0.89 ± 0.05
15/HP 18	1500 ± 360	21.7 ± 7.9	189 ± 39	0.016 ± 0.004	0.13 ± 0.01
16/HP 20	1.0 ± 0.3	0.51 ± 0.34	1.8 ± 0.4	0.53 ± 0.38	1.91 ± 0.67
17/HP 21	0.5 ± 0.1	< 0.10	0.4 ± 0.1	< 0.20	0.78 ± 0.20
18/HP 22	4.6 ± 0.7	0.57 ± 0.33	5.1 ± 0.7	0.13 ± 0.07	1.13 ± 0.14
19/HP 23	20.3 ± 3.8	< 2.50	34.6 ± 5.5	< 0.12	1.70 ± 0.26
20/HP 24	35.7 ± 4.2	1.35 ± 1.16	37.1 ± 4.3	0.04 ± 0.03	1.04 ± 0.06
21/HP 26	2.8 ± 0.4	< 0.28	2.8 ± 0.4	< 0.10	0.98 ± 0.12
22/HP 27	18.3 ± 2.7	< 0.59	15.2 ± 2.3	< 0.03	0.83 ± 0.09
23/HP 29	31.2 ± 4.0	< 0.92	30.5 ± 3.9	< 0.03	0.98 ± 0.09
24/HP 30	4.9 ± 0.7	< 0.27	4.9 ± 0.7	< 0.14	1.00 ± 0.14
25/HP 31	44.5 ± 7.0	< 1.53	58.3 ± 8.9	< 0.03	1.31 ± 0.13

Note: The results highlighted in bold print indicate the presence of DU in samples. Samples 4/HP 5 and 5/HP 5a had very low masses, and it was not possible to prepare samples for alpha spectrometric measurements so the results were omitted.

identified in 5 samples collected near military barracks: HP 9, HP 10, HP 11, HP 16 and HP 18. In the samples of lichen and mosses collected in independent yards in Han Pijesak villages near the barracks (in houses 1, 3, 4, 5 and 6), no traces DU was found and this fact indicates that radioactive aerosols produced by the bombing did not contaminate the area.

Based on the results of this study and other work [11-14], the conclusion that biological samples of lichen and moss are good accumulators of radioactivity and therefore good bio-monitors of the presence of DU in the environment, is confirmed.

The detection of DU in samples from the environment by alpha spectrometric method is, compared to gamma spectrometric method, proved to be more accurate and reliable, as well as necessary because it provides significantly lower detection threshold and directly determines the activity ratio $^{234}\text{U}/^{238}\text{U}$.

REFERENCES

- [1] W. Burkart, P.R. Danesi, J.K. Hendry, " Properties, use and health effects of depleted uranium, Internat.l Congress Series 1276, pp.133-136, 2005.
- [2] D. Cullen and D.Weir, " International Coalition to Ban Uranium Weapons: A Question of Responsibility: depleted uranium weapons in the Balkans, Report, eds: ICBUW, Bridge5Mill, 22a Beswickstreet, Ancoats, Manchester, M4 7HR, UK, pp.1-23, 2010.
- [3] Depleted Uranium in Bosnia and Herzegovina, Post-Conflict Environmental Assessment, United Nations Development Programme (UNEP) Report, Geneva, Switzerland, pp. 69-79, 2003.
- [4] Z.S. Žunić, I. Čeliković, S. Tokonami, T. Ishikawa, P. Ujić, A. Onischenko, M. Zhukovsky, G. Milić, B. Jakupi, O. Čuknić, N. Veselinović, K. Fujimoto, S.K. Sahoo and I. Yarmosjhenko, "Collaborative Investigations on Thoron and radon In Some Rural Communities of Balkans, Radiation Protection Dissymetry, Vol.141, No4, pp.346-350, 2010.
- [5] Z.S. Žunić, J.W. Mietelski, S. Blazej, P. Gaca, E. Tomankiewicz, P. Ujić, I. Čeliković, O. Čuknić, M. Demajo, "Traces of DU in samples of environmental bio-monitors (non-flowering plants, fungi) and soil from target sites of the Western Balkan, Journal of Environmental Radioactivity 99, pp.1324-1328, 2008.
- [6] J.J. La Rosa, E.L. Cooper, A. Ghods-Esphahani, V. Jansta, M. Makarewicz, S. Shawky, N. Vajda, "Radiochemical method used by the IAEA's laboratories at Seibesdorf for the determination of 90 Sr, 144 Ce, and Pu radionuclides in environmental samples collected for the international Chernobyl Project, Journal of Environmental radioactivity 99: pp. 183 -209, 1992.
- [7] J.W. Mietelski, M. Jasinska, K. Kozak, E. Ochab, "The method of measurements used in the investigation of radioactive contamination of forests in Poland", Applied Radiation and Isotopes 47, pp. 1089 -1095, 1996.
- [8] M. Zarić, S. Petković, Z. Deviz, "The use of depleted uranium ammunition during NATO aggression against the Federal Republic of Yugoslavia, Archive of oncology 9, pp. 215-217, 2001.
- [9] J.W. Mietelski, M.P.R. Waligorski, Z.S. Žunić, "On problems related to the deployment of depleted uranium weapons in the Balkans, Archive Of Oncology 9, pp. 219-223, 2001.
- [10] P. Gaca, Z.S. Žunić, J.W. Mietelski, E. Tomankiewicz, M.P.R. Waligorski, "Experimental results on the environmental samples collected around sites in south Serbia, Kosovo and Montenegro where DU weapons were deployed in 1999", Radioactivity in the Environment (A companion series to the Journal of Environmental Radioactivity), eds: Mc Laughlin, J.P., Simopoulos S.E., Volume 7 ISSN 1569-4860/DOI 10.1016/ S 1569-4860(04)07090-1, pp. 1056 – 1063, 2005.
- [11] U. Sansone, P.R. Danesi, S. Barbizzi, M. Belli, M. Campbell, S. Gaudino, G. Jia, R. Ocone, A. Pati, S. Rosamilia, "Radioecological survey at selected sites hit by depleted uranium ammunitions during the 1999 Kosovo conflict", The Science of the Total Environment 281, pp. 23-35, 2001.
- [12] S. Loppi, F. Riccobono, Z.H. Zhang, S. Savić, D. Ivanov, S.A. Pirintsos, "Lichen as biomonitors of uranium in the Balkan area", Environmental Pollution 125, pp. 277 -280, 2003.
- [13] G. Jia, M. Belli, U. Sansone, S. Rosamilia, S. Gaudino, "Concentration and characteristics of depleted uranium in water, air and biological samples collected in Serbia, Montenegro" Applied Radiation and Isotopes 63, pp. 38 -399, 2005.
- [14] G. Jia, M. Belli, U. Sansone, S. Rosamilia, S. Gaudino, "Concentration and characteristics of depleted uranium in biological and water samples collected in Bosnia and Herzegovina, Journal of Environmental radioactivity 99, pp.183 -209, 2006.

WindSim® Computational Flow Dynamics Model Testing Using Databases from Two Wind Measurement Stations

Đorđe Klisić, Miodrag Zlatanović, and Ilija Radovanović

Abstract—Data gathered for the last several years from the two wind stations, located at the Šušara fields, was used to create local wind climate and meteorological parameter database. Extrapolation of the values contained in the database to an area of several square kilometers in the vicinity of the measurement stations, and to a height corresponding to technical properties of wind turbines, serves as a tool for planning future wind farms. While predicting wind resources, some uncertainties can occur which are usually related to measured data quality and reliability of extrapolation procedure. In case of hilly terrains with complex spatial configuration, reliability of the wind resources prediction is directly dependent to applied model of air mass movement dynamics. Focus of this paper was testing of the Computational Flow Dynamics (CFD) model implemented in the WindSim® software package. Testing was performed by comparing values of the measured and simulated mean wind speed at 30m. By varying and correcting the boundary conditions it was shown that applied model was able to predict mean wind speed value of one station while using the mean wind speed value of the second wind station as input information in the simulation, with an error comparable to measurement uncertainty. Simulation of air mass movement gave an insight to a wind speed fields at 30m for a spring – summer period. These results are important for the future wind exploitation in Serbia, and can provide better analysis of the climate conditions at the agricultural and vineyard area of Šušara fields.

Index Terms—CFD model testing, wind fields over rough terrains, wind resource prediction, WindSim® simulation.

This paper was financed by the Ministry of Education and Science, Government of the Republic of Serbia, as a part of the project TR 32043 – Development and modeling of low power energy efficient, adaptable, multiprocessing and multisensory electronic systems. Part of the results in this paper was presented at 55th conference ETRAN, Banja Vrućica, June 6th-9th, 2011.

Đ. Klisić is with the Electro-technical Faculty, University of Belgrade, 73 King's Alexander blvd, 11128 Belgrade, Serbia. (Phone: +38164/151-99-29; e-mail: klisic_djordje@etf.rs)

M. Zlatanović is with the Electro-technical Faculty, University of Belgrade, 73 King's Alexander blvd, 11128 Belgrade, Serbia. (E-mail: ezlatano@etf.rs).

I. Radovanović is with the Electro-technical Faculty, University of Belgrade, 73 King's Alexander blvd, 11128 Belgrade, Serbia. (E-mail: ilijaradovanovic@hotmail.com).

I. INTRODUCTION

EXTENSIVE exploitation of fossil fuels during the last century and the increasing emission of green house gasses led to significant upgrowth of the global mean temperature. In comparison, today global mean temperature is at least 1 °C higher than it was at the beginning of the last century, and according to some models, we will have to prepare for a very grim future. These models estimate, that if the humanity keeps this level of industrial growth and green house gasses emission, we can expect the increase of the mean global temperature to be as high as 6.4 °C at the end of the 21th century [1]. The consequences of such a radical global warming effect will be devastating, and it is doubtful if the planet could overcome this degree of human negligence. Renewable energy resources, such as wind power, hydropower, tidal forces, geothermal energy, are offering solution for this eminent threat to our planet. Many countries all over the world are embracing and developing technologies related to renewable energy sources, with wind power at the first place. It's estimated that today energy production from wind power participate in the global energy production with 2.5%, [2] and that some countries such as Denmark, Portugal and Spain have about 15% - 20% of stationary electricity production from wind [2].

Serbia, on its path to become EU member, is planning to incorporate in its energy production renewable energy resources, predominantly by introducing wind power and expanding hydropower capacities. At this moment, Serbia's energy production from renewable energy resources is around 6%, mainly due to hydropower plants [3]. Plan is for the wind power to account in for 87 MW of installed power and 100GWh of produced energy in 2012 [4].

According to study made in 2002 [5] it was shown that Serbia's capacity for wind power installment is 1300 MW, which is around 15% of total power production in Serbia. Studies [5]–[8], were made during the last decade with a goal to map wind resources in Serbia, and create map of the average wind speed over the territory of Serbia. Conclusion of these studies is that the wind speed is grates in Southern Banat region, and Vršac's mountains region, and that these two regions have the biggest wind potential in the country. Map of the average wind speed over the territory of Serbia is presented

in Fig. 1.

Computational Flow Dynamics (CFD) is a numerical model for solving fluid dynamics equations. Model implemented in software package WindSim[®] is based on solving simplified Navier – Stokes equations or RANS (Reynolds-Averaged Navier–Stokes). RANS are time-averaged equations of motion for fluid flow. The main idea behind these equations is Reynolds decomposition, whereby an instantaneous quantity is decomposed into its time-averaged and fluctuating quantities. These equations can be used with approximations based on knowledge of the properties of flow turbulence to give approximate time-averaged solutions to the Navier–Stokes equations. In general this means that the non-linear part of these equations is transformed to be linear. Downside of this approximation is a significant influence on the results and its precision [9], [10].

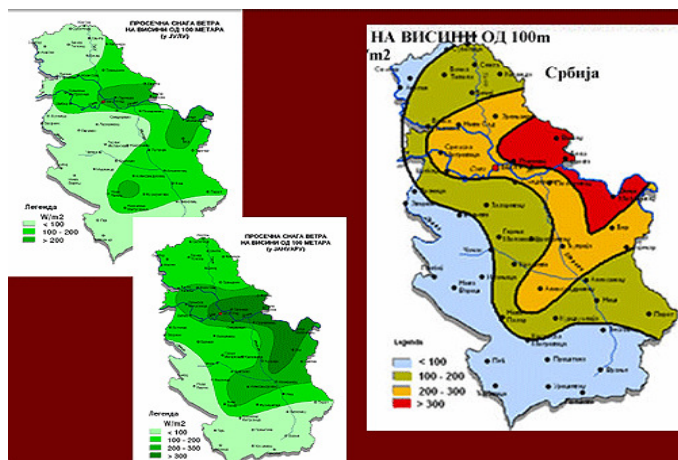


Fig. 1. Wind speed map at 100m over the territory of the Republic of Serbia. (On the left side distribution for winter and summer period, on the right side distribution for the whole year)[7].

When an air mass is traveling uphill, one of its parts is going to continue its movement in the same direction, following the mountain side, and the other part will usually separate from the main flow and start falling back to the surface in a circular path if the side is too steep (inclination greater than 20°). Also, when an air mass hits side of a hill or mountain, turbulent motion occurs as well. These two effects cannot be described with the Linear Flow Model, and thus many software packages using LFM cannot account for these effects. Even in case of hill with sides not steep enough to induce flow separation, wind speed prediction will deviate from measured value significantly when using LFM instead of CFD. Some software packages introduced methods for overcoming these limitations. E.g. WASP, one of the most commercially used wind prediction software packages, tried to bypass this problem [11] by introducing ruggedness index (RIX) [12], [13]. RIX is good solution that improves precision of the predicted results significantly over the complex terrains. Still, CFD method is more reliable and robust in case of flow split and turbulences, since it can account for these two effects

directly, without additional parameters or factors in the simulation. Flow separation, turbulences, and air mass flow over rugged terrain is illustrated in Fig. 2.

Wind speed simulation over some particular area is defined by a proper selection of boundary conditions at the borders of the area of interest and the height of the geostrophic wind above the surface. Boundary conditions considered by WindSim[®] software package are:

- Height at which the wind speed is considered to be constant
- Value of the speed at that height
- Boundary condition at top of the boundary level

The last parameter is related to terrain complexity. There are two selections for this parameter: fixed pressure, and non-frictional wall. First selection is better in case of hilly or mountain terrains and the second one is more efficient while predicting wind speeds over the fields, planes and grasslands. [14] Since the terrain at the “Šušara fields” is situated on the cultivated sand dyne and it’s mostly hilly, lacking any flat surface, better choice for this parameter was fixed pressure approximation.

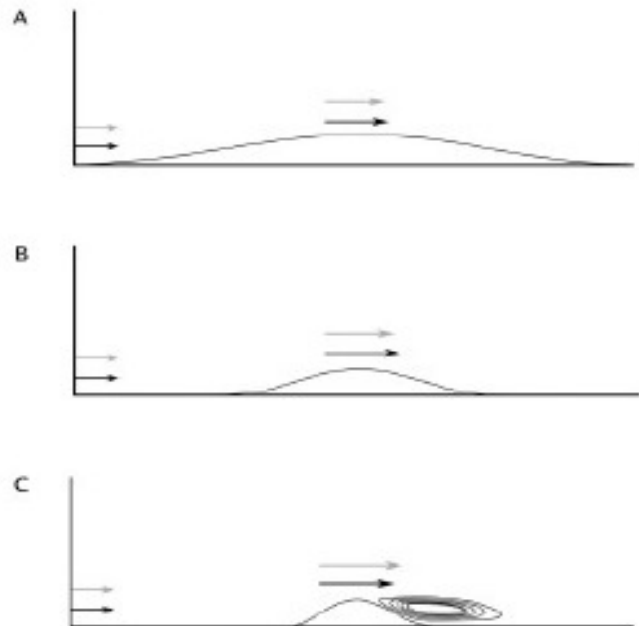


Fig. 2. Air mass flow in case of A) slightly rugged terrain, B) medium rugged terrain, C) highly rugged terrain (picture taken from [10]).

Data about boundary conditions can be obtained from the nearest meteorological measurements stations of the official institutions. Since the “Šušara fields” is a very remote area, far away from any official meteorological station (the nearest one is 30 km far and it’s located in the town of Banatski Karlovci), and due to its complex orography, it wasn’t any competent enough available data to be used in the simulation. This is why it was necessary to find valid boundary conditions values using some other method.

Testing of the WindSim CFD model was performed by comparing measurement results of the wind characteristics gathered from two measurement stations located at Šušara fields with the wind speed simulation results provided by the software package. Applied model for simulation confirmation and determination of boundary conditions is used as a starting verification of the model competence [15], [16]. Variation of different values of the boundary conditions is used to project and predict expected wind field raster of the second measurement mast at location B, using wind speed data from the first measurement mast at location A. If the model calculates satisfying values while predicting A on B, next step is to perform same operation, only in opposite direction, so one can get confirmation that the model will make good prediction in case of mast B being used to calculate wind field raster at location A. If the test in both directions are not contradictive with the measured values and deviate from the measured data within defined values, it can be considered that the model can be applied for an air mass movement simulation over the specified location, and that the simulation results are valid. 2D wind speed raster at 30 m height above the ground level at the chosen location will be presented in the paper.

II. LOCATION OF MEASUREMENT STATION

Based on the wind speed estimation studies, Šušara fields locality is situated in the area with the greatest wind potential in South-East (SE) Banat. This locality represents a unique geo-morphological configuration shaped in a form of a 10km long and 500 m wide cultivated sand dune. This sand dune reaches heights from 40 to 100 m above the surrounding plains. It's situated at the northern border of the Special Nature Reserve (SNR) "Deliblato Sands". Because of its geo-morphological origin, as a relict of a former Pannonian sea, wind had great influence on its creation. Since the dominant wind over this locality is SE wind, also known as "Košava", thus, this sand dune has the same orientation as the dominant wind that shaped it for several millennia. Terrain configuration and orientation is presented in the Fig. 3.

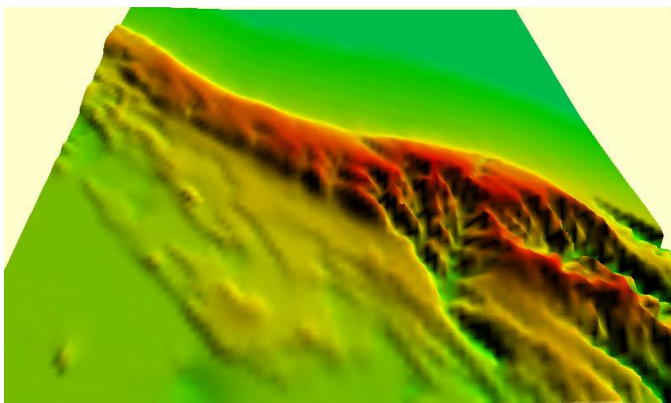


Fig. 3. Orography of Šušara fields locality.

Local inhabitants, living in the villages in the vicinity of Šušara fields, have century long tradition of wind power utilization. During the last years of the 19th century, first wind

mill was constructed in the village of Šušara, 1.5 km south from the Šušara fields locality, with the purpose of mechanical propulsion of the local water station and mechanical workshop. These facts indicate that there is a significant wind potential, since the villagers were able to utilize it with great success more than hundred years ago.

Study of the climate conditions over selected locality was performed by utilization of two specialized measurement stations for gathering and primary processing of the meteorological data. Measurement masts are 50 m high. (Fig. 4) Anemometers are installed at 30, 40, and 50 m, and the corresponding wind vanes are installed at heights of 30 and 50 m. Location of the first measurement mast, marked as A, is on the SE side of the locality, situated on the top of the prominent hill, with the UTM coordinates 021.188 °E 44.939 °N (highest point of the Zagajica hills formation). On the other hand, second mast, marked as B, is installed at the location with the UTM coordinates 21.126 °E 44.959 °N, at the NW of the sand dune plateau. These two locations were selected, because location A potentially has the greatest wind potential, and the location B, on the other hand, has the lowest within the borders of the Šušara fields locality. Data gathered from these two stations at characteristic locations should enable more precise estimation of the local wind resource potential. Data gathering from the measurement stations, along with initial processing, are preface in the realization of the Šušara fields project, which should include up to 60 MW of the installed power, according to the project plans and energy license [17].

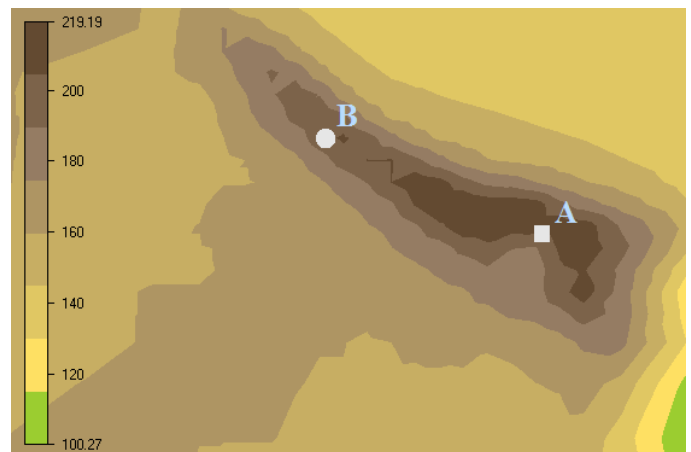


Fig. 4. Location of the measurement masts at the locality. Scale on the left represents height above the sea level in meters.

III. SENSORS

Hardware used in this field study of the wind potential over the Šušara fields locality consists of two 50 m tall measurement masts NRG TallTower. Both masts were equipped with four anemometers NRG #40C placed at heights of 30, 40, and 50 m. Along with the anemometers, two wind vanes NRG #200P were installed as well at heights of 30 and 50 m. Anemometers have 0.3 m/s offset and measurement error of $\pm 1\%$. For data transfer was used Symphonie

iPackGPS (GSM/GPRS) data logger. Within the logger, data is being saved on a SD card with some basic encryption. Data written to SD card consists of 10 minute values of the measured quantities along with the calculated standard deviation measured every 2 second during the 10 minute interval. Since the locality is far from any kind of infrastructure, additional power supply was needed to provide necessary electricity. For that purpose, car battery was installed, along with 5 W solar panel.

IV. MODEL TESTING

In this paper, group of authors used WindSim[®] software package in combination with WAsP wind analysis software tool. WAsP 8.2 was predominantly used for primary statistical analysis of the data gathered from the measurement masts, and to derive wind roses from the data in the OWC module. On the other hand, WindSim[®] was used for extrapolation of meteorological data and for wind speed fields prediction over the locality. To perform this simulation, some additional data input was needed. Primarily, creation of a good orography 3D model of the locality was crucial. Next step was preparation of the roughness and obstacle maps. 3D map of the orography was prepared according to geographic maps with 1:25000 ratio in GlobalMapper and WAsP map editor. WindSim[®] model was tested with approximation that roughness of the forest present at the locality is uniform with the length $z_0=0.03$ m.

WindSim[®] is software package for wind data analysis. Its GUI has a step-by-step design, and consists of several modules. First step is to define density of the surface grid, so the region of interest (defined by the location of two measurement masts) has bigger resolution. Before that, basic input data such as orography map and statistically processed wind databases were prepared in WAsP and its modules. Next step in WindSim[®] GUI is sector analysis and proper selection of the boundary conditions for CFD simulation. Comparison of simulated and real data served as a control if adequate boundary conditions were selected. Thus the best, and the easiest, but more time consuming method for finding proper boundary conditions was brute force algorithm. First simulation goal was to find adequate boundary condition parameters that will give results similar to measured at location B, using the data from location A. When the proper set of boundary condition parameters for this case was found, another simulation was performed, but in opposite direction. These two steps were repeated until the difference between measured and simulated data was negligible. Local characteristics, such as orography, terrain roughness, and obstacles have great influence on wind characteristics at lower heights, while at greater heights are becoming insignificant, since the geostrophic characteristics will be dominant. For this paper, only available sets of data were ones from the 30 m height above the ground from both measurement masts.

V. RESULTS

Data from measurement stations were gathered during the

five year period, and for this paper authors had at their disposal data for the three month period from spring to summer 2010, so that the estimated roughness values correspond to the vegetation period. Data was first processed in OWC wizard (module of WAsP wind assessment tool). Results were wind roses for both masts. Using these wind roses, mean wind speed for the three month period at 30 m was predicted. For the masts A and B this speeds were 4.96 m/s and 4.70 m/s respectively. Also, they were used as a referent measured values that will be compared with the simulated wind roses from a WindSim[®] simulation (Fig. 5).

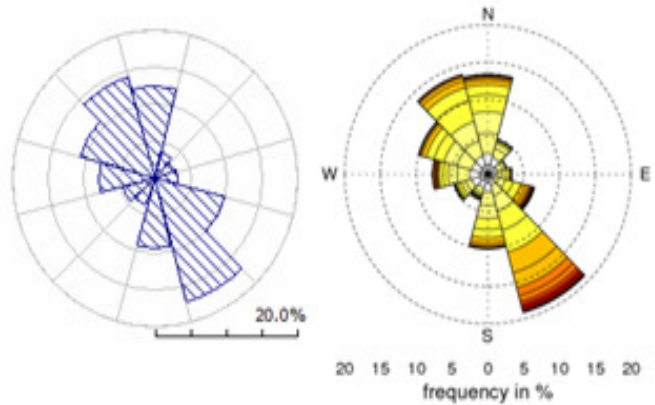


Fig. 5. Wind rose for the mast A calculated in OWC wizard (left) and wind rose of transfer climatology at the location of the mast A as a simulation result in WindSim (right).

Simulation testing was performed by constantly changing values of the boundary conditions parameters. Inadequate selection of boundary conditions parameters led to incorrect predictions of wind fields over the locality. E.g., if the selected maximum height of the simulation is too high, simulation will not be able to account terrain effects on the wind fields, and if the maximum height is too low, small changes in the boundary conditions will produce significant fluctuations in the resulting wind fields. It was noticed that in some cases measured and predicted wind roses were almost the same, which is the proof that simulation didn't managed to include terrain effects because of the inappropriate boundary conditions (Fig. 6).

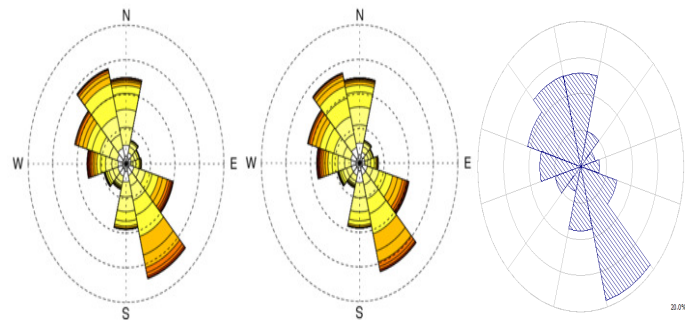


Fig. 6. Wind rose of the measured set of data from the mast A (left), wind rose as a result of simulation at location B using data from A (middle), Wind rose of the measured data form mast B (right).

Also, this will have influence on the wind speed fields prediction as well. Results presented in Fig. 7 shows how

inadequate parameters of the simulation will produce wind map that will have highest wind speed values even at the location of the mast B which has the lowest wind speeds at Šušara fields locality.

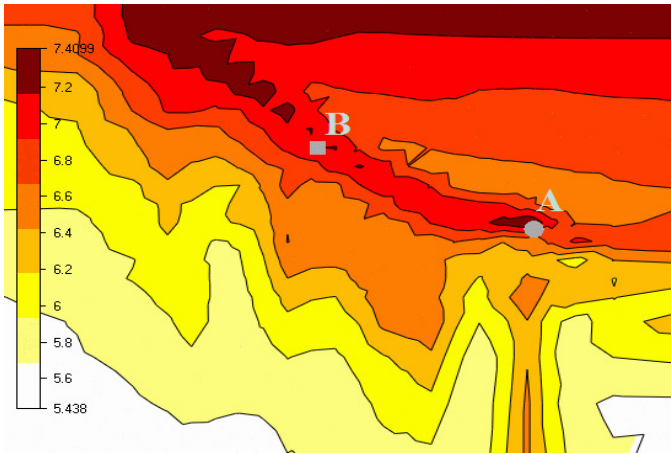


Fig. 7. Wind filed prediction at 30m, using inadequate boundary conditions. As a result wind fields with the grates energy potential can be found near locality B as well, which is contradictory to measured data.

After many attempts, proper set parameters was found providing prediction error of 1-2 % for the mean wind speed during the period of measurement while predicting climatology on second site using the data from the first site. This means that mean wind speed prediction error is 0.05-0.11 m/s and it is comparable to anemometers' measurement error which is $\pm 1\%$. Results of a mean wind speed value prediction during the period of measurement are given in Table I.

TABLE I
MEAN WIND SPEEDS AT 30 M FOR THE MUSTS A AND B (MAIN DIAGONAL OF THE TABLE) AND MODEL PREDICTIONS FOR THE CASES $A \rightarrow B$ AND $B \rightarrow A$ RESPECTIVELY (OTHER DIAGONAL)

MAST AND ITS COORDINATES	MAST A (30 m) x=514812.6 m y=4976275 m	MAST B (30 m) x=509947 m y=4978416 m
MAST A (30 m) x=514812.6 m y=4976275 m	4.96 m/s	5.07 m/s
MAST B (30 m) x=509947 m y=4978416 m	4.65 m/s	4.70 m/s

This type of testing is used for the first approximation of the model certainty. Based on the similarity of measured and simulated wind roses, it can be assumed that the used fluid dynamics model is satisfying, so the right set of the boundary condition parameters can be found. Simulation using these parameters will make insignificant error, comparable to instrument measurement error, while predicting mean wind speeds at 30 m. Height profile was not part of this study, since authors only had available wind speed data at 30 m, so the model of local atmospheric stratification was not verified.

Using proper set of boundary conditions parameters, simulation calculated wind speed raster over the Šušara fields locality. Fig. 8 illustrates areas with the highest wind speed at

the given height. These areas can be considered as the potential candidate for installation of the wind turbine of the same or similar height.

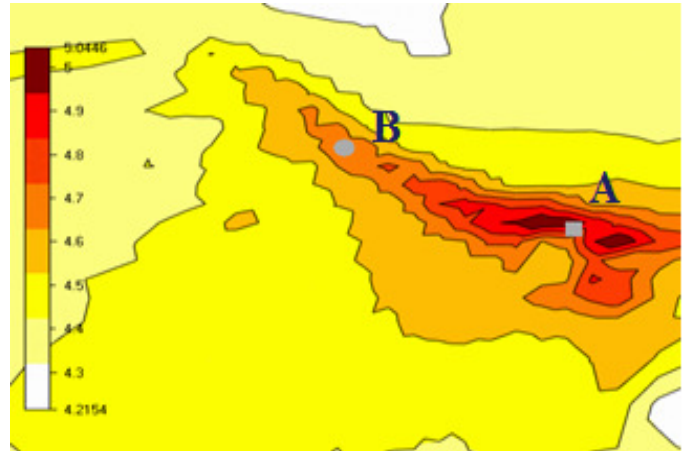


Fig. 8. Wind speed prediction over the Šušara fields locality at 30m above the ground. Area around the mast A has the grates wind potential, while the area around mast B has the lowest.

Area of the Zagajica hills (location of the mast A) has the greatest wind potential within the borders of the Šušara fields locality. On the other hand, location of the second mast (mast B) is less windy because of the influence of the local orography. Wind speed decreasing trend from SE to NW is evident, confirming "Košava" to be dominant wind here, which played an important role in the process of relief formation of this locality throughout millennia.

VI. CONCLUSION

Preliminary testing of the WindSim CFD model was performed using Šušara fields locality as an example. Since the locality has areas of complex orography and the linear fluid dynamic model would not be able provide good results, the CFD model was tested. Mean wind speed from at the location of two measurement masts during the period data gathering was used as a comparison parameter for measured and simulated data. Difference between transfer climatology derived from calculated and simulated data at 30 m above the locality of Šušara fields was calculated by varying boundary conditions and simulation parameters, and it was within 2% corresponding to measurement error of the sensors. Due to a insufficient data about the stratification of atmosphere at the locality, brute force algorithm was used to find a proper set of boundary conditions and simulation parameters. Results confirm that the CFD model, and the WindSim software using it, is excellent choice of software tool for wind fields prediction for Šušara fields locality at 30 m above the ground. Calculations showed that the measurement masts are approximately situated at locations with highest and lowest wind potential. These results are important for future wind power harvesting and climatology conditions analysis over the Šušara fields locality. Further model analysis will comprise of sector testing, and climatology extrapolation to different heights.

REFERENCES

- [1] IPCC (2007-05-04). "Summary for Policymakers" (PDF). ClimateChange 2007: The Physical Science Basis. Contribution of Working Group I to the Fourth Assessment Report of the Intergovernmental Panel on Climate Change. Available: <http://www.ipcc.ch/pdf/assessment-report/ar4/wg1/ar4-wg1-spm.pdf>. Jul 2009.
- [2] World Wind Energy Report 2010, World Wind Energy Association. February 2011.
- [3] Đeređ N., Kalmar Krnajski Jović Z., Apostol I., "Renewable energy resources in Serbia, recommendations, potentials, criteria", Center of ecology and sustainable development, December 2008.
- [4] Tešić M., Filipović D., "Strategy realization program for development of energetic of republic of Serbia in AP Vojvodina for 2007- 2012 period", Executive council of AP Vojvodina, Provincial Secretariat for Energy and Mineral Resources, April 2007.
- [5] R. Putnik et. al., "Possibilities of wind energy utilization for electric energy production – case study", Electric Power Industry of Serbia, Belgrade, 2002.
- [6] Case study of energy potential of Serbia for solar radiation and wind power utilization. Study EE704-1052A, Center for multidisciplinary studies. 2004.
- [7] Katić V. Ćosić I., "Wind atlas of AP Vojvodina – case study", Faculty of technical science, Novi sad, December 2008.
- [8] Zlatanović M., "The use of wind energy in Serbia –Natural conditions and practical policy", Jefferson Institute, December 2009. Available: <http://www.jeffersoninst.org/>
- [9] Gravdahl A.R., "Meso Scale Modeling with a Reynolds Averaged Navier-Stokes Solver. Assessment of wind resources along the Norwegian coast." International Energy Agency Annex XI, Risø Denmark, October 1998.
- [10] Milashuk S., W.A. Crane, "Wind speed prediction accuracy and expected errors of RANS equations in low relief inland terrain for wind resource assessment purposes", Environmental Modelling & Software 26, pp. 429 – 433, 2011.
- [11] Bowen A. J., Mortensen N. G., Exploring the limits of WAsP, "The wind atlas analysis and application program", paper O15.2, EU wind energy conference, May 1996.
- [12] Mortensen N. G., Heathfield D. H., Myllerup L., Landberg L., Rathmann O., "Getting Started with WAsP 8" Risø National Laboratory, Roskilde, Risø-I-1950(ed.2)(EN), March 2004.
- [13] Pianigiani M., "Comparison of Ansys CFX and WAsP for Sarfanngua ", Master Thesis, Technical University of Denmark, February 2009
- [14] WindSim 5.0, *Getting started*, September 2010.
- [15] Llombart, A., Mallet, A., Burillo, N., Alvarez, O., Talayero, A., „Influence of Orography on Wind Resource Assessment Programs“, European wind energy conference, Milano, 2007.
- [16] V. Riedel and F. Durante, "Harvest time in the mountains: round robin numerical flow simulation in wind energy", part 2, DEWI 32, pp. 12–26, 2008.
- [17] Ministry of Mines and Energy, the list of issued permits for wind power energy. Available online: www.mem.gov.rs

Robust adaptive system identification of steam separator process in thermal power plants

Goran S. Kvašček, Aleksandra Lj. Marjanović, and Željko M. Đurović

Abstract—Industrial practice imposes the problem of measuring physical quantities in terms of quality, which is the primary requirement of process control with good performance, and further processing of data in terms of application of algorithms to detect and isolate failures. In order to overcome the phenomenon of outliers, which is common in industrial practice, it is necessary to apply some of the techniques of robust identification. This paper presents a new approach to robust adaptive identification which was used to identify the parameters of steam separator. It would be possible to apply techniques for the failure detection and isolation based on the model of the process, as well as in terms of better process control. The comparison with the classical approach was carried out and demonstrated the efficacy proposed algorithm.

Index Terms—Fault detection, robust process identification, steam separators, thermal power plants.

I. INTRODUCTION

THE needs of modern industry are growing every day and the application of advanced process control techniques, modern equipment maintenance and servicing and energy efficiency is required. To satisfy these requirements it is necessary to know the process in terms of its characteristics and model, and it is very important to apply some procedure for early fault detection and isolation. Many of the methods which are dealing with these problems are based on the knowledge of a good process model, and therefore we can design modern process control, as well as FDI systems to quickly detect and isolate faults in complex systems.

In order to obtain a good process model special attention should be paid to the identification process, including the selection of an appropriate model, the process and model inputs, and identification methods. If the process is time variant, it is necessary to perform identification in real time, which further complicates the problem in terms of automation procedures without human supervision. In industrial practice,

a large number of measurements are under the influence of high-level noise, which significantly reduces the performance of identification systems. A large number of methods assume that the measuring noise is with normal distribution and then it is possible to effectively estimate the parameters of the system. If the measurement noise does not have Gaussian distribution, it is necessary to apply more complex techniques to achieve satisfactory results. The paper presents a new robust adaptive parameters estimation procedure [1], [2] based on QQ-plot [3], [4] which can effectively deal with processes that have measurements with pulse noise, so called outliers.

For better performance and effective process control it is necessary to have reliable sensors and actuators. It is also of great importance to have a procedure that can efficiently detect not only the failures of individual components, but to monitor changes of their characteristics over time, so that timely servicing or calibration equipment facility can be done. Such a system should possess characteristics such as reliability and efficiency in terms of rapid and timely detection of failure, but also a small number of false alarms to avoid disfiguring the confidence in decisions made by the system.

The paper will show methods for M-robust estimation of system parameters that will be applied to a concrete example of the process of water steam separation in the steam power plant Kostolac TEKO B1. This example will illustrate the application of the algorithm on a process that has a measurement with a high degree of impulse noise (outliers), which significantly affects the recursive identification of parameters in real time, with which the standard identification methods cannot cope in terms of achieving performance. Results of identification can be used to monitor the system operation, to detect and isolate failures, as well as changes in the performance of individual components, such as water level and flow sensors in this case.

The paper is structured as follows: Following the Introduction, Section 2 contains a detailed description of the steam drum system in a thermal power plant boiler, as well as an explanation of relevant processes which take place in the system. Section 3 proposes a method for robust adaptive estimation of process parameters, which is extremely important for the identification of parameters of the analyzed subsystem, given the pulse noise present in the measurements. Finally, Section 4 discusses specific results of application of the proposed approach in a real steam separator system.

This research was supported by the Ministry of education and science, Republic of Serbia, contract No. TR32038 and No. III42007. Some results of this paper were presented at 55th ETRAN Conference, Banja Vrućica, June 6-9, 2011.

G. S. Kvašček is with the School of electrical engineering, University of Belgrade, (corresponding author: +381 11 3218437; e-mail: kvascev@etf.bg.ac.rs).

A. Lj. Marjanović is with the School of electrical engineering, University of Belgrade, (e-mail: amarjanovic@etf.bg.ac.rs).

Ž. M. Đurović is with the School of electrical engineering, University of Belgrade, (e-mail: zdjurovi@etf.bg.ac.rs).

II. ROBUST ADAPTIVE SYSTEM IDENTIFICATION BASED ON QQ PLOTS

Let us consider a linear, time invariant, discrete system defined as:

$$y(i) = -\sum_{k=1}^n a_k y(i-k) + \sum_{k=1}^m b_k u(i-k) + \xi(i) \quad (1)$$

where $y(i)$, $u(i)$, and $\xi(i)$ are the system output, measurable input and noise, respectively. The linear regression form of (1) is given as:

$$y(i) = Z^T(i)\Theta + \xi(i) \quad (2)$$

where the regression vector is

$$Z^T(i) = [-y(i-1) \dots -y(i-n) \ u(i-1) \dots u(i-m)] \quad (3)$$

and $\Theta^T = [a_1 \dots a_n \ b_1 \dots b_m]$ represents a vector of unknown system parameters.

System identification can be reduced to minimization of following criteria:

$$J_k(\Theta) = \frac{1}{k} \sum_{i=1}^k \rho(v(i, \Theta)) \quad (4)$$

where $v(i, \Theta) = y(i) - \hat{y}(i | \Theta)$ is the output prediction error or measurement residual, and $\rho(\cdot)$ is a loss function, which for maximum likelihood is defined as $\rho(\cdot) = -\ln p(\cdot)$, where $p(\cdot)$ is the probability density function. If the noise distribution is Gaussian, then minimization of (4) is classical least square method. If there is an impulse noise in measurements, then the application of this approach is inadequate because of poor performance. Huber recommended that the probability density function in such cases should be chosen as a normal distribution in the middle and exponential in the tails. For such a PDF, Huber's loss function is defined as:

$$\rho(x) = -\ln(p(x)) = \begin{cases} \frac{x^2}{2\sigma^2}, & \text{if } |x| \leq k \\ \frac{k|x|}{\sigma^2} - \frac{k^2}{2\sigma^2}, & \text{if } |x| > k \end{cases} \quad (5)$$

A recursive M-robust estimation can be described with the following equations:

$$\Theta(i) = \Theta(i-1) + \Gamma(i) Z(i) \Psi[v(i, \Theta(i-1))]; \quad \Theta(0) = \Theta_0$$

$$v(i, \Theta) = y(i) - Z^T(i)\Theta \quad (6)$$

$$\Gamma(i) = \Gamma(i-1) - \frac{\Gamma(i-1) Z(i) Z^T(i) \Gamma(i-1)}{w^{-1} + Z^T(i) \Gamma(i-1) Z(i)}; \quad \Gamma(0) = \gamma^2 I$$

where the influence function is defined as:

$$\Psi(x) = \rho'(x) = \min \left(\max \left(\frac{x}{\sigma^2}, -\frac{k}{\sigma^2} \right), \frac{k}{\sigma^2} \right) \quad (7)$$

For ε -contaminated noise with probability density function:

$$p = (1-\varepsilon)N(0, \sigma^2) + \varepsilon N(0, \sigma_o^2) \quad (8)$$

where the outlier variance is much greater than noise variance, $\sigma_o^2 \gg \sigma^2$. Now, it is possible to define the M-robust

influence function:

$$\Psi(\cdot) = [-\ln(p)]' \quad (9)$$

In order to apply this kind of recursive identification, it is necessary to estimate parameters of PDF that define the signal, using QQ diagrams and then construct a M-robust influence function (9), using the results of equation (8), shown in Fig. 1, for different parameters ε , σ and σ_o .

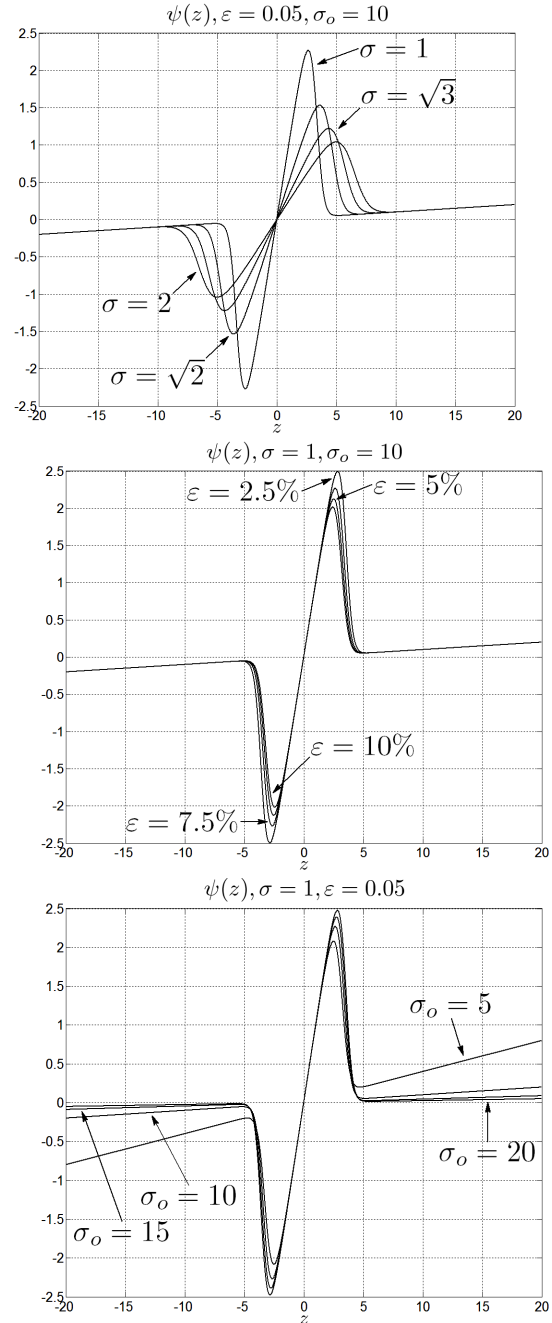


Fig. 1. Influence function for different parameters.

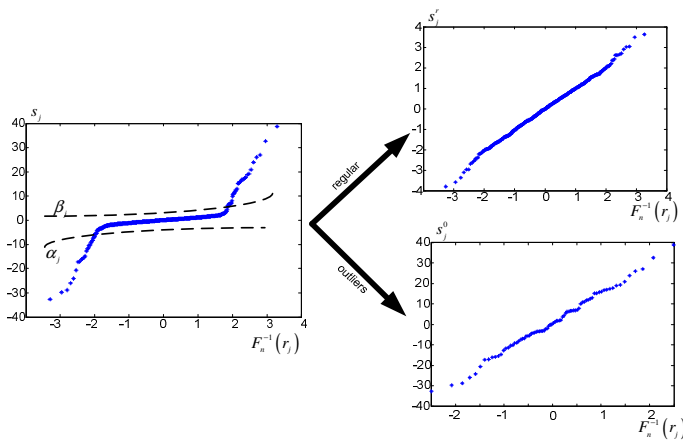


Fig. 2. Data classification (regular and impulse noise measurements). QQ-plot before and after data classification.

The algorithm consists of the following steps:

- classification of data into two categories, using QQ plot techniques, as shown in Fig. 2, the regular data and outliers. It is first necessary to determine curves α and β , and then it is easy to perform the classification of data,
- then perform the estimation of the parameters of statistics from equation (8), using the least squares method
- determine contamination degree \mathcal{E} , as a ratio between contamination of detected outlier and the total number of measurements on a particular window,
- then construct M-robust influence function obtained by including parameters in Equation (9)
- the final estimation is done using the parameters of the system in equations (6)

III. STEAM SEPARATOR PARAMETER IDENTIFICATION OF THERMAL POWERPLANT KOSTOLAC B1

Thermal power plants are the largest generators of electricity in Serbia, contributing more than 65% to the overall power supply. As such, their operational efficiency and stability needs to be maximized. Special emphasis is placed on reliable long-term operation in terms of negotiated delivery commitments, operation per design criteria for energy efficiency, and longevity of the facility. It is, therefore, extremely important to monitor vital subsystems and their individual components, such that early detection of any change in characteristics, or faults, will prevent accidents, down time, and substantial financial loss.

The paper addresses steam drums in thermal power plant boilers [5]-[7]. A boiler is a unit in which the chemical energy of fossil fuel is converted into heat energy of steam. Fig. 3 shows the basic structure of a steam boiler. An even number of mills (usually 6 or 8) break up and grind coal and then a mixture of coal and preheated air is routed to a furnace via a system of ducts. In parallel, the oxygen needed for combustion is provided by an air supply fan. On the way to the furnace,

the air is additionally heated to enhance combustion. Temperatures inside the furnace are as high as 1400 °C, such that all its parts need to be resistant to such temperatures.

Feedwater pumps deliver partially heated water to the steam drum via an economizer, and then additional pumps discharge the water into a system of pipes where multi-stage heating takes place inside the boiler and the water is converted into steam. The steam drum also removes residual drops of water from the steam. The steam is then delivered to a multi-stage superheater where it is heated to about 540 °C at a nominal pressure (usually 165-175 bars) before it leaves the boiler, and the superheated steam continues on to the turbine.

Specifically, at the TEK0 B1 Unit of the Kostolac Thermal Power Plant, the diameter of the steam drum is 0.9 m and its height is about 24 m (Fig. 1(b)). Even a small water level variation inside the steam drum results in noticeable steam pressure fluctuations and affects the technical conditions of the process. If the water level is too high, emergency relief valves open to remove excess water and this improves the operational efficiency of the unit. However, if the water level is too low, after a certain time a boiler shutdown procedure is initiated automatically, to protect the piping from overheating. As a result, maintenance of the required water level is a very important control requirement.

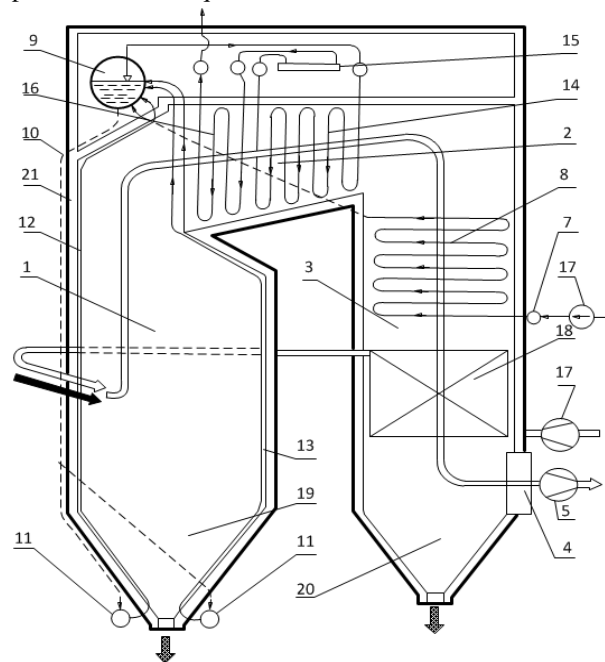


Fig. 3. Schematic of a typical boiler: 1-Exhaust fan, 2-Feedwater pumps, 3-Main feedwater control valve, 4-Economizer, 5-Steam drum, 6-Primary preheater, 7-Secondary preheater, 8-Air supply fan, 9-Air preheater.

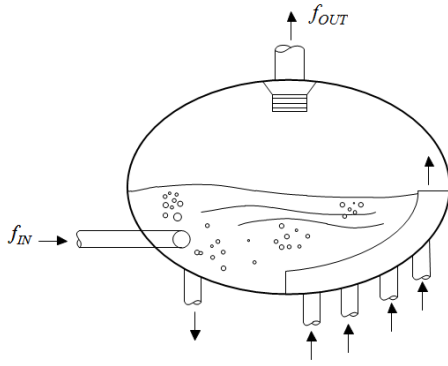


Fig. 4. Steam drum: f_{IN} - input feedwater flow, f_{OUT} - fresh steam output flow.

Given that the water level in the steam drum depends on the water flow to the drum and the steam flow from the drum, and since an integrating effect is inherent in the process, the following discrete separator model in the form of discrete transfer functions is proposed:

$$Y(z) = \frac{B_1(z)}{A(z)} f_{IN}(z) + \frac{B_2(z)}{A(z)} f_{OUT}(z) \quad (10)$$

where $Y(z)$ is water level in stem drum, $f_{IN}(z)$ feedwater flow, and $f_{OUT}(z)$ steam flow on the output (Fig. 4).

Using comparative analysis of models of different order, it was concluded that the minimum order model that adequately describes the system is three, and the proposed forms of polynomials in the numerator and denominator are:

$$\begin{aligned} A(z) &= 1 + a_1 z^{-1} + a_2 z^{-2} + a_3 z^{-3} \\ B_1(z) &= b_{11} z^{-1} + b_{12} z^{-2} + b_{13} z^{-3} \\ B_2(z) &= b_{21} z^{-1} + b_{22} z^{-2} + b_{23} z^{-3} \end{aligned} \quad (11)$$

This model is not adequate for modeling the dynamics of the system. Taking this into account, and that the process is integrator type, a priori information was implemented into the model as:

$$Y(z) = \frac{B_1(z)}{A(z)(1-z^{-1})} f_{IN}(z) + \frac{B_2(z)}{A(z)(1-z^{-1})} f_{OUT}(z) \quad (12)$$

In time domain nine parameters model is presented as:

$$\Delta h[k] = - \sum_{i=1}^3 a_i \Delta h[k-i] + \sum_{i=1}^3 b_{1i} f_{in}[k-i] + \sum_{i=1}^3 b_{2i} f_{out}[k-i] \quad (13)$$

where $\Delta h[k] = h[k] - h[k-1]$ is the level difference in two time sample.

The water-level signal noise cannot be modeled in the usual manner, with Gaussian zero-mean distribution. Such a measurement sequence includes sporadic high-intensity noise, or outliers. This can be attributed to the fluid level measurement procedure which involves differential pressure measurements in the steam drum, where a large liquid and steam fluctuations produce measurement noise. Pulse noise originates from sudden evaporation and the appearance of

large steam bubbles inside the vessel, which rapidly separate on the surface and create a pressure disturbance. This nature of the measurement noise prevents the application of standard identification procedures, so the paper proposes robust adaptive parameter estimation which is highly efficient in the case of measurements with pulse noise.

Proposed procedure is applied and the results of estimation of level and measured levels are presented, in Fig. 5, for 24 hour time period without system fault. Estimation of level is satisfactory, and this is a verification of the proposed procedure, as well as the order of adopted model. Fig. 6 shows the movements of the model parameters (13) in time. It is obvious that the contribution of robust estimation is significant, in the sense that the occurrence of impulsive noise does not affect the procedure as significantly as a disturbance.

The Figs 7 and 8 show the estimation of water level in the water/steam separator in the system when there is a failure, which is modeled as a multiplicative failure (30%) measuring the water level and water flow.

During the real time recursive estimation it is necessary to determine the forgetting factor, as the balance between the speed of detection of parameter changes and the quality of identification. As the appearance of impulse noise significantly affects the deterioration of estimation, it is necessary to increase the forgetting factor, and thus slow down the detection of changes in the state system. As the proposed procedure significantly reduces the impact of poor impulse measurements, the forgetting factor may have a low value and thus affect the reduced time to detect failures.

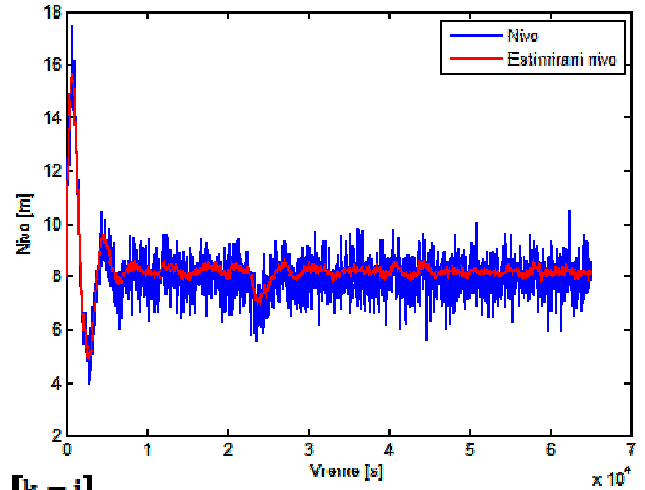


Fig. 5. Estimated water level (red) and measured water level (blue) in steam drum without fault.

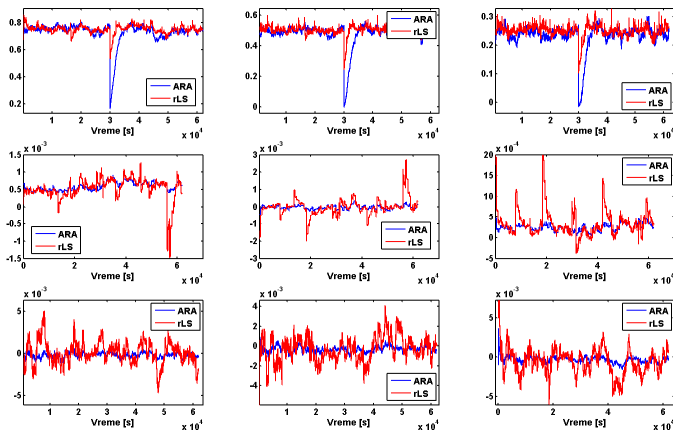


Fig. 6. Movement of estimated parameters in time: proposed method (blue) and recursive least squared method (red).

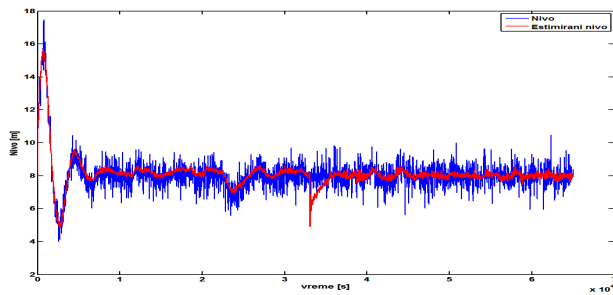


Fig. 7. Estimated level (red) and measured water level (blue) in steam drum with level sensor fault.

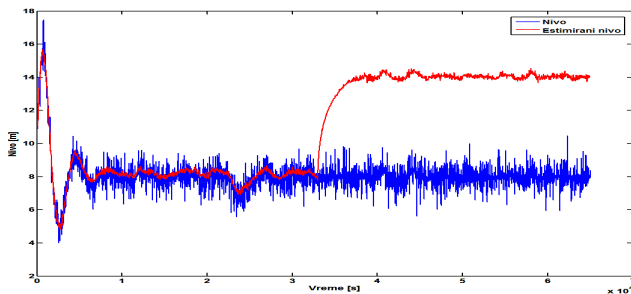


Fig. 8. Estimated level (red) and measured water level (blue) in steam drum with feedwater flow sensor fault.

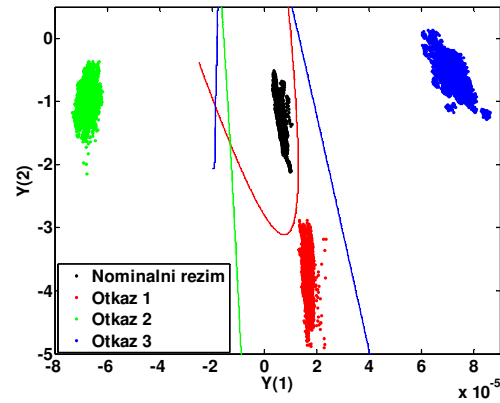


Fig. 9. Classes of operating regimes after dimension reduction: nominal regime without fault (black), level sensor fault (red), feedwater flow sensor fault (blue), steam flow sensor fault (green).

IV. CONCLUSION

In this paper an adaptive method for robust estimation of system parameters based on QQ-plots and its application on a system of power plant steam separator TEKO Kostolac B1 320~MW nominal power has been presented.

A comparison with the classical recursive least squares method has been done, and the significant improvement in the estimation of parameters of the system has been shown. These results become usable for better process control, and they can be applied also to detect failures in the steam separator system, after using techniques for dimension reduction as shown in Fig. 9.

REFERENCES

- [1] Venables, W. N. and Ripley B.D.: 'Modern Applied Statistics with S', (Berlin: Springer, 2002)
- [2] Huber, P. J.: 'Robust Statistics', (New York: John Wiley, 1981)
- [3] Barnett, V.D., and Lewis, T.: 'Outliers in Stochastic Data', (New York: John Wiley, 1978)
- [4] Đurović, Ž.M., and Kovačević, B.D.: 'QQ plot approach to robust Kalman filtering', Int. J. of Control, 1995, 4, (61), pp. 837-857
- [5] Flynn, D., 'Thermal Power Plant Simulation and Control', The Institution of Electrical Engineers, London, 2003.
- [6] Z. Mićević, 'Kotlovska postrojenja', Energoprojekt Enel d.d., Beograd, 1999.
- [7] Lj. Brkić, T. Živanović, 'Parni kotlovi', Mašinski fakultet Univerziteta u Beogradu, Beograd, 2007.

Multi-Core Platform for DTV/STB Functional Testing in Real-Time

Dusan Milosavljevic and Vladimir Zlokolica

Abstract—This paper presents a platform for DTV/STB functional testing, based on detection and measurement of video artifacts that originate from packet loss errors in transport stream. The system is capable for real-time processing of the DTV/STB video stream utilizing processing power of modern multi-core platform.

Index Terms—Packet-loss error detection, software parallelization, video quality assessment, video streaming.

I. INTRODUCTION

ALONG with the development of multi-core platforms for personal computers, the past decade was marked by digitalization of television. Digitalization of television signal transmission was first performed in satellite transmission (DVB-S), and later the process of digitalizing was spread to terrestrial transmission, which is still carried out (DVB-T) in many countries. The choice of coding video signals depends on the available bandwidth. MPEG standard has been accepted for digital broadcasting of television signal as the basic and most commonly used for transmission of standard definition (SD) video content, whose basic concept is a digital packetized stream. By digital video transmission, it is obtained higher bandwidth utilization of transmission medium, and solved the problem of partial admission of broadcasted video signal, which is one of the basic conditions for guaranteeing the quality of service. However, the transmission errors that occur and which cannot be removed in the process of decoding by variety of methods may lead to packet losses in the transport stream. Such errors undermine the subjective quality of video content that in digital broadcasting has become very relevant for providing QoS [5], [6], [19], [22]-[24]. The new video services such as IPTV, Mobile TV and Internet Video Streaming rely on digital video transmission over networks, where the effects of packet-losses, due to various errors, are more frequent and more

pronounced on the quality of video content [2].

In order to provide high quality experience of broadcasted video content to the end user, DTV and STB (set-top box) receivers apply error-concealment or complete discarding of poor quality video content based on decision from quality assessment as common approach. The correct and reliable functionality of DTV error concealment and error correction features is of great importance to the quality of video content that is experienced by the end user. In order to verify the required functionality of DTV devices, it is necessary to be tested in a realistic environment [25], [24] where device response on digital signal transmission errors is examined. The main functionality of the DTV/STB receiver, in addition to demodulation and signal decoding, is to provide the minimum required quality level of video content that is presented for certain error rate level in transport stream. Based on available and undamaged information extracted from bit-stream, the DTV/STB receiver tries to conceal errors manifested as visual degradation on video content by reconstructing missing information from video stream. Successful error concealment is directly related to broadcast video content and the number of lost packets. Consequently, based on the degree of visual degradation in video frames receiver determines whether to display decoded content of video stream over which is previously applied error concealment techniques. If the visual degradation of video frame is unacceptable due to high amount of present artifacts, the receiver should reject current video content and abort presentation of video frame on output. In this case from DTV is expected to show black screen with “no signal” message displayed or frozen video until better video quality is obtained.

This paper presents the implementation of DTV testing platform based on software solution algorithm for the detection of lost packets (PLD - Packet Loss Detection) [1] which gives a measure of errors during transport on the basis of artifacts in the image that impair visual quality of video content, primarily for video streams that are broadcasted over network. The software implementation of PLD algorithm is part of platform for testing TV and STB devices that provide a measure of video degradation that originate from packet loss errors in transmission. The emphasis is on the realization of such complex algorithm to explore the use of modern Intel multi-core architecture in the digital video signal processing. The main goal is to achieve execution times required for real time processing of video stream (by) applying the principles of

This work was partially supported by the Ministry of Education and Science of the Republic Serbia under the project No. 44009, year 2010. Part of results in this paper is presented on 55th ETRAN conference, Banja Vrucica, 6-9 June 2011.

D. Milosavljevic is with the Faculty of Technical Science, University of Novi Sad (e-mail: dusan.milosavljevic@rt-rk.com).

V. Zlokolica is with the Faculty of Technical Science, University of Novi Sad (e-mail: vladimir.zlokolica@rt-rk.com).

parallel programming and optimization techniques, that imply utilizing vector instructions (SSE, AVX) and OpenMP [26] standard for parallelization.

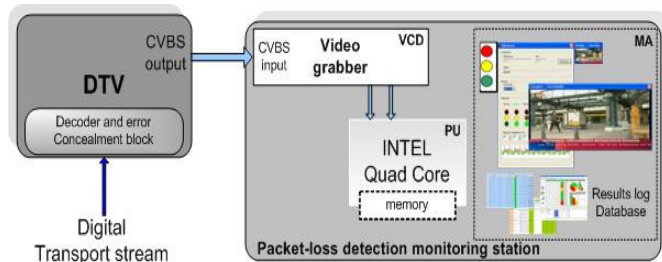


Fig. 1. Detailed description of the proposed system for the DTV functional testing.

II. GENERAL PLATFORM OVERVIEW FOR DTV TESTING

A. System description

In Fig. 1 the testing platform for DTV/STB devices is shown as separate testing station. The packet-loss detection monitoring station is a portable and modular Windows based embedded PC system, which is intended to be used by the DTV set and STB manufacturers or R&D, production and field device testing for packet-loss error issues (measurement and detection). The base of the platform is an Intel multi-core platform of the second generation (codenamed Sandy Bridge) where the software solution of PLD algorithm is being executed. The main idea of the platform for testing DTV and STB receivers is to record media raw video directly from receiver by HDMI or CVBS outputs, which is further processed in real time by PLD algorithm to determine amount of artifacts that originate from packet loss errors. If the amount of artifacts is found to be above a predefined threshold, which is directly proportional to subjective visual perception, the DTV under investigation is acknowledged as dysfunctional. This platform consists of the three main components: (i) Video capturing device (VCD); (ii) Processing Unit (PU); (iii) Monitoring application (MA). The DTV under investigation is excited by digital transport stream, after which decoder of DTV/STB performs demodulation and consequently applies implemented error concealment techniques. The input of VCD is raw video signal extracted directly from DTV external sources such as CVBS or HDMI outputs. The captured raw video data is further streamed to The PU block, where the packet-loss detection is performed in real-time on INTEL multi-core platform. The PU provides the output measures for packet-loss errors corresponding to each frame and to the particular video sequence segment (VSS), which in our application is set to 50 frames (equals approximately 1s duration period). The latter is used to signal at the system output the packet-loss occurrence with three output states: (i) no error (labeled as green); (ii) undetermined/questionable error detection (labeled as yellow); (iii) certain error detection (labeled as red). These semaphore states are also shown in Fig.

1. The MA block is responsible for managing test processes and determining states of test outcomes. Beside main functions and graphically displaying the test result the MA block is used to store testing results in database for later statistical analysis and debugging.

B. Use Cases

Beside primary functions such as inspecting the functionality of DTB devices there is another suitable use-case of presented platform. The use cases differ from each other in context environment in which same platform is used. The primary testing function is present on Fig. 2 where behavior of device under investigation is compared to referent device which functionality is proven in terms of error concealment specification. Furthermore, testing outcome can be conducted using non referenced method, when obtained PLM is investigated in respect to expected threshold specification in formed database. The other functionality of platform implies video quality monitoring measuring packet loss error rate of broadcasted stream. This configuration can be easily set if device under investigation is replaced with proven device. Video quality monitoring provided by this platform is very suitable for inspecting current error rate in broadcasted video streams that may be at level where error concealment methods become useless to decrease impact on video quality. Since packet losses is proportional to bit error rate, in noisy environment PLM measure could be useful to indicate low SNR of broadcasted signal.

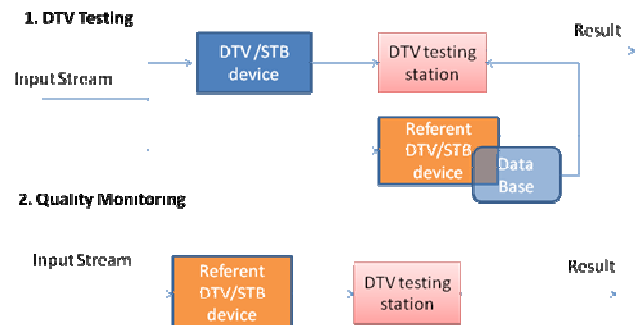


Fig. 2. System use cases for different set up environment: (top) – primary platform function for DTV testing; (bottom) – quality monitoring function.

III. PROPOSED PACKET LOSS ERROR DETECTION ALGORITHM

In an MPEG-2 based video stream, data loss reduces quality depending strongly on the type of the lost information. Losses of syntactic data, such as headers and system information, affect the quality differently than losses of semantic data such as pure video information (e.g. motion vectors, DCT coefficients, etc.). Furthermore, the quality reduction depends on the location of the lost semantic data due, not only to the predictive structure of MPEG-2 video coded streams, but also to the visual relevance of the data [3].

The packet loss errors can affect different information and they manifest as visual blocking artifacts with block-wise

shapes, of different sizes, textures and colors. In Fig. 3, example of degraded video frame is shown.

In the past and recently, a considerable number of papers have addressed the topic of packet-loss error modeling [5]-[8], detection and monitoring [11]-[20] and its concealment [9], [10] in various video streaming applications such as broadcast [12], mobile [18], [20] and IP [19], [21], [22]. In [7], [17], [18] authors propose a parametric model for quality assessment based on network-level measurements and processed data in the transport stream. Alternatively, another approach for packet-loss video quality monitoring has been investigated in [11]-[15], where solely decoded and error concealed video frames are used for estimating packet-loss error. The latter approach is much more difficult task but is useful in case when only raw video data is available as it is the case for the end-user applications such as mobile devices and TV. Additionally, a hybrid approach where both the encoded and decoded video information is used for packet-loss detection was reported in [16].

The proposed packet-loss measurement algorithm is based on processing the decoded video stream, i.e., only the raw image information, where the packet-loss measure for the VSS is determined as a square root of the weighted square sum of the detected artifacts in each frame separately (PLM_i):

$$PLMS = \sqrt{\sum_i w_i PLM_i} \quad (1)$$

Specifically, only the artifact measures (from each frame separately) that are found to be above a predefined threshold TA are included in the sum. This is regulated by weight factors w_i which values are 1 if PLM is higher than Ta. The algorithm is based on detecting blocking artifacts identifying the significant “sharp” horizontal edges that blocking artifacts consist of. Based on the vertical gradients, sharp horizontal edges (for both luminance and chrominance components), with low gradient activity in the local neighborhood, are determined. The algorithm procedure is divided on three separate sequential computations:

- 1) Gradient Evaluation (GE)
- 2) Gradient Filtering (GF)
- 3) Gradient Grouping and Summations (GGS)

A. Gradient Evaluation (GE)

First step of PLD algorithm is computation of vertical gradients applying the high pass filter with coefficients [-1.1]. The horizontal luminance gradients are computed as $G_{YH}(m,n)=|Y(m,n)-Y(m-1,n)|$, the vertical luminance gradients as $G_{YV}(m,n)=|Y(m,n)-Y(m,n-1)|$ and the chrominance vertical gradients as $G_{CV}(m,n)=(|U(m,n)-U(m,n-1)|+|V(m,n)-V(m,n-1)|)/2$, where Y , U and V refer to the luminance and chrominance components, and m and n are horizontal and vertical coordinates, respectively. The vertical gradients are further used to determine steep (sharp) horizontal edges with accentuated low gradient activity in the local neighborhood perpendicular to the edge direction. Left and/or right side of the edge are observed, based on which two types of sharp

(significant) edges are determined (2): (i) left sharp edge (E_L) and (ii) right sharp edge (E_R);

$$E_L^{(H)} = K_1 G_y(m,n) - K_2 (K_3 G_y(m,n-1) + G_y(m,n-2) + G_y(m,n+1)) \quad (2)$$

$$E_R^{(H)} = K_1 G_y(m,n) - K_2 (K_3 G_y(m,n+1) + G_y(m,n+2) + G_y(m,n-1)) \quad (3)$$

where K_1 , K_2 and K_3 are parameter constants used for fine tuning and G stands for the luminance and chrominance vertical gradients, as previously defined.



Fig. 3. Video frame degraded by packet-loss.

B. Gradient Filtering

After the sharp horizontal edges (corresponding to vertical gradients) are computed for the color and luminance components, it is applied low-pass filtering along the edge direction using 5-tap filter in order to reject spurious edges from further calculation. On both the luminance and chrominance components the following filtering is performed.

C. Gradient Grouping and Summations

After the sharp horizontal edges have been determined for the luminance and chrominance components, they are grouped separately within the overlapping blocks and summed in a particular manner where only the edge filtered (EF) values that are larger than a predefined threshold (T_E) are considered and included in the summation. In case of the color components only the vertical gradients are utilized, sharp horizontal edges, and summed separately for the “left” (SEF_{CHL}) and “right” (SEF_{CHR}) edges. Based on that the final blocking measure from color components for the whole frame is determined as $CM = SEF_{CHL} + SEF_{CHR}$, where the overlapping block is marked as “artifact affected” due to packet-loss if CM is larger than a predefined threshold T_{CHA} .

For the luminance components we perform more complex horizontal gradient and horizontal edge analysis, in order to determine the amount of the degradation since the luminance component carries more important information than the chrominance components. In case of luminance components the overlapping block (size of $B_X \times B_Y$ as 32×24 in our implementation) is divided in B_Y lines and for each line the number of connected horizontal edge pixels related to either “left” or “right” edges is calculated. The existence of the “edge line artifact” is acknowledged if the any of the sum (CN) is larger than a predefined threshold T_{CN} . Based on this, we consider two cases: (i) single artifact lines ($T_{CN} = B_X/2$)

and (ii) paired artifact lines ($TCN=B_x/4$). In case (ii), only the paired lines with vertical gap of 4, 8 and 16 lines are taken into account for artifact calculation since the block wise artifacts are in most cases assumed to be of 4 lines width and the slice and macro-block wise artifacts are assumed to be of either 8, 16 or more lines width.

D. Final measure

The final artifact measure PLM_i , for a video frame i , due to packet-loss is determined as a sum of detected the "artifact affected" overlapping blocks, that come from the color horizontal sharp edges and the luminance horizontal sharp edges (single and multiply paired).

IV. ALGORITHM IMPLEMENTATION WITH SOFTWARE OPTIMIZATIONS AND PARALLELIZATION

In this section it is generally described optimizations and parallelization strategies used in implementation.

Since the target platform is multi-core Intel platform, in the implementation of PLD algorithm the vector instructions from SSE and AVX instruction set are used. Vector instructions are particularly suitable for video processing and image processing, where the on different data are applied the same operation (SIMD - Single Instruction Multiple Data). The new platform features new AVX instruction set, which provides twice as wide operands in the vector instructions in comparison to the SSE instruction set. Therefore, it enables two times higher level of parallelization for floating point arithmetic. AVX instruction set includes only arithmetic operations on vector floating-point types.

A. Vectorization

The AVX instruction set is utilised in a special version of the software solution only in the last stage of processing, which requires the calculation upon floating point values. When calculating vertical gradients (GE block) a vector of 16 pixels with a single-byte values from two successive rows of the both YUV components is loaded. Then, because of possible overflow in calculations of absolute difference of two vectors due to SSE instructions limitations. each vector must be unpacked into two vectors of two-byte pixel values. After subtraction and operation of the absolute values are performed, the two result vectors are obtained that are further packed into one vector with 16 values of the calculated vertical gradient.

By calculating the gradients in one iteration it is produced 16 gradient values for the respective position of the input vectors. The two resulting vectors of 8 short integer words are repacked into a single vector of 16 bytes. Repacking seems as wasteful operations, because in the next step for sharp edges computation type conversion of values is performed. However, a vector of 16 bytes can be loaded in one memory transaction, thereby saving memory bandwidth by favoring execution of multiple instruction instead of multiple memory access. The calculation of sharp edges requires transition from integer arithmetic to floating point arithmetic. At this stage initially calculated gradients has to be converted from "char"

to: "float" type, what causes a change in the organization of data within the vector, as well as reducing the parallelization degree of vector instructions. Hence, from one 16 byte vector four values are obtained and incorporated in parallel for arithmetic operations related to the "sharp" edge calculation. Preparation of vector processing includes unpacking 16 byte vectors and creating vectors of four 32 bit float values.

In computation of sharp edge gradients, for each vector of four from previous phase (4 vectors of floats produced from vector of 16 bytes) is necessary to supply three vectors from adjacent rows in frame with gradient values, in accordance with relations (2) and (3).

Block for filtering the significant sharp edges (GF) is implemented as a one-dimensional convolution using corresponding SSE instructions

Filtered values of characteristic edges are grouped into overlapping blocks of size 32x24 pixels in the final stage of processing (GGS) in which they are further summarized after they are previously compared with the vector of a certain threshold value. Overlapping blocks are moved by 4 elements in the horizontal or vertical directions within video frame with corresponding filtered sharp edge values. Block moving by 4 elements (float values) is particularly suitable because it provides a memory-aligned read of vector within overlapping block that has to be aligned to 16 bytes in case of using SSE instructions. Aligned memory read to the size of vector is much faster than unaligned read, since it spends only one memory access to transfer the entire vector of data at once [27].

To reduce the number of instructions to calculate the partial sums in overlapping block, and save valuable memory bandwidth when overlapping block is moved horizontally or vertically, it is applied re-using of the partial sum values of the neighbouring overlapping block from the previous position.

B. Multi-core Parallelization

Special attention in the process of optimizations and parallelization is taken on work scheduling and work balancing for algorithm processing stages across the processor cores. Parallel processing on multi cores is achieved using OpenMP [28] parallel application programming interface, which is defined as extension for C programming language.

Parallelization to multiple cores is based on the SPMD [29], [30] (Single Program Multiple Data) known methodology that corresponds to data-parallel model of the data domain decomposition paradigm. There are two implemented variants of solutions that use the decomposition of the data in two different domains.

The first method involves the data decomposition in the spatial domain, where the work from all processing stages of algorithm is distributed by geometric data partitioning from one video frame on horizontal parts that is intended to be processed in parallel on each core. The frame is divided vertically in horizontal continuous sections as many as there are processor cores available. The second method involves the data decomposition in the time domain, where consecutive frames from video sequence are assigned to each core for

processing. Number of video frames that are processed at the same time is determined by the number of cores.

By the appropriate OpenMP constructs, static scheduling of work-load distribution among program threads is chosen to minimize the time required for scheduling and invoking program threads that are being executed on associated processor cores. The applied data partitioning in processing provides balanced workload for threads, therefore any possible mutual waiting is avoided. The only interaction between the processing threads is the reduction of private sums that contain number of detected artifacts blocks in each section or group assigned to particular thread in computation. At that point the degradation levels, computed on each core separately, have to be summed to provide the final packet-loss detection measure.

V. EXPERIMENTAL RESULTS

The results for the proposed algorithm for measurement of the visual artifacts due to packet-loss were evaluated on several SD video sequences in progressive and interlace format; a group of interlace sequences considered belong to one packetized transport stream and the sequences in progressive format belong to the other considered transport stream. In the following we first present results concerning the algorithm sensitivities to artifacts and image content, as well as the robustness and accuracy of the proposed quality monitoring and detection system. After that we show the performance results in terms of the processing time per frame achieved by optimizations in context of vectorization with SSE and AVX instruction sets, and multi core parallelization.

A. Metric verification results

In order to test the performance of the proposed packet-loss measurement algorithm, we have first applied it on simulated attenuated signal (as it is the case in transmission), which is an input transport stream (progressive format) degraded (by software means) by 6 levels, where the first degradation level corresponds to non-degraded video sequences. In the second degradation level, in every 100.000 bits one bit was randomly set to zero. Additionally, in degradation level 3, two bits were degraded, in level 4 four bits, in level 5 eight bits and in level 6 sixteen bits were degraded. In order to obtain reliable results, we have made 3 series of the 6 degradation levels, where in each series different set of bits were degraded and thus different video artifacts were introduced to decoded video sequences. After that, the video stream was unpacked and decoded (the pre-trial decoder incorporated drops frozen frames) in order to acquire video content for display and analysis. Within the video stream three video sequences (length of approximately 500 frames) with different spatial and temporal context were considered and processed.

The results were also compared to the state-of-the-art algorithm [12]. In Fig. 4, the performance results for the three video sequences (in progressive format within one transport stream) in three degradation series with the 6 degradation levels are shown. From the figure, one can observe that the proposed PLMS measure is monotonically increasing function

with the packet loss degradation level growth and is relatively robust against different video sequences in different degradation series. Although the results for sequences 3 in Fig. 5 are slightly different from those for the sequences 1 and 2, we argue that the proposed PLMS algorithm shows nevertheless good consistency. Namely, depending on the spatial and temporal context in different video sequences, the packet-loss error can be more or less apparent and more or less successful error concealment can be done within the decoding process. Consequently, small result variations for different sequences are acceptable and in practice inevitable.

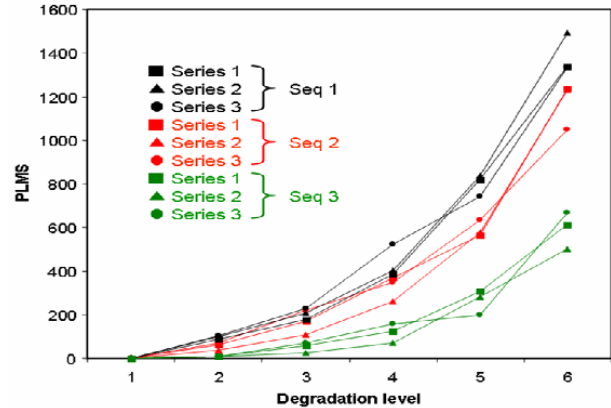


Fig. 4. The PLMS of three different SD video sequences in progressive format with 6 degradation levels and 3 series, where the first degradation level corresponds to the non-degraded video stream.

Additionally, we have compared the results of the proposed PLD algorithm to the algorithm for packet-loss impairment metric (PIM) of [12] (measure for the whole video sequences was also determined in the same manner as for the PLD algorithm), which is presented for one degradation series in Fig. 8. From the figure it is clear that the proposed method is superior in terms of the higher sensitivity to different degradation levels, while the robustness against different sequences is similar.

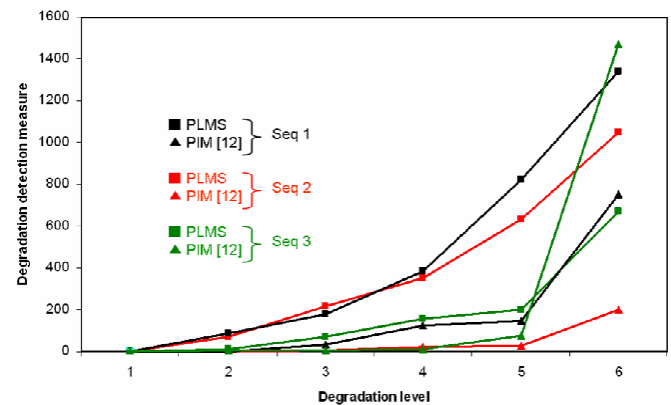


Fig. 5. A comparison between the proposed PLMS algorithm and PIM [12] on three different SD video sequences in progressive format with 6 degradation levels and 1 series, where the first degradation level corresponds to the non-degraded video stream.

B. Processing performance results

Performance results were obtained using standard video sequences SD of resolution 720 x 576 at 25 frames (per second in progressive video, that are randomly corrupted in manner as previously described. All measured performance results are expressed as execution given in milliseconds for processing per video frame. Performance measurements were conducted on last generation Intel i7 2600K with 4 GB of DDR3 RAM operating on 1600 MHz for two different clock processors frequencies.

The results for increased processor clock speeds have been obtained in order to investigate the ultimate limits of the system and get maximum possible performance results.

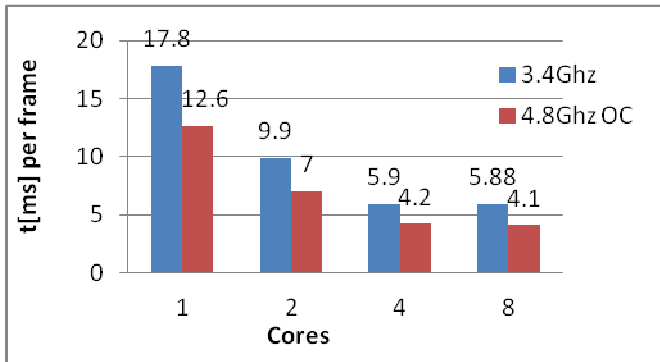


Fig. 6. Parallelization performance results achieved by SSE instruction set and spatial domain decomposition.

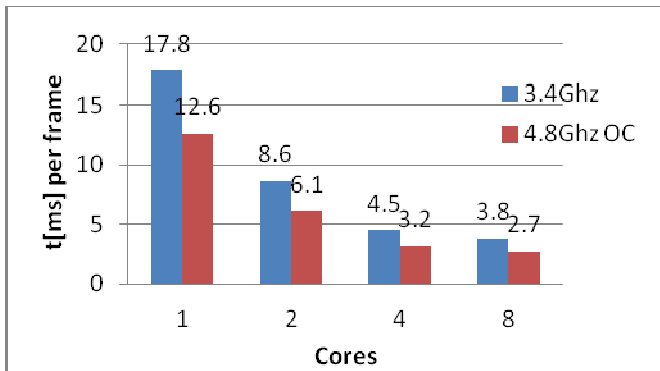


Fig. 7. Parallelization performance results achieved by SSE instruction set and time domain decomposition.

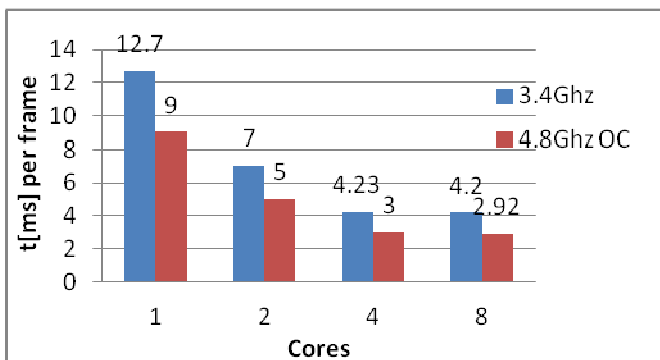


Fig. 8. Parallelization performance results achieved by AVX instruction set and spatial domain decomposition.

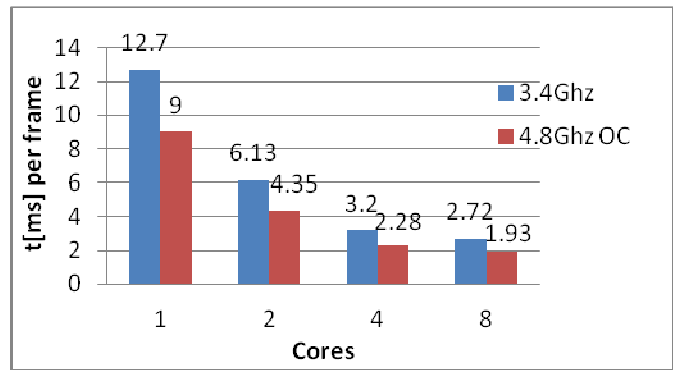


Fig. 9. Parallelization performance results achieved by AVX instruction set and time domain decomposition.

Execution time results of referent version of software solution considered as scalar naive implementation that is executed sequentially on one processor core for clock frequencies 3.4 and 4.8 GHz are respectively 73 and 52 ms per frame.

Important note for the results on 8 cores is that processor contains only four physical cores that can execute two independent stream of instructions from different program threads and expose up to 8 logical cores to applications. This technique is known as Hyper-Threading on Intel platforms. Targeted executions time for real time processing for a video stream with 25 frames per second is 40 ms per frame.

VI. CONCLUSION

In the implementation of the algorithm that is part of a platform for functional testing of DTV systems, video stream processing in real time is achieved on the Intel platform. The biggest limitation that affects the performance scalability on Intel multi-core platforms is the off-chip memory bandwidth that becomes the most precious and most expensive resource in terms of impact on overall performance. Although multi-core platform of the last generation relaxes this limitation through higher memory bandwidth, optimization techniques aimed at the rational use of this resource will likely provide a proportional scaling performance for parallel applications on future architectures with a much larger number of cores. Another important factor for increasing the performance of parallel applications is the efficient use of cache, which allows independent and simultaneous operation executing on processor cores without waiting for data and conflicting for exclusive access to shared memory. Implemented solution with applied optimization and efficient parallelization has processing capability of testing DTV devices with video streams of high definition resolution (HD).

REFERENCES

- [1] N. Teslic, V. Zlokolica, V. Pekovic, T. Tekcan, M. Temerinac, "Packet-Loss Error Detection system for DTV and set-top box functional testing", IEEE Transactions on CE, Volume 56, Issue 3, August 2010.
- [2] O. Verscheure, P. Frossard, and M. Hamdi, "User-oriented QoS analysis in mpeg-2 video delivery," Real-Time Imaging, vol. 5, pp. 305-314, 1999.
- [3] H.-C. Shyu and J.-J. Leou, "Detection and concealment of transmission errors in MPEG-2 images - genetic algorithm approach," IEEE

- Transactions on Circuits and Systems for Video Technology, vol. 9, no. 6, pp. 937–948, September 1999.
- [4] A. R. Reibman, D. Poole, "Characterizing packet loss impairments in compressed video," in International Conference on Image Processing, San Antonio, Texas, USA, 2008, IEEE, vol. 5, pp. 77–88.
 - [5] Y. J. Liang, J. G. Apostolopoulos, B. Girod, "Analysis of Packet Loss for Compressed Video: Effect of Burst Losses and Correlation Between Error Frames," IEEE Transactions on Circuits and Systems for Video Technology, Vol. 18, No. 7, July 2008, pp. 861-874.
 - [6] G. Haßlinger and O. Hohlfeld, "The Gilbert-Elliott Model for Packet Loss in Real Time Services on the Internet," in 14th GI/ITG Conference on Measurement, Modeling, and Evaluation of Computer and Communication Systems, 2008, pp. 269-286.
 - [7] S. Kanumuri, P.C. Cosman, A.R. Reibman, and V.A. Vaishampayan, "Modeling Packet-Loss Visibility in MPEG-2 Video," IEEE Transactions on Multimedia, vol. 8, no. 2, pp. 341–355, April 2006.
 - [8] T. Zhang, U. Jennehag, Y. Xu, "Numerical modeling of transmission errors and video quality of MPEG-2," Signal Processing: *Image Communication* 16, 2001, 817-825.
 - [9] E. Asbun, E. J. Delp, "Real-time Error Concealment in Compressed Digital Video Streams, Picture Coding Symposium, Portland, OR, USA, 1999.
 - [10] S. Kaiser, K. Fazel, "Comparison of error concealment techniques for an MPEG-2 video decoder in terrestrial TV-broadcasting," Signal Processing: *Image Communication*, Vol. 14, 1999, pp. 655-676.
 - [11] R.V. Babu, A. S. Bopardikar, Perkis A., and O. I. Hillestad, "Noreference metrics for video streaming applications," in 14th International Workshop on Packet Video, Irvine, California, USA, December 2004.
 - [12] H. Rui, C. Li, and S. Qiu, "Evaluation of packet loss impairment on streaming video," Journal of Zhejiang University SCIENCE B, vol. 7, pp. 1–7, 2006.
 - [13] N. Montard and P. Bretilon, "Objective quality monitoring issues in digital broadcasting networks," IEEE Transactions on Broadcasting, vol. 51, no. 3, pp. 269–275, September 2005
 - [14] D. Shabtay, N. Raviv, and Y. Moshe, "Video packet loss concealment detection based on image content," in 16th European Signal Processing Conference, August 25-29, 2008., Lausanne, Switzerland.
 - [15] E. P. Ong, S. Wu, M. H. Loke, S. Rahardja, J. Tay, C. K. Tan, L. Huang, "Video quality monitoring of streamed video," in International Conference on Acoustics, Speech and Signal Processing, Taipei, Taiwan, 2009, IEEE, pp.1153-1156.
 - [16] T. Yamada, Y. Miyamoto, M. Serizawa, "No reference video quality estimation based on error concealment effectiveness," 16th International Packet Video Workshop, 2007, Lausanne, Switzerland.
 - [17] R. Reibman, V. A. Vaishampayan, and Y. Sermadevi, "Quality monitoring of video over a packet network," IEEE Transactions on Multimedia, vol. 6, no. 2, pp. 327–334, April 2004.
 - [18] . Gustaffson, G. Heikkila, and M. Pettersson, "Measuring multimedia quality in mobile networks with an objective parametric model," in International Conference on Image Processing, San Diego, USA, 2008, IEEE, vol. 5, pp. 405–408.
 - [19] S. Tao, J. G. Apostolopoulos, R. Guerin, "Real-Time Monitoring of Video Quality in IP Networks", International Workshop on Network and Operating System Support for Digital Audio and Video, Stevenson, Washington, USA, 2005, pp. 129–134.
 - [20] T. Liu, G. Cash, W. Chen, C. Chen, J. Bloom, "Real-time Video Quality Monitoring for Mobile Devices," in Proceedings of the 44th Annual Conference on Information Sciences and Systems, Princeton, USA, 2010.
 - [21] D. Károly, T. Szemethy and Á. Bakay, "System and Signal Monitoring for IPTV Set-Top-Box Systems". Regional Conference on Embedded and Ambient Systems RCEAS'07. November 2007. Budapest, Hungary.
 - [22] M. S. Siddiqui, S. O. Amin, C. S. Hong, "A Set-top Box for End-to-end QoS Management and Home Network Gateway in IMS," IEEE Transactions on Consumer Electronics, Vol. 55, No. 2, May 2009, pp. 527-534.
 - [23] Y.-W. Suh, S.-H. Kim, M.-S. Kim, J.-Y. Choi, J.-S. Seo, "A Novel Integrated Measurement and Analysis System for Digital Broadcasting," IEEE Transactions on Consumer Electronics, Vol. 55, No. 2, May 2009, pp. 56-62.
 - [24] S. D. Servetto, K. Nahrstedt, "Broadcast Quality Video over IP," IEEE Transactions on Multimedia, Vol. 3, No. 1, March 2001.
 - [25] P.-C. Liu, Y.-D. Lin, W. J. Tsai, "Video Quality in Set-Top Box: Improving Test Productivity While Retaining Quality Index," in Proc. International Computer Symposium, Taipei, Taiwan, Vol.3, pp.1185-1189, Dec., 2006.
 - [26] The OpenMP Architectures review Board "OpenMP – The OpenMP API specifications for parallel programming.", Available: <http://www.openmp.org>
 - [27] Shameem Akhter, Jason Roberts: *Multi-Core Programming, Increasing Software Performance through Software Multi-Threading*, Intel Press, 2006.
 - [28] Barbara Chapman, Gabriele Jost, Ruud van der Pas: *Using OpenMP Portable Shared Memory Parallel Programming*, MIT Press Cambridge, 2008.
 - [29] Tymothy G, Mattson, Beverly A. Sanders: *Patterns for Parallel Programming*, Software Patterns Series, 2004.
 - [30] Richard Gerber, *Software Optimization Cook-Book*, Intel Press 2002

Electronic Solution to the QTUD Method for Materials Testing

Zoran Ebersold, Nebojša Mitrović, and Slobodan Đukić

Abstract—The method for defectoscopy of materials that uses separated ultrasonic heads for emitting and reception of signals i.e. ultrasonic transmission defectoscopy has not been much in use in science and engineering until now. This method consists of an ultrasonic head for emitting signal and only a single ultrasonic head for its reception. The method described in this paper is named quadrasonic transmission ultrasound defectoscopy (QTUD). It is an ultrasonic defectoscopy method for materials testing that uses a single ultrasonic head for emitting and four ultrasonic heads for receiving of ultrasonic signal. The advantage of this method is its suitability even with porous materials, all based on relatively low frequencies (about few tens of kHz). Therefore, electronic components are cheaper, so the wide application of this method, both in science and industry is possible.

Index Terms—Defectoscopy, quadrasonic transmission method, ultrasonic transmission defectoscopy.

I. INTRODUCTION

SOUND waves represent propagation of oscillations and can be spread out in solid, liquid and gaseous state [1]. Sound waves are also called ultrasonic waves or ultrasound if their frequency is higher than 20 kHz [2]. This frequency is often cited as the upper limit of the sensitivity range for human hearing. Defectoscopy is a scientific discipline concerned with finding errors i.e. defects in materials. When the ultrasound is used for testing, this method is named as ultrasonic defectoscopy. Samples that are undergoing ultrasound testing do not receive any damage, and therefore this method is listed as a non-destructive material testing method. This method can easily be integrated into technological process of production or as a final stage for control for semi-finished or finished products. Ultrasound defectoscopy is applied primarily in optical opaque materials, materials that strongly absorbs X-rays and in metals where application of electromagnetic signals is not possible due to the “skin effect” [3].

Various methods for the purpose of ultrasound defectoscopy of solid objects have been already developed [4, 5]. Properties of these methods depend on the application and objectives of the

measurement. Propagation time and the intensity of ultrasonic waves are the parameters obtained by ultrasonic defectoscopy. These parameters can be applied in various mathematical algorithms [6, 7] for analyzing the condition of a given sample. Usually, applied technique of ultrasound defectoscopy is based on the same ultrasound head for emitting and reception, where the method uses the impulse echo technique. This is common method in the literature and in industry. The impulse echo method currently represents the main “trend” within the ultrasound defectoscopy [8]. However, the application of this method is under high frequencies (several GHz). This causes a huge absorption of ultrasonic waves in samples. Therefore, application of ultrasonic impulse echo method is not possible on very porous materials.

The procedure discussed in this paper has been neglected and developed as a method for using separate heads for ultrasonic emission and reception. The literature provides data on this method employing one head for emitting ultrasound signal and one single ultrasonic head (i.e. sensor) for receiving. The method with two separate heads is named the “transmission ultrasound method”.

The aim of this study is to present a concept and technical solution developed for the improvement of transmitting ultrasonic method of defectoscopy for materials with one ultrasonic head(for emitting an ultrasound) and four heads (for the reception), i.e. quadrasonic transmission ultrasound defectoscopy (QTUD). It aims to provide a contribution to the development of science and technology, improving a transmission of ultrasonic method in an effective method for defectoscopy of materials, especially for porous materials. The main advantage of the QTUD method over previous ultrasound methods based on impulse echo methodology is the application of much lower frequencies (about a few tens of kHz, for example 45 kHz). Therefore, it can be successfully applied even on the extremely porous samples (for example various sintered polymers, sintered metals and various indirectly and directly laser-sintered materials).

The block diagram shown in the Fig. 1 represents an operating principle of the QTUD assembly. The components shown in the scheme are: function generator, an ultrasonic transmitter S1, ultrasonic sensors as receivers P1, P2, P3 and P4, adapters A1, A2, A3 and A4 as signal pre-amplifiers, four-channel analogue to digital (A/D) converters and a computer for digital signal processing with appropriate software. For

A part of the findings shown in this work is presented on the 55th ETRAN Conference, Banja Vrućica, Teslić, BIH, 6-9. June 2011.

Z. Ebersold is with the University of Applied Sciences, Augsburg, Germany, (e-mail: zoran.ebersold@hs-augsburg.de)

N. Mitrović and S. Đukić are with the University of Kragujevac, Technical Faculty, Čačak, Serbia (e-mail: nmitrov@tfc.kg.ac.rs, sdjukic@tfc.kg.ac.rs).

signal control during measurement an oscilloscope and frequency meter were used.

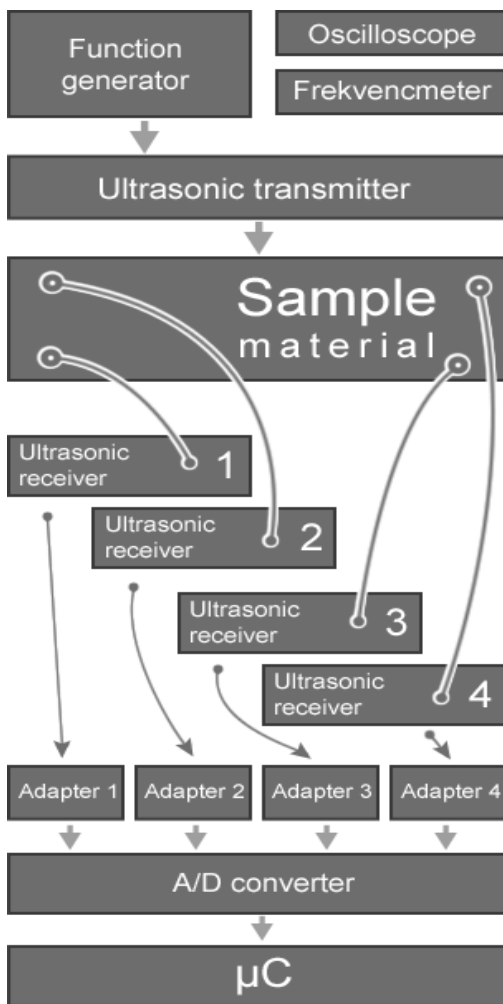


Fig. 1. Block scheme of the QTUD method.

II. METHODOLOGY

The sample material is mounted on the holder which keeps the sample stable i.e. the ultrasonic transmitter (S1) and four ultrasonic sensors (P1, P2, P3 and P4) can be positioned so as to ensure confidential contact with the sample. Fig. 2 shows part of the apparatus of the QTUD method, i.e. insert (a) shows the location of transmitter (S1), insert (b) shows the position of four ultrasonic sensors (P1, P2, P3 and P4) mounted on the sample material. Fig. 3 shows three-dimensional positions of all ultrasonic heads on the sample material. Point marked as S1, with coordinates (x_s, y_s, z_s) stands for the position of ultrasound head (transmitter) on the surface of the sample material provided at the bottom of the sample. Points marked as P1, P2, P3 and P4, have coordinates:

- P1 (x_1, y_1, z_1) ,
- P2 (x_2, y_2, z_2) ,
- P3 (x_3, y_3, z_3) ,
- P4 (x_4, y_4, z_4)

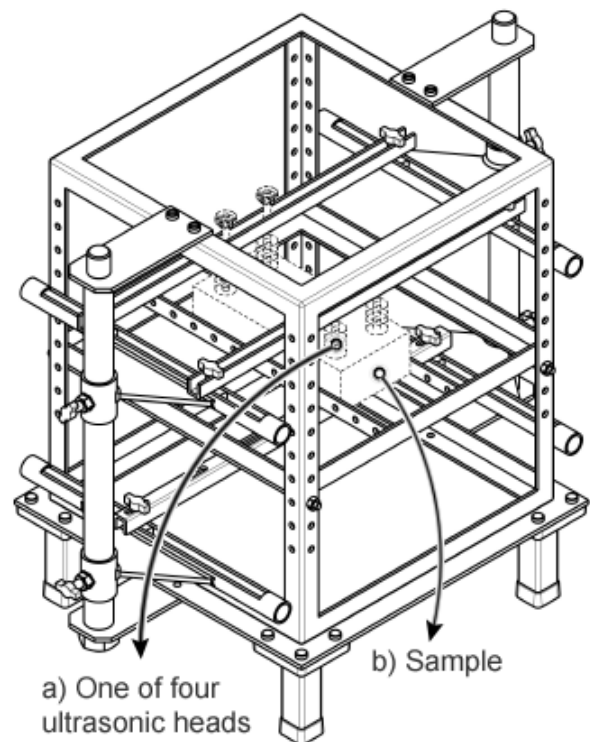
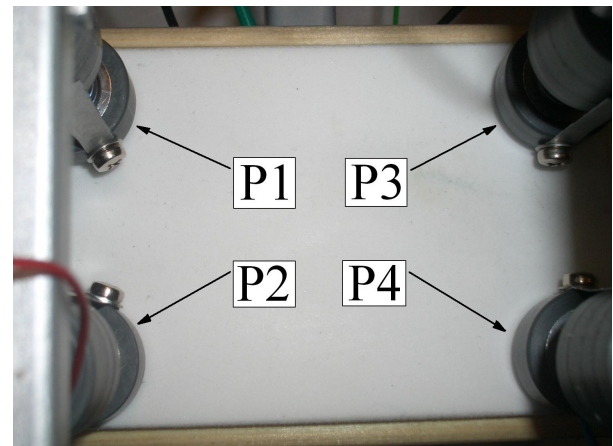
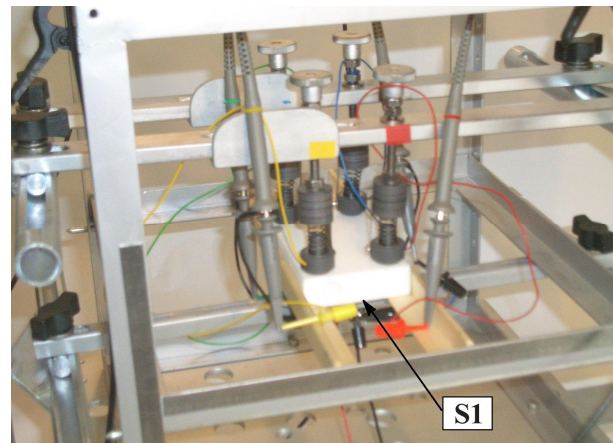


Fig. 2. Apparatus for the QTUD method.

as the positions of contact ultrasonic heads (which are ultrasound receivers) on the surface of the sample material. These positions are on the opposite, upper side of the sample material. The distance from coordinate zero value of xyz system to the point S1 is seen as a vector in three dimensions. It is analogue with the distances to the origin points P1, P2, P3 and P4. Fig. 3 presents the relationship among the vectors \vec{r}_1 , \vec{P}_1 and \vec{S}_1 . As it is situation for vector \vec{r}_1 we have similar relations for vectors \vec{r}_2 , \vec{r}_3 and \vec{r}_4 :

$$\vec{r}_2 = \vec{P}_2 - \vec{S}_1$$

$$\vec{r}_3 = \vec{P}_3 - \vec{S}_1$$

$$\vec{r}_4 = \vec{P}_4 - \vec{S}_1$$

Given these coordinates and using mathematical algorithms that can be applied for the purpose of analyzing the signal, the conclusions about the state within the sample material can be made. These conclusions can be derived on the basis of delay time of ultrasonic waves as well as on the differences in the amplitudes received by the ultrasonic receiver heads.

The ultrasound head S1 (transmitter), emits ultrasonic wave that passes through the sample. If the receiving ultrasound heads P1, P2, P3 and P4 are placed symmetrically in relation to the transmitter S1 and if it is assumed that the structure of the tested sample does not contain any material defect, the ultrasonic waves emitted from S1 arrive in the same time at any of the receiving heads P1, P2, P3 and P4. Furthermore, the signals received by P1, P2, P3 and P4 have the same amplitude. This is of particular importance for the employed experimental circuit.

In the case when an investigated sample contains material defect, the largest delay of ultrasonic signals will be at the ultrasonic head closest to the defect. The value of this delay is proportional to the speed of ultrasound through the material from which the sample was made.

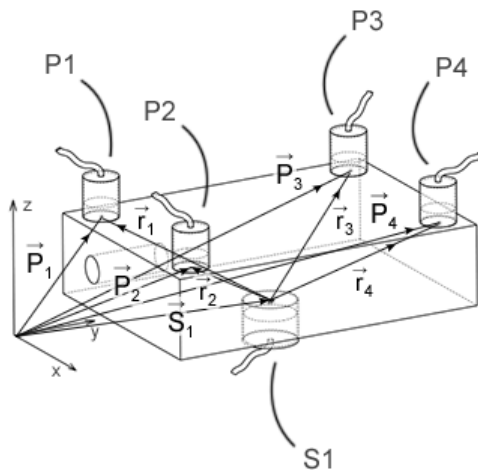


Fig. 3. Relationships for vectors \vec{S}_1 , \vec{r}_1 , \vec{r}_2 , \vec{r}_3 , \vec{r}_4 , \vec{P}_1 , \vec{P}_2 , \vec{P}_3 , \vec{P}_4 .

For a given material it is a physical constant that must be already known in order to be able to perform a calculation. The ability of the system to provide sufficient precision and register the delay of ultrasound signals substantially depends on the resolution of analog digital converters used. It should be noted that the high-quality A/D converters with high resolution are a significant investment.

In the case when a sample contains a material defect, the attenuation of ultrasonic signal amplitude is strongest in the ultrasonic head closest to the defect. This amplitude is really smaller than other amplitudes and it can be registered by relatively simple and cheap A/D converters.

The method presented here, offers a possibility of using both principles, i.e. signal delay and amplitude attenuation. Based on the above said, the conclusion can be made about defect existence within the investigated sample.

III. ELECTRONIC DESIGN

Fig. 4 shows the electronic design scheme. It includes the following components: function generator G1, ultrasonic emitter S1, ultrasonic sensors as receivers P1, P2, P3 and P4. There are also preamplifiers of the signal N1, N2, N3 and N4 as well as analogue digital (A/D) converters B1, B2, B3 and B4. Additionally, there are some instruments for electronic control: oscilloscope A1 and frequency meter A2. The electronic design of QTUD methods contains four electronic measurement channels consisting of incentives from the physical processes in the form of transmission of ultrasonic signal, the sensor, adapter and A/D converter. At the end of these measuring channels is the computer which performs further signal processing. Connections between the displayed electronic devices and the computer are presented as d1, d2, d3 and d4.

The function generator G1, powered by the 220V/50 Hz (voltage u_p), generates a signal frequency of 45 kHz (voltage u_s). This signals u_s is fed to the ultrasonic transmitter S1, which is an ultrasonic head with the voltage-controlled crystal. The ultrasound signal transmitter and reception sensors are piezoelectric devices made of lead zirconium titanate (PbZrTiO).

Ultrasound was transmitted through the sample material and was received more or less attenuated, i.e. more or less delayed in receiving ultrasonic sensors P1, P2, P3 and P4. Over piezoelectric effect these receivers convert mechanical vibrations into analog electrical voltages. Voltages from the receivers P1, P2, P3 and P4 are brought to preamplifiers of the signal N1, N2, N3 and N4, and subsequently to A/D converters B1, B2, B3 and B4.

By analyzing delay times of individual signals, or respectively differences in amplitudes of individual signals and using the appropriate mathematical algorithm, the state of examined samples i.e. the existence of defects in the material can be foreseen.

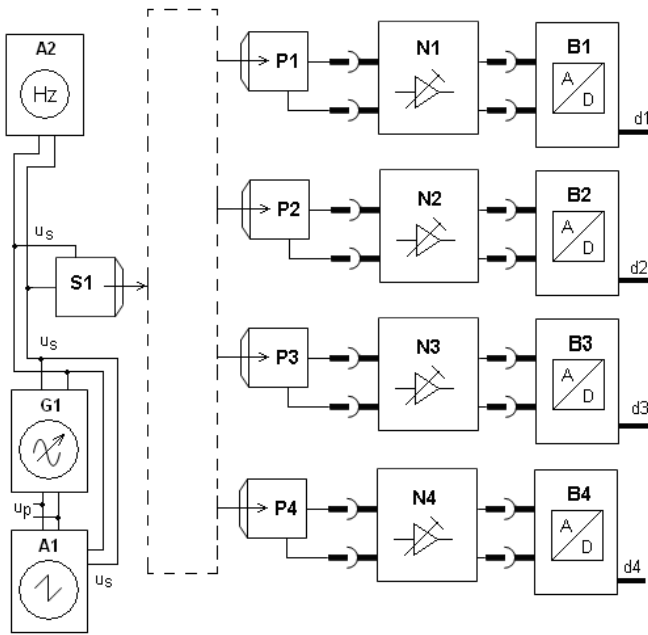


Fig. 4. Electronic design of QTUD method.

IV. COORDINATES DETERMINATION SYSTEM

Coordinates determination system is a sub-system inside experimental set, comprising the following electronic components: transmitters of infrared signals E11, E21, E31, E41 and E51; receivers of infrared signals E12, E21, E32, E42 and E52 along with signal handlers E13, E23, E33, E43 and E53.

Components E51, E52 and E53 are used in case when ultrasonic head S1 (the transmitter of ultrasonic signal provide at the bottom of the sample) can be moved, i.e. spatial position of S1 can be changed. During the experiment, head S1 is firmly fixed. It can be assumed that spatial coordinates are already known and constant.

Fig. 5 shows a block scheme of the coordinates determining system consisting of distributor A3 for powering the transmitters E11, E21, E31, E41 and E51 by voltage u_3 . These transmitters emit infrared signals by photo cells so that the photo transistors inside the receivers E12, E22, E32, E42 and E52 react on precisely directed infrared signal. The signal handlers E13, E23, E33, E43 and E53 generate individual voltages u_{12} , u_{22} , u_{32} , u_{42} and u_{52} . These voltages turn on signal handling photo diodes D15, D25, D35, D45 and D55. Specified voltages generated by the signal handlers are grounded over the A4 module, inside which the signal handling photo diodes are placed. This A4 module is used as distributor of voltage u_3 for the signal handlers. Receivers of infrared signals are mounted on mechanical rails so they can be moved on the outer part of the mechanical experimental set. After the sample material is placed and fixed and the ultrasonic heads are mounted, every individual receiver of infrared light (E12, E22, E32, and E42) is moved along the

rails, until individual signaling photo diodes (D15, D25, D35, and D45) are lit up and the position taken.

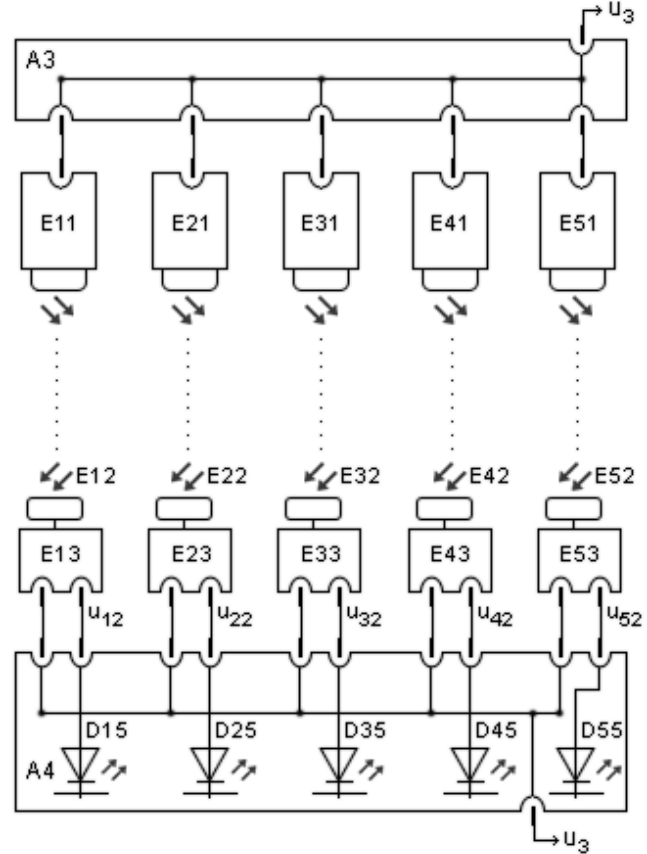


Fig. 5. Block scheme of system for determining coordinates.

Fig. 6 shows electric circuit of the transmitter E11, where the output degree presents the diode D12 which, when directly polarized, emits infrared light. To ensure proper functioning of the diode D12 it is necessary to provide dc constant current, where the purpose of T11 transistor comes in. To provide dc current constant through the output diode, it is necessary to keep T11 at an optimal operating point. For that purpose we use diodes D13 and D14 which maintain constant base voltage of 1.2 V. Diode D11 sends a signal that indicates that transmitter E11 is operational. Fig. 6 shows a circuit for the created receiver of infrared light E12 and E13. Input stage is photo-resistor F0 whose electrical resistance decreases from 10 M Ω to 3 M Ω when illuminated.

Following the changes of resistance of diode D11 there is also a change in relationship between input voltages of operational amplifier LM741 i.e. V_{op} , where the value going under the value of the V_{op+} , and in that case voltage from V_{iz} increase from 1.2V to around 9V (close to the u_3 voltage). This switches on the output transistor T1 which powers LED diode D15 over module A4. Led diode D15 notifies that the optical connection between receiver and transmitter of infra red signal is established and indicates that the read-out position of individual receiver can be performed. This creates an easy and accurate procedure of determining the coordinates of ultrasonic receiver sensors.

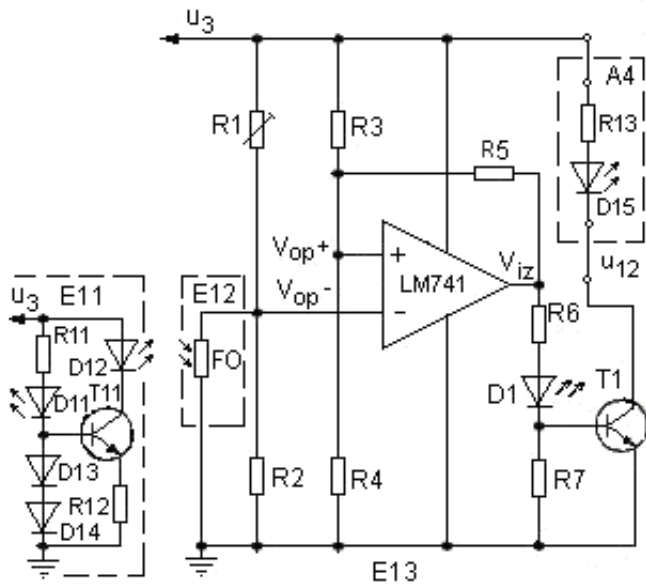


Fig. 6. Circuits of transmitter E11 and receiver E12/E13.

V. RESULTS

In the experimental procedure the investigated sample contains embedded defect. The measurement was conducted over a sample made of a piece of "PORPOLAST" plate [9]. It is made of sintered polyethylene with a few additives, for various industrial fluidizing floors and filter applications. These plates are manufactured in different thicknesses and formats to be further processed to disks, or weld constructions, and they are highly porous material. This sample is shown in Fig. 7 (high $H = 19.8$ mm, width $W = 66$ mm, length $L = 104$ mm). The built-in defect is located near the ultrasonic head P1, in the form of hole (cal1) with a diameter of 11.5 mm and depth of 46 mm. During the performed measurement, the variant of recording attenuation of amplitude of ultrasonic signal was chosen. The attenuation of the received amplitude is largest in the ultrasound receiver that is closest to the defect. For these performed experiments instead of the A/D converters B1, B2, B3 and B4 and computer (see Fig. 1 and Fig. 4), digital signals are measured with a digital oscilloscope Owon PDS 5022S. Results of the measurement with digital oscilloscope are shown in Fig. 8.

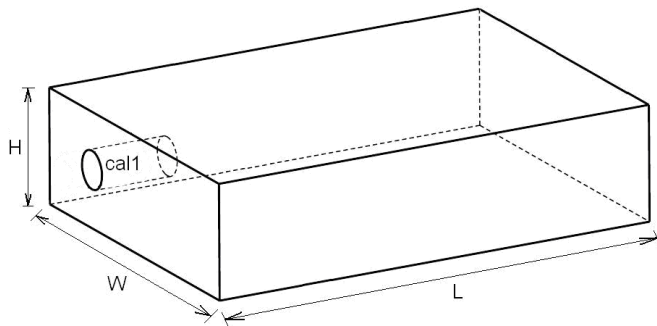


Fig. 7. Sketch of the sample used for the measurement.

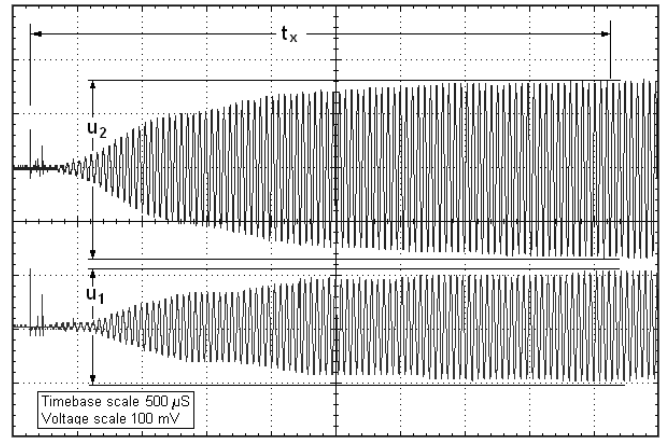


Fig. 8. Results of the measurement from the digital oscilloscope.

The upper part of the diagram corresponds to the recorded signal from the ultrasonic receiving head P2, whereas the bottom part of the diagram shows recorded signal of head P1. Voltage levels of u_1 and u_2 represent the particular maximums of the received amplitudes. Voltage u_1 in this case is 330 mV peak-to-peak while voltage u_2 is 200 mV. Recognition of persistently received amplitude is not automated. For this reason issue with automation the dimensions are graphically marked in the diagram.

Fig. 8 shows time t_x , which stands for the distance between voltages u_1 and u_2 on the horizontal time axis. This distance is characterized by time after which it comes to persisting voltages of receiving heads and when loading of values for those voltages for further calculations can be executed. After time t_x , a signal with permanently lower amplitude can be observed at the receiving head P1 (located above the defect).

In order to obtain a series of measured values, further measurements using the pattern above can be repeated with the same dimensions of samples but with difference in the radius and depth of built-in defect. Then, groups of obtained data will enable the formation of tables that provide information about the existence of defects within the sample. As a next step, the samples with actual defects (occurring as a result of an error within the production cycle) can be performed.

VI. CONCLUSION

Ultrasonic defectoscopy is a scientific discipline that deals with finding errors i.e. defects in materials, especially in optically opaque materials that strongly absorb X-rays or in metals in which application of electromagnetic signals due to the skin effect is not possible. A method that uses ultrasonic pulse echo technique, which includes only a single head used for emitting and reception of ultrasonic waves, used to be preferred in engineering and science. The impulse echo method currently represents the main "trend" within the ultrasound defectoscopy, but application of this method with

high frequencies (order of several GHz) causes excessive absorption of ultrasonic waves within sample. Therefore, on very porous materials defectoscopy by ultrasonic impulse echo method is not possible. The procedure presented in this paper represents a further development of a method with separate ultrasound heads for emitting and reception of ultrasonic waves. The QTUD method comprises a single head as a transmitter of ultrasound signal and four ultrasonic sensors as the receivers of ultrasound.

Electronic solution contains function generator, one ultrasonic emitter, and four ultrasonic sensors as receptors, and components for signal amplification, analogue digital converters and a microcontroller unit or optionally a computer for processing digital signals. If the investigated sample contains material defect, the largest delay of ultrasonic signals will be at the ultrasonic head closest to the defect. Also, the attenuation of ultrasonic signal amplitude is the strongest in the ultrasonic head closest to the defect. The observed amplitude is substantially lower than other amplitudes and registration can be performed by relatively simple and cheap A/D converters. The presented method enables using both principles: signal delay and amplitude attenuation.

Therefore, the conclusion can be made about defects in the

sample. In the experimental procedure, the measurement was conducted on a sample made from sintered polyethylene plate which is a highly porous material. For the QTUD method, the application for European patent in the Central German Patent Office was made in October 2010 [10].

REFERENCES

- [1] G. Sorge, *Faszination Ultraschall*, Stuttgart: Teubner Verlag, 2002.
- [2] E. Schrüfer, *Elektrische Meßtechnik: Messung elektrischer und nichtelektrischer Größen*, Leipzig: Hanser Fachbuchverlag, 2007.
- [3] H. Kuttruff, *Physik und Technik des Ultraschalls*, Stuttgart: S. Hirtzel Verlag, 1988.
- [4] C. Cooke, *An Introduction to Experimental Physics*, Florida: CRC Press, 1996.
- [5] G. Simpson, J. Blitz, *Ultrasonic Methods of Non destructive Testing*, Dordrecht: Springer, 1996.
- [6] C. Weissmantel, C. Hamann, *Grundlagen der Festkörperphysik* Berlin: Springer Verlag, 1997.
- [7] K. Jänich, *Vektoranalysis*, Berlin: Springer, 2008.
- [8] J. Gobrecht, *Werkstofftechnik - Metalle*, München, Oldenbourg Wissenschaftsverlag, 2006.
- [9] Durst Filtertechnik GmbH, D-74354 Besigheim-Ottmarsheim, Germany.
- [10] Deutsches Patent- und Markenamt (DPMA) ("German patent office"), München.

Using Easy Java Simulations in Computer Supported Control Engineering Education

Milica B. Naumović, Nataša Popović, and Božidar Popović

Abstract—This paper presents the software tool Easy Java Simulations (EJS) designed to build the interactive applications in Java. It has been created to be used by students, professors and scientists without special programming skills, and it is particularly suitable for use in engineering education. The problem known in optimal control theory as brachistochrone problem is considered confirming the ability of EJS tool to build networked solutions with high degree of interactivity and visualization.

Index Terms—Control engineering education, distance learning, optimal control, simulation.

I. INTRODUCTION

THE rapid development of information and communication technologies allowed the educational process to become independent of time and space. This facilitated the introduction of distance learning in regular curriculum and simplified educational process both for teachers and students.

Interactive scientific simulations play important role in control systems education. They help students to understand the behavior of system or phenomenon under study in an appropriate way. Virtual and remote laboratories help them even more, since students can perform their laboratory work from any place at any time. Simulations, virtual and remote laboratories intended to be used in distant learning courses are located on the university servers. Distant users access them via Internet using their PCs or mobile devices and perform lab work through on-line experimentation services. This flexible education paradigm is shown in Fig. 1.

Sophisticated interactive simulations are usually created in Java programming language. Development of such simulations

This paper was supported in part by project Grant III44004 (2011-2014) financed by Ministry of Education and Science, Republic of Serbia. Some results of this paper were presented at 55th ETRAN Conference, Banja Vrućica, June 6-9, 2011.

Milica B. Naumović is with the Faculty of Electronic Engineering, University of Niš, Aleksandra Medvedeva 14, 18000 Niš, Serbia (phone: +381 18 529 441; fax: +381 18 588 399 ; e-mail: milica.naumovic@elfak.ni.ac.rs).

Nataša Popović is with the Faculty of Electrical Engineering, University of East Sarajevo, East Sarajevo, Bosnia and Herzegovina (e-mail: natasa.popovic@etf.unssa.rs.ba).

Božidar Popović is with the Faculty of Electrical Engineering, University of East Sarajevo, East Sarajevo, Bosnia and Herzegovina (e-mail: bozidar.popovic@etf.unssa.rs.ba).

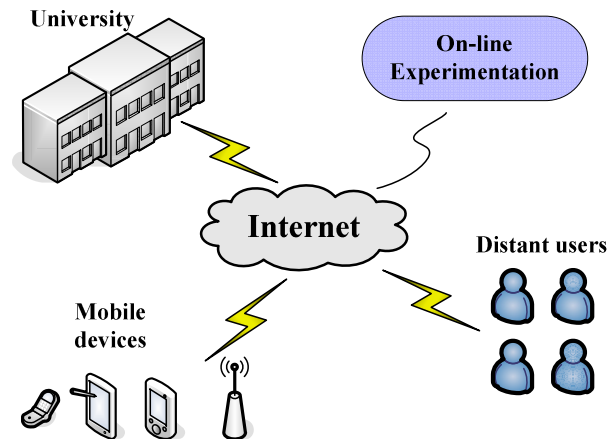


Fig. 1. Scheme of the flexible education paradigm.

demands a lot of time and advanced programming skills. This means that in general only professional programmers can develop them. Scientists, professors and students, who were not professional programmers, were unable to develop them, although they had all necessary theoretical knowledge and understanding of system or phenomenon to be simulated. A group of scientists recognized this as a problem, and started to work on a software tool that would meet the requirements of non-professional programmers in developing useful and effective interactive simulations. This resulted in new software tool based on Java that was, because of its simplicity and ease in use, symbolically called Easy Java Simulations (EJS).

Useful interactive simulations, in the form of remote and virtual labs can be created with Easy Java Simulations [1]-[5] in almost every scientific field. The numerous examples of such simulations can be found in [1], [2]. Particularly interesting was to investigate the possibility to use EJS in optimal control theory to demonstrate the famous brachistochrone problem [6]-[8], and its solution. The results of this investigation are presented further.

The layout of the paper is as follows: in Section II we give a brief review of the brachistochrone problem solution that is one of the earliest applications of the calculus of variations; Section III addresses to Easy Java Simulations, as a modeling tool for rapid creation of simulations in Java. A concrete implementation related to the analysis of movement along the

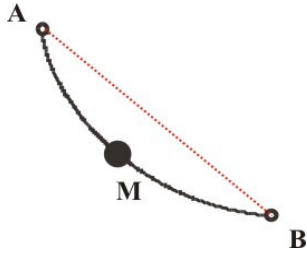


Fig. 2. The Brachistochrone Problem (Acta Eruditorum, June 1696, p. 269).

cycloid is illustrated in Section IV. Finally some conclusions of the work are presented.

II. THE BRACHISTOCHRONE PROBLEM

A. A Problem Formulation and Solution Elements

The brachistochrone problem is one of the oldest problems that in fact initiated efforts towards calculus of variations [6].

Namely, in the June 1696 issue of Acta Eruditorum, Johann Bernoulli posed Invitation to all mathematicians to solve a new problem, which can be simply stated as follows [7]:

If in a vertical plane two points A and B are given, then it is required to specify the orbit AMB of the movable point M, along which it, starting from A with zero speed, and under the influence of its own weight, arrives at B in the shortest possible time.

Set the coordinate system as in Fig. 3. Let us note at some point the position of the particle M with mass m . Its kinetic and potential energy are respectively given by $mg(H - y)$ and $mv^2/2$, and, according to the conservation of energy, their sum is constant, i.e.

$$mg(H - y) + \frac{mv^2}{2} = K. \quad (1)$$

At the beginning, let the material point move without the initial speed ($y = 0$ and $v = 0$), and so $mgH = K$. In this way we get

$$v^2 = 2gy. \quad (2)$$

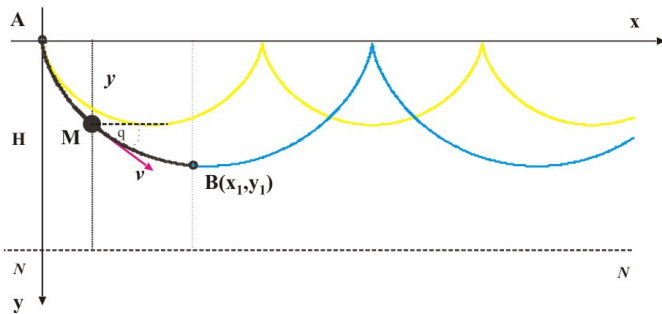


Fig. 3. Geometric interpretation of the brachistochrone problem.

Since $v = \frac{ds}{dt}$ and $\left(\frac{ds}{dx}\right)^2 = \left(\frac{dy}{dx}\right)^2 + 1$, it follows

$$dt = \frac{ds}{\sqrt{2gy}} = \frac{\sqrt{1+y'^2}}{\sqrt{2gy}} dx, \quad (3)$$

where

$$y' \stackrel{\text{def}}{=} \frac{dy}{dx}. \quad (4)$$

The total duration of the movement from A to B to be minimized is then given by

$$T = \frac{1}{\sqrt{2g}} \int_0^{x_1} \sqrt{\frac{1+y'^2}{y}} dx. \quad (5)$$

B. The Variational Calculus – The Necessary Conditions for Minimum

We consider the problem of selecting a continuously differentiable function $x(t) \in \mathfrak{X}$ with respect to the set of all real-valued, continuously differentiable functions, in order to minimize the cost function

$$J(x) = \int_{t_0}^{t_f} \Phi[x(t), \dot{x}(t), t] dt \quad (6)$$

on the interval $[t_0, t_f]$. Therefore, it is necessary to determine the optimal trajectory $\hat{x}(t)$ from the set of all admissible trajectories $x(t)$. It is assumed that the function Φ is continuous in x, \dot{x} , and t , as well as has continuous partial derivatives with respect to x and \dot{x} [6]. Recall that the cost function given in (6) is known as the LAGRANGE form. An admissible, but not necessarily optimal trajectory $x(t)$ for all $t \in [t_0, t_f]$ can be expressed as

$$x(t) = \hat{x}(t) + \varepsilon \eta(t), \quad (7)$$

where ε is a small number, and $\eta(t)$ is a variation in $x(t)$. Applying the theory of the variational calculus the necessary conditions can be developed [6]:

$$\frac{\partial \Phi}{\partial x} - \frac{d}{dt} \frac{\partial \Phi}{\partial \dot{x}} = 0, \quad (8)$$

and

$$\frac{\partial \Phi}{\partial \dot{x}} \eta(t) = 0, \quad \text{for } t = t_0, t_f. \quad (9)$$

The partial differential equation (8) is commonly known as the EULER-LAGRANGE (\mathcal{E} - \mathcal{L}) equation, while the associated transversality conditions are given by (9). By this equations a

two-point boundary value differential equation is specified which, when solved, determines a candidate for an optimal trajectory in terms of a known Φ .

Some particular cases of $\mathcal{E}\text{-}L$ are:

① Suppose that the EULER function $\Phi[x(t), \dot{x}(t), t]$ is independent of the variable x (in dynamics this variable is called an ignorable coordinate). Then, $\mathcal{E}\text{-}L$ results in

$$\frac{d}{dt} \frac{\partial \Phi}{\partial \dot{x}} = 0 \Rightarrow \frac{\partial \Phi}{\partial \dot{x}} = \text{const.}, \quad (10)$$

which is the principle of conservation of conjugate momentum in dynamics.

② Suppose we consider a time invariant system and the EULER function $\Phi[x(t), \dot{x}(t), t]$ is independent of the time t .

Then we write:

$$\frac{\partial \Phi}{\partial x} - \frac{d}{dt} \frac{\partial \Phi}{\partial \dot{x}} = \frac{\partial \Phi}{\partial x} - \frac{\partial^2 \Phi}{\partial x \partial \dot{x}} \dot{x} - \frac{\partial^2 \Phi}{\partial \dot{x}^2} \ddot{x} = 0, \quad (11)$$

or

$$\dot{x} \frac{\partial \Phi}{\partial x} - \frac{\partial^2 \Phi}{\partial x \partial \dot{x}} \dot{x}^2 - \frac{\partial^2 \Phi}{\partial \dot{x}^2} \ddot{x} = \frac{d}{dt} \left[\Phi - \dot{x} \frac{\partial \Phi}{\partial \dot{x}} \right] = 0. \quad (12)$$

This means that

$$\Phi - \dot{x} \frac{\partial \Phi}{\partial \dot{x}} = \text{const.}, \quad (13)$$

which is referred to as the conservation of the Hamiltonian. It is in the literature known as the Beltrami identity.

③ If $\Phi[x(t), \dot{x}(t), t]$ is independent of \dot{x} , then EULER-LAGRANGE equation becomes simply

$$\frac{\partial \Phi}{\partial x} = 0. \quad (14)$$

C. The Solution of the Brachistochrone Problem

In space-relative terms as in solving the brachistochrone problem (5), we have the EULER-LAGRANGE condition

$$\frac{\partial \Phi}{\partial y} - \frac{d}{dx} \frac{\partial \Phi}{\partial y'} = 0. \quad (15)$$

Since the Lagrangian $\Phi[y, y', x] = \sqrt{(1+y'^2)}/y$ in (5) is particularly nice since x does not appear explicitly. Therefore, $\partial \Phi / \partial x = 0$, and we can immediately use the Beltrami identity

$$\Phi - y' \frac{\partial \Phi}{\partial y'} = C, \quad (16)$$

which yields

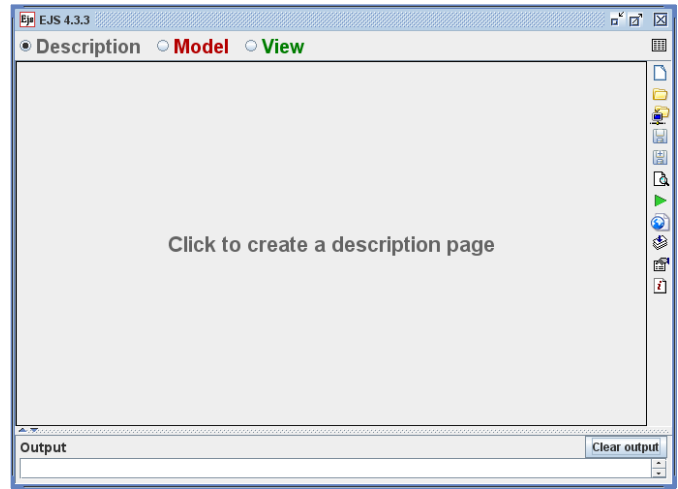


Fig. 4. EJS structure.

$$\frac{1}{\sqrt{2gy}\sqrt{1+y'^2}} = C. \quad (17)$$

After squaring both sides and rearranging we can compute

$$\left[1 + \left(\frac{dy}{dx} \right)^2 \right] y = k^2, \quad (18)$$

where the square of the old constant C has been expressed in terms of a new positive constant $k^2 (= 1/2gC^2)$. The equation (18) can easily be solved by the parametric equations

$$\begin{aligned} x &= \frac{1}{2}k^2(\theta - \sin \theta) \\ y &= \frac{1}{2}k^2(1 - \cos \theta) \end{aligned} \quad (19)$$

III. EASY JAVA SIMULATIONS FUNDAMENTALS

Easy Java Simulations is a freeware, open-source tool developed in Java, specifically designed for the creation of interactive dynamic simulations [1]. EJS was developed for the Open Source Physics Project [2], which was established to create and distribute curricular material for physics computation. As a free software tool, EJS is not only used in creating interactive simulations, but also to create virtual and remote laboratories [1], [2]. A very important feature of EJS for the control systems education is its possibility to use Matlab and LabView as external applications. This actually, enabled EJS to be used in remote laboratories development.

EJS architecture is based on the model-view-control paradigm [4]. It means that interactive simulations must consist of the following parts:

- system or phenomenon description using variables and relations among them,
- graphical representation of the system or phenomenon states,

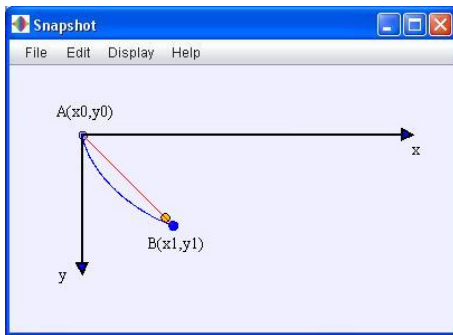


Fig. 5. Snapshot of the first cycloid simulation cycle.

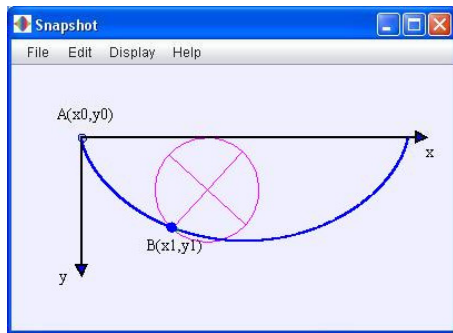


Fig. 6. Snapshot of the second cycloid simulation cycle.

- the specifications of the user's actions to perform on the simulation

Following the model-view-control paradigm, simulations in EJS are structured in two main parts: the Model and the View [3]-[5] (see Fig. 4). Additionally, there is a part named Description which contains the theoretical introduction of simulated system and gives students instructions how to use the simulation. The Model describes the behavior of the system or phenomenon under study using pages with variables, ordinary differential equations, and Java code. The View

Name	Initial value	Type	Dimension
xmin	0	double	
xmax	200	double	
ymin	0	double	
ymax	200	double	
dt	0.02	double	
vel	8	double	
pi	Math.PI	double	
bt	10000	int	
g	9.81	double	
		double	

Fig. 7. EJS Model part.

provides the visualization of the simulation and graphical elements for user interaction. Model and View are interconnected so that any change made in the Model automatically reflects on the View and, vice versa, any user interaction with the simulation automatically modifies the value of responding model variable.

The Model of the system is created by defining the set of variables that describe the system state and specifying the equations that determine how this state changes with time [5]. Ordinary differential equations are written in EJS ODE editor in a way similar when writing them on a paper. If necessary, additional Java code can be written in order to show, more faithfully, system behavior during simulation execution. Besides that, some user defined classes, methods and actions can be realized writing this additional Java code, especially when the simulated system or phenomenon is complex. The View is created using a built-in library of ready-to-use graphical elements. These elements have the properties which values can be modified to customize the elements' behavior and visual display. In this way it is possible to connect properties of the view's graphical elements with model variables. Graphical elements properties also provide the possibility of evoking user defined actions when user interacts with the simulation.

When both the Model of the system and the View are defined, EJS generates the simulation Java source code, compiles it, packages it into a .jar file, and runs it as an independent process. The simulation can also be generated as an applet, so that the simulation execution can be controlled from the web browser [5].

IV. CYCLOID VIRTUAL LAB

A. Building the virtual lab

The cycloid simulation is designed to encompass two cycles.

The first cycle shows moving of two particles from point A to point B of which the orange one is moving along the straight red line and the blue one along the unknown path. It can be seen that the blue particle reaches point B before the orange one, moving along a curve, Fig. 5.

The second cycle shows the rolling of a circle along the x-axis together with the blue particle fixed on it, Fig. 6. This cycle proves that the curve obtained by moving the blue particle in the first cycle is a cycloid. The building of the virtual lab in EJS implies the definition of both the Model and the View.

Defining the Model

The first step in building the simulation is defining the Model as it is given in Fig. 7. Although the Model part of EJS consists of six sections only four of them were used to develop cycloid simulation.

The most important task in defining the Model is to choose model variables in an appropriate way. This means that

variables have to be chosen to be easily used to describe particles moving, to obtain clear visual display, and to provide simple user interaction. In the Variable section general variables, variables for the blue particle moving, variables for orange particle moving and variables for simulation visualization are defined. Variables that describe size and ratio of all graphical elements necessary for simulation, constants π and g (gravitational acceleration), and number of cycloid points are defined in general variables tab. Variables to define moving of blue particle and circle, and orange particle are defined in two separate tabs and some of them are: blue particle moving period, blue particle acceleration, circle radius, circle center coordinates, kinetic, potential and total energy. The last tab contains variables which determine what graphical elements are to be displayed in a particular simulation cycle, and whether the energy plots are to be visible or not.

The Initialization section contains simulation initial conditions, and the Evolution section contains ordinary differential equations which describe moving of both particles. A simple Java code to control simulation execution is written in the Fixed relations section as well as relations necessary for computation of kinetic, potential and total energy. This Java code determines the duration of simulation cycles and whether the simulation is to be paused or reset. The simulation is paused when the first cycle terminates, and is reset when the second cycle terminates.

Defining the View

Visual display of simulation is necessary for controlling the simulation execution. It provides simulation visualization and user interaction.

The View part of cycloid simulation is divided in drawing frame and plotting panel, Fig. 8. Drawing frame consists of drawing panel and buttons panel. Drawing panel contains all view elements necessary for simulation visualization (particles shape, arrows for x -axis and y -axis, text, trace for obtaining cycloid, analytic curve for displaying the cycloid,...), and

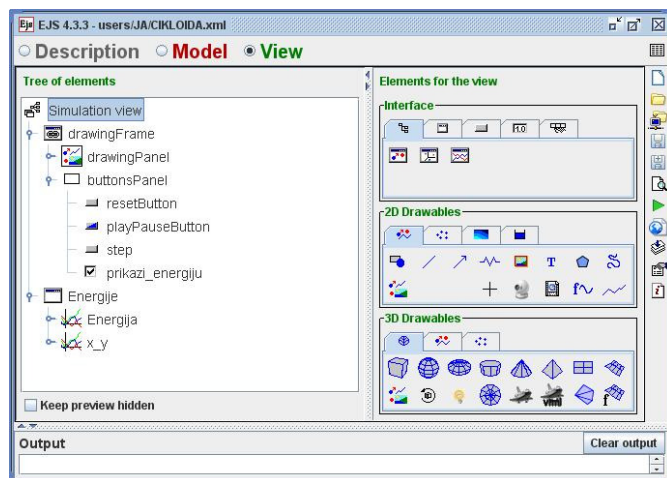


Fig. 8. EJS View panel with elements.

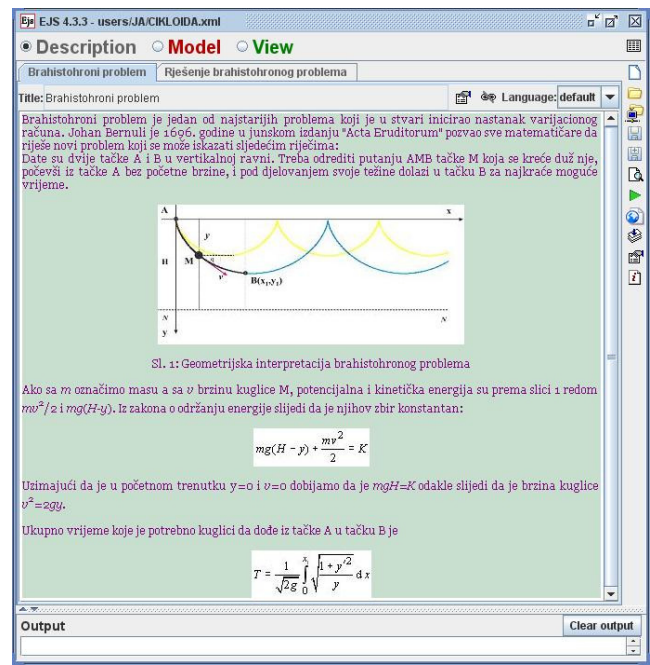


Fig. 9. EJS Description part.

buttons panel contains buttons for simulation execution control and user-simulation interaction (play/pause, step and reset buttons, check box to turn on and of energy plots). Plotting panel displays energy plots and shows changes of x and y with time.

Defining the Description

Description part of cycloid simulation contains pages with basic theoretical information regarding the brachistochrone problem and its solution, Fig. 9.

B. Running the virtual lab

The cycloid simulation can be run as a stand-alone application and as an applet. For the distance learning implementation it is more convenient to run it as an applet given in Fig. 10.

The contents of the generated HTML page can be seen on the left side of the page. The first two items represent theoretical introduction to the brachistochrone problem and its solution. Selecting them student gets familiar with the problem to be simulated. Clicking on simulation item, the applet is generated on the right side of the page. The control of the simulation execution and interaction are obtained by clicking on one of the control buttons (reset, play, and step). For showing the energy plots the check box has to be selected. In this way student can track how the energies of a blue particle change depending on its position. Fig. 11 shows potential (blue trace) and kinetic energy (red trace), and proves that total energy (green trace) is constant over the whole duration of blue particle movement as stated in Section II. This figure also shows the change of blue particle position along x -axis and y -axis.

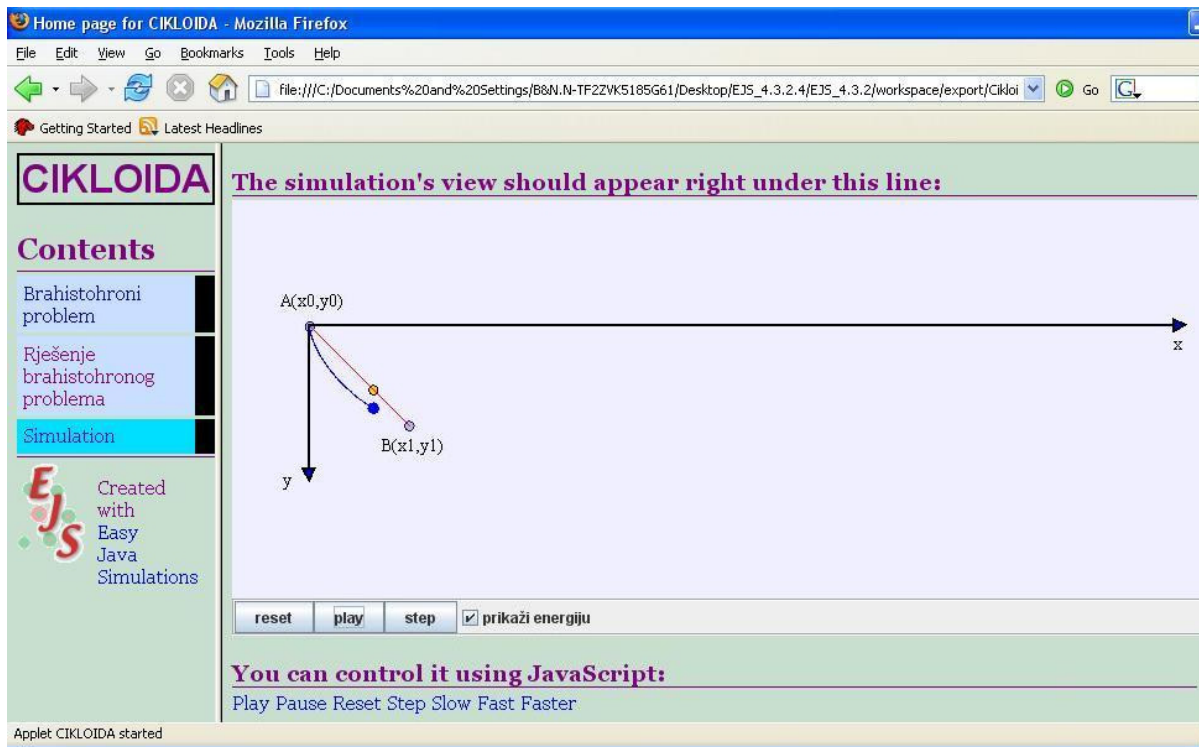


Fig. 10. Running cycloid simulation as an applet.

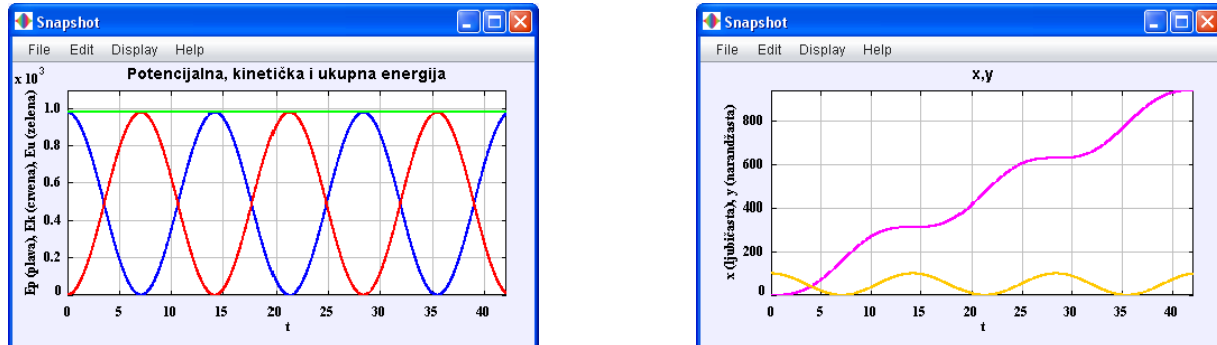


Fig. 11. Snapshots of energy plots and how x and y changes with time.

V. CONCLUSION

In this paper we presented a new approach to building the special interactive environment to be used in control systems education. It is based on the idea that the non-programming instructors create their own innovative pedagogical tools. To illustrate this approach, in order to improve the learning in optimal control theory, a concrete application in Easy Java Simulations related to the brachistochrone problem is developed. Future work will apply primarily to new uses of the considered concept.

REFERENCES

- [1] Easy Java Simulations' Home Page. Available: <http://fem.um.es/Ejs>
- [2] The Open Source Physics Project, Available: <http://www.opensourcephysics.org>
- [3] F. Esquembre, Easy Java Simulations: A Software Tool to Create Scientific Simulations in Java, *Comput. Phys. Commun.*, vol. 156, no. 2, pp. 199–204, Jan. 2004.
- [4] J. Sánchez, S. Dormido, F. Esquembre, R. Pastor, Interactive Learning of Control Concepts Using Easy Java Simulations, Available: http://www.imamu.edu.sa/dcontent/IT_Topics/java/ip_2_aad_34290345.pdf
- [5] S. Dormido, H. Vargas, J. Sanches, N. Duro, R. Dormido, S. Dormido-Canto, F. Esquembre, Using Web-based laboratories for control engineering education, Intern. Conf. on Engin. Education – ICEE 2007, Coimbra, Portugal, September 2007, Available: <http://www.dia.uned.es/proyectos/dpi2004-01804/documents/congresos/Congreso41.pdf>
- [6] F.L. Lewis, V.L. Syrmos, *Optimal Control*, John Wiley&Sons Inc., New York, 1995, ch. 5.
- [7] Sussmann, H.J., Willems, J. C., 300 Years of Optimal Control: From The Brachistochrone to the Maximum Principle, *IEEE Control Systems*, Vol. 17, No. 3, 1997, pp. 32-44.
- [8] Sage, A. P., White Ch. C., *Optimum Systems Control*, Englewood Cliffs, NJ: Prentice-Hall, 1977, ch. 3.

Analysis of Software Realized DSA Algorithm for Digital Signature

Bojan R. Pajčin and Predrag N. Ivaniš

Abstract—In this paper the realization of one algorithm for digital signature, DSA (Digital Signature Algorithm), is presented. In the algorithm, for calculating the variables needed to generate public and private key, one-way hash function, SHA (Secure Hash Algorithm), is used. A method of realization of SHA and DSA is presented, and the time required to digitally sign messages of different sizes and time required to generate the keys are measured. The results are compared with the analogous result based on another software implemented system for digitally signing with hash function and RSA algorithm.

Index Terms—Digital signature, hash function, public key encryption algorithms, software implementation.

I. INTRODUCTION

PUBLIC-KEY algorithms (also called asymmetric algorithms) are designed so that the key used for encryption is different from the key used for decryption. Furthermore, the decryption key cannot (at least in any reasonable amount of time) be calculated from the encryption key [5, 6]. The algorithms are called “public-key” because the encryption key can be made public: A complete stranger can use the encryption key to encrypt a message, but only a specific person with the corresponding decryption key can decrypt the message. In these systems, the encryption key is often called the public key, and the decryption key is often called the private key. Sometimes, messages will be encrypted with the private key and decrypted with the public key; that protects the integrity of the sender (authenticity of the message). This is used in digital signatures.

A one-way hash function, often called compression function, message digest, fingerprint, cryptographic checksum, is central to modern cryptography. One-way hash functions are another building block for many protocols. Hash functions have been used in computer science for a long time. A hash

function is a function, mathematical or otherwise, that takes a variable-length input string (called a pre-image) and converts it to a fixed-length (generally smaller) output string (called a hash value) [5]. A simple hash function would be a function that takes pre-image and returns a byte consisting of the XOR of all the input bytes. A one-way hash function is a hash function that works in one direction: It is easy to compute a hash value from pre-image, but it is hard to generate a pre-image that hashes to a particular value [5]. The hash function previously mentioned is not one-way: Given a particular byte value, it is trivial to generate a string of bytes whose XOR is that value. A good one-way hash function is also collision-free: It is hard to generate two pre-images with the same hash value. The hash function is public; there’s no secrecy to the process. The security of a one-way hash function is its onewayness. The output is not dependent on the input in any discernible way. A single bit change in the pre-image changes, on the average, half of the bits in the hash value. Given a hash value, it is computationally unfeasible to find a pre-image that hashes to that value.

The purpose of digital signature is to confirm the authenticity of the message content (proof that the message has not changed on the way between sender and recipient) and to ensure a guarantee of the sender identity. Base of digital signature is the contents of the message. Author (call him person A) using a certain cryptographic algorithms, firstly creates a fixed length record of its arbitrary length message, which fully reflects the content of the message (a hash value). After that, he performs certain operations over this record, using several other parameters and his secret key, and thus generates a digital signature that is sent along with the message. When the recipient (call him person B) receives a message with a digital signature, using the sender's public key (public key of person A) and the summary record of messages, which makes himself, and applying of certain operations as a result gets a number. Person B compares that number with the number who has received in the form of digital signature and thereby determines the authenticity of the message. Considering that operations in the message summary (hash value) use a secret key, nobody else can generate the digital signature except the person who sending the message (the only person A knows its secret key). This way, the recipient (person B) knowing the sender's public key (A) is a sure that just got a message from him, because the calculated value match only if

Ministry of Science and Technological Development of the Republic of Serbia has partially funded project TR32007 “Multiservice optical transport platform OTN10/40/100 Gbps with DWDM/ROADM and Carrier Ethernet functionalities.” Part of results in this paper was presented at the 55th ETRAN conference, Banja Vrućica, 6-9. June 2011.

B. R. Pajčin is with the IRITEL A.D., Belgrade, Serbia (phone: 00 381 11 3073 451; fax: 00 381 3073 434; e-mail: bojan@iritel.com).

P. N. Ivaniš, is with Faculty of Electrical Engineering, University of Belgrade, Belgrade, Serbia (e-mail: predrag.ivanis@etf.rs).

the sender's public key corresponding to his secret key, which person A is used to generate a digital signatures.

In the next section will be presented the most frequently used hash functions today, Secure Hash Algorithm (SHA) [7], and briefly will be described its operation. It will be described operation of DSA algorithm [2], public key algorithm, which is part of the DSS standard. The above-mentioned hash function and DSA are software implemented and integrated in the system to digitally sign, and that system is the subject of this paper.

II. SHA

NIST (*National Institute of Standards and Technology*), along with the NSA (*National Security Agency*), designed the *Secure Hash Algorithm* (SHA) for use with the *Digital Signature Standard* (DSS). SHA produces a 160-bit hash.

First, the message is padded so that its length is just 64 bits short of being a multiple of 512. This padding is a single 1-bit added to the end of the message, followed by as many zeros as are required. Then, a 64-bit representation of the message's length (before padding bits were added) is appended to the result. These two steps serve to make the message length an exact multiple of 512 bits in length (required for the rest of the algorithm), while ensuring that different messages will not look the same after padding. After that, Five 32-bit variables are initialized as follows:

$A = 0x67452301,$
 $B = 0xefcdab89,$
 $C = 0x98badcfe$
 $D = 0x10325476,$
 $E = 0xc3d2e1f0$

The main loop of the algorithm then begins. It processes the message 512 bits at a time and continues for as many 512-bit blocks as are in the message. First the five variables are copied into different variables: a gets A , b gets B , c gets C , d gets D , and e gets E . The main loop has four rounds of 20 operations each. Each operation performs a nonlinear function on three of a , b , c , d , and e , and then does shifting and adding. SHA's set of nonlinear functions is:

$$f_t(X,Y,Z) = (X \wedge Y) \vee ((\neg X) \wedge Z), \text{ for } t = \text{od } 0 \text{ do } 19$$

$$f_t(X,Y,Z) = X \oplus Y \oplus Z, \text{ for } t = \text{od } 20 \text{ do } 39$$

$$f_t(X,Y,Z) = (X \wedge Y) \vee (X \wedge Z) \vee (Z \wedge Y), \text{ for } t = \text{od } 40 \text{ do } 59$$

$$f_t(X,Y,Z) = X \oplus Y \oplus Z, \text{ for } t = \text{od } 60 \text{ do } 79$$

Four constants are used in the algorithm [7]:

$K_t = 0x5a827999, \text{ for } t = \text{od } 0 \text{ do } 19$
 $K_t = 0x6ed9eba1, \text{ for } t = \text{od } 20 \text{ do } 39$
 $K_t = 0x8f1bbcdc, \text{ for } t = \text{od } 40 \text{ do } 59$
 $K_t = 0xca62c1d6, \text{ for } t = \text{od } 60 \text{ do } 79$

(If you wonder where those numbers came from: $0x5a827999 = 21/2 \ /4$, $0x6ed9eba1 = 31/2 \ /4$, $0x8f1bbcdc =$

$51/2 \ /4$, and $0xca62c1d6 = 101/2 \ /4$; all times 232.)

The message block is transformed from 16 32-bit words (M_0 to M_{15}) to 80 32-bit words (W_0 to W_{79}) using the following algorithm:

$$W_t = M_t, \text{ for } t = 0, 1, \dots, 15$$

$$W_t = (W_{t-3} + W_{t-8} + W_{t-14} + W_{t-16}) \lll 1, \text{ for } t = 16, 17, \dots, 79$$

If t is the operation number (from 0 to 79), W_t represents the t -th sub-block of the expanded message, and $\lll s$ represents a left circular shift of s bits, then the main loop looks like [7]:

$$TEMP = (a \lll 5) + f_t(b,c,d) + e + W_t + K_t$$

$$e = d,$$

$$d = c,$$

$$c = b \lll 30,$$

$$b = a,$$

$$a = TEMP$$

Fig. 1 shows one operation. After all of this, a , b , c , d , and e

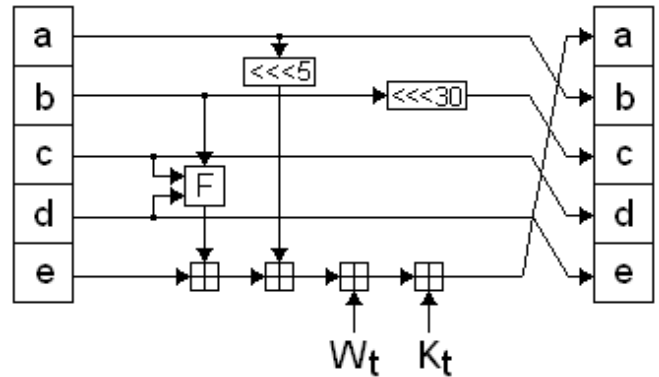


Fig. 1. Figure 1: One SHA operation.

are added to A , B , C , D , and E respectively, and the algorithm continues with the next block of data. The final output is the concatenation of A , B , C , D , and E

III. SECURITY OF SHA

There are two brute-force attacks against a one-way hash function. The first is the most obvious: Given the hash of message, $H(M)$, an adversary would like to be able to create another document, M' , such that $H(M) = H(M')$. The second attack is more subtle: An adversary would like to find two random messages, M , and M' , such that $H(M) = H(M')$. This is called a collision, and it is a far easier attack than the first one.

The birthday paradox is a standard statistics problem. How many people must be in a room for the chance to be greater than even that one of them shares your birthday? The answer is 253. Now, how many people must there be for the chance to be greater than even that at least two of them will share the same birthday? The answer is surprisingly low: 23. With only 23 people in the room, there are still 253 different *pairs* of people in the room.

Finding someone with a specific birthday is analogous to the

first attack; finding two people with the same random birthday is analogous to the second attack. The second attack is commonly known as a birthday attack.

Assume that a one-way hash function is secure and the best way to attack it is by using brute force. It produces an m -bit output. Finding a message that hashes to a given hash value would require hashing 2^m random messages. Finding two messages that hash to the same value would only require hashing $2^{m/2}$ random messages.

Hash functions of 64 bits are just too small to survive a birthday attack. Most practical one-way hash functions produce 128-bit hashes. This forces anyone attempting the birthday attack to hash 2^{64} random documents to find two that hash to the same value, not enough for lasting security. NIST, in its Secure Hash Standard (SHS), uses a 160-bit hash value. This makes the birthday attack even harder, requiring 2^{80} random hashes.

SHA is very similar to MD4 [9], but has a 160-bit hash value. The main changes are the addition of an expand transformation and the addition of the previous step's output into the next step for a faster avalanche effect. Ron Rivest made public the design decisions behind MD5 [10], but SHA's designers did not. Here are Rivest's MD5 improvements to MD4 and how they compare with SHA's [6]:

- 1) "A fourth round has been added." SHA does this, too. However, in SHA the fourth round uses the same f function as the second round.
- 2) "Each step now has a unique additive constant." SHA keeps the MD4 scheme where it reuses the constants for each group of 20 rounds.
- 3) "The function G in round 2 was changed from $((X \wedge Y) \vee (X \wedge Z) \vee (Z \wedge Y))$ to $(X \wedge Z) \vee (Y \wedge (\neg Z))$ to make G less symmetric." SHA uses the MD4 version: $((X \wedge Y) \vee (X \wedge Z) \vee (Z \wedge Y))$.
- 4) "Each step now adds in the result of the previous step. This promotes a faster avalanche effect." This change has been made in SHA as well. The difference in SHA is that a fifth variable is added, and not b , c , or d , which is already used in f . This subtle change makes the den Boer-Bosselaers attack against MD5 impossible against SHA.
- 5) "The order in which message sub-blocks are accessed in rounds 2 and 3 is changed, to make these patterns less alike." SHA is completely different, since it uses a cyclic error-correcting code.
- 6) "The left circular shift amounts in each round have been approximately optimized, to yield a faster avalanche effect. The four shifts used in each round are different from the ones used in other rounds." SHA uses a constant shift amount in each round. This shift amount is relatively prime to the word size, as in MD4.

This leads to the following comparison: SHA is MD4 with the addition of an expand transformation, an extra round, and better avalanche effect; MD5 is MD4 with improved bit hashing, an extra round, and better avalanche effect [6].

Because SHA produces a 160-bit hash, it is more resistant to

brute-force attacks (including birthday attacks) than 128-bit hash functions.

IV. DSA

In August 1991, The National Institute of Standards and Technology (NIST) proposed the Digital Signature Algorithm (DSA) for use in their Digital Signature Standard (DSS). This is Public-Key Digital Signature Algorithm.

DSA is a variant of the Schnorr and ElGamal signature algorithms, and is fully described in [2]. The algorithm uses the following parameters:

p = a prime number L bits long, when L ranges from 512 to 1024 and is a multiple of 64. (In the original standard, the size of p was fixed at 512 bits [1]. This was the source of much criticism and was changed by NIST [2].)

q = a 160-bit prime factor of $p - 1$.

$g = h^{(p-1)/q} \bmod p$, where h is any number less than $p - 1$ such that $h^{(p-1)/q} \bmod p$ is greater than 1.

x = a number less than q .

$y = g^x \bmod p$.

The algorithm also makes use of a one-way hash function: $H(m)$. The standard specifies the Secure Hash Algorithm..

The first three parameters, p , q , and g , are public and can be common across a network of users. The private key is x ; the public key is y .

To sign a message, m :

- 1) Sender generates a random number, k , less than q .
- 2) Sender generates

$$r = (g^k \bmod p) \bmod q$$

$$s = (k^{-1} (H(m) + xr)) \bmod q$$

The parameters r and s are her signature; she sends these to recipient.

- 3) Recipient verifies the signature by computing

$$w = s^{-1} \bmod q$$

$$u_1 = (H(m) \cdot w) \bmod q$$

$$u_2 = (rw) \bmod q$$

$$v = ((g^{u_1} \cdot y^{u_2}) \bmod p) \bmod q$$

If $v = r$, then the signature is verified.

Proofs for the mathematical relationships are found in [2].

Real-world implementations of DSA can often be speeded up through precomputations. Notice that the value r does not depend on the message. You can create a string of random k values, and then precompute r values for each of them. You can also precompute k^{-1} for each of those k values. Then, when a message comes along, you can compute s for a given r and k^{-1} . This precomputation speeds up DSA considerably.

V. DSA PRIME GENERATION

Lenstra and Haber pointed out that certain moduli are much easier to crack than others [3]. If someone forced a network to use one of these "cooked" moduli, then their signatures would

be easier to forge. This isn't a problem for two reasons: These moduli are easy to detect and they are so rare that the chances of using one when choosing a modulus randomly are almost negligible—smaller, in fact, than the chances of accidentally generating a composite number using a probabilistic prime generation routine.

In [2] NIST recommended a specific method for generating the two primes, p and q , where q divides $p - 1$. The prime p is L bits long, between 512 and 1024 bits long, in some multiple of 64 bits. The prime q is 160 bits long. Let $L - 1 = 160n + b$, where L is the length of p , and n and b are two numbers and b is less than 160.

- 1) Choose an arbitrary sequence of at least 160 bits and call it S . Let g be the length of S in bits.
- 2) Compute $U = \text{SHA}(S) \oplus \text{SHA}((S + 1) \bmod 2^g)$, where SHA is the Secure Hash Algorithm.
- 3) Form q by setting the most significant bit and the least significant bit of U to 1.
- 4) Check whether q is prime.
- 5) If q is not prime, go back to step 1.
- 6) Let $C = 0$ and $N = 2$.
- 7) For $k = 0, 1, \dots, n$ let $V_k = \text{SHA}((S + N + k) \bmod 2^g)$
- 8) Let W be the integer:

$$W = V_0 + 2^{160}V_1 + \dots + 2^{160(n-1)}V_{n-1} + 2^{160n}(V_n \bmod 2^b)$$
 and let:

$$X = W + 2^{L-1}$$
 Note that X is an L -bit number.
- 9) Let: $p = X - ((X \bmod 2q) - 1)$. Note that p is congruent to 1 mod $2q$.
- 10) If $p < 2^{L-1}$, then go to step 13.
- 11) Check whether p is prime.
- 12) If p is prime, go to step 15.
- 13) Let $C = C + 1$ and $N = N + n + 1$.
- 14) If $C = 4096$, then go to step 1. Otherwise, go to step 7.
- 15) Save the value of S and the value of C used to generate p and q .

In [2], the variable S is called the "seed," C is called the "counter," and N the "offset".

The point of this exercise is that there is a public means of generating p and q . For all practical purposes, this method prevents cooked values of p and q . If someone hands you a p and a q , you might wonder where that person got them. However, if someone hands you a value for S and C that generated the random p and q , you can go through this routine yourself. Using a one-way hash function, SHA in the standard, prevents someone from working backwards from a p and q to generate an S and C .

This security is better than what you get with RSA. In RSA, the prime numbers are kept secret. Someone could generate a fake prime or one of a special form that makes factoring easier. Unless you know the private key, you won't know that. Here, even if you don't know a person's private key, you can confirm that p and q have been generated randomly.

VI. SECURITY OF DSA

A. Attacks against k

Each signature requires a new value of k , and that value must be chosen randomly. If anyone ever recovers k that sender used to sign a message, perhaps by exploiting some properties of the random-number generator that generated k , he can recover sender's private key, x . If anyone ever gets two messages signed using the same k , even if he doesn't know what it is, he can recover x . And with x , anyone can generate undetectable forgeries of sender's signature. In any implementation of the DSA, a good random-number generator is essential to the system's security [6].

B. Dangers from using Common Modulus

Even though the DSS does not specify a common modulus to be shared by everyone, different implementations may. For example, the Internal Revenue Service is considering using the DSS for the electronic submission of tax returns. What if they require every taxpayer in the country to use a common p and q ? Even though the standard doesn't require a common modulus, such an implementation accomplishes the same thing. A common modulus too easily becomes a tempting target for cryptanalysis. It is still too early to tell much about different DSS implementations, but there is some cause for concern.

C. Subliminal Channel in DSA

Gus Simmons discovered a subliminal channel in DSA [6]. This subliminal channel allows someone to embed a secret message in his signature that can only be read by another person who knows the key. According to Simmons, it is a "remarkable coincidence" that the "apparently inherent shortcomings of subliminal channels using the ElGamal scheme can all be overcome" in the DSS, and that the DSS "provides the most hospitable setting for subliminal communications discovered to date." NIST and NSA have not commented on this subliminal channel; no one knows if they even knew about it. Since this subliminal channel allows an unscrupulous implementer of DSS to leak a piece of the private key with each signature, it is important to never use an implementation of DSS if you don't trust the implementer.

VII. SOFTWARE REALIZATION

Fig. 2 and Fig. 3 show the block diagram of the realized system for the digital signature. The program is fully written in the Delphi programming language and development environment that has been used is Borland Delphi 7. Delphi is an object-oriented programming language used to implement applications that run in the Windows operating system, and is particularly suited for graphical applications and graphical user interfaces (GUI). The syntax of the language is similar to Pascal syntax, and the original name of Delphi was Object Pascal. In addition to the main libraries that are used for programming, BigInt library is used for operations with large numbers (numbers greater than 64 bits). Procedures and

functions of BigInt library are used for measurement time, too.

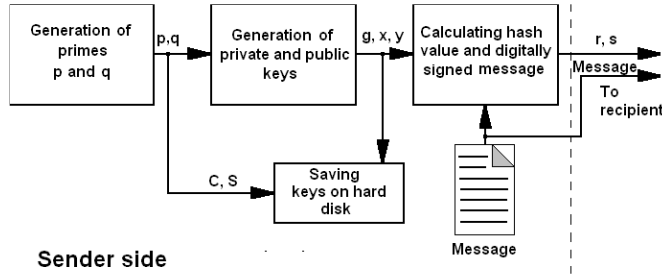


Fig. 2. Block diagram of realized system for digital signature – sender side.

Hereinafter, will be tested a presented system for digitally signing DSA, and the results will be used to compare this system with a digital signature system based on hash functions and RSA algorithm [8]. In order to credibility compare of these two systems, in both implementation used identical algorithm and the same software implementation of SHA hash functions, system simulation and measurement results were carried out on the same computer and the time test of digital signing the message used the same samples, i.e. the same file.

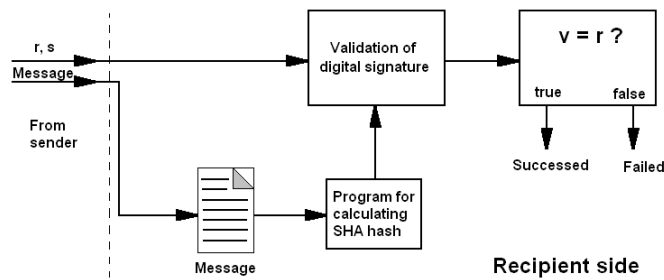


Fig. 3. Block diagram of realized system for digital signature – recipient side.

The user of software that implemented DSA may choose public and private key length by selecting the prime number p bit-length, which can be between 512 and 1024 bits, and the selected length is multiple of 64. In purpose of testing DSA algorithm were used prime numbers p of length 1024 bits, and by thus is determined the length of public keys y , which are also length 1024 bits. When you choose what will be the size of p , by pressing a button in the program generate keys and then save them in a given location on your computer. After the keys are remembered as .id files on your computer, the user is able to use a generated key many times to sign the message. The public key is freely distributed and shared with other users so that they were able to verify the signature, while the private key, or file in which is preserved, stored on a computer, thus leaving for the use only for the person whose identity is represented by the private key. Block for generating prime numbers p and q is implemented as described in Chapter 4. Due to the conditions in steps 5 and 14, mentioned in above chapter, to get the prime numbers that satisfy the conditions is necessary to repeatedly execute a block of commands, and therefore the time required to generate p and q varies depending on the number of repeat loops. Table I is given a

TABLE I
TIME TO GENERATE 1024-BIT KEYS

Time	Min [ms]	Average [ms]	Max [ms]
DSA	28.93	354.8173	1437.738
RSA	/	45.7217	/

minimum, maximum and average time needed to generate 1024-bit DSA key algorithm. By comparison, the next line in the same table gives the time needed to generate a key the same length using RSA.

For the source of messages a user can choose either a text that will write or a file from his computer (images, movies, documents ...). In case the message is chosen file, program presents that file as a sequence of bytes, and then in the sequence adds bits on way presented in the description of SHA hash function. After adding bits, the total sequence length is a multiple of 64 (one element of the array, byte = 8 bits; 64 bytes = 512 bits). When the message for signing is text entered directly in program, then each character of text will be presented to byte values corresponding to the ASCII character representation (table). On this way program makes array of bytes from text message. There is adding bits on the end of this array too, so a length is a multiple of 64. Now we compute SHA hash value of this array as described earlier in Chapter 2. By using a hash value, randomly generated number k , and previously generated and calculated parameters (p , q , g and x) is calculating a digital signature in the manner explained in the description of the DSA algorithm (Chapter 3). Times needed to compute the digital signature, depending on the size of messages are presented in Table II. These results are shown on Fig. 4, too. These sizes of test message were used because 20 KB is the average size of e-mail without attachments, 100 KB is size of a written document, 500 KB is size of medium

TABLE II
TIME [MS] NEEDED TO DIGITALLY SIGN MESSAGES OF DIFFERENT SIZES

Message	20KB	100KB	500KB	1MB	3MB
DSA	2.7197	5.3297	18.077	37.588	98.789
RSA	6.563	9.162	21.951	40.616	101,04

resolution jpg images, 1 MB is size of high resolution image, and 3 MB is size of mp3 songs.

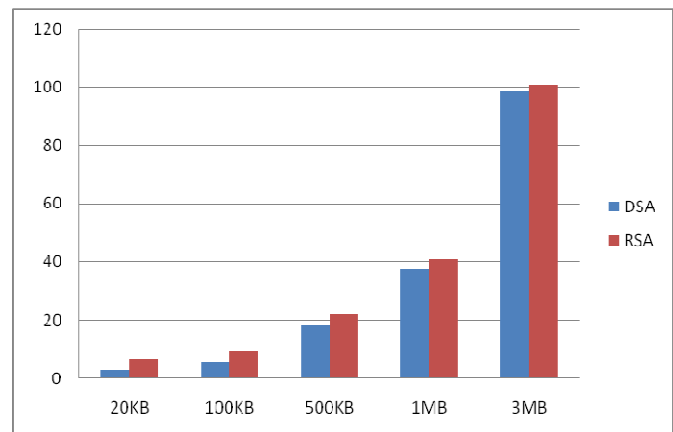


Fig. 4. Time [ms] needed to digitally sign messages of different sizes.

The validation of digital signature and sender authentication is performed in the last block of the scheme in Fig. 3. Mathematical operations, described in Chapter 3, are applied in the block for checking digital signature. These operations use the sender's public key, the received message and digital signature. First you need to calculate a hash value of message. In our test for calculating a hash value of the received message, and for checking the correctness of code that calculates the SHA hash values, we used a free SlavaSoft's HashCalc 2.02 software. At the end if v equals r then we can safely say that the message is transferred in an unmodified form and that is from the same sender whose public key we decipher the message. If the compared values are different message should be rejected because it is in transmission its content is changed or it is not from the person who allegedly signed. Signature verification procedure in the depicted software implementation of the DSA algorithm takes an average of 2.97 ms, while the same operation for the RSA algorithm required 5.817 ms.

VIII. CONCLUSION

With 512-bits key DSA wasn't strong enough for long-term security. With 1024-bits key it is, and for that reason is used in this software implementation.

DSA keys generation is a much slower than the RSA algorithm, the time required to digitally sign messages are similar, if larger files are signed (on the order MB and larger), while the DSA is faster at the signing of small files and text messages, as at verifying the digital signature.

Unlike RSA, DSA can't be used for the encryption or key distribution, but this is not the point of the DSS standard. This is a digital signatures standard. It is possible to use these two

algorithms for realization another system for digital signatures, which would use DSA for digital signing and RSA for keys distribution. The reason for usage DSA for signing, and not RSA, is security, because it offers the possibility to check the manners in which primes p and q are generated. The RSA algorithm, prime numbers are kept confidential, and verification that they intentionally used their specific values is possible only with the knowledge of the private key. At DSA algorithm only publicly available variables S and C (seed and counter) can be used for checking without disclosing the private key.

REFERENCES

- [1] National Institute of Standards and Technology, NIST FIPS PUB XX. „Digital Signature Standard“, U.S. Department of Commerce, DRAFT, 19 Aug 1991.
- [2] National Institute of Standards and Technology, NIST FIPS PUB 186. „Digital Signature Standard“, U.S. Department of Commerce, May 1994.
- [3] A. K. Lenstra and S. Haber, letter to NIST Regarding DSS, 26 Nov 1991.
- [4] G. J. Simmons, „The Subliminal Channels of the U.S. Digital Signature Algorithm (DSA)“, Proceedings of the Third Symposium on: State and Progress of Research in Cryptography, Rome: Fondazione Ugo Bordoni, 1993, pp. 35 – 54.
- [5] D. Drajić, P. Ivaniš, “Uvod u teoriju informacija i kodovanje”, *Akadska misao*, Beograd, 2009.
- [6] B. Schneier, “Primenjena kriptografija”, *Mikro knjiga*, Beograd, 2007.
- [7] IETF RFC 4634 - US Secure Hash Algorithms (SHA and HMAC-SHA), <http://www.ietf.org/rfc/rfc4634.txt>.
- [8] B. Pajčin, P. Ivaniš, “Softverska realizacija sistema za digitalno potpisivanje sa heš funkcijama i RSA algoritmom”, *Infoteh-Jahorina 2011*, Jahorina 2011.
- [9] IETF RFC 1186 - The MD4 Message Digest Algorithm, <http://www.ietf.org/rfc/rfc1186.txt>.
- [10] IETF RFC 1321 - MD5 Message-Digest Algorithm, <http://www.ietf.org/rfc/rfc1321.txt>.

Design of Low Cost Force Sensor System for Human Machine Interaction – Force Feedback Joystick

Miloš Petković and Goran S. Đorđević

Abstract—The paper describes a low cost force sensor system ready to be evaluated in force-feedback joystick designed for a medical haptics application. It is based on low-cost parts from home appliance scale with strain gauge technology, and of-the-shelf IC instrumentation amplifier. The development process, electronic circuitry and designed software are presented. Experimental results give a good ground to believe that this approach can provide sufficient quality in further development of human-machine interaction algorithms.

Index Terms—Force feedback joystick, low cost design, strain gauges, software aided design.

I. INTRODUCTION

FORCE feedback joysticks are well established as haptic interfaces [1]. Many studies have shown that force feedback can boost performance in various applications of remote control, steering, haptic tasks [1, 3], telepresence, etc. The fact that they are still not accepted when it comes to medical applications opens an issue of their redesign towards price cut, better algorithms, and better integrated drive electronics. In this paper we present a low-cost force sensor system based on strain gauges mounted on thin metal feet, integrated in a force feedback joystick that has a standard mechanical design. We discussed purposefulness of such approach in developing a low-cost laboratory setup for development, validation and verification in order to check if the solution meets specifications. Such system then can be used for further developments in haptic algorithms.

II. GLOBAL OVERVIEW OF THE JOYSTICK

During development, the master device which process data and drives joystick is supposed to be PC. In order to cut the initial costs and increase flexibility in interfacing towards PC,

This paper was supported by Project Grant III44004 (2011-2014) financed by Ministry of Education and Science, Republic of Serbia. Part of this paper and results were presented at 55th conference of ETRAN, Banja Vrućica, 6-9. Jun 2011.

M. Petković is with Faculty of Electronic Engineering, University of Niš, Aleksandra Medvedeva 14, 18000 Niš, Serbia (phone: +381 69 4948449; e-mail: milos.petkovic@elfak.ni.ac.rs).

G. S. Đorđević is with Faculty of Electronic Engineering, University of Niš, Aleksandra Medvedeva 14, 18000 Niš, Serbia (e-mail: goran.s.djordjevic@elfak.ni.ac.rs).

Humusoft acquisition card MF624 was chosen. It supports integration into LabView, Matlab and Simulink. Global overview of the joystick system is shown in Fig. 1.

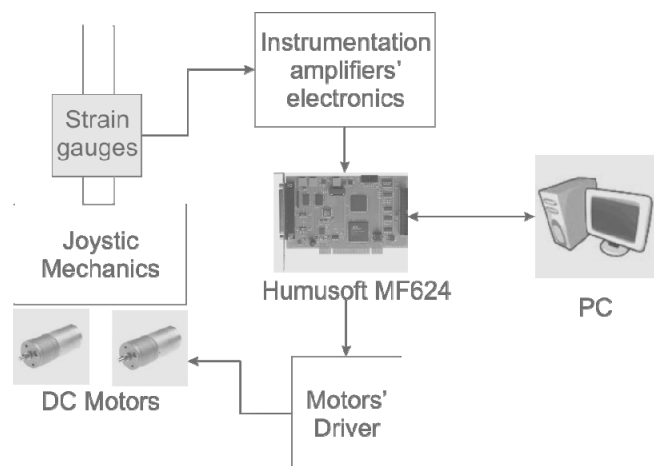


Fig. 1. Overview of the force feedback joystick system.

Mechanics is based on 2 dof gimbal mechanism [4].

Force feedback joystick is powered by two DC motors, producing 2 dofs at the handle. Due to kinematic properties of mechanism, the handle movements are produced by coupled movement of the two motor axes. That means that there must be defined correct kinematic transformation between the two sets of angles, internal, and external. Drivers for motors are currently being developed.

Four strain gauges of single low cost 20\$ kitchen scale are used. Each strain gauge is already attached to piece of metal plate of T shape. Joystick handle consists of three distinct pieces, as shown in Fig. 2. The root of the handle is connected to the joystick mechanism. Upper part of two T plates is attached at the upper part of root of handle on opposite sides. Plates are aligned parallel to one another with strain gauges facing out. In that way bending of metal plates in one direction will produce opposite resistance changes of gauges and thus increase in overall sensitivity. Lower part of T plates is attached to short middle part of handle. Another pair of T plates is attached in similar manner but rotated 90° relative to the first pair of plates. In that way each pair of sensors will be used to measure bending force applied at handle for perpendicular axis. These axes will be called X and Y axis of

joystick for further reference. The lower part of second pair of plates is attached to lower part of third part of the handle. This part is held in hand. In order to decrease torsion on handle, rotating cylinder is placed over this part of handle. Cylinder is coupled with handle via bearings.

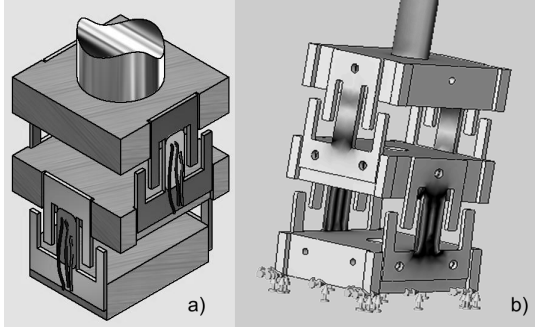


Fig. 2. Sensor plates' configuration on handle (a), with FEM analysis of stress under the force applied at the handle (b).

III. ELECTRONICS OF THE SENSOR SYSTEM

A. Sensors

Strain gauge used here is a strip resistor, where positive or negative change in length of strip resistor results in increase or decrease of its resistance. Similarly, change in width will produce the same effect but with opposite changes in resistance. Widening of strip causes resistance to decrease and vice versa. When attached to surface of object that can bend or stretch strip resistance will vary accordingly with deformation. If deformation is cause of some force applied to object then this force can be measured indirectly via change in resistance. Strip is usually pre-shaped in a specific way to increase its sensitivity. Usually it is zigzagged. Some shapes are better for particular applications than the others.

Temperature drift affect both, the object and the gauge. If the plate expands due to temperature it will stretch gauge and false readings could occur. Intrinsic resistance of strip is also temperature dependent. Therefore, special care has to be taken, possibly in two ways. Material of gauge can be chosen so that temperature deformation of object and intrinsic resistance temperature change cancel each other out. This is called Self-Temperature-Compensation or STC and is somewhat harder to achieve. The easier way is to use Wheatstone bridge. If two or all four resistors are under same temperature effect then differential result is almost unaffected.

Due to the fact the strain gauges came cheap, there is no datasheet available for them. Furthermore strain gauge on one metal plate is sealed with white glue and cannot be seen. Three connecting wires are only coming out of white goo. Cross resistance between each line was measured with multimeter. Resistance was approximately 500 Ω between two pairs and 1 k Ω between third pair. Therefore conclusion is that two 500 Ω resistors are connected in series and wires are attached to their common point and ends.

Since both resistors are from the same side of the metal

plate it is highly likely that one resistor is used just for temperature compensation. That means that its resistance maintains unchanged with bending of plate. However, resistance does change due to temperature. Used alongside in Wheatstone bridge it will compensate temperature changes of resistance of the first resistor.

Another possibility is that the resistance of the second resistor changes with bending but in opposite direction than that of first one and thus increases sensitivity.

Changes in resistance due to bending are almost impossible to detect with multimeter. Hence, configuration of resistors was left unknown. Never the less application circuit of both configurations is the same, half bridge configuration. Since pair of T plates are placed in parallel, on each side of handle, to increase overall sensitivity then a full bridge strain gauge configuration is formed. This is shown in Fig. 3.

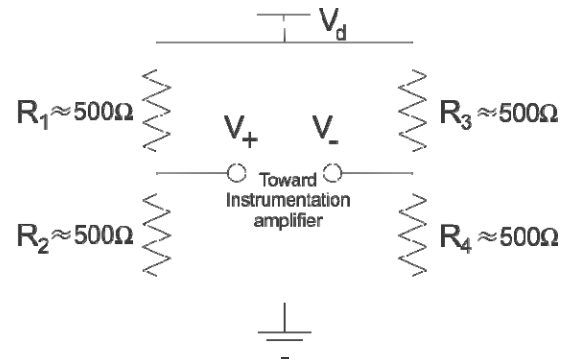


Fig. 3. Full bridge configuration of strain gauges of a pair of parallel plates.

Middle point voltages marked with V_+ and V_- are feed further to instrumentation amplifier. Differential voltage is expressed through equation (1):

$$V_+ - V_- = \frac{R_2 R_3 - R_1 R_4}{(R_1 + R_2)(R_3 + R_4)} V_d \quad (1)$$

$$V_+ = \frac{R_2}{R_1 + R_2} V_d \quad V_- = \frac{R_4}{R_3 + R_4} V_d.$$

As previously mentioned, resistor values are almost equal, $R_1 = R_2 = R_3 = R_4 = R = 500 \Omega$. Maximal difference between resistors is less than 1 Ω . Later on with fine tune offset calibration it was estimated at about 0.1-0.2 Ω .

In the case that one resistor is for force sensing and the other is just for temperature compensation the resistor values R_1 to R_4 are given with set I) in (2).

$$\begin{aligned} \text{I) } R_1 &= R - \Delta R + \delta & \text{II) } R_1 &= R - \Delta R + \delta \\ R_2 &= R + \delta & R_2 &= R + \Delta R + \delta \\ R_3 &= R + \Delta R + \delta & R_3 &= R + \Delta R + \delta \\ R_4 &= R + \delta & R_4 &= R - \Delta R + \delta \end{aligned} \quad (2)$$

ΔR represents change of resistance due to physical deformation of the resistor. It is assumed that change of R_1 and R_3 is approximately equal in amount, but different in sign of course. Influence of temperature is represented with δ and it is also assumed that it is same for all resistors, what is fairly truthful. If values from I-(2) are substituted in (1) then the

differential voltage becomes:

$$V_+ - V_- = \frac{\Delta R}{2R\left(1 + \frac{\delta}{2R}\right)} V_d \cdot \frac{1}{1 - \left(\frac{\Delta R}{2R + 2\delta}\right)^2} \quad (3)$$

Since $\Delta R/(2R) < 10^{-3}$ then $(\Delta R/(2R))^2 < 10^{-6}$. This means that denominator in equation (3) is almost 1. Consequently the differential voltage is defined with:

$$V_+ - V_- = \frac{\Delta R}{2R\left(1 + \frac{\delta}{2R}\right)} V_d \quad (4)$$

In the case that both resistors are used for sensing purposes then resistor values R_1 to R_4 are given with set II) in (2). By substituting these in (1) one gets the expression (4). Therefore, (4) represents the differential voltage for the second case of resistors configuration. This proves previous claim that no datasheet is necessary for kitchen scale strain gauge sensors to be used, as it results in same application circuit.

Most of the strain gauges are made of constantan (Ni 45%, Cu 55%, usually) alloy [2]. This material is relatively cheap and has several good qualities [2, 5]:

- Fairly good sensitivity or gauge factor of 2 ± 0.1 .
- Low, negative temperature coefficient of approx. 10 ppm/°C at about 20 °C.
- Self-temperature compensation is easily achieved.
- Non-linearity of less than 10^{-3} for $\Delta l/l < 10^{-3}$.

Having in mind that device will be used for medical purposes where room temperature range will be 25 ± 15 °C. Therefore, temperature change δ will be at most 0.015% of resistance value R , or 0.075Ω . Since $\delta/2R$ is less than 10^{-4} the nominator in (4) can be rounded up to $2R$.

Mismatch in resistor values do affect gain and offset but linearity is affected with just 10^{-4} .

B. Electronic

Schematic diagram of sensor's system electronic is shown in Fig. 4. Supply voltage for strain gauge is 5 V. This voltage was chosen for two reasons. It is low enough not to cause heating of resistors and big enough to give moderate differential voltage. Instrumentation amplifier used for amplification of differential voltage has CMRR of min 100dB allowing single supply voltage to be used for strain gauge.

It was estimated that differential voltage is in range of much less than 1mV. The target voltage is ± 9 V since full voltage input range for Humusoft ADC is ± 10 V. Desired gain was first estimated to be close to 10000. Further experiments showed that the desired gain should be 1776 for X-axis gauges and 1826 for Y-axis gauges. Difference in gains is due to slight difference in levers for these two sets of sensors. Used instrumentation amplifier AD620 has nicely programmable gain G selection with one resistor R_g , with dependency given with (5). Since single standard resistors were used to set gains, precise desired gains could not and did not need to be achieved. However, PCB was designed so that two parallel resistors, R_{gpX} and R_{gX} for X axis amplifier,

and R_{gpY} and R_{gY} for Y axis amplifier, can be used for more accurate gain selection. That is why R_{gX} and R_{gY} have no values in Fig. 4. Standard resistance that achieves closest gains to desired ones is 27Ω . The gain is then 1830.

$$G = \frac{49.4k\Omega}{R_g} + 1 \quad (5)$$

Advantage of using integrated instrumentation amplifier, like AD620, over a discrete one that consists of three operational amplifiers, is save in time and money.

During the testing it was noticed that there is high noise on ± 12 V output power supply lines of Humusoft MF624 acquisition card. Variations in voltages of about 100 mV in average also would occur whenever acquisition process was started. Since the same voltage supplies AD620 and gain has to be high, there were a lot of variations in output signal of amplifier even if no stress was applied on sensors. Therefore, additional voltage regulators for ± 10 V had to be used. Although voltage regulators did the job there was still a lot of noise coming out from environment. It was introduced through the long cable connecting acquisition card and sensors electronics board. Noise level was at about 5 to 10 mV even after moderate digital signal processing. Digital filter is supposed to be of moderate processing length since it is to be implemented later on in microcontroller, and since moderate latency is acquired. Therefore, cables were replaced with shielded audio ones and kept at minimum of about 1.5 m in length. That lowered the noise level down to 15 mV in average before digital filtering and below 1mV after digital filtering.

Since there were slight mismatch in resistors that lead to almost 2 V of amplified signal offset, additional offset regulating resistors had to be inserted in series with gauge's one. It was deduced from experiments that one strain gauge has slightly higher mismatch with other strain gauges. It could be possible that during phase of holes drilling by electrical discharge machining in metal T plates, it was strained or damaged by heat. Other possibility is that it was just production variation. No matter the reason, resistor had to be placed to lower the offset for one axis. Since mismatch is only about 0.1 to 0.2 Ω multi turn trimmer of 10 Ω were used. As it can be seen in Fig. 4, two trimmers per sensor set were used for two reasons. Firstly, with small turns, big jumps in trimmer resistance occurs when near zero resistance is desired at trimmers. Even in 25 turns trimmer. By adding extra offset with second 15 turn trimmer, of about 0.3-0.5 Ω , a more precise offset cancelation was achieved. Trimmer with lower numbers of turns are cheaper and could be used for this trimmer. Second reason is that flexibility is made due to no special attention to strain gauge placement is needed. Also this is the reason for placing the other pair of trimmers for the second axis' gauges. Besides, the second pair of trimmers was used to lower small offset of 0.5 V in amplified voltage for second axis. It was not really necessary and could have been removed after the software calibration.

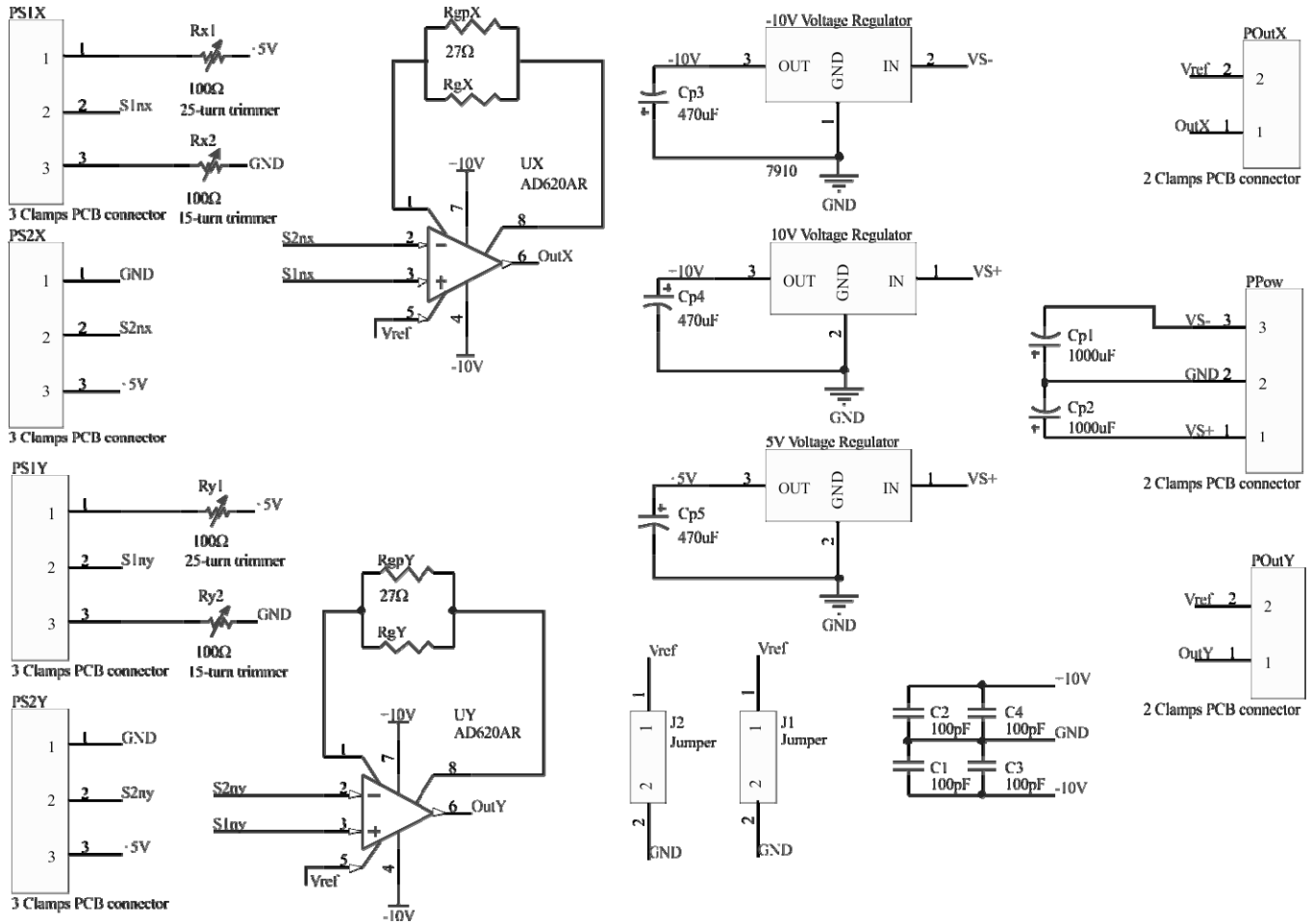


Fig. 4. Schematic diagram of sensor's system electronic.

I. MEASUREMENT

A. Setup

Matlab and Simulink software are used to collect data from Humusoft card. Simulink and Real Time Windows Target were chosen for data collection and processing, and control for force feedback joystick because they offer a flexible framework, easy programming, and C code generation for later uses. Besides, Matlab Virtual Reality Toolbox is planned to generate data for later simulation and testing of force feedback joystick.

Digital filter processing is needed to remove intrinsic resistor noise and EMI. Since both of these noises were unknown until completion of electronic and tasting, GUI based digital filter processing and implementation tool was designed in Matlab. Main task of this tool was to:

- acquire various length of data and truncate initial values,
- show graphically acquired data and its spectrum,
- design filter block for Simulink model and test it by filtering acquired data,
- view graphically filtered data and its spectrum,

- implement designed filter block into Simulink model for calibration, and control.

For calibration purpose a GUI based tool was designed that:

- acquire data for both axes,
- truncate variations induced by filter; initial conditions are all zeros which will create sort of step input data,
- finds mean value for truncated filtered data and maximal deviation,
- stores data for force of various intensity and direction applied on handle in table, that can be saved in excel document,
- it presents results for various force measurements in a concise and informative manner.

Since no precise force reference was available, the testing and calibration method was then based on gravity force and known weights. Handle was screwed tight at the end of horizontal threaded rod, as shown in Fig. 5 and 6. Arrow pointer, made from bended sheet of metal, was put on to rod and fastened with two nuts. The rod was placed through hole of vertical wooden plate. It was fastened with nut from handle side of wood and with butterfly nut from the other side. By using butterfly nut, for easy loosening and tightening, rod can

be easily rotated horizontally. From the front side of the wooden plate, as marked in Fig. 5, a radial scale was attached. Scale has lines radiating from the rod's hole. Solid lines mark 10° increment. Dotted lines mark 5° increments in between of solid ones. In this way the pointer rod can be rotated at 5° and 10° increments with estimated precision of $\pm 1^\circ$. Vertical wooden plate is attached firmly to horizontal one that has counter weight at opposite end. Since no upper part of handle had been made yet a screw was screwed at the most upper T plate holder. Weight was hanged via string to this screw. Aware of change of lever and thus the moment, weight was increased proportionally. The desired maximal weight to be measured was 2 kg at the center of handle. Equivalent to this is approximately 4 kg at the screw.

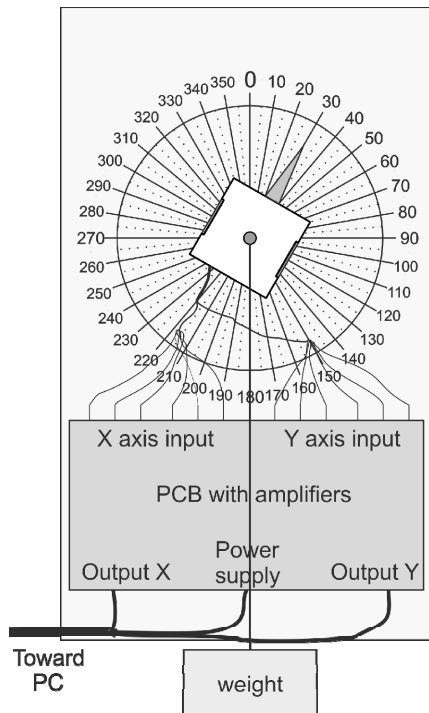


Fig. 5. Testing and calibration setup's front view.

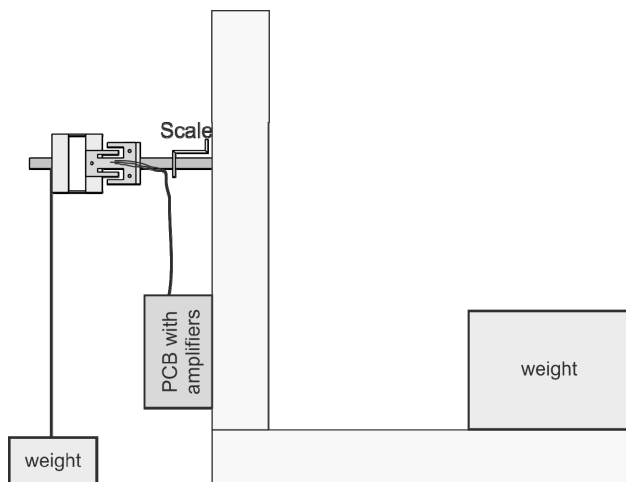


Fig. 6. Testing and calibration setup's side view.

The sling was made as short as possible. Unfortunately, even small oscillations were detected. Long settling times were required especially for heavier mass. Settling time for maximal mass of 4 kg was about 5 min in average when careful rotation was done. So the data set for calibration was planned with awareness of long waiting time. Nice linearity was already observed in the phase of electronics testing. Having that in mind it was estimated that only 4 distinct weights were good enough both for calibration and testing. Although nice sinusoidal characteristic for angular change in force was noticed angle in increments of 10° were chosen in order to achieve better visual effect of plotted data, and accuracy as well.

B. Result

Graphical representation of some of the measured data is given in Figs 7 and 8. The linearity of data is almost perfect for a set of masses at constant angle. Angle is measured between vertical axis and the scale's arrow in clockwise direction. For example, 0° is equivalent to maximal force on Y axis and no force on X axis. Sensor's voltage for both axes, for reference angle of 0 degrees and weight set of 0, 0.5, 1 and 4 kg, are shown in Fig. 7. This data set is characteristic. It clearly shows that angle offset exist for X axis. The same applies for Y axis.

Also, nice sinusoidal result can be seen for constant mass and angles varying from 0° to 350° . One set of sinusoids for weight of 1 kg is shown in Fig. 8. A plain sinusoid was fitted in X axis sinusoid from Fig. 8. Difference between measured data and fitted sinusoid is shown in Fig. 9. Since majority of values from Fig. 9 are below zero it can be deduced that beside angle offset there is a DC offset as well. Same procedure proves existence of small Y axis offset.

C. Sources of errors

Further data analysis is on the way. Even now we know some apparent source of errors that can be removed if measuring setup is enhanced. For instance some slight bending of rod was detected when heavier masses were applied. This will cause nonlinearity in mass-voltage characteristic. This error can be removed if vertical wooden plate is replaced with metal one with tighter hole, and if the rod length is shorten. Also the vertical plate was not ideally parallel with vector of gravity force and sometimes it moved a little because it was not firmly fixed. So with little more time and money accuracy of system can be enhanced. However for now we assume that hand tremor will produce more noise than the current level of accuracy. Much in the same way the pendulum had affected the measurements.

To sum up, most of our error sources can be removed, although it is not currently needed, since we achieved what we desired.

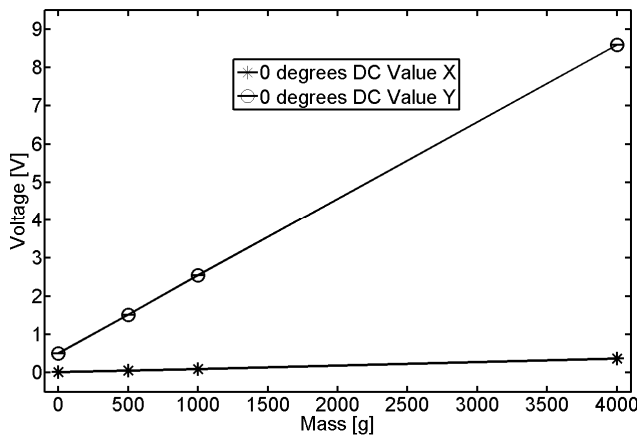


Fig. 7. Sensor's voltage for 0 deg and 0, 0.5, 1 and 4 kg of weight.

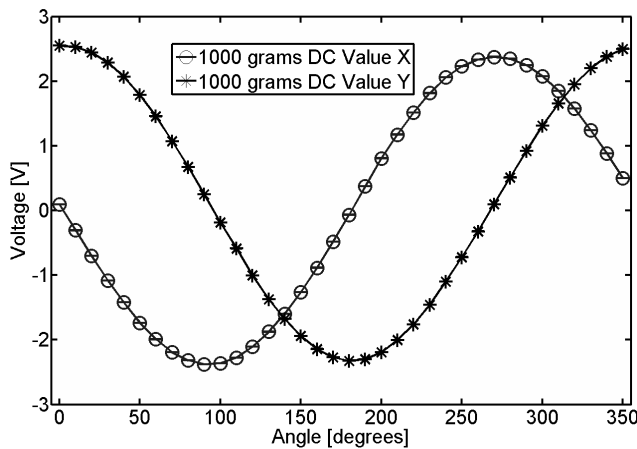


Fig. 8. Sensor's voltage for 0° to 350° and 1 kg of weight.

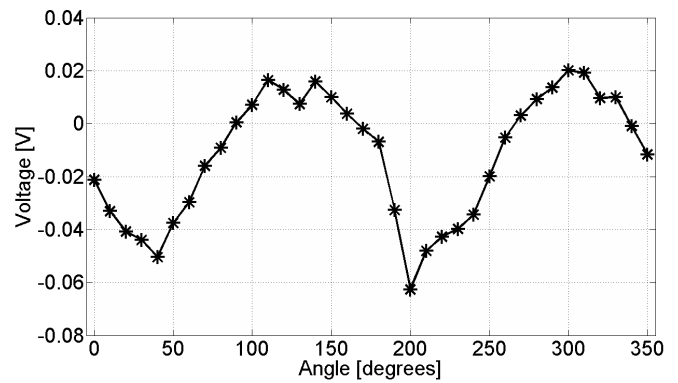


Fig. 9. Difference between measured X axis data from Fig. 8 and plain sinusoid fitted into it.

II. CONCLUSION

Design of inexpensive force sensors system to be used in feedback joystick for medical applications is discussed in the paper. We showed that it is possible to make a force sensing system out of a low-cost kitchen scale strain gauges. Visual representation of measured data showed that notable linearity is acquired. For constant force direction change from 0° to 350° sinusoidal voltage dependency occurs. Further data analysis is currently on the way. Calibration models are being further improved. Although we obtained promising results it was not our intention to replace high quality sensors available on the market, like ATI automation's f/t sensors. They are able to measure force and torque in 3 axes with great precision but due to the silicon strain gauge technology, they cost a fortune. Solid precision sensors for measuring force in 2 axes are acceptable starting solution in force feedback joystick for remote simple medical procedures that require only rotation of the tool.

REFERENCES

- [1] A. K. Thorsten, *Engineering Haptic Devices*, Springer, 2009.
- [2] A. L. Window, *Strain gauge technology*, Springer, 2nd edition, 1992.
- [3] M. Tavakoli, *Haptics for Teleoperated Surgical Robotic Systems*, World Scientific, 2008.
- [4] A. Pytel, J. Kiusalaas, *Engineering Mechanics: Dynamics*, Cengage Learning, 3rd edition, SI edition, 2010.
- [5] "Strain gauge: Sensitivity." Internet: www.efunda.com/designstandards/sensors/strain_gages/strain_gage_sensitivity.cfm [Apr. 15, 2011].

Two Dimensional Finite Element Method-Based Simulation of the Brownian Motion of a Spherical Particle in Water

Katarina Radulović and Sylvia Jeney

Abstract—One of the most attractive experimental methods for measuring the forces starting in the subnano range is photonic force microscopy (PFM). A proper use of the PFM is based on tracking movements of test particles in a given environment that is essentially Brownian. Brownian motion of test particles can be used for calibration and for determination of viscoelastic parameters of the environment. Our goal is to determine the two-dimensional mean square displacement (MSD) of a spherical silica particle in water which is subject to random thermal forces. The problem is modeled and simulated in commercial software package ANSYS 12.1-Mechanical APDL.

Index Terms—Brownian motion, finite element method modeling, optical tweezers, particle tracking, photonic force microscopy.

I. INTRODUCTION

THE Atomic Force Microscope (AFM) was considered to be the ideal tool for physical studies of live biological specimens. However, the rough surface of a cell often prevents the tip of a mechanical cantilever from following the fine topographic details. Furthermore, forces of several tens of piconewtons can deform soft cellular structures, such as the plasma membrane. Therefore, a scanning probe microscope without a mechanical contact, which works with extremely small loading forces, is desirable. Such an instrument, the Photonic Force Microscope (PFM), has been developed at the European Molecular Biology Laboratory (EMBL) in Heidelberg ten years ago [1]. This three-dimensional scanning probe technique is based on optical tweezers (OT), scientific manipulation technique that uses a highly focused laser beam to provide an attractive or repulsive force to physically hold and move small objects [2]. Small objects like nano-particles, living cells, bacteria and viruses in physiological solution can be manipulated and positioned in 3D with a precision of a few

nanometers [3]. Compared with AFM techniques, the mechanical cantilever of the AFM is replaced with optical tweezers and the cantilever tip by a trapped bead. The optical forces generated by an OT are typically in the piconewton range, making it an ideal tool for studying the mechanics of individual molecules. In the same time, an optically trapped dielectric particle acts as a probe, which, driven by thermal noise (Brownian motion), scans its local environment in a volume determined by the optical trap. In that way, the viscoelastic parameters of the environment can be obtained. This approach, called microrheology, typically measures the mean square displacement (MSD) of the Brownian particle. The optical trap is taken to be a potential well with a stiffness k , controlled by the power of a laser beam. The proper use of PFM (precisely, the proper interpretation of experimental results) needs a calibrated optical trap, that is, a precisely defined stiffness constant k . There are several ways to do this, and all of them involve the observation of the bead's Brownian motion, while it is in the trap's potential well [4]. Those are the reasons why it is so important to know the parameters of the Brownian particle's trajectory. The main problem in Brownian movement monitoring is that due to the small trapping force constants, thermal position fluctuations of the probe are relatively large in comparison to the thermal motion of an AFM cantilever. So, the three-dimensional position of the bead must be measured with a spatial and temporal resolutions in the nanometre and microsecond range, respectively.

The Brownian motion is an erratic-type motion, carried out by a particle immersed in a fluid under the effect of the collisions it undergoes with the molecules of the fluid. The origin of the random motion was first successfully explained by Einstein as the amplification of the statistical fluctuations of the surrounding fluid molecules. Since then, the theory of Brownian motion has found broad applications in the description of phenomena in many fields in science and even in financial models. Due to the fractal nature of a diffusive Brownian particle's trajectory, the length of the path traveled in a given time interval is unknown. Therefore, the particle's velocity is ill-defined, leading to confusion in early attempts to connect the particle's apparent velocity to the temperature as demanded by the equipartition theorem [5]. The mean square

K.R. wishes to acknowledge funding by the Serbian Ministry of Education and Science through the project TR 32008. Some results of this paper were presented at 55th ETRAN Conference, Banja Vrućica, June 6-9, 2011.

K. Radulović is with the ICTM – Center of microelectronic technologies and syngle crystals, Njegoševa 12, 11000 Belgrade (email: kacar@nanosys.ihtm.bg.ac.rs).

S. Jeney is with the Institut de Physique de la Matière Complexe, Ecole Polytechnique Fédérale de Lausanne (EPFL), CH-1015 Lausanne, Switzerland.

displacement (MSD), on the other hand, can be measured and it was shown by Einstein to increase linearly with time t : $\langle [x(t)]^2 \rangle = 2dDt$, where $\langle [x(t)]^2 \rangle$ is the mean square displacement (MSD) in one dimension of a free Brownian particle during time t , d is dimensionality, and D is the diffusion constant. The diffusion constant can be calculated by $D = k_B T / \gamma$, where k_B is Boltzmann's constant, T is the temperature, and γ is the Stokes viscous drag (friction) coefficient.

This stochastic description of the interactions of the particle with the surrounding fluid must break down at short timescales, where the particle's inertia becomes significant. In the inertia-dominated regime, termed ballistic, the particle's autocorrelation function has a peak. Loosely speaking, after receiving an impulse from the surrounding fluid molecules, the particle flies in a straight line with constant velocity before collisions with fluid molecules slow it down and randomize its motion.

In the ballistic regime the MSD approaches $(k_B T / m) t^2$ below the momentum relaxation time of a particle with mass m , $\tau_p = m / \gamma$. Because of the lower viscosity of gas, compared with liquid, the τ_p of a particle in air is much larger. This lowers the technical demand for both temporal and spatial resolution for measurements in a gas environment. The main difficulty of performing high-precision measurements of a Brownian particle in air, however, is that the particle will fall under the influence of gravity. This problem could be overcome by using optical tweezers to simultaneously trap and monitor a silica bead in air and vacuum, allowing long-duration, ultra-high-resolution measurements of its motion. Some recent simulations as well as experiments showed that, even for timescales much larger than τ_p , there are deviations from random diffusive behavior, originating from the inertia of the surrounding fluid, which leads to long-lived vortices caused by and in turn affecting the particle's motion [6]. These hydrodynamic memory effects introduce an intermediate regime between the purely ballistic $\sim t^2$ and the diffusive $\sim 2Dt$ scaling, where the MSD takes on a rather complicated form.

In addition, the correct hydrodynamic treatment modifies the MSD in the ballistic regime to $(k_B T / m^*) t^2$, where m^* is an effective mass given by the sum of the mass of the particle and half the mass of the displaced fluid.

The equation that successfully describes the probe motion over entire time domain is the classical phenomenological Langevin' equation. For the sake of simplicity, the one-dimensional Langevin equation is discussed:

$$m \frac{d^2 x}{dt^2} = -\gamma \frac{dx}{dt} + F(t) + F_{ext}(t) \quad (1)$$

We associate a coordinate x with the Brownian particle's position. Two forces, both characterizing the effect of the fluid, act on the particle of mass m : a viscous friction force $-\gamma(dx/dt)$, characterized by the friction coefficient $\gamma > 0$, and a fluctuating force $F(t)$, representing the unceasing impacts of the fluid molecules on the particle. The fluctuating force is

considered to be an external force, and is called the Langevin force. In the absence of a potential, the Brownian particle is said to be 'free'. In the Langevin model, the friction force γ and the fluctuating force $F(t)$ represent two consequences of the same physical phenomenon (namely, the collisions of the Brownian particle with the fluid's molecules). To fully define the model, it is necessary to characterize the statistical properties of the random force.

We assume that the average value of the Langevin force vanishes, $\langle F(t) \rangle = 0$. The autocorrelation function of the random force, $g(\tau) = \langle F(t)F(t + \tau) \rangle$ is an even function of τ , decreasing over a correlation time. The correlation time is of the order of the mean time interval separating two successive collisions of the fluid's molecules on the Brownian particle. If this time is much shorter than the other characteristic times, such as for instance the relaxation time, we can represent $g(\tau)$ as a delta function. Most often, it is also assumed, for convenience, that $F(t)$ is a Gaussian process (normal distribution). All the statistical properties of the Langevin force are then calculable if only its average and its autocorrelation function are given.

Let us assume that an external force is applied to the particle. This force $F_{ext}(t)$ adds to the random force $F(t)$. In the case of OT, $F_{ext}(t) = k x(t)$, this means that the restoring force of the optical trap is proportional to the bead displacement from its equilibrium position, the bottom of the trap's potential well.

An analytical solution for the one-dimensional Langevin' equation is known. However, the two(three)dimensional problem is too complex to be analytically solved. Therefore, we present a finite element (FE)-based simulation as a suitable tool for determining values of the parameters that can be compared with the values extracted from the experimental results on PFM.

II. SIMULATION PROCEDURE

The finite element model of the problem is given in Fig. 1. According to Maxwell fluid model, the viscoelastic material is represented by a purely viscous damper and a purely elastic spring connected in series [7]. Water is pure viscous fluid. Because of that, it is modeled by a dashpot connected with the particle at the one end, and with constrained translational degree of freedom (DOF) at the other end. For symmetric dashpots along the global X and Y directions, COMBIN14 [8] elements are used. COMBIN14 has longitudinal and/or torsional capabilities in one, two, and three dimensional applications. The element is defined by two nodes, a spring constant (k) and damping coefficients $(c_v)_1$ and $(c_v)_2$, where the damping coefficient c_v is given by $c_v = (c_v)_1 + (c_v)_2 \nu$ (ν is the fluid velocity). In these simulations, we used the linear coefficient $(c_v)_l$, only. It is equal to the friction coefficient γ given by Stokes' law (for the small spherical bead): $\gamma = 6\pi\nu R$, and depends on the shear viscosity ν of the fluid and the particle radius R . The translational displacements along X and Y, at the damper ends, are constrained (X and Y displacements

are zero, green triangles on the Fig. 1).

A thermal force load is applied in the center of the bead. To obtain X and Y components of the thermal force, F_X and F_Y , that satisfy the conditions for fluctuating random force, the Latin Hypercube Sampling method from multivariate normal distribution is used (Matlab Statistics toolbox [9]). The size (N) of the generated 2 column matrix sample (F_X , F_Y) was selected in such a way that corresponds to the length of time interval in which the simulation should be performed.

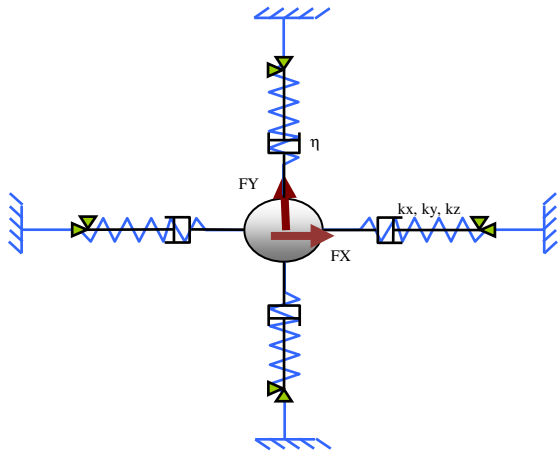
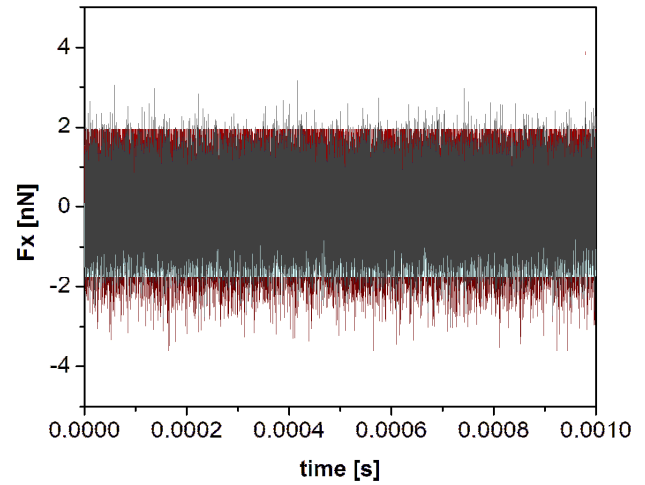


Fig. 1. Illustration of the simulated system. The viscous fluid is represented by a dashpot connected with the particle at the one end, and with constrained translational DOF at the other end. The optical trap is also symbolized by a harmonic spring.

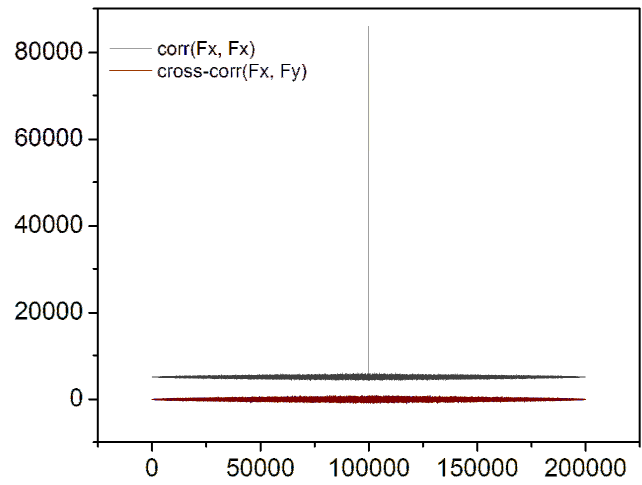
For example: time range 10ns-1ms is divided in 100,000 data points with time step (collision time) of 10 ns. For simplicity, in Fig. 2(a) the X component of the generated thermal force is shown, only, whereas in Fig. 2(b), the F_X autocorrelation and $F_X(F_Y)$ cross-correlation sequences (length $2N-1$) are shown. It is obvious that autocorrelation and cross-correlation functions of generated thermal force components are delta and zero functions, respectively. The harmonic potential of optical trap generated by OT is characterized by elastic (spring) constant k . A two-node element, COMBIN14 with elastic capabilities (spring constant

TABLE I
THE VALUES OF MATERIAL AND GEOMETRY PARAMETER USED IN SIMULATION

Material Properties	Geometry Properties
silica bead: $EY=70\text{GPa}$ Poisson ratio=0.2 $\rho=2000\text{kg/m}^3$	silica bead: $r=0.5\ \mu\text{m}$
fluid: dynamic viscosity $\nu=10^{-3}\text{Pa}\cdot\text{s}$	$L_{\text{dash-pot}}=15\ \mu\text{m}$ $L_{\text{trap}}=20\ \mu\text{m}$
optical trap: spring constant $k_x=350\ \mu\text{N/m}$ $(k_y=100\ \mu\text{N/m})$	



(a)



(b)

Fig. 2. (a) The F_X component of random thermal force. F_X is $N \times 1$ array ($N=100,000$), generated by Latin Hypercube Sampling method (Matlab Statistics toolbox), (b) The autocorrelation and cross-correlation sequences of $F_X(F_Y)$ thermal force component given in Figure 2a). The cross-correlation can be neglected compared to autocorrelation delta peak.

defined) is used for modeling optical trap. In the case of symmetric (spatial homogeneity) optical trap, spring constants in both X and Y directions are the same ($k_x=k_y$). The strength of optical trap depends on the spring constant value.

In Table I, the values of material and geometry parameter used in simulation are given.

A structural transient analysis is performed with multiple load steps using DO loop. Time step and number of steps had to be selected to meet the available computer resources. The maximum number of steps is limited to 100,000. Depending on the time range, for the collision time, values of 10, 50 or 100 ns were chosen (time ranges: 10 ns – 1 ms, 50 ns – 5 ms, and 0.1 μs – 10 ms). As the results of simulations, the displacements in both X and Y directions are obtained.

As an example, in Fig. 3 the displacements in both directions (X and Y) for “free” 0.5 μm silica particle in water under thermal fluctuating force, are given.

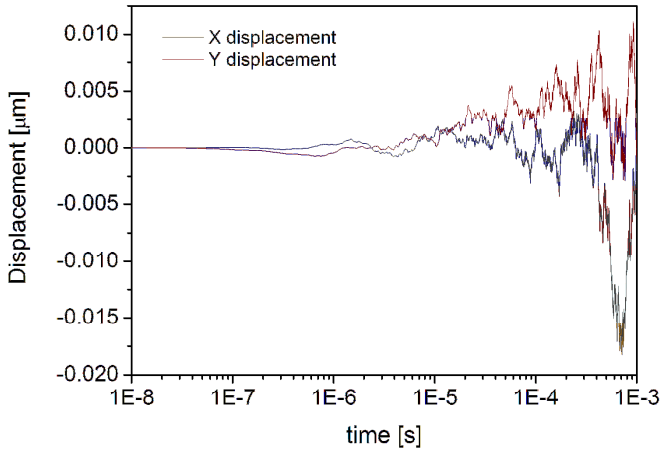


Fig. 3. The results of two dimensional finite element based simulation of Brownian motion of “free” 0.5 μm silica bead in water, under thermal fluctuating force, whose X component (FX) is given in Fig. 2(a). The term “free” means that bead is not optically trapped.

Based on the displacement values, the bead trajectories, as well as the Mean Square Displacements (MSD) are calculated.

$$MSD(\tau) = \langle \Delta r(\tau)^2 \rangle = \langle [r(t+\tau) - r(t)]^2 \rangle$$

where $r(t)$ is the position of the particle at time t , and τ is the lag time between the two positions. The average $\langle \dots \rangle$ designates a time-average over τ .

III. RESULTS AND DISCUSION

The simulations under different load conditions are performed:

- Thermal fluctuation of the silica bead in water – without optical trap
- Thermal fluctuation of the silica bead in water – with a symmetric optical trap
- Thermal fluctuation of the silica bead in water – with an asymmetric optical trap

From Brownian trajectories of both “free” silica bead and silica bead trapped by OT, given in Fig. 4 it is obvious that volume exploited by bead is determined by strength of the optical trap. Optical trap is homogeneous, $k_x = k_y$.

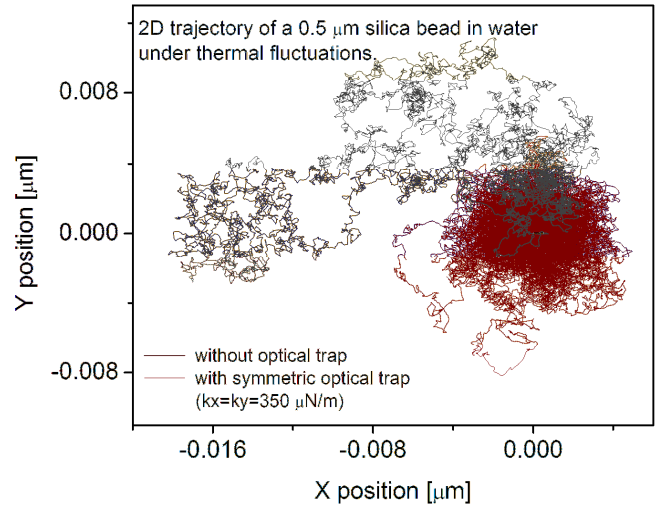


Fig. 4. Two-dimensional trajectories of a 0.5 μm “free” (gray line, top and left) and “trapped” (red line, right) silica bead in water under thermal load force. The spring constants of optical trap in both directions are the same, $k_x = k_y$ (symmetric optical trap).

Fig. 5(a) shows MSD of “free” bead as a function of time over four decades. Two regimes of the particle motion can be observed, ballistic ($t < 0.1 \mu\text{s}$) and diffusive at $t > 0.1 \mu\text{s}$. The slope of the simulated MSD curve at short time scale is double that of the MSD curve at long scale in the log-log plot. At very short time scale, MSD is predicted to be proportional to $\frac{k_B T}{m^*} t^2$ (ballistic regime). m^* is an effective mass, by which the hydrodynamic memory effect can be modeled. At the long time scale the MSD increases linearly in time (diffusive regime). Fig. 5(b) displays in more details the Brownian motion at long-time scale in linear-linear plot. The simulated curve is fitted with a linear equation ($y = a + b \cdot x$), and the value of slope b , 1.9134 is obtained. From the slope value, the value of diffusivity D of $4.78 \mu\text{m}^2/\text{s}$ is calculated. That is the accepted value for the viscosity of water at room temperature (Table II). MSD versus t , at short time-scale is shown in detail in Fig. 5(c)). This curve is fitted with an Allometric2 equation ($y = a + b \cdot x^c$). In the script box the values of the equation parameters are given ($c = 1.963$, $b = 3.47E6 \mu\text{m}^2/\text{s}^2$). The value of m^* can be estimated based on the value of parameter b . The value of parameter c , obtained by fitting confirms the quadratic dependence MSD(t).

The influence of optical trap symmetry on the Brownian trajectory of 0.5 μm silica bead in water is shown in Fig. 6. These trajectories are simulated over five orders of magnitude in timescale from 50 ns to 5ms (time of correlation is 50 ns).

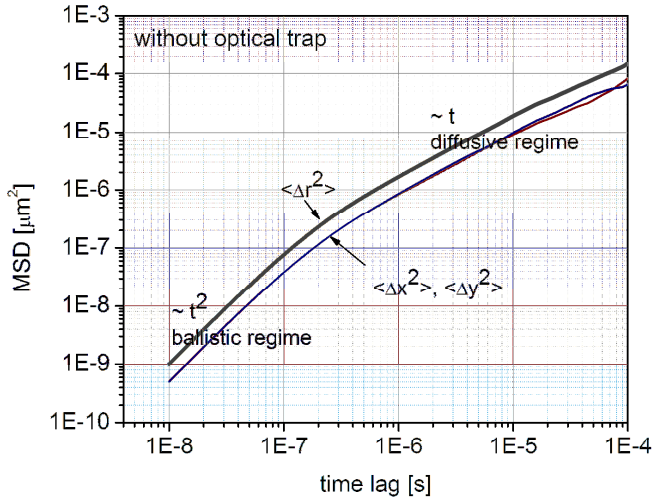


Fig. 5(a). The MSD of a 0.5 μm silica sphere in water. At long time plot ($t > \tau_p \sim 0.1 \mu\text{s}$) the slope of MSD is ~ 1 in log-log scale (diffusive regime), while at short time scale ($t < \tau_p$) the slope of MSD is ~ 2 in log-log plot (ballistic regime).

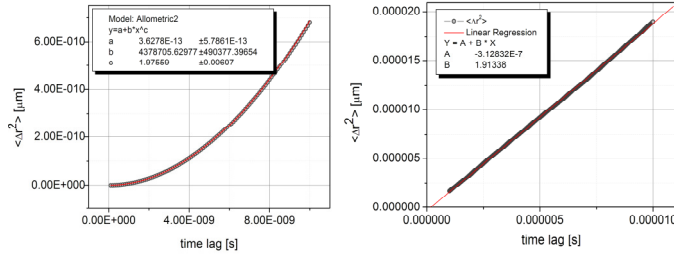


Fig. 5(b). The MSD of a 0.5 μm silica sphere in water at short time-scale given in details. $\langle \Delta r^2 \rangle$ is fitted with Allometric2 curve $a+b*t^c$, and the power c obtained by fitting is ~ 2 , that is characteristic of ballistic motion.

Fig. 5(c). The MSDs of a 0.5 μm silica sphere in water at long time scale shown in details. $\langle \Delta r^2 \rangle$ is fitted with linear curve $a+b*t$, and the slope b obtained by fitting is $\sim D$, where D is the diffusion coefficient.

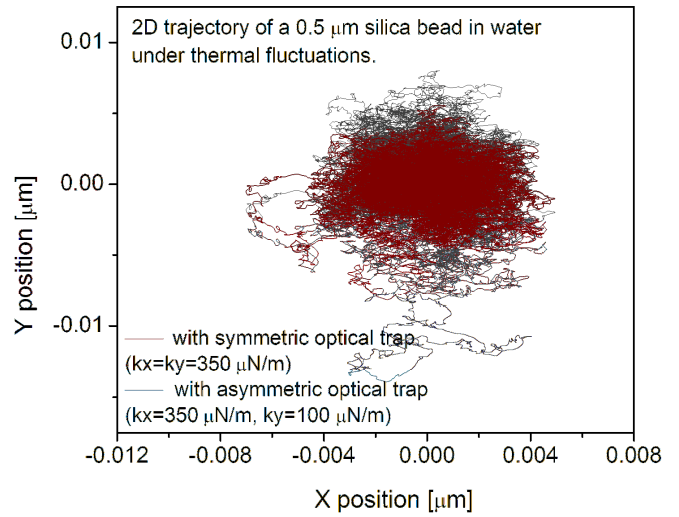


Fig. 6. Two-dimensional trajectories of a 0.5 μm silica bead in water under thermal load force, when bead is trapped by symmetric optical trap, $k_x=k_y=350 \mu\text{N/m}$ (—), and asymmetric optical trap, $k_x=350 \mu\text{N/m}$, $k_y=100 \mu\text{N/m}$ (--).

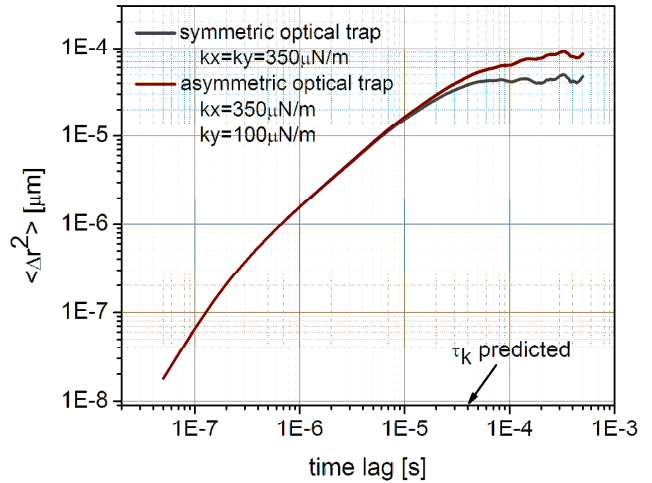


Fig. 7. The MSD of a 0.5 μm trapped silica sphere in water: (—) symmetric ($k_x=k_y$), (--) asymmetric optical trap. After time τ_k , the MSD reaches the plateau. The value of plateau depends on the spring constant of the trap.

The Fig. 7 shows that MSD in the case of optically trapped bead increase and then reach the plateau determined by optical trap strength. In the case of symmetrically trapped bead, the MSD reaches the plateau around $\tau_k = 0.05 \text{ ms}$ (the predicted value of τ_k is 0.03 ms, Table II). The values of MSD on the plateau is about $2.2 \times 10^{-5} \mu\text{m}^2$, that is in good agreement with theoretically predicted value $\frac{2k_B T}{k}$ (Table II), where k is the spring constant of the optical trap. In the case of asymmetric optical trap ($k_x=350 \mu\text{N/m}$, $k_y=100 \mu\text{N/m}$), x-position MSD reaches plateau around 0.05 ms, while y-position MSD (and therefore $\langle \Delta r^2 \rangle$) continues to grow (Fig. 7).

IV. CONCLUSION

We used a very simple Maxwell model to investigate the influence of the different parameter of the model (geometry, material properties..) on the Brownian motion of a silica bead

TABLE II
COMPARISON OF THE VALUES OF PARAMETERS THAT CHARACTERIZE THE BROWNIAN MOVEMENT OF BEAD IN WATER, UNDER THERMAL FLUCTUATION

Parameter	Value obtained by theoretical prediction	Value calculated from the results of simulations
$\tau_p = \frac{m}{\gamma}$	0.1 μs	0.08 μs
$\tau_k = \frac{\gamma}{k}$	0.027 ms	0.03 ms
Diffusion coefficient $D = \frac{k_B T}{\gamma}$	0.446 $\mu\text{m}^2/\text{s}$	0.478 $\mu\text{m}^2/\text{s}$
MSD plateau (in the case of trapped bead) $\frac{2k_B T}{k}$	2.36E-5 μm^2 ($k=350 \mu\text{N/m}$) 8.28E-5 μm^2 ($k=100 \mu\text{N/m}$)	2.2E-5 μm^2 ($k=350 \mu\text{N/m}$) 8E-5 μm^2 ($k=100 \mu\text{N/m}$)

in water under thermal fluctuating force. The parameters we can change are: the spring constants of optical trap, the bead radius, and the fluid viscosity. From Table II, it is obvious that the results of simulations are in good agreement with the theoretical predictions. The main advantage of the FE based modeling and simulation is that it can consider two(three) dimensional problem for which there is no analytical solution. An analytical solution is almost impossible to find, because the interaction of variables is not known. By changing the values of parameters in the simulation, and comparing the results with the experimental ones, the value of fluid dynamic viscosity can be obtained, if the radius of the probe, and temperature are known. Also, the FE based simulation allows to specify how the variables change with temperature, frequency... In this way it is possible to make conditions close to real experimental conditions. The main disadvantage of this simple model is that viscous fluid can be modeled as a dashpot with friction coefficient γ , in the case of small spherical particle only (Stokes law). If we have a probe of some other geometry, one of the more complicated modeling approaches must be used: solid modeling – where the surrounding medium is meshed with a finite element that supports the viscoelastic properties of materials given in terms of Prony series, or FLOTRAN analysis with Arbitrary Lagrangian – Eulerian (ALE) formulation for moving domains. By using some of these approaches, the influence of surrounding fluid would be more accurately included in the simulation. However, these

approaches make the problem very complex, because besides the load force that is complex enough, we introduce a very complex model of the surrounding fluid. In such a way, the simulations became very demanding. The authors' intention is to continue work in these directions.

REFERENCES

- [1] E.-L. Florin, A. Pralle, J. K. Heinrich Horber, E. H. K. Stelzer "Photonic Force Microscope Based on Optical Tweezers and Two-Photon Excitation for Biological Applications", *Journal of structural biology* 119, 202–211, 1997.
- [2] A. Ashkin, J. M. Dziedzic, J. E. Bjorkholm, S. Chu, "Observation of a single-beam gradient force optical trap for dielectric particles", *Opt. Lett.* 11, 288, 1986.
- [3] S. Jeney, F. Mor, R. Koszali, L. Forro, and V. Moy, "Monitoring ligand-receptor interactions by photonic force microscopy", *Nanotechnology*, 21, 255102(8pp), 2010.
- [4] S. Jeney, E.-L. Florin and J.K.H. Horber, "Use of Photonic Force Microscopy to study single-motor-molecule mechanics", *Kinesin Protocols, I. Vernos*, (Humana Press, Totowa, NJ, 2000) pp.91-107.
- [5] T. Li, S. Kheifets, D. Medellin, M. G. Raizen, "Measurements of the instantaneous velocity of a Brownian particle", *Science*, Vol 328, 1673-1675, 25 June 2010.
- [6] R. Huang, I. Chavez, K. M. Taute, B. Lukic, S. Jeney, M. G. Raizen and Ernst-Ludwig Florin, "Direct observation of the full transition from ballistic to diffusive Brownian motion in a liquid", *Nature Physics*, 27 March 2011, doi:10.1038/NPHYS1953
- [7] M. Grimm, S. Jeney, T. Franosch, "Brownian motion in a Maxwell fluid", *Soft Matter*, 7, 2076-2084, 2011, doi:10.1039/c0sm00636j
- [8] ANSYS Release 12.1
- [9] Matlab Release 2007.

An Adaptive Clustering Procedure with Applications to Fault Detection

Milan R. Rapaić, Milena Petković, Zoran D. Jeličić, and Alessandro Pisano

Abstract—A novel adaptive clustering procedure is presented in this paper. Among the basic properties of the proposed algorithm is that the number of clusters is not known a priori, it is updated automatically based on the available data. Previous knowledge regarding data source (data generating process), if available, can be used for initialization purposes. However, the algorithm can be used even if such information is not available. The entire data set need not be known in advance, and further, the algorithm does not store previously seen data points. The computation complexity is relatively low and the entire procedure may be implemented recursively (in “real-time”). The proposed procedure is designed primarily for condition monitoring and fault detection in industrial plants. Performances of the proposed algorithm have been demonstrated by an illustrative example.

Index Terms—Classification, clustering, novelty identification, fault detection and isolation (FDI), condition monitoring.

I. INTRODUCTION

A NUMBER of classification and clustering techniques have been applied successfully in various fields of science and engineering. A general overview of different statistical procedures can be found in [1], while a gamut of soft computing techniques, including techniques based on artificial neural networks, support vector machines (SVMs) and fuzzy logic, is presented in [2].

Most of the proposed techniques are capable of distinguishing among several fixed and *a priori* known classes (cluster centers). There are however cases in which all classes are not known in advance, and also cases where the properties of the existing classes change (evolve) over time. In such cases it would be preferable to use a classification algorithm which is capable of learning from the input data stream and evolving

(adapting) with it.

Fault detection and isolation (FDI) is an important field of modern process engineering. A survey of modern approaches to fault diagnosis can be found in [3]-[5]. It has been claimed [3] that any fault diagnosis technique can be seen as (or at least reduce to) a classification procedure: a fault is either present or it is not. A more sophisticated diagnosis classifier would even be capable of distinguishing among different types of faults, and thus perform fault isolation. However, it is rather difficult to develop a diagnosis procedure which would be capable of identifying novel faulty conditions, ones not seen during design phase. Also, most FDI techniques are incapable of coping with the drift of some of the existing working conditions. The ability to identify novelties and adapt to the changing environmental conditions is identified as one of the desirable features of any fault diagnosis technique [3].

The aim of the present paper is to present an adaptive clustering procedure capable of identifying novelties and respond to changes in the input data stream. When applied in an FDI setting, the proposed procedure should be capable of detecting working conditions which occur for the first time during the exploitation of the algorithm. These newly recognized working conditions can be labeled as either nominal or faulty by an experienced operator. The proposed technique can be seen as an evolving classifier and is inspired by the on-line identification procedure proposed by Angelov and Filev in [6], as well with the *eClass* family of evolving fuzzy classifiers [7]. It is also of interest to note that a preliminary version of the proposed algorithm has been addressed also in [8] and [9], where a number of experimental case studies have been considered. The proposed technique may be seen as an alternative to the classical model-based fault detection techniques [10] and also to hybrid fault detection techniques, such as the one presented in [11].

The key underlying notion of information potential is introduced in Section II. The information potential used here is different than the information potential utilized in [7]. The general structure of the proposed adaptive clustering procedure is presented in Section III. Specialization of the proposed algorithm for FDI purposes is described in Section IV. Experimental results are presented in Section V. Concluding remarks are left for Section VI.

M.R.R., M.P. and Z.D.J. would like to acknowledge financial support of Serbian Ministry of Science and Technological Development, grant no. 32018. Some results of this paper were presented at 55th ETRAN Conference, Banja Vrućica, June 6-9, 2011.

M. R. Rapaić is with Computing and Control Department, Faculty of Technical Sciences, University of Novi Sad; Trg Dositeja Obradovića 6. 21000 Novi Sad (phone: 303-555-5555; fax: 303-555-5555; e-mail: rapaja@uns.ac.rs).

M. Petković is with Computing and Control Department, Faculty of Technical Sciences, University of Novi Sad (e-mail: milena5@uns.ac.rs).

Z. D. Jeličić is with Computing and Control Department, Faculty of Technical Sciences, University of Novi Sad (e-mail: milena5@uns.ac.rs).

A. Pisano is with Department of Electrical and Electronic Engineering (DIEE), University of Cagliari, Cagliari, Italy.

II. INFORMATION POTENTIAL

In [7] Angelov and Filev proposed an adaptive clustering procedure relying on the notion of the **information potential**. An information potential of a point with respect to an ordered set of points is a *measure of similarity* between the point and the set. If the information potential of a point is high, the point is representative with respect to other points within the set. Points with the highest values of the information potential are candidates for cluster centers.

Let us define the notion of the information potential more formally. Consider a set of n *features*, each of which is represented as a real number. The *feature space* \mathcal{F} is therefore a subset of \mathcal{R}^n . Let $\mathbf{z} \in \mathcal{F}$ be an arbitrary *feature vector* and let $\mathcal{Z} = \{\mathbf{z}_j \mid j = 0..N\} \subseteq \mathcal{F}$ be an ordered set of known feature vectors. The assumption is that the classification is made on-line, recursively as each new feature point becomes available. Elements of the feature set are ordered in the same sequence they become available: \mathbf{z}_0 is the first obtained feature vector, \mathbf{z}_N is the most recent one. In order to emphasize the generality of the proposed classifier, the feature vectors will be denoted simply as the *data points*.

The **mean square distance** of a data point \mathbf{z} with respect to the ordered data set \mathcal{Z} is defined as [7]

$$S(\mathbf{z}, \mathcal{Z}) = \frac{1}{N+1} \sum_{j=0}^N \|\mathbf{z} - \mathbf{z}_j\|^2, \quad (1)$$

where $\|\cdot\|$ denotes the standard Euclidean 2-norm,

$$\|\mathbf{x}\| = \sqrt{\mathbf{x}^T \mathbf{x}} \quad (2)$$

and T in superscript denotes matrix- (or in this case, vector-) transposition. As usual, all vectors are implicitly assumed to be column-vectors. Angelov and Filev defined the information potential as a Cauchy-type function of the mean square difference

$$P(\mathbf{z}, \mathcal{Z}) = \frac{1}{1 + S(\mathbf{z}, \mathcal{Z})}. \quad (3)$$

The important property of the information potential is that its value cannot change abruptly. The information potential is computed with respect to all previously seen data points, and thus if the underlying data shift in the feature space, it would take some time for the value of the information potential to reflect this change. Normally this is good and desirable, since it is the basic mechanism providing resilience to measurement noise. Any outliers, invalid and noisy data points, would typically be isolated and thus would not have the capability of significantly changing potential values. However, in the fault diagnosis setting, the fact that all previous data points are taken into consideration may impose a significant drawback. It is the nature of faults to appear after long periods of nominal process operations. Depending on the sampling rate, after some operation time the nominal data points in \mathcal{Z} will vastly outnumber faulty ones. Consequently, the ability of the average square distance (and thus also the information

potential) to detect changes in the feature data stream will be impaired.

To overcome this problem, the notion of mean square distance will be redefined in the current paper. Let us define the **exponentially windowed mean square distance** between an arbitrary data point \mathbf{z} and all data points belonging to \mathcal{Z} as

$$S(\mathbf{z}, \mathcal{Z}, \lambda) = (1 - \lambda) \sum_{j=0}^N \lambda^{N-j} \|\mathbf{z} - \mathbf{z}_j\|^2 \quad (4)$$

where $\|\cdot\|$ may, in principle, denote an arbitrary norm in the feature space. In the sequel, however, $\|\cdot\|$ will always denote the **weighted Euclidean 2-norm**, defined as

$$\|\mathbf{x}\| = \sqrt{\mathbf{x}^T \mathbf{W} \mathbf{x}} \quad (5)$$

with \mathbf{W} being a suitably chosen, positive definite, symmetric matrix. Practically, the weight matrix is usually diagonal, and serves the purpose of data scaling. Thus, the overall mean square distance (1) is replaced by the mean square distance (4) which effectively takes into consideration the recent points only. In fact, only the points appearing within an exponential time window are accounted for. The parameter λ controls the width of this window and has the same purpose as the forgetting factor in the recursive least squares algorithm. The λ parameter should be chosen in range $[0,1]$ Depending on the sample rate, the noisiness of the signal and the dynamics of the process, the usual choice is between 0.9 and 1.

The information potential can be defined as a Cauchy function of the newly introduced exponentially weighted mean square distance (3). This is the approach proposed in [7] and also used in [9]. It is however also possible to use other, more general definitions. Let us define the potential of a data point \mathbf{z} with respect to the data set \mathcal{Z} as a positive, real-valued mapping of the exponentially weighted mean square distance, $P(\mathbf{z}, \mathcal{Z}, \lambda) \equiv P(S(\mathbf{z}, \mathcal{Z}, \lambda))$, with the following properties: for all $S \geq 0$,

$$(P1) \quad P(S) \in [0,1],$$

$$(P2) \quad P(S) = 1 \Leftrightarrow S = 0$$

$$(P3) \quad P(S) = 0 \Leftrightarrow S \rightarrow \infty$$

$$(P4) \quad P \text{ is a differentiable, monotonically decreasing function of } S, \quad P'(S) < 0.$$

The first property (P1) simply states that a potential takes values from a compact set $[0, 1]$. The property (P2) states that a point \mathbf{z} has the potential equal to 1 if and only if all the points in \mathcal{Z} are equal to \mathbf{z} , i.e. if and only if for all $\mathbf{z}_j \in \mathcal{Z}$, $\mathbf{z} = \mathbf{z}_j$. (P3) states that the potential becomes equal to zero if and only if the distance to at least some point in \mathcal{Z} grows without an upper bound; a situation which is not to be expected in practice. (P4) implies that there is a well-defined

inverse function $P^{-1} : [0, 1] \rightarrow [0, +\infty]$. It is easily seen that the Cauchy-type function (3) satisfies requirements (P1)-(P4).

Any functions satisfying properties (P1)-(P4) can be considered as a mean proximity measure. In fact, the clustering procedure can be designed solely on the basis of the mean square distance, but it is more convenient to use the notion of the information potential. By using the information potential, the proposed algorithm can be tightly related to the entire family of fuzzy classifiers, as well as to the evolving eClass classifiers [2], [7].

An important property of the previously introduced average square distance and information potential is that it is possibly to compute them recursively. In other words, any classification algorithm which is based on them can be implemented in real time. This is shown by the following two theorems. The following conventions be adopted in the proof: $P(\mathbf{z}, \mathcal{Z}_k, \lambda) \equiv P_k(\mathbf{z})$, $S(\mathbf{z}, \mathcal{Z}_k, \lambda) \equiv S_k(\mathbf{z})$.

Theorem 1. Let $S(\mathbf{z}_k, \mathcal{Z}_k, \lambda) \equiv S_k(\mathbf{z}_k) \equiv S_k$ be defined by (4), and let the norm be defined as in (5). The following recursion holds

$$S_k = \lambda S_{k-1} + 2\lambda(1-\lambda)(\mathbf{z}_k - \mathbf{z}_{k-1})^T \mathbf{W} \mathbf{F}_k + \lambda(1-\lambda) \|\mathbf{z}_k - \mathbf{z}_{k-1}\|^2 Z_k, \quad (6)$$

$$S_0 = 0, \quad (7)$$

$$\mathbf{F}_k = \lambda \mathbf{F}_{k-1} + \lambda Z_{k-1} (\mathbf{z}_{k-1} - \mathbf{z}_{k-2}), \quad (8)$$

$$\mathbf{F}_0 = \mathbf{0}, \quad (9)$$

$$Z_k = \lambda Z_{k-1} + 1, \quad (10)$$

$$Z_0 = 0. \quad (11)$$

Proof. The key point is to note that

$$\begin{aligned} \|\mathbf{z}_k - \mathbf{z}_j\|^2 &= (\mathbf{z}_k - \mathbf{z}_j)^T \mathbf{W} (\mathbf{z}_k - \mathbf{z}_j) \\ &= (\mathbf{z}_k - \mathbf{z}_{k-1} + \mathbf{z}_{k-1} + \mathbf{z}_j)^T \mathbf{W} (\mathbf{z}_k - \mathbf{z}_{k-1} + \mathbf{z}_{k-1} + \mathbf{z}_j) \\ &= \|\mathbf{z}_k - \mathbf{z}_{k-1}\|^2 + 2(\mathbf{z}_k - \mathbf{z}_{k-1})^T \mathbf{W} (\mathbf{z}_k - \mathbf{z}_j) \\ &\quad + \|\mathbf{z}_{k-1} - \mathbf{z}_j\|^2 \end{aligned}$$

By means of the above expression, it is readily obtained that

$$\begin{aligned} S_k &= (1-\lambda) \sum_{j=0}^k \lambda^{k-j} \|\mathbf{z}_k - \mathbf{z}_j\|^2 \\ &= (1-\lambda) \sum_{j=0}^{k-1} \lambda^{k-j} \|\mathbf{z}_k - \mathbf{z}_j\|^2 \\ &= (1-\lambda) \|\mathbf{z}_k - \mathbf{z}_{k-1}\|^2 \sum_{j=0}^{k-1} \lambda^{k-j} \\ &\quad + (1-\lambda) 2(\mathbf{z}_k - \mathbf{z}_{k-1})^T \mathbf{W} \sum_{j=0}^{k-1} \lambda^{k-j} (\mathbf{z}_k - \mathbf{z}_j) \\ &\quad + (1-\lambda) \sum_{j=0}^{k-1} \lambda^{k-j} \|\mathbf{z}_{k-1} - \mathbf{z}_j\|^2 \end{aligned}$$

By defining

$$\begin{aligned} Z_k &= \sum_{j=0}^k \lambda^{k-j} \\ \mathbf{F}_k &= \sum_{j=0}^k \lambda^{k-j} (\mathbf{z}_k - \mathbf{z}_j), \end{aligned}$$

the recursive expressions (6), (8) and (10) are obtained using simple algebraic manipulations.

Theorem 2. Let $S(\mathbf{z}_i^*, \mathcal{Z}_k, \lambda) \equiv S_k(\mathbf{z}_i^*)$ be defined by (4), and let the norm be defined by (5). Then

$$S_k(\mathbf{z}_i^*) = (1-\lambda) \|\mathbf{z}_k - \mathbf{z}_i^*\|^2 + \lambda S_{k-1}(\mathbf{z}_i^*). \quad (12)$$

Proof. By definition,

$$S_k(\mathbf{z}_i^*) = (1-\lambda) \sum_{j=0}^k \lambda^{k-j} \|\mathbf{z}_i^* - \mathbf{z}_j\|^2.$$

The recursive form is obtained by extracting the most recent term in the sum

$$\begin{aligned} S_k(\mathbf{z}_i^*) &= (1-\lambda) \sum_{j=0}^{k-1} \lambda^{k-j} \|\mathbf{z}_i^* - \mathbf{z}_j\|^2 + (1-\lambda) \|\mathbf{z}_i^* - \mathbf{z}_k\|^2 \\ &= \lambda(1-\lambda) \sum_{j=0}^{k-1} \lambda^{k-1-j} \|\mathbf{z}_i^* - \mathbf{z}_j\|^2 + (1-\lambda) \|\mathbf{z}_i^* - \mathbf{z}_k\|^2 \end{aligned}$$

which is equivalent to (12).

The two theorems above testify that it is possible to implement a recursive clustering procedure based on an arbitrary potential function provided it depends solely on the exponentially windowed mean square distance (4). The Theorem 1 shows how to compute the potential of the new feature vector, while the Theorem 2 shows how to recursively update the potential of the cluster centers.

III. GENERAL STRUCTURE OF THE PROPOSED ADAPTIVE CLUSTERING ALGORITHM

The information potential defined in the previous section reflects a measure of similarity between the current and recent process behavior. If the information potential of the feature point associated with the current process behavior is high, then there has not been any sudden change in the process behavior. If, however, the potential of the current feature is low, then the abrupt change in process behavior is likely to have happened in recent past.

The algorithm itself keeps track of a certain number of data points (features) which previously had high values of the information potential. These features will be referred to as **focal points** or **foci**, and sometimes also as **nodes**. Each node is, in fact, a feature vector found to be the most representative for certain area of the feature space (and thus for certain working condition in the FDI setting). The set of all nodes defines the underlying **knowledge base** of the algorithm.

Information potential is computed recursively for each of the existing nodes using Theorem 2. The **active node (active focus)** is the one with the highest value of the information potential. The **estimated current working condition** is the

condition associated with the active node. Thus, the classification is performed in a *winner-takes-all* manner.

In order to provide adaptability the information potential is also computed for the most recently observed feature point (the **current feature**). If this information potential is high, *higher than the potential of any of the existing feature points*, the current feature vector is more representative of the current working regime than any of the focal points present: *the knowledge base of the algorithm should be modified*. The modifications can be twofold. If some of the previously seen clusters changed slightly, or if a better representative of an existing cluster is found, the position of some focal points changes, but the knowledge base remain of the same size. If, however, a new cluster (potentially, a new working condition) is found, the knowledge base grows. More precisely, if the current working condition is similar to some of the existing nodes, the existing node is replaced by the current feature vector. If, on the other hand, the current feature is far from any of the existing nodes, the current feature is proclaimed as the new focal point and the underlying data structure of the algorithm grows. The pseudo-code of the algorithm is presented in Listing 1.

The algorithm may be initialized on the basis of *a priori* knowledge. In this case, the initial nodes are selected as the expected positions of typical cluster centers in the feature space. In the FDI setting, the initial nodes should be selected so to correspond to nominal working conditions and also to the typical faults. If, however, a priori knowledge is not available, the algorithm may be left uninitialized. In such a case, the first feature vector is selected as the initial node.

Listing 1. *Pseudo-code of the proposed adaptive clustering procedure.*

1. Choose an appropriate feature generator.
2. Choose algorithm parameters.
3. Initiate the knowledge base
4. **BEGIN LOOP**
5. Obtain current feature vector
6. Compute, on the basis of Theorem 1, the information potential of the current feature vector.
7. Compute, on the basis of Theorem 2, the information potential of the existing nodes.
8. **IF** the information potential of the current feature vector is higher than the information potential of all existing nodes **THEN**
9. **IF** the current feature vector is close to some of the existing nodes **THEN**
10. Modify the knowledge base: replace the closest existing node with the current feature vector
11. **ELSE**
12. Extend the knowledge base: create a new node equal to the current feature vector.
- END IF**
- END IF**
- END LOOP**

In any time instant, the number of working conditions the algorithm may identify is equal to the number of nodes. Each node is representative for a set of feature values, i.e. each node

is representative for a specific working condition of the underlying process.

The proposed algorithm, or better say its knowledge base, may be seen as an self-adaptive artificial neural network (ANN) with structure presented in Fig. 1. The hidden layer of the network contains the nodes of the algorithm. Once a new measurement is available, the existing nodes are compared to it, similar as with the radial basis function neural networks (RBF-NN). The difference is that the information potential is used as the basis for comparison, not the algebraic distance. The advantage of using the information potential is in the considerable robustness to noise and outliers [7]. Apart from that, the neural network is constantly being trained, both in the terms of its parameters (positions of the nodes in the hidden layer) as well as in terms of its structure, since the number of nodes is growing.

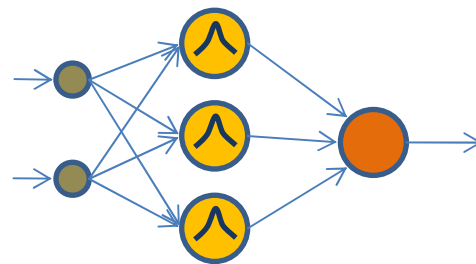


Fig. 1. The general, network-like structure of the knowledge base.

IV. SPECIALIZATION OF THE PROPOSED ALGORITHM FOR FDI

When applying the proposed adaptive clustering procedure in the field of fault detection it is important to select a **feature generator** properly. A feature generator is an algorithm, or a device, which extracts features from process measurements. In this paper, we consider faults which change the dynamic behavior of the process under consideration. Thus, it is natural to choose a *Kalman filter* [12] as a feature generator. Once the dynamic behavior of the process changes, so will the estimated values of its model parameters.

The proposed adaptive classification algorithms will search for the points in the parameter space which are most representative for current working regimes. If the underlying process is nonlinear, which is usually the case, a single working conditions may be described by multiple linear models, i.e. by several focal points in the feature space.

It is impossible for the detection algorithm to automatically detect that several focal points are in fact related to the same working condition. This should be done by an experienced operator. The operator should also be responsible for accurately describing each of the focal points, or at least as labeling them as nominal or faulty. Even more, a detailed description may be assigned to each of the recognized working conditions. In the case of faulty working regimes, the assigned description may even contain a prescription of actions needed to either fix the faulty conditions or minimize its impact. Thus, the proposed algorithm is most effective when suitably combined with expert knowledge. The overall structure of the proposed fault diagnosis system is presented in Fig. 2.



Fig. 2. The general structure of the proposed adaptive FDI scheme.

V. EXPERIMENTAL VERIFICATION

Consider the pneumatic experimental setup presented in Fig. 3. The air flow is actuated by means of a pneumatic servo-valve (**PV**), which is controlled by means of a standard current signal via current/pressure converter (**IPC**). The pressure is measured by means of a pressure meter (**PM**) and a pressure transmitter (**PT**). Behind the setup presented in Fig. 3. there is an air tank. The tank can be opened (connected to the rest of the pneumatic setup) or closed by means of a manual on/off valve (**MV**). Output valves (**OV**), simulating air consumers, are also manual.

The following experiment has been conducted. The two working conditions of the experimental setup are:

1. the air tank is opened (**O**);
2. the air tank is closed (**C**).

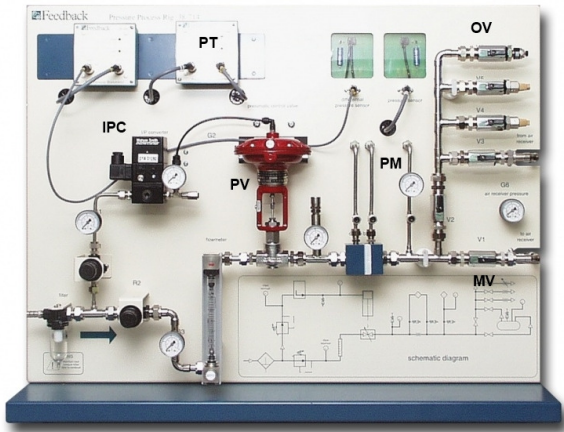


Fig. 3. The pneumatic experimental setup.

Initially, the knowledge base of the algorithm has been kept empty: the clustering procedure is unaware of both working conditions. The state of the system is changed in the manner presented in Table I. The process model is assumed in the form

$$y[k] = -a y[k-1] - b y[k-2] + c u[k-1] + d u[k-2], \quad (13)$$

where a , b , c and d are the parameters obtained by means of the Kalman filter, y is the pressure signal and u is the servo-valve command signal. The forgetting factor of the Kalman filter was selected as 0.99 . Both the system order and the forgetting factor have been selected empirically. The value of

TABLE I
THE SCHEDULE OF WORKING REGIMES IN THE EXPERIMENT

Start Time (sec)	Stop Time (sec)	Duration (sec)	Working Regime
0	325 (5 min 25 sec)	325 (5 min 25 sec)	TANK CLOSED
325 (5 min 25 sec)	460 (7 min 40 sec)	135 (2 min 15 sec)	TANK OPENED
460 (7 min 40 sec)	555 (9 min 15 sec)	95 (1 min 35 sec)	TANK CLOSED
555 (9 min 15 sec)	660 (11 min 00 sec)	105 (1 min 45 sec)	TANK OPENED
660 (11 min 00 sec)	875 (14 min 35 sec)	225 (3 min 45 sec)	TANK CLOSED
875 (14 min 35 sec)	1003 (16 min 43 sec)	128 (2 min 8 sec)	TANK OPENED

forgetting factor provided a good trade-off between detection speed and robustness to measurement noise.

Even if the process is in a fixed working regime, some time is needed for the outputs of the Kalman filter to settle to their steady-state values. During this transient, the outputs of the Kalman filter are not relevant for the actual process behavior, but are primarily influenced by the internal dynamics of the Kalman filter itself. Thus it is preferable for the clustering procedure to ignore a certain amount of data initially received from the feature generator. In the current experiment the first 1000 samples coming from the Kalman filter are discarded, and the adaptive classification is effectively initiated with 1000 samples delay with respect to the feature generation process.

The λ parameter of the proposed adaptive classification scheme is chosen to be 0.99 , the same as the forgetting factor of the Kalman filter. New focal points were introduced if the distance between the candidate focus (current feature vector with high value of the information potential) and the closest existing focal point is greater than 0.25 .

Input and output data, i.e. valve command and pressure value, measured during the experiment are presented in Fig. 4. The algorithm has been implemented on a National Instruments cRIO (Compact RIO) real time controller. The sampling rate was 0.1 sec. It is noticeable from the figures that the dynamics of the system with opened air tank is considerably slower comparing to the dynamics of the system with air tank closed. The difference in the dynamic behavior is also clearly noticeable in the outputs of the Kalman filter, presented in Fig. 5. The final results of adaptive classification are presented in Fig. 6. The parameters of each particular focal point (node) found by the adaptive classifier are presented in Table II.

TABLE II
 LINEAR MODELS OBTAINED BY THE PROPOSED ADAPTIVE CLUSTERING PROCEDURE

Model No.	a	b	C	D	Associated state
1	0	0	0	0	INITIAL
2	-1.1088	0.1203	-0.0588	0.0644	TRANSIENT
3	-1.795	0.6788	-0.0487	0.0465	TANK CLOSED
4	-1.3836	0.3834	-0.03973	0.0388	TANK CLOSED
5	-1.8992	0.9009	-0.0479	0.0479	TANK CLOSED
6	-3.9408	2.9310	-0.0667	0.0670	TRANSIENT
7	-2.7386	1.7312	-0.0009	0.0003	TRANSIENT
8	-0.5470	-0.4672	-0.0004	-0.0025	TANK OPENED
9	-0.8566	-0.1449	-0.0072	0.0036	TANK OPENED

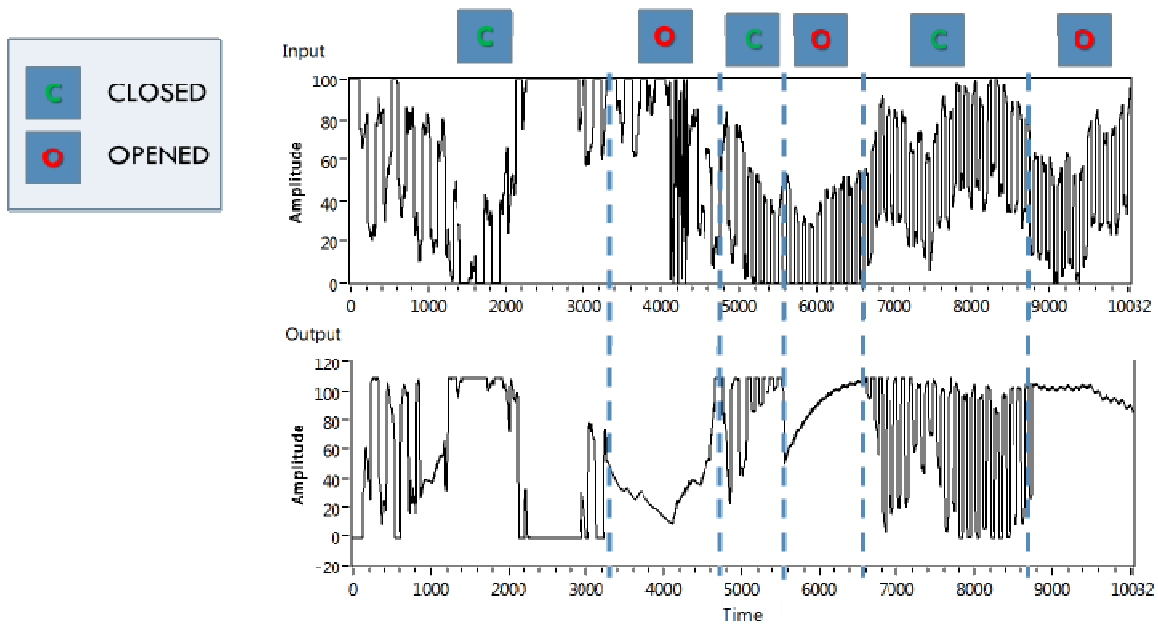


Fig. 4. Input and output data collected during the experimental run. Vertical dashed lines denote instants when the working condition has been changed. Letter above the figure denote the state of the air tank: **O** – opened, **C** – closed. The time axis shows sample indices (multiples of 100ms) from the beginning of the experiment. Vertical lines denote approximate boundaries between working conditions.

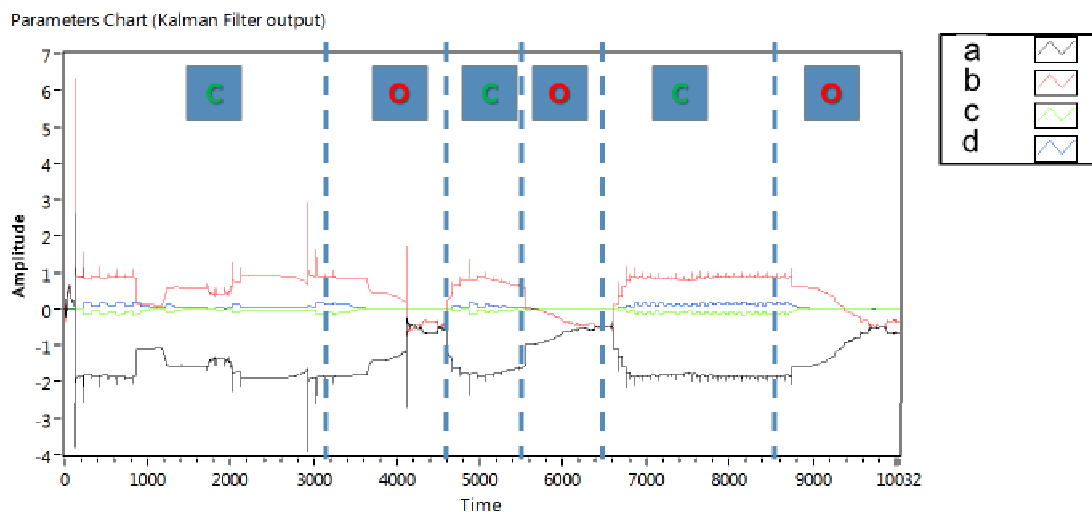


Fig. 5. Estimated values of the parameters of the second-order process model, i.e. the outputs of the Kalman filter. The time axis shows sample indices (multiples of 100ms) from the beginning of the experiment. Vertical lines denote approximate boundaries between working conditions. Upper labels denote the active working conditions: **C** denotes that the air tank is closed, **O** denotes that the air tank is opened.

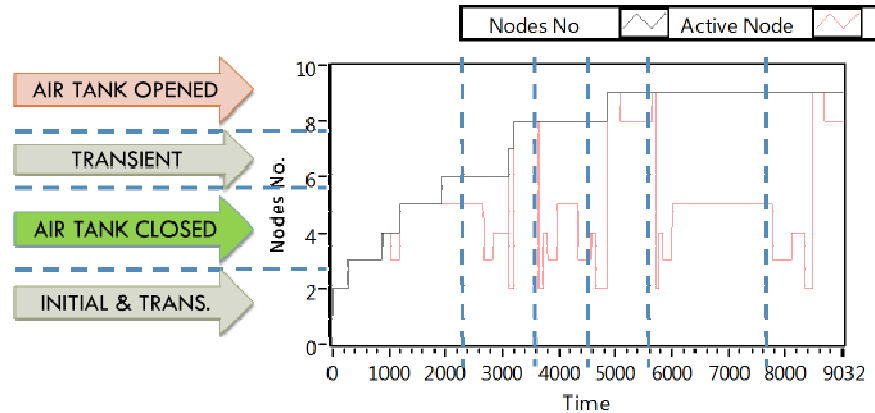


Fig. 6. The output of the proposed adaptive classification algorithm. Lower line denotes the index of the active focal point, while the upper line denotes the total number of focal points. Arrows on the left denote the focus indices corresponding to each particular working condition. The time axis shows sample indices (multiples of 100 ms).

The initial state is the one with all parameter values equal to zero. These are the initial parameters provided by the Kalman filter and it is taken as the first focus since the knowledge base is initially empty. Foci indexed 3, 4 and 5 may be associated with the working condition when the air tank is closed (disconnected from the rest of the system). Foci indexed with 8 and 9 may be associated with the working condition which is active when the air tank is opened. Multiple focal point are associated with single working condition due to the nonlinearity of the process. The association of working conditions and focal points cannot be made automatically; it should be made by an experienced operator the first time any of the focal points is detected. In this particular case, it is made after the experimental run, by observing the correlation between the actual working condition and the index of the active focus. However, once the association is created, it can be used for automatic fault detection, since during further occurrences of the same fault (or in general, of the same working condition) the regime description will remain available.

I. CONCLUSION

An adaptive classification procedure with emphasis to applications in fault detection and isolation has been presented in the current paper. The key underlying concept is the notion of the information potential (3) defined by means of exponentially weighted average distance of the current feature point with respect to the set of all previously seen features. The information potential defined in such way allows for recursive computations and thus, real-time, on-line implementation.

The fault detection algorithm based on the presented adaptive clustering procedure is capable of detecting novelties and to evolve in accordance to changes in the plant under consideration. However, the detection speed, especially when the measurement noise is high, may be low. For the example presented in this paper the detection delay is 30 seconds in

average. For some processes and in certain applications this is acceptable. However, in a number of industrial settings such a delay is too high. In such cases, one can use standard observer based detection schemes [11] and sacrifice novelty detection for speed. A hybrid approaches, which would combine the proposed algorithm with observer based strategies, would be particularly interesting and is a subject of further line of research.

REFERENCES

- [1] A. J. Izenman, "Modern Multivariate Statistical Techniques: Regression, Classification and Manifold Learning", Springer Science + Business Media, 2008
- [2] V. Kecman, "Learning and soft-computing: support vector machines, neural networks and fuzzy logic models", MIT Press, 2001.
- [3] V. Venkatasubramanian, et al, "A review of process fault detecton and diagnosys, Part I: Quantitative model-based methods", *Computers and Chemical Engineering*, 27:293-311, 2003
- [4] V. Venkatasubramanian, et al, "A review of process fault detecton and diagnosys, Part II: Qualitative models and search strategies", *Computers and Chemical Engineering*, 27:313-326, 2003
- [5] V. Venkatasubramanian, et al, "A review of process fault detecton and diagnosys, Part III: Process history based methods", *Computers and Chemical Engineering*, 27:327-346, 2003
- [6] P. P. Angelov, D. P. Filev, "An Approach to Online Identification of Takagi-Sugeno Fuzzy Models", *IEEE Transaction on Systems, Man, and Cybernetics – Part B: Cybernetics*, 34(1), 2004
- [7] P.P. Angelov, D.P. Filev, N. Kasabov (eds.), "Evolving Inteligent Systems – Theory and Applications", John Willey and Sons, Inc. 2010
- [8] FTN, Novi Sad and colaborators, "Design and implementation of real time software for patern recognition and fault detection", *Progress Report for Task 4.2, PRODI project*.
- [9] M. R. Rapaić, M. Petković, Z.D.Jeličić, "Prilagodljivi postupak za grupisanje podataka sa primena u otkrivanju grešaka u radu industrijskih procesa", Proceedings of LV ETRAN Conference, Teslić, Bosnia and Herzegovina, 2010
- [10] S.X. Ding, "Model-based fault diagnosis techniques: design schemes, algorithms, and tools", Springer Verlag, Berlin Heidelberg, 2008
- [11] M.R.Rapaić, Z.D.Jeličić, A.Pisano, E.Usai, "Second-order sliding modes and soft computing techniques for fault detection", Proc. of the 8th European Workshop on Advanced Control and Diagnosis ACD 2010, Ferrara, Italy, pp. 271-277, November 2010.
- [12] K.J.Astrom, B.Wittenmark, "Computer Controlled Systems – Theory and Design", Prentice Hall, 1997.

Schematic Representation for Illustrating the Procedure of Optical Noise Figure in Erbium-doped Fiber Amplifier (EDFA) and Praseodymium-doped Fiber Amplifier (PDFA)

Abdel Hakeim M. Husein and Fady I. EL-Nahal

Abstract—The erbium-doped fiber amplifier (EDFA) operating at 1530 nm wavelength and the praseodymium-doped fiber amplifier (PDFA) at 1300 nm wavelength are promising components for optical fiber communications due to their high gain, high saturation powers, low noise and low crosstalk. In this paper, using comprehensive models which take into account the spectroscopic properties of the fiber amplifiers, we have analyzed the temperature-dependent noise figure effects on both EDFAs and PDFAs.

Index Terms—EDFA, PDFA, gain, noise, noise figure.

I. INTRODUCTION

RARE earth doped fiber amplifiers and lasers are important tools in understanding and designing new optical devices. EDFAs are attractive devices for single-mode fibers in optical communication systems in the 1530 nm wavelength band which is known as a third window for fiber optic communication. EDFAs have many advantages such as high gain and low noise in optical communication networks.

EDFAs are characterized by gain which depends on temperature and this feature is very interesting in the modern optical transmission systems which use wavelength division multiplexing (WDM) [1]. Various temperature values in published works have then been used to experimentally find the gain at optimum amplifier lengths by analytical solution of the rate equation derivation [2–5]. The temperature-dependent gain and noise figure (NF) in EDFAs have been studied theoretically and experimentally for 980 nm and 1480 nm with the EDFAs of different lengths. These results have shown that the NF is temperature dependent [6].

Praseodymium Pr^{3+} -doped fiber amplifiers (PDFAs) are now attracting more interest, because they expected to play a vital role in upgrading 1300 nm optical systems that are used

in almost all terrestrial optical telecommunication networks [7]. PDFAs have the quantum efficiency of the $^1\text{G}_4 \rightarrow ^3\text{H}_5$ of the transition in the 1300 nm wavelength region [8–11]. For this point, the low-phonon-energy glass hosts are needed to examine the amplifier span and all optical link-capacity.

Recently, some efforts have been methodically made to develop these types of optical amplifiers for utilizing over a wide range of temperatures. Especially, one major issue of PDFA research is to develop the gain efficiency with low NF of PDFA using ZBLAN (ZrF_4 , BaF_2 , LaF_3 , AlF_3 , NaF) fluoride, sulfide (GeGaS) and some borate-based glasses as a host material [12–15]. In addition, the temperature dependence of the gain characteristics of PDFAs is critical for these systems.

In this work, we have compared the noise figure of EDFA and PDFA amplifiers after solving the rate equation by including the temperature effect observed on the transitions. The numerical results are given for both EDFA and PDFA amplifiers, operating at the 1530 nm and 1300 nm signal wavelengths respectively. EDFAs are widely used in the third window so a wider band WDM that would cover the band from 1300 to 1550 nm can be achieved [8]. The great interest in PDFA amplifiers results from the fact that an important part of the fiber optic network worldwide uses the 1300 nm second communication window. The variation of NF over the temperature range $-20\text{ }^\circ\text{C}$ to $+60\text{ }^\circ\text{C}$ was studied for different amplifier lengths.

II. SCHEMATIC REPRESENTATION OF NF

This work will give understanding of the physical concept of two and four level fiber amplifiers and obtaining the noise figure of the signals at different temperature range by using rate equation technique. The energy levels amplification mechanism for erbium Er^{3+} and praseodymium Pr^{3+} ions doped in glass hosts are shown in Fig. 1 and Fig. 2 respectively.

The single-mode fiber doped Er^{3+} ions can be considered homogeneously broadened in a two-level amplification system. Fig. 1 illustrates the energy diagram of erbium ions in glass hosts, R_S denotes the stimulated absorption and emission rates

A. H. M. Husein is with the Al-Aqsa University, Physics Department, P.O. Box 4051, Gaza, Gaza Strip, Occupied Palestinian Territories (phone: +970(59)9165678; fax: 970(8) 286 5309; e-mail: hakeim00@yahoo.com).

F. I. El-Nahal is with the Islamic University of Gaza, Electrical Engineering Department, Gaza, Gaza Strip, Occupied Palestinian Territories (e-mail: fnahal@iugaza.edu.ps).

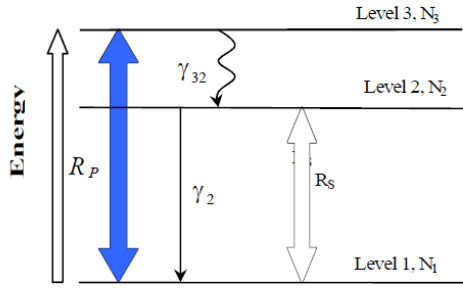


Fig. 1. The energy diagram of erbium ions in glass hosts such as silica tellurite and fluorozirconate.

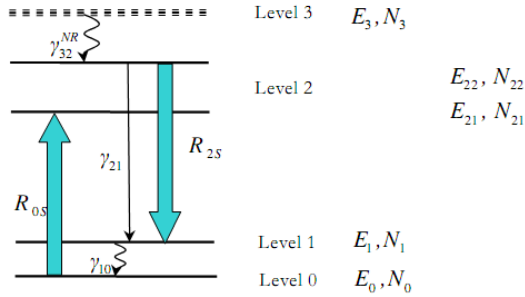


Fig. 2. The energy levels and amplification mechanism for Pr^{3+} ions in glass hosts.

associated with the signal between the population inversion densities N_1 and N_2 of the lower (ground) and upper (metastable) levels, respectively, the first and the second (metastable) levels respectively and R_p refers to both the pumping rate from the first to the third level and the stimulated emission rate between them. N_1 , N_2 and N_3 are population of Er^{3+} -ions in the first, second and third level, respectively. γ_2 is the transition probability, which is the sum of the spontaneous radiative and nonradiative transition probabilities from the metastable to the ground level. γ_{32} is the transition probability per unit time for an Er^{3+} ion and represents the thermal relaxation from the upper state (third level) to the lower state (second level) [16], then the rate equation can be written as

$$\frac{dN_1}{dt} = -R_p(N_1 - N_3) + \gamma_2 N_2 + R_s(N_2 - N_1) \quad (1)$$

$$\frac{dN_2}{dt} = -R_s(N_2 - N_1) - \gamma_2 N_2 + \gamma_{32} N_3 \quad (2)$$

$$\frac{dN_3}{dt} = R_p(N_1 - N_3) - \gamma_{32} N_3 \quad (3)$$

The rate equations are solved the conditions of steady state, where all of the level populations are time invariant, i.e. $dN_i/dt = 0$, ($i = 1, 2, 3$).

$$N_1 = N \frac{R_p \beta + R_s + \gamma_{21}}{R_p(1 + 2\beta) + R_s(2 + \beta) + \gamma_{21}} \quad (4)$$

$$N_1 = N \frac{R_p \beta + R_s + \gamma_{21}}{R_p(1 + 2\beta) + R_s(2 + \beta) + \gamma_{21}} \quad (5)$$

where $\beta = \frac{N_m}{N_{m-1}} = \exp(-\Delta E_m / k_B T)$ [19] is the Boltzmann's

population relation where $\Delta E_m = E_m - E_{m-1}$ is the energy difference between the third and the second level, k_B is the Boltzmann's constant ($k_B = 1.38 \times 10^{-23} \text{ J/K}$), and T is the temperature in degrees Kelvin [20].

The gain of EDFA amplifier is given by [21]

$$G = \exp[\Gamma_s \sigma_s^a (\eta N_2 - N_1) L] \quad (6)$$

where σ_s^a is the signal absorption cross sections, L is the length of the fiber, η is the ratio between the signal emission and absorption cross sections and Γ_s is the signal mode overlap factor of the fiber with erbium distribution and dimensionless integral overlap. The amplified spontaneous emission (ASE) is taken into consideration, but the excited state absorption (ESA) effect is neglected for simplicity. The noise figure as a function of the signal gain, input and output ASE spectral densities, in decibel (dB) is given by

$$NF(\text{dB}) = 10 \log_{10} \left(\frac{1}{G} + \frac{P_{ASE}^o(\lambda_s)}{G h \nu_s} - \frac{P_{ASE}^i(\lambda_s)}{h \nu_s} \right) \quad (7)$$

where $1/G$ is the beat noise, P_{ASE}^i and P_{ASE}^o are the amplified input and the amplified output ASE spectral density respectively, ν_s is the frequency of the signal wavelength and $h = 6.626 \cdot 10^{-34} \text{ Js}$ is the Planck constant.

The population of Pr^{3+} levels is labeled as N_0 , N_1 , N_2 , N_3 , N_4 and N_5 respectively, and also the total population density N is taken as $N = N_0 + N_1 + N_2 (=N_{21} + N_{22}) + N_3 + N_4 + N_5$. In this point, the special names of N_2 and N_0 are the population densities of metastable and ground levels, respectively. The amplified spontaneous emission (ASE) is also neglected, as the signal input power was significantly above the equivalent ASE noise power. Also it includes the effect of the signal photon (ESA) to have better accuracy. To calculate all of the population of Pr^{3+} at steady state conditions, the effects of pump ESA and the cooperative upconversion are not taken into consideration. On the basis of the energy level diagram shown in Fig. 2, and using upper conditions the rate equation for Pr^{3+} population density can be written as follows

$$\frac{dN_3}{dt} = R_p N_0 - R_p N_3 - \gamma_{32} N_3 \quad (8)$$

$$\frac{dN_{22}}{dt} + \frac{dN_{21}}{dT} = R_{0s} N_0 - R_{2s} N_{22} - N_{22} \gamma_{21} + \gamma_{32} N_3 \quad (9)$$

$$\frac{dN_1}{dt} = R_{2s} N_{22} + \gamma_{21} N_{22} - \gamma_{10} N_1 \quad (10)$$

$$\frac{dN_0}{dt} = R_p N_3 - R_p N_0 - R_{0s} N_0 + \gamma_{10} N_1 \quad (11)$$

The rate equations are solved under the conditions of steady state, where all of the level populations are time invariant, i.e. $dN_i/dt = 0$, ($i = 1, 2, 3$).

$$N_{22} = N \frac{R_p}{\gamma + R_p(1 + 1/\beta) + R_{2s}} \quad (12)$$

The gain of PDFFA amplifier is given by [20]

$$G = \exp[\Gamma_s \sigma_{2s} N_{22} L] \quad (13)$$

where L represents the length of Pr^{3+} -doped amplifier and G denotes the signal gain and σ_{2s} is the stimulated emission cross section of transitions. The NF of the amplifier is defined as then degradation in signal-to-noise ratio from input to output of the amplifier, NF in decibel (dB) is given by:

$$NF(\text{dB}) = 10 \log_{10} \left[\frac{1}{G} \left(1 + \frac{P_{ase} \Delta \nu}{GP_{in}} \right) + \frac{1}{G} \frac{P_{ase} \Delta \nu}{h \nu_s} \left(1 + \frac{P_{ase} \Delta \nu}{2GP_{in}} \right) \right] \quad (14)$$

where $(1/G)$ is the signal-spontaneous beat noise, P_{ase} is the ASE power density, P_{in} is the signal power density, ν_s is the frequency of the input signal, and $\Delta \nu$ is the optical linewidth of the amplifier.

III. RESULTS AND DISCUSSION

The numerical calculations of the approximate expression of the noise figure of EDFA amplifier has been carried out. For simplicity the energy difference between levels of metastable is considered as 300 cm^{-1} in the room temperature. The relevant fiber parameters values for an Al/P-silica erbium-doped fiber amplifier Symbols Definitions are shown in Table 1 [21].

For numerical calculation, the fiber parameters for Pr^{3+} doped sulfide and ZBLAN amplifiers are taken from [22, 23]. The parameters and their values used in calculation are shown in Table 2. As can be noted from Table 2, the stimulated emission cross section of GeGa-sulfide glass is larger than the cross section of ZBLAN one. The lifetime of the transition τ is an important quantity to evaluate the amplifier performance since, if it is short, it then becomes necessary to pump very hard to maintain a population inversion. Here σ_{03} is the stimulated absorption of Pr^{3+} transitions ν_p and ν_s are the pump and signal frequencies respectively, P_p and P_s are the pump and signal powers respectively, Γ_p and Γ_s are the overlap factors; A_p and A_s are the effective doped areas of the core corresponding to pump and signal powers respectively, and h

TABLE I
THE RELEVANT FIBER PARAMETERS VALUES FOR AN AL/P-SILICA ERBIUM-DOPED FIBER SYMBOLS DEFINITIONS [21]

Symbol	Definition	Value
σ_s^e	Signal emission cross- section	$5.7 \times 10^{-25} \text{ m}^2$
σ_s^a	Signal absorption cross- section	$6.6 \times 10^{-25} \text{ m}^2$
σ_p^e	Pump emission cross- section	$6.6 \times 10^{-25} \text{ m}^2$
σ_p^a	Pump absorption cross- section	$2.44 \times 10^{-25} \text{ m}^2$
τ	Life time	10.8 ms
N	Erbium concentration	$3.86 \times 10^{24} \text{ m}^{-3}$
λ_s	Signal wavelength	1530nm
λ_p	Pump wavelength	1480nm
ν_s	Signal frequency	$1.96 \times 10^{14} \text{ Hz}$
ν_p	Pump frequency	$2.027 \times 10^{14} \text{ Hz}$
$P_{ASE}^+(L)$	Copropagating ASE power	0.15mW
α_s	Signal absorption constant	0.5 m^{-1}
L	Fiber length	0 to 45m
P_p^i	Input pump power	30mW

TABLE II
PARAMETERS AND THEIR VALUES USED IN CALCULATIONS FOR THE Pr^{3+} -DOPED SULFIDE AND ZBLAN FIBER AMPLIFIERS

Parameters	GeGa-sulfide Ref.[23]	ZBLAN Ref.[24]
σ_{03}	$9.7 \times 10^{-26} \text{ m}^2$	$4.24 \times 10^{-26} \text{ m}^2$
σ_{2s}	—	$1.2 \times 10^{-26} \text{ m}^2$
τ	360 μs	110 μs
N	$7.82 \times 10^{25} \text{ m}^{-3}$	$4.80 \times 10^{25} \text{ m}^{-3}$
λ_s	1310 nm	1300 nm
λ_p	1028 nm	1017 nm
A_p, A_s	15.40 μm^2 , 12.30 μm^2	8.04 μm^2
Γ_p, Γ_s	0.38, 0.40	0.6
L	8 m	36 m

is Planck's constant. At room temperature for simplicity, the energy interval between N_{22} and N_{21} levels of GeGa-sulfide and ZBLAN-based Pr^{3+} ions are assumed to be close to 500 and 400 cm^{-1} , respectively. The relevant fiber parameters for both EDFA and PDFA models depend on the temperature range $-20 \text{ }^\circ\text{C}$ to $+60 \text{ }^\circ\text{C}$.

A. Noise Figure versus Length for Er^{3+}

It was noted from Fig. 3 that the noise figure swiftly increases for 0–6 m length and there is no important effect of temperature dependency at different temperatures, while it is still low at lengths greater than 6 m. There is little noise effect at a variety of temperatures in this region (<6 m) because the gain and noise figure is low enough due to the length of the EDFA, as a result, the population inversion ratio is very low. If the EDFA length is low enough, the population inversion is very low so that the absorption and emission rates are low but we can find the temperature-dependent gain (temperature-dependent absorption and emission) and noise effect. It was noted that the variation of noise figure via the EDFA length in spectral contribution of copropagating ASE power. For different temperature the NF is nearly the same with some variation for different length up to 45 m.

B. Noise Figure versus Length for Pr^{3+}

For both GeGa-sulfide-based and ZBLAN-based Pr^{3+} -doped fiber amplifiers over the temperature range from $-20 \text{ }^\circ\text{C}$ to $60 \text{ }^\circ\text{C}$, the variations of noise figure with the length of the amplifier are considered. The results for the GeGa-sulfide based amplifier are shown in Fig. 4 and Fig. 5 respectively. It is obvious from the results that the signal noise figure rises with decreases in the length, at the same time the NF declines when the temperature decreases. However the NF decreases with increasing the length. Furthermore, the NF increases when the temperature rises.

We have analyzed the noise performance in EDFAs and PDFAs under different operating conditions. When comparing the two models, It is clear that the NF for the both the EDFA and PDFAs increases with temperature. However, for the

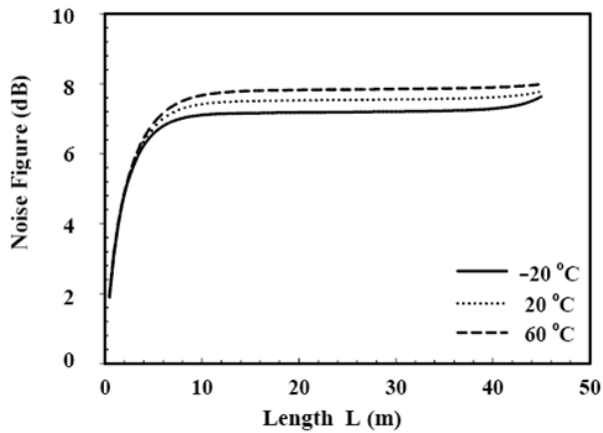


Fig. 3. Temperature-dependent noise figure analysis (the change of noise figure via erbium-doped fiber length in the spectral contribution of copropagating ASE power of 0.15 mW and when $P_p^i(0) = 30$ mW and $P_s(0) = 10$ μ W).

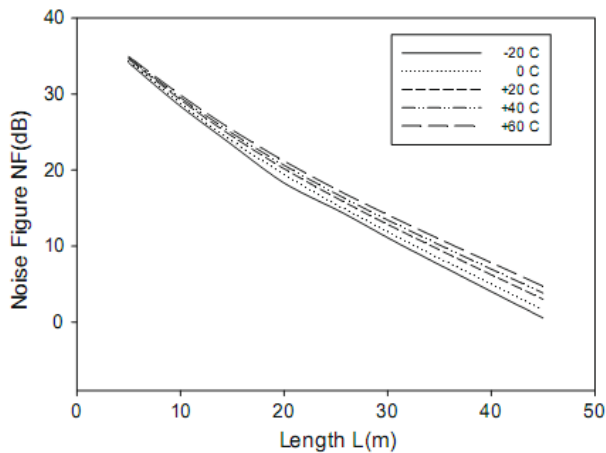


Fig. 4. The change of the noise figure with temperature and length of ZBLAN based Pr^{3+} -doped fiber amplifier for a signal input power of -30 dBm and pump power of 20 dBm.

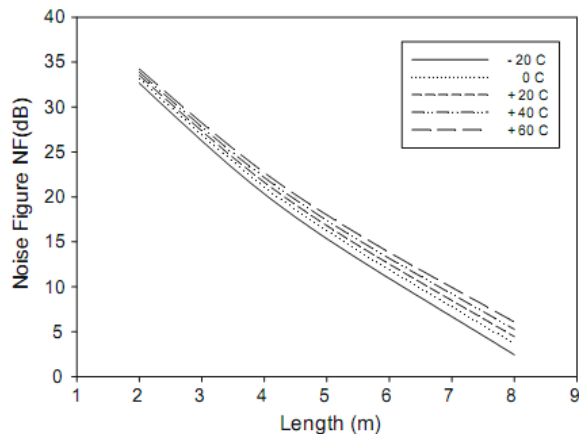


Fig. 5. The change of the noise figure with temperature and length of GeGa-sulfide based Pr^{3+} -doped fiber amplifier for a signal input power of -30 dBm and pump power of 20 dBm.

EDFA amplifier there is no variation of NF with temperature for lengths below 6 m. This can be explained by the fact that the population inversion ratio is very low. For any further

increase in length it can be seen that NF increases with temperature, at the same time the NF stays almost constant with any further increase in the length. On the other hand, for the PDFA, the NF increases with increasing the temperature, at the same time, the NF decreases with increasing the length. This is due to the Boltzmann distribution change. PDFA amplifier, being a four-level system, the noise figure can be easily obtained compared with EDFA. The NF performance of the PDFA is comparable with that of EDFA. However the NF in EDFA is more sensitive to operating conditions at peak wavelengths, while PDFA it is not sensitive to operating conditions. We found that the NF is strongly signal wavelength dependent due to lower population inversion in EDFAs and due to ground state absorption (GSA) in PDFAs. We have confirmed that the NF is independent of numerical aperture (NA) for both amplifiers.

IV. CONCLUSION

The erbium-doped fiber amplifier is an attractive candidate for 1530 nm systems because of its very low noise and high gain, while praseodymium-doped fiber amplifier is for 1300 nm systems. The two models have been introduced as simple schematic representations for energy levels and amplification mechanisms (Two levels for Er^{3+} and four levels for Pr^{3+}). The basic rate equation models have been carried out, including the temperature effect to obtain the signal noise figure of the erbium and praseodymium-doped fiber amplifiers at research level. Moreover, we have shown the possibility of obtaining an analytical solution of the rate equations in some practical temperature ranges to comprehend the noise figure of both fiber amplifiers.

REFERENCES

- [1] J. Kemtchou, M. Duhamel, P. Lecoy, "Gain temperature dependence of erbium-doped silica and fluoride fiber amplifiers in multichannel wavelength-multiplexed transmission systems", *IEEE J. Lightwave Technol.* 15 (11), pp. 2083-2090, 1997.
- [2] M. Peroni, M. Tamburrini, "Gain in erbium-doped fiber amplifiers: A simple analytical solution for the rate equations", *Opt. Lett.*, 15(15), pp. 842 - 844, 1990.
- [3] N. Kagi, A. Oyobe, K. Nakamura, "Temperature dependence of the gain in erbium-doped fibers", *IEEE J. Lightwave Technol.* 9 (2), pp. 261-265, 1991.
- [4] C. Berkdemir, S. Özsoy, "On the Temperature-Dependent Gain and Noise Figure Analysis of C-Band High-Concentration EDFAs with the Effect of Cooperative Upconversion", *Journal of Lightwave Technology*, 27 (9), pp. 1122-1127, 2009.
- [5] K. Furusawa, T.M. Monro, D.J. Richardson, "High gain efficiency amplifier based on an erbium doped aluminosilicate holey fiber", *Opt. Express*, 12 (15), pp. 3452-3458, 2004.
- [6] M. Yamada, M. Shimizu, M. Horiguchi, M. Okayasu, "Temperature dependence of signal gain in Er^{3+} -doped optical fiber amplifiers", *IEEE J. Quantum Electron.*, 28 (3), pp. 640-649, 1992.
- [7] Y. Ohishi et al., "Pr³⁺-doped fluoride fiber amplifier operating at 1.31 μm ", *Opt. Lett.* 16 (22), pp. 1747-1749, 1991.
- [8] G. Lawton, "Optical Amplifiers Technology and System", IGI Publisher, 1999.
- [9] Y. Ohishi et al., OFC91, Postdeadline Paper PD2, (1991)
- [10] Y. Miyajima et al., Top. Meet. Opt. Amp. Appl., Postdeadline Paper PD1, 1991.

- [11] B. Pedersen, W.J. Miniscalco, R.S. Quimby, "Optimization of Pr³⁺:ZBLAN fiber amplifiers", *IEEE Photon. Technol. Lett.*, 4 (5), pp. 446-448, 1992.
- [12] S.H. Yuan, *J. Non-Cryst. Solids* 215, 1997, 108.
- [13] K. Itoh et al., *J. Non-Cryst. Solids*, pp. 256-257, 1999, 1.
- [14] D.R. Simons, A.J. Faber, H. de Waal, "Pr³⁺-doped GeS_x-based glasses for fiber amplifiers at 1.3 μm," *Opt. Lett.*, 20 (5), pp. 468-470, 1995.
- [15] P. Sirivastava, S.B. Rai, D.K. Rai, "Effect of lead oxide on optical properties of Pr(3+) doped some borate based glasses" , *J. Alloys Compd.* 368. 1-7 ,2004.
- [16] E. Desurvire, "Erbium-Doped fiber Amplifiers; Principle and Applications" (John Wiley and Sons. Inc, New York, 1994.
- [17] C. Berkdemir, S. Ozsoy, "Modelling consideration of praseodymium-doped fiber amplifiers for 1.3μm wavelength applications", *Opt. Commun.* 269, pp. 102-106, 2007.
- [18] A. Yariv, *Quantum Electronics*, Third Edition, John Wiley, New York, 1988, 220.
- [19] W.J. Miniscalco, R. S. Quimby, "General procedure for the analysis of Er³⁺ cross sections", *Opt. Lett.*, 16 (4), pp. 258-260, 1991.
- [20] P. C. Becker, N. Olsson, J. Simpson, "Erbium -Doped Fiber Amplifiers: Fundamentals and Technology", Academic Press, San Diego, (Copyright by Lucent Technologies) 1999.
- [21] M. C. Lin, and S. Chi, "The Gain and Optimal Length in the Erbium-Doped Fiber Amplifiers with 1480 nm Pumping" *IEEE Photonics Tech. Lett.* 4 (4), pp. 354-356, 1992.
- [22] D. R. Simons, Eindhoven University of Technology Research Reports, ISBN 90-386-0496-3, Nov. 1995.
- [23] Ohishi, T. Kanamori, Y. Terunuma, M. Shimizu, M. Yamada, and S. Sudo, "Investigation of efficient pump scheme for Pr³⁺ doped fluoride fiber amplifiers", *IEEE Photon. Technol. Lett.*, (6), pp. 195 - 198, 1994.

Dynamics of Closed-loop ADC-NOT-DAC Circuits

Arthur E. Edang, Fredison A. Corminal, and Felicito S. Caluyo

Abstract—This article introduces a class of dynamical maps based on triadic circuits consisting of analog-to-digital converter (ADC), NOT gate/s, and a digital-to-analog converter (DAC). A NOT gate placed along one of the digital lines between the ADC and DAC produces a nonlinear transfer relationship. When the DAC's analog output is fed back as input to the ADC, the resulting closed-loop system exhibits a rich array of bifurcations leading to pseudo-randomness. Simulated results from a mathematical model match fairly well with those derived from an electronic circuit realization.

Index Terms—Analog-to-digital converter, bifurcation, digital-to-analog converter, map, NOT gates.

I. INTRODUCTION

ELECTRONICS and difference equations share a kind of affinity, especially in the study of nonlinear dynamics. This relationship is seen in circuit realizations of discrete-time systems such as those described by the logistic [1]–[9], tent [10]–[13], sine-circle [14]–[15], Henon [16]–[18], and Bernoulli [19]–[21] maps. These maps were first studied numerically, and it was usually after that that circuits were used to demonstrate and validate the results of mathematical predictions.

Conversely, there were circuits that existed long before engineers were able to present maps to describe them. An example is a thyristor circuit whose maximal values of anode-cathode voltages bifurcated as the frequency of the ac source was varied [22]. This led to the formulation of a first return map as a function of breakover voltage and ac frequency. Another is a discrete model reported by Chua and Lin [23] which arose from a second-order digital filter using 2's complement overflow nonlinearity in its accumulator. Then, there is a digital phase-locked loop whose nonlinearity is due to the combined effect of quantization and a sinusoidal phase detector [24]. Its output was observed to be periodic, quasi-periodic, and something more complex – all of which were later found to be consistent with the predictions of a novel

difference equation. Underlying maps were also discovered in the operation of switching dc-dc power converters, particularly in the buck [25]–[26] and boost [27]–[28] regulators. Maps were likewise seen in low-pass and band-pass sigma-delta modulators [24].

Recently, it was reported in [29] that a family of maps arises from a closed-loop tandem of an analog-to-digital converter (ADC) and a nonlinearized digital-to-analog converter (NDAC). In that study, nonlinearity was observed after cutting one of the digital lines between the two converters, and tying it to logical *High* that severed input of the DAC. Other nonlinearities were created when additional lines were likewise altered, or instead tied to logical *Low*.

In this paper, the authors extended the membership of NDAC-based generators. The contribution is a class of triadic circuits consisting of an analog-to-digital converter (ADC), NOT gate, and a digital-to-analog converter (DAC). The presence of a logical inverter along one of the data lines from the ADC to the DAC results in a nonlinear relationship between the analog input and output signals of the two converters. Moreover, when the analog output is looped back to the input, it is observed that the circuit behaves as a map and generates a bifurcating sequence of bytes when a parameter is varied. More maps are found when other data lines are likewise altered, or NOT gates are simultaneously inserted in several lines. In that regard, this paper aims to report the results from investigations on sample members of this class of dynamical maps.

The rest of the paper is organized as follows: Section II presents the transfer curves of some of these new nonlinearities, their mathematical representations, and the numerically-derived bifurcation diagrams with respect to an identified system variable. In Section III, the details of the electronic circuit realization of one of these maps are discussed. The study is concluded in Section IV.

II. ADC-NOT-DAC TRIAD

In Fig. 1, one of (2^n-1) ways to put NOT gates between n -bit converters is shown. As a means to distinguish one interposal from another, we introduce the following notation: for an 8-bit system, the positions of 'N' within a code indicate where the inverters are. For example, N111-1111 for Fig.1 means that an inverter was placed between the ADC's most significant bit (MSB) output and the corresponding MSB input of the DAC,

A.E.Edang is with Don Bosco Technical College, Mandaluyong, Philippines (phone: 632-531-8081; fax: 632-531-6644) and also with De La Salle University, Manila, Philippines (e-mail: aeedang@yahoo.com).

F.A.Corminal was with Don Bosco Technical College, Mandaluyong, Philippines.

F.S. Caluyo is with Mapua Institute of Technology, Muralla St., Intramuros, Manila, Philippines.

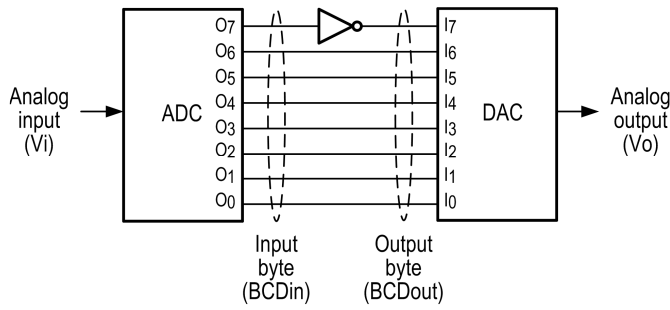


Fig. 1. ADC-NOT-DAC arrangement for producing a nonlinear transfer relationship.

while other data lines were left unchanged. In the following sections, three more configurations are presented: 1N11-1111, 1NN1-1111, and N1N1-1111.

A. Transfer Curve

The inclusion of the NOT gates forms several interesting input-output relationships. As depicted in each transfer curve of Fig. 2, $BCDin$ stands for the ADC's binary-coded decimal (BCD) output, and $BCDout$ refers to the DAC input. In the case of Fig. 2a, one may observe that whenever the MSB of $BCDin$ is *Low*, $BCDout$ exceeds $BCDin$ by 2^7 . Conversely, when MSB is *High*, $BCDin$ is 2^7 units lower than $BCDout$. From these and a similar examination of Fig. 2b, the transfer function when there is a single inverter along the k^{th} data line may be generalized as

$$BCDout = \begin{cases} BCDin + 2^k & (I_k = 0) \\ BCDin - 2^k & (I_k = 1) \end{cases} \quad (1)$$

where I_k is the k^{th} bit of the input byte. Here, we assume that the least significant bit (LSB) is at line $k=0$. Then, with a slight modification, this expression can be likewise applied to Fig. 2c and Fig. 2d which have two inverters, one each along the k^{th} and j^{th} data lines, such that

$$BCDout = \begin{cases} BCDin + 2^j + 2^k & (I_j, I_k) = (0, 0) \\ BCDin + 2^j - 2^k & (I_j, I_k) = (0, 1) \\ BCDin - 2^j + 2^k & (I_j, I_k) = (1, 0) \\ BCDin - 2^j - 2^k & (I_j, I_k) = (1, 1) \end{cases} \quad (2)$$

B. Nonlinear Map

In each of the mentioned ADC-NOT-DAC triads, a map was produced when analog output (V_o) was looped back to the analog input (V_i). Taking into account discretization at the ADC input, the system can be modeled by considering the dynamics of $BCDout$. Assuming that $BCDout = g(BCDin)$ as discussed in Section II-A, it can be shown that

$$BCDout_{m+1} = g(\lfloor (VREF / REF+) \times BCDout_m \rfloor) \quad (3)$$

where $\lfloor \cdot \rfloor$ is the floor function, $VREF$ and $REF+$ are the reference voltages of the DAC and ADC, and m and $m+1$ refer to the previous and present integer states of $BCDout$,

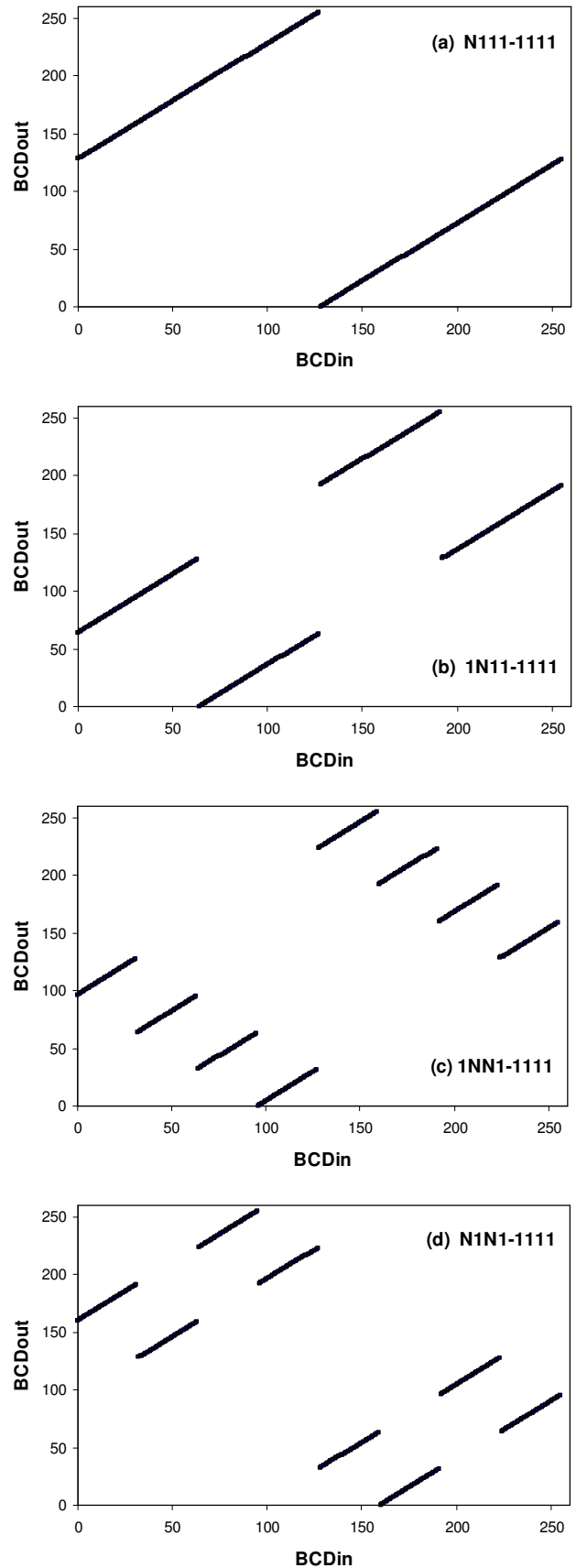


Fig. 2. Transfer curves for map (a) N111-1111, (b) 1N11-1111, (c) 1NN1-1111 and (d) N1N1-1111.

respectively. Note that (3) is identical to the map in [29] but now allows a larger membership for $g(\cdot)$.

Numerical analysis showed that, for a fixed $REF+$, the maps exhibit many bifurcations as $VREF$ was varied. For each map, we initially set $BCDout=g(0)$ and $VREF=0$, ran the algorithm for 300 rounds to allow the transitory trajectories to die down, then recorded the ensuing 300 integer states of $BCDout$. This procedure was repeated for $VREF=\{0.02, 0.04, 0.06, \dots\}$ until it reached the point when the resulting $BCDout$ sequence

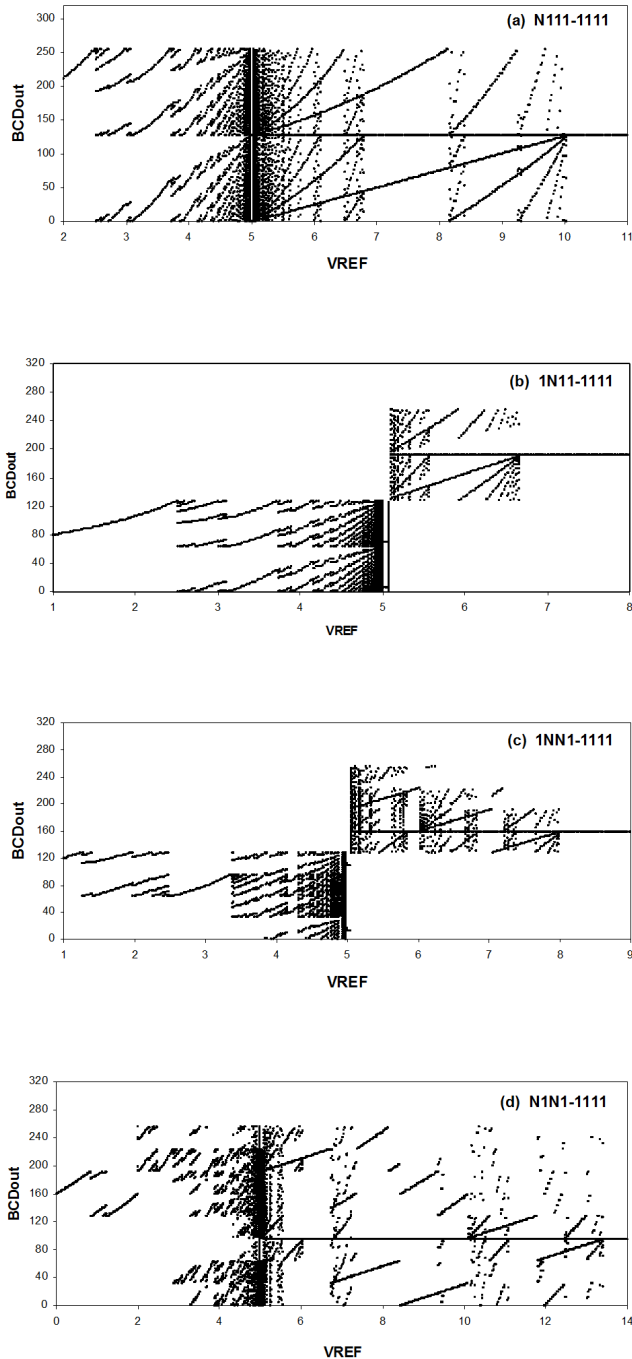


Fig. 3. Bifurcation diagrams for map (a) N111-1111, (b) 1N11-1111, (c) 1NN1-1111 and (d) N1N1-1111.

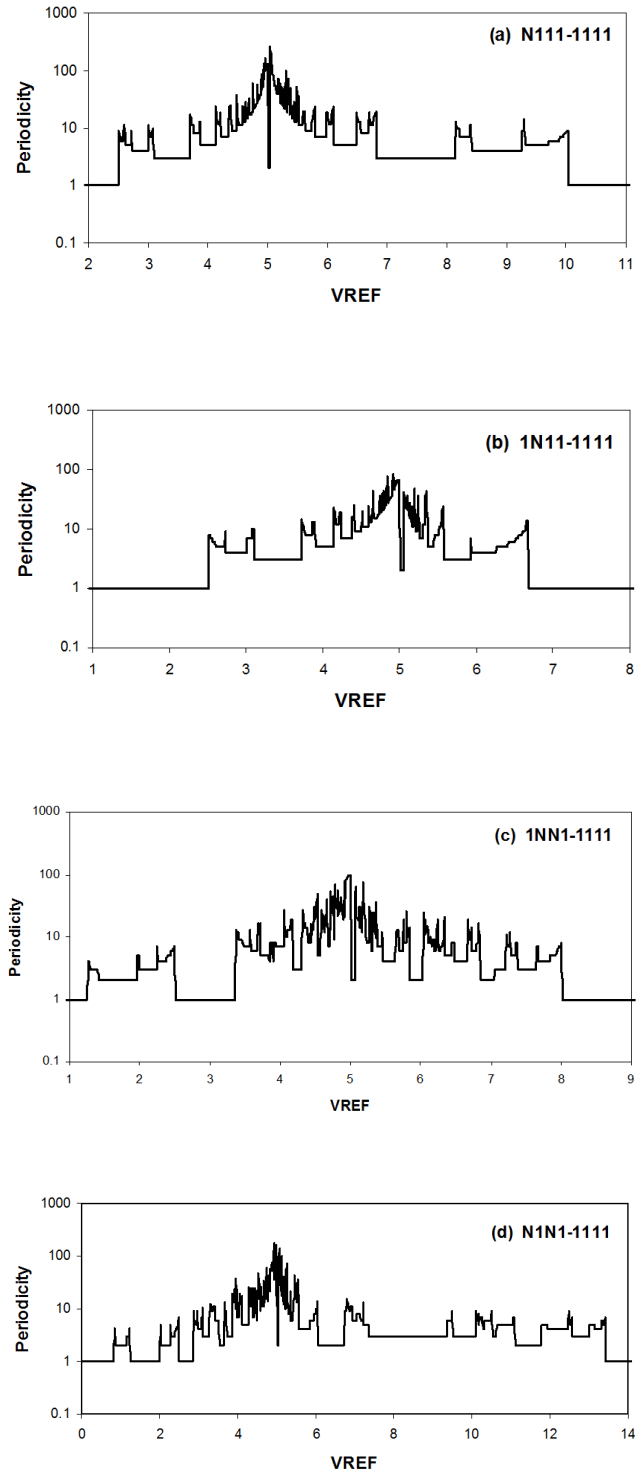


Fig. 4. The number of periodic BCD outputs per cycle as $VREF$ is varied for map (a) N111-1111, (b) 1N11-1111, (c) 1NN1-1111 and (d) N1N1-1111. It was assumed that $REF+=5.00$.

finally settled to a period-1 cycle. Results are depicted in Fig. 3. Alternatively, Fig. 4 shows the periodicity of $BCDout$ for different $VREF$ values.

For N111-1111 (Fig. 3a and Fig. 4a), a series of fixed points with increasing $BCDout$ values precede the first periodic orbit

($P_{initial}$) which is a period-9 cycle at $VREF=2.51$. Within the range of 2.51 to 10.03, the map exhibits cycles whose periodicities (P) vary from $P_{min}=2$ at $VREF=5.01-5.03$, up to $P_{max}=251$ when $VREF=5.04$. That range ends with $P_{final}=9$ before the map bifurcates to a terminal fixed point at $BCDout_{final}=127$. These dynamical highlights together with those of the other ADC-NOT-DAC maps are summarized in Table 1.

III. ELECTRONIC CIRCUIT REALIZATION

Fig. 5 shows the electronic circuit implementation of the N111-1111 map. The core units consist of: (a) flash-type ADC (U1), (b) current-mode DAC (U4) [30], (c) NOT gate (U2c) between the converters, and (d) an octal D-type flip-flop (U3) for storing the results out of every iteration. Other details about the circuit and its operation are discussed in [29]. From the output (V_{o2}) of the auxiliary DAC (U5), the different bifurcations may be viewed when a sawtooth waveform is applied to the $VREF$ of U4. Result is shown in Fig. 6.

While there is qualitative resemblance for most parts of the graphic when compared with Fig. 3a, one may observe a considerable disparity in the vicinity of $VREF=5.00$. In this region, there appear several fixed points whereas the numerical simulation shows only a period-2. The oscilloscope also showed that those points were wandering up and down without any discernable pattern.

A plausible explanation for this behavior is rooted in the transition of the map to higher $VREF$ s. A finer numerical scan, in this case from $VREF=4.999$ to $VREF=5.000$, reveals that each pair of period-2 states occurring at $VREF=5.000$ corresponds to a particular $BCDout$ found among the period-129 states of $VREF=4.999$. This relationship is shown in Fig. 7.

Considering that the sawtooth generator in Fig. 5 is not

TABLE I
DYNAMICAL HIGHLIGHTS OF ADC-NOT-DAC MAPS AT REF+=5.00

NDAC map	VREF range	$P_{initial}$	P_{final}	P_{min}	P_{max}	BCDout final
N111-1111	2.51-10.03	9	9	2	251	127
1N11-1111	2.52-6.67	8	14	2	84	191
1NN1-1111	1.26-8.01	4	8	1	97	159
N1N1-1111	0.84-13.42	4	7	1	174	95

synchronized with the circuit's CLK signal, it can be argued that $BCDout$ value at $VREF=4.999$ just as $VREF$ steps up to 5.000 volts is inconsistent; hence the ensuing period-2 states could be any of 129 pairs. It is likely that in every fresh cycle of the sawtooth, new period-2 states are filled. This results in the appearance of jerky bright spots on an analog oscilloscope and because visual persistence is inherent in scopes, one tends to see more than a pair of spots at any time.

It can be adduced that there is agreement between numerical and experimental results. Computer simulation shows the map's long-term behavior when its bifurcation parameter is repeatedly varied in a consistent manner. On the other hand, experimental results depict the map's response to a non-ideal bifurcation signal generator. Both asymptotic and transient states are exposed.

IV. CONCLUSION

We have introduced a new class of circuits based on ADC-NOT-DAC triads, which extends the membership of a previously reported nonlinear map. The circuit can find application in secure communications, particularly in data encryption and message authentication or hashing. The latter uses irreversible algorithms to generate unintelligible information out of a much larger message from the sender. Within hashing programs there are functions that employ

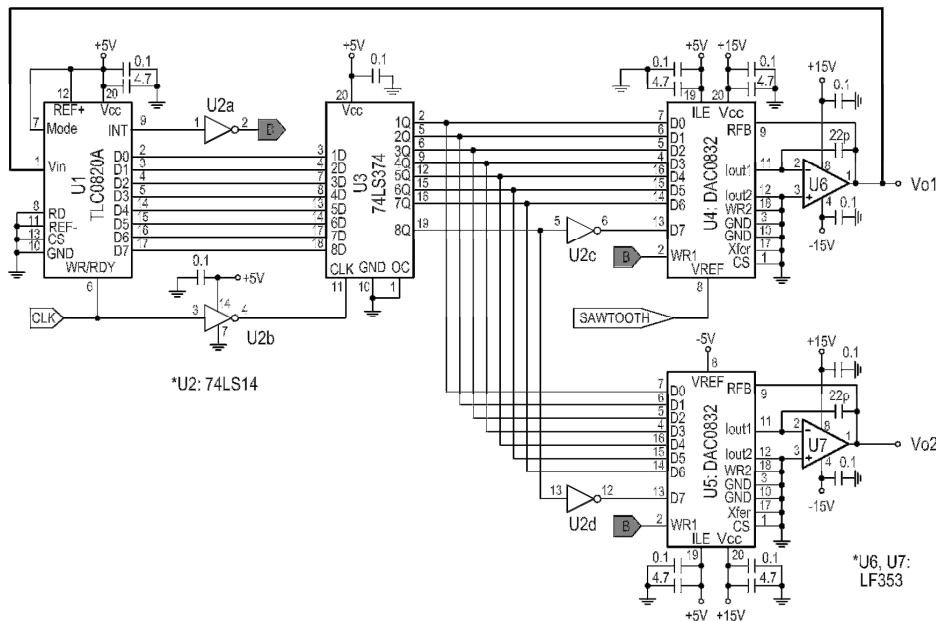


Fig. 5. Circuit realization for N111-1111 map.

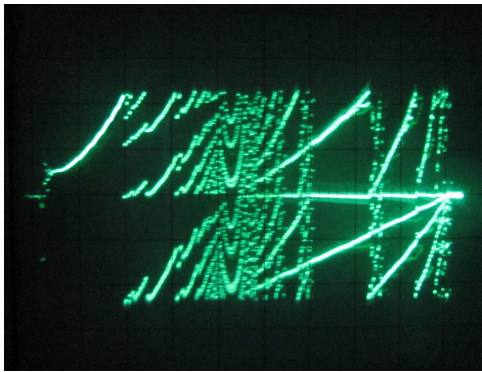


Fig. 6. Bifurcation plot for map N111-1111 circuit. Ch.1 (0.1V/div) at U4's VREF; Ch.2 (0.1V/div) at V_{o2} .

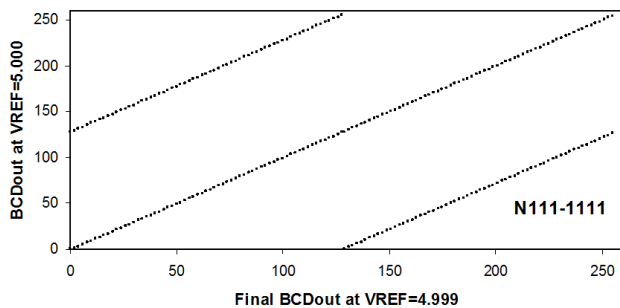


Fig. 7. Relationship between the terminal *BCDout* state at $VREF=4.999$ and the ensuing period-2 states at $VREF=5.000$ for map N111-1111.

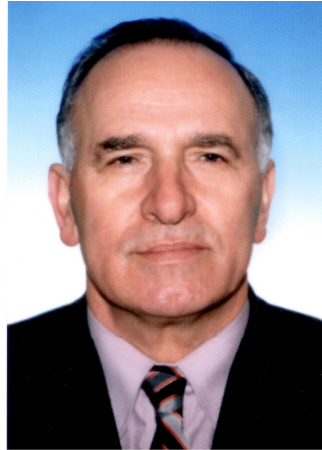
modulo addition and subtraction, exclusive-OR, bit-swapping and bit-rotation, and randomized initializations. With this collection, the first author is investigating the utility of NDAC-based sequences in constructions for hash functions.

In contrast with popular maps that are built out of analog devices, the triadic NDAC map is predominantly digital. This feature makes interfacing easier, and frees the microprocessor from the task of generating pseudo-random sequences for cryptographic encryption. Furthermore, the adjustable *VREF* augurs the possibility of a secure system similar to frequency-hopping spread spectrum. This is a target area of forthcoming investigations.

REFERENCES

- [1] T. Mishina, T. Kohmoto, and T. Hashi, "Simple electronic circuit for the demonstration of chaotic phenomena," *Am. J. Phys.*, vol. 53, no. 4, pp. 332-334, Apr. 1985.
- [2] G.C. McGonigal and M.I. Elmasry, "Generation of noise by electronic iteration of the logistic map," *IEEE Trans. CAS.*, vol. CAS-34, no. 8, pp. 981-983, Aug. 1987.
- [3] M.J.S. Smith, "An analog integrated neural network capable of learning the Feigenbaum Logistic map," *IEEE Trans. Circuits and Systems*, vol. 37, no. 6, pp. 841-844, Jun. 1990.
- [4] H. Tanaka, S. Sato, K. Nakajima, "Integrated circuits of map generators," *IEICE Trans. Fundamentals*, vol. E82-A, no.2, pp. 364-369, Feb. 1999.
- [5] K. Murali, S. Sinha, and W. L. Ditto, "Realization of the fundamental NOR gate using a chaotic circuit," *Physical Review E*, vol. 68, no. 016205, 2003.
- [6] E. H. Hellen, "Real-time finite difference bifurcation diagrams from analog electronic circuits," *Am. J. Phys.*, vol. 72, no. 4, pp. 499-502, Apr. 2004.
- [7] M. Suneel, "Electronic circuit realization of the logistic map," *Sadhana*, vol. 31, part 1, pp. 69-78, Feb. 2006.
- [8] A. Diaz-Mendez, J.V. Marquina-Perez, M. Cruz-Irisson, R. Vazquez-Medina, and J.L. Del-Rio-Correa, "Chaotic noise MOS generator based on logistic map," *Microelectronics journal*, vol. 40, pp. 638-640, 2009.
- [9] H. R. Pourshaghghi, R. Ahmadi, M. R. Jahed-Motlagh, and B. Kia, "Experimental realization of a reconfigurable three input, one output logic function based on a chaotic circuit," *Int. J. Bifurc. Chaos*, vol. 20, no. 3, pp. 715-726, 2010.
- [10] H. Tanaka, S. Sato, and K. Nakajima, "Integrated circuits of map chaos generators," *Analog Integrated Circuits and Signal Processing*, vol. 25, pp. 329-335, 2000.
- [11] K. Eguchi, F. Ueno, T. Tabata, H. Zhu, and T. Inoue, "Simple design of discrete-time chaos circuit realizing a tent map," *IEICE Trans. Electron.*, vol. E83-C, no. 5, pp. 777-778, May 2000.
- [12] T. Addabbo, M. Alioto, A. Fort, S. Rocchi, and V. Vignoli, "The digital tent map: performance analysis and optimized design as a low-complexity source of pseudorandom bits," *IEEE Trans. On Instrumentation and Measurement*, vol. 55, no. 5, pp. 1451-1458, Oct. 2006.
- [13] I. Campos-Canton, E. Campos-Canton, J.S. Murguia, and H.C. Rosu, A simple electronic circuit realization of the tent map, *Chaos, Solitons and Fractals*, doi:10.1016/j.chaos.2008.10.037, 2008.
- [14] E. del Moral Hernandez, G. Lee, and N. H. Farhat, "Analog realization of arbitrary one-dimensional maps," *IEEE Trans. CAS-I*, vol. 50, no.12, pp. 1538-1547, Dec. 2003.
- [15] A. Farfan-Pelaez, E. Del-Moral-Hernandez, J. Navarro S. Jr, and W. Van Noije, "A CMOS implementation of the sine-circle map," *IEEE Circuits and Systems*, pp. 1502-1505, 2005.
- [16] A. Rodriguez-Vazquez, J. L. Huertas, A. Rueda, B. Perez-Verdu, and L. O. Chua, "Chaos from switched-capacitor circuits: discrete maps," *Proceedings of the IEEE*, vol. 75, no. 8, pp. 1090-1106, Aug. 1987.
- [17] T. Morie, S. Sakabayashi, M. Nagata, and A. Iwata, "CMOS circuits generating arbitrary chaos by using pulsewidth modulation techniques," *IEEE Trans CAS-I*, vol. 47, no. 11, pp. 1652-1657, Nov. 2000.
- [18] G. Grassi and D. A. Miller, "Theory and experimental realization of observer-based discrete-time hyperchaos synchronization," *IEEE Trans. CAS-I*, vol. 49, no. 3, pp. 373-378, Mar. 2002.
- [19] L. Zhi-zhong and Q. Shui-sheng, "Discrete-time chaotic circuits for implementation of Tent Map and Bernoulli Map," *Journal of electronic science and technology of China*, vol. 3, no. 3, Sep. 2005.
- [20] O. Katz, D. A. Ramon, and I. A. Wagner, "A robust random number generator based on a differential current-mode chaos," *IEEE Trans. VLSI Systems*, vol. 16, no. 12, pp. 1677-1686, Dec. 2008.
- [21] M. Delgado-Restituto and A. Rodriguez-Vazquez, "Integrated chaos generators," *Proceedings of the IEEE*, vol. 90, no. 5, pp. 747-767, May 2002.
- [22] Y. Yasuda and K. Hoh, "A unified first return map model for various types of chaos observed in the thyristor," *IEICE Trans. Fundamentals*, vol. E78-A, no. 5, pp.550-552, May 1995.
- [23] L. O. Chua and T. Lin, "Chaos in digital filters," *IEEE Trans. Circuits and Systems*, vol. 35, no. 6, pp. 648-658, Jun. 1988.
- [24] O. Feely, "Nonlinear dynamics of discrete-time electronic systems," *IEEE Circuits and Systems Society Newsletter*, vol. 11, no. 1, pp. 1-12, Mar. 2000.
- [25] S. Banerjee, M.S. Karthik, G. Yuan, and J. A. Yorke, "Bifurcations in one-dimensional piecewise smooth maps -Theory and applications in switching circuits," *IEEE Tran. CAS-I*, vol. 47, no. 3, pp. 389-394, Mar. 2000.
- [26] M. Ruzbehani, L. Zhou, and M. Wang, "Bifurcation diagram features of a dc-dc converter under current-mode control," *Chaos, Solitons and Fractals*, vol. 28, pp. 205-212, 2006.
- [27] C.K. Tse, "Flip bifurcation and chaos in three-state boost switching regulators," *IEEE Trans. CAS-I*, vol. 41, no.1, pp.16-23, Jan. 1994.
- [28] T. Saito, T. Kabe, Y. Ishikawa, Y. Matsuoka, and H. Torikai, "Piecewise constant switched dynamical systems in power electronics," *Int. J. Bifurc. Chaos*, vol. 17, no. 10, pp. 3373-3386, 2007.
- [29] A. Edang, J. K. Leynes, R. L. Ella, R. Labayane III, and C. Santiago, "Nonlinear maps from closed-loop tandems of A-to-D and D-to-A converters," *Commun Nonlinear Sci Numer Simulat*, vol.16, pp. 1483-1489, 2011.
- [30] S. Franco, *Design with operational amplifiers and analog integrated circuits 3rd ed.* McGraw-Hill, 2002, pp. 570-571

In Memoriam



Prof. Đemal Kolonić (1942-2011)

On December 3rd, 2011, Đemal Kolonić, Professor at the Faculty of Electrical Engineering, University of Banja Luka and a member of the Editorial Board of the “Electronics” journal since its foundation, passed away.

Prof. Đemal Kolonić was born on July 5th, 1942 in Ljubija near Prijedor – SFRY. He received a B.Sc. degree from the Technical Faculty of Banja Luka, from Department of Electronics and Telecommunications in 1966. The same year, he became Assistant in the Department of Telecommunications. As an Assistant Professor (1974-1984) and Associate Professor (from 1984 to the end of working life), he lectured the following subjects: Fundamentals of Telecommunications, Digital Telecommunications, Information Theory and Transmission Systems, Telecommunications in Power Systems, and Communication Theory at both the undergraduate and graduate study programs at the Faculty of Electrical Engineering in Banja Luka. He was the Head of Department of Telecommunications for many years and the Vice Dean and Dean of the Faculty of Electrical Engineering in Banja Luka in two mandates. As a young assistant, in the field of his interest, Kolonić recognized the worldwide known and even today up-to-date book “Introduction to Statistical Communication Theory” (1960) written by Dr. David Middleton, the pioneer of modern Statistical Communication Theory. The result of this interest was the master thesis entitled “Statistical Prediction of Telecommunication Signals” that he defended in 1973 at the Faculty of Electrical Engineering in Belgrade. From this work, two main directions arose in Prof. Kolonić’s research - statistical telecommunications and information theory (language/speech as a source of information, coding).

Prof. Kolonić’s distinct scientific contributions are in the fields of prediction and generation of speech signals, as well as speaker recognition based on specific characteristics of

digitized speech. After defending the doctoral thesis entitled “The Speaker Recognition Based on Short-Term Contours of the Speech Signal Fundamental Frequency” at the Faculty of Electrical Engineering in Belgrade in 1978, he definitely became a pioneer and one of the leading scientists of former Yugoslavia in the field of digital processing of the speech signal. Significant attention has been paid to Kolonić’s research of the model parameters for vowels generation in Serbo-Croatian, electronic identification of the speaker, estimation of the bandwidth required for digitized speech transmission, the influence of the telecommunication channel and noise on the quality of compressed speech, etc.

By investigating the possibilities for reduction of the channel capacity required for speech signal transmission, Prof. Kolonić showed that this reduction could be achieved by finding low bitrate source coders with guaranteed quality of the reconstructed speech signal, and spectrally efficient modulation techniques. Finally, he proposed a futuristic speech channel under the conditions of the finitely solved automatic recognition continual speech problem, independent on the speaker and the text synthesizer and independent on the speaker and dictionary. By this approach, the theoretical goal aimed by current practical solutions in the field of speech transmission was defined.

A number of Prof. Kolonić’s papers were dedicated to analysis of LL-DPLL (Lead Lag – Digital Phase Locked Loop). He proposed a new approach to analysis of phase locked loop based on an equation that defines normalized change in phase loop error. By analyzing LL-DPLL with RWF (Random Walk Filter), and assuming the existence of the difference between the reference and the loop frequency with presence of the additive white Gaussian noise, the detailed fundamental equation of LL-DPLL was derived, and steady-

state conditions in loop, range of loop lock, and the corresponding stationary phase error was found.

Kolonić's scientific papers dedicated to vector quantization and coding of speech signal were recognized. He applied vector quantization directly to sets of the speech signal samples, and then to sets of LPC and RELP coder parameters. In that way, the possibility for "gap filling" at middle and low bit rates of the speech signal was enabled. He proposed the application of various quantizers for bandpass signals. He pointed out the need for extension of analytical results in psychoacoustic cognitions regarding the meaning of the individual frequency bands of speech signal. He proposed a new approach to coding of the residual speech signal for 16 kbps bit rates based on delta modulation.

Prof. Kolonić published, with his associates, several distinguished papers dedicated to the Braille alphabet and the interface between a standard and Braille alphabet as well. The authors mapped 3×2 matrices, containing elements that belong to the binary set $[0, 1]$, with the elements of the Braille alphabet relief. In that way, the possibility for application of the error correcting codes algebra was enabled. This method extensively incorporates the Hamming distance as a parameter for estimation of code robustness against interference. One solution for the modification of Braille code based on maximization of the minimum Hamming distance was proposed. In that way, the balanced involvement of individual "dots" (tactile pins) in the interface was achieved. This was indicated by corresponding a priori probabilities of the individual tactile pin activities, which directed to increasing corresponding entropies compared to the standard Braille alphabet.

Prof. Kolonić's field of research covered the application of Bayesian decision theory as well. He emphasized the need for primary processing of the data obtained by measurements or by observing a certain process or space in order to select the necessary and sufficient number of measured data, and to emphasize the properties of the individual objects. This approach increases the distance between the data in the decision space. Furthermore, attractive application of linear orthogonal transformations (KL-T, F-T, W-T, H-T) was suggested in the primary processing. His particular emphasis was on a discrete cosine transformation (DCT), with real kernel functions, and with the property that these transformations take the same form as corresponding inverse transformations. He pointed out that DCT is almost optimal transformation for autoregressive AR(p) processes, and in

particular, AR(1), where exists considerable correlation between successive values of the signal. As a part of the DAAD program, he gave a lecture entitled "Bayesian and Neuman-Pearson Criteria in Communication and Radar Technology" at the Institute for Applied Physics (Johan Wolfgang Goethe Universität Frankfurt am Main, December 12th, 1997).

Over the twenty years, prof. Kolonić collaborated on research projects in "Rudi Čajavec" company in Banja Luka. I would like to emphasize his contribution to the project of radio signal transmission based on spread spectrum techniques. His theoretical research was directly applied to the field of synchronization of the direct sequence (Direct Sequence Spread Spectrum – DSSS) and frequency hopping (Frequency Hopping Spread Spectrum – FHSS) systems, and to the field of various DPLL (Digital Phase-Locked Loop) systems in particular. Moreover, prof. Kolonić was actively involved in: solving the problems of telecommunication network planning and design, the telecommunication network topologies, optimal human-computer interaction, systems for control and rational utilization of electrical energy, the impact of RF and electromagnetic fields on the environment and human health. Generally, the results of his scientific and professional research have been applied mostly to the following fields: speech coding for efficient transmission and storage, speech machines, teleconferencing systems, speech and speaker recognition, word detection systems, speech synthesis, systems for human-computer interaction), and systems for help to persons with sight, hearing and speech impairments.

The contribution of prof. Kolonić to the popularization of the work of two world famous scientists from former Yugoslavia – Nikola Tesla and Mihajlo Pupin, is invaluable.

Prof. Kolonić has not completed many research projects initiated at the end of eighties and early nineties of the last century. He was prevented by decomposition of former Yugoslavia, which he was very fond of, with the well-known consequences. One of his unfinished projects is a book "Signals and Systems in Communications".

I will remember prof. Kolonić as a great teacher, devoted and responsible scientist, excellent associate and, above all, a wonderful man.

Branko Dokić,
Editor-in-Chief

Instruction for Authors

Editorial objectives

In the review "Electronics", the scientific and professional works from different fields of electronics in the broadest sense are published. Main topics are electronics, automatics, telecommunications, computer techniques, power engineering, nuclear and medical electronics, analysis and synthesis of electronic circuits and systems, new technologies and materials in electronics etc. In addition to the scientific and professional works, we present new products, new books, B. Sc., M. Sc. and Ph.D. theses.

The main emphasis of papers should be on methods and new techniques, or the application of existing techniques in a novel way. Whilst papers with immediate application to particular engineering problems are welcome, so too are papers that form a basis for further development in the area of study.

The reviewing process

Each manuscript submitted is subjected to the following review procedures:

- It is reviewed by the editor for general suitability for this publication;
- If it is judged suitable two reviewers are selected and a double review process takes place;
- Based on the recommendations of the reviewers, the editor then decides whether the particular article should be accepted as it is, revised or rejected.

Submissions Process

The manuscripts are to be delivered to the editor of the review by the e-mail: electronics@etfbl.net.

Upon the manuscript is accepted for publication, the author receives detailed instructions for preparing the work for printing.

Authors should note that proofs are not supplied prior to publication and ensure that the paper submitted is complete and in its final form.

Copyright

Articles submitted to the journal should be original contributions and should not be under consideration for any other publication at the same time. Authors submitting articles for publication warrant that the work is not an infringement of any existing copyright and will indemnify the publisher against any breach of such warranty. For ease of dissemination and to ensure proper policing of use, papers and contributions become the legal copyright of the publisher unless otherwise agreed.

ELECTRONICS, VOL. 15, NO. 2, DECEMBER 2011

SPECIAL SECTION ON 55th CONFERENCE ETRAN	
GUEST EDITORIAL	1
BRATISLAV MILOVANOVIC BIOGRAPHY	2
ZORAN JAKŠIĆ BIOGRAPHY	3
<hr/>	
IMPROVED PLL FOR POWER GENERATION SYSTEMS OPERATING UNDER REAL GRID CONDITIONS	5
Evgenije M. Adžić, Milan S. Adžić, and Vladimir A. Katić	
LINEARIZATION OF TWO-WAY DOHERTY AMPLIFIER BY USING SECOND AND FOURTH ORDER NONLINEAR SIGNALS	13
Aleksandar Atanasković and Nataša Maleš-Ilić	
REALIZATION OF PRIMITIVES BY USING SVM FOR HUMANOID ROBOT WALK GENERATION	19
Branislav Borovac, Mirko Raković, and Milutin Nikolić	
REAL TIME METHOD FOR IMAGE RECOGNITION AND CATEGORIZATION	25
Ivan Božić and Ivan Lazić	
MATLAB/SIMULINK IMPLEMENTATION OF WAVE-BASED MODELS FOR MICROSTRIP STRUCTURES	
UTILIZING SHORT-CIRCUITED AND OPENED STUBS	31
Biljana P. Stošić, Darko I. Krstić, and Jugoslav J. Joković	
POPULATION EXPOSURE TO DEPLETED URANIUM IN THE HAN PIJESAK REGION	39
Zora Žunić, Rodoljub Simović, Zoran Čurguz, Olivera Čuknić, Jerzy Mietelski, Predrag Ujić, Igor Čeliković, Predrag Kolarž, Branko Predojević	
WINDSIM® COMPUTATIONAL FLOW DYNAMICS MODEL TESTING USING DATABASES	
FROM TWO WIND MEASUREMENT STATIONS	43
Đorđe Klisić, Miodrag Zlatanović, and Ilija Radovanović	
ROBUST ADAPTIVE SYSTEM IDENTIFICATION OF STEAM SEPARATOR PROCESS IN THERMAL POWER PLANTS	49
Goran S. Kvaščev, Aleksandra Lj. Marjanović, and Željko M. Đurović	
MULTI-CORE PLATFORM FOR DTV/STB FUNCTIONAL TESTING IN REAL-TIME	54
Dusan Milosavljević and Vladimir Zlokolica	
ELECTRONIC SOLUTION TO THE QTUD METHOD FOR MATERIALS TESTING	61
Zoran Ebersold, Nebojša Mitrović, and Slobodan Đukić	
USING EASY JAVA SIMULATIONS IN COMPUTER SUPPORTED CONTROL ENGINEERING EDUCATION	67
Milica B. Naumović, Nataša Popović, and Božidar Popović	
ANALYSIS OF SOFTWARE REALIZED DSA ALGORITHM FOR DIGITAL SIGNATURE	73
Bojan R. Pajčin and Predrag N. Ivaniš	
DESIGN OF LOW COST FORCE SENSOR SYSTEM FOR HUMAN MACHINE INTERACTION – FORCE FEEDBACK JOYSTICK	79
Miloš Petković and Goran S. Đorđević	
TWO DIMENSIONAL FINITE ELEMENT METHOD-BASED SIMULATION OF THE BROWNIAN	
MOTION OF A SPHERICAL PARTICLE IN WATER	85
Katarina Radulović and Sylvia Jeney	
AN ADAPTIVE CLUSTERING PROCEDURE WITH APPLICATIONS TO FAULT DETECTION	91
Milan R. Rapaić, Milena Petković, Zoran D. Jeličić, and Alessandro Pisano	
<hr/>	
PAPERS	
SCHEMATIC REPRESENTATION FOR ILLUSTRATING THE PROCEDURE OF OPTICAL NOISE FIGURE IN ERBIUM DOPED FIBER AMPLIFIER (EDFA) AND PRASEODYMIUM-DOPED FIBER AMPLIFIER (PDFA)	98
Abdel Hakeim M. Husein and Fady I. EL-Nahal	
DYNAMICS OF CLOSED-LOOP ADC-NOT-DAC CIRCUITS	103
Arthur E. Edang, Fredison A. Corminal, and Felicito S. Caluyo	
<hr/>	
IN MEMORIAM PROF. ĐEMAL KOLONIĆ (1942-2011)	109
